TU Delft

Delft University of Technology

Pilot-Induced Oscillations and Control Surface Rate Limiting: Comprehension, Analysis, Mitigation, and Detection

Klyde, D.H.

DOI
10.4233/uuid:5c7e535b-0110-488a-b9d5-073ee3c39059

Publication date
2022

Document Version
Final published version

Citation (APA)
Klyde, D. H. (2022). *Pilot-Induced Oscillations and Control Surface Rate Limiting: Comprehension, Analysis, Mitigation, and Detection*. [Dissertation (TU Delft), Delft University of Technology]. https://doi.org/10.4233/uuid:5c7e535b-0110-488a-b9d5-073ee3c39059

Important note
To cite this publication, please use the final published version (if applicable).
Please check the document version above.

Copyright
Other than for strictly personal use, it is not permitted to download, forward or distribute the text or part of it, without the consent of the author(s) and/or copyright holder(s), unless the work is under an open content license such as Creative Commons.

Takedown policy
Please contact us and provide details if you believe this document breaches copyrights.
We will remove access to the work immediately and investigate your claim.

This work is downloaded from Delft University of Technology.
For technical reasons the number of authors shown on this cover page is limited to a maximum of 10.

Pilot-Induced Oscillations and Control Surface Rate Limiting: Comprehension, Analysis, Mitigation, and Detection

David H. Klyde

Pilot-Induced Oscillations and Control Surface Rate Limiting: Comprehension, Analysis, Mitigation, and Detection

Proefschrift

ter verkrijging van de graad van doctor
aan de Technische Universiteit Delft,
op gezag van de Rector Magnificus prof. dr. ir. T.H.J.J. van der Hagen,
voorzitter van het College voor Promoties,
in het openbaar te verdedigen op
woensdag 6 juli 2022 om 12:30

door

David Howard KLYDE

Master of Science in de ingenieurswetenschappen,
California State Polytechnic University, Pomona, USA
geboren in Buffalo, New York, USA

Dit proefschrift is goedgekeurd door de promotoren:

Prof. dr. ir. M. Mulder
Dr. ir. M. M. van Paassen

Samenstelling promotiecommissie:

Rector Magnificus	voorzitter
Prof. dr. ir. M. Mulder	Technische Universiteit Delft, promotor
Dr. ir. M. M. van Paassen	Technische Universiteit Delft, promotor

Onafhankelijke commissieleden:

Prof. dr.ir. D.A. Abbink	Technische Universiteit Delft
Prof. dr. E.K.A. Gill	Technische Universiteit Delft
Prof. dr. P. Masarati	Politecnico di Milano, Italy
Prof. dr. J. Valasek	Texas A&M University, USA
D.G. Mitchell, MSc.	Mitchell Aerospace Research, USA

Keywords: Aircraft handling qualities, pilot-induced oscillations, human control

Printed by: Ipskamp Printing

Design: D. H. Klyde

TU Delft
Delft University of Technology

STI SYSTEMS TECHNOLOGY INC.

Copyright © 2022 by D.H. Klyde

ISBN 978-94-6421-792-6

An electronic version of this dissertation is available at

http://repository.tudelft.nl/.

CONTENTS

SUMMARY

Pilot-Induced Oscillations and Control Surface Rate Limiting:
Comprehension, Analysis, Mitigation, and Detection

David H. Klyde

From the Wright Flyer to fly-by-wire, the phenomenon of pilot-induced oscillations (PIO) has persisted, evolving with the complexity of the airframes and their associated flight control systems. Though airframe designers have long recognized the threat posed by PIO, each generation has been forced to address the issue whether identified in developmental flight test, operational flight test, or mission operations. A desired outcome of the research presented in this thesis is that these occurrences may be minimized in the second century of powered flight through enhanced comprehension and mitigation methods. To begin, it is recognized that the most significant threat of PIO in fly-by-wire aircraft comes from pilot interactions with a nonlinear flight control system response characterized by control surface actuator rate limiting, the so-called Category II PIO, and as such is the focus of this thesis. As this work was carried out over three decades, the thesis is separated into three distinct parts that address Comprehension and Analysis Methods, Category II PIO Mitigation Methods, and PIO Detection.

Part I: Comprehension and Analysis Methods begins with the nature of control surface actuator rate limiting. Using a simple model, the linear characteristics of the actuator response are completely defined in terms of its time constant. As such, the linear response is only frequency dependent. For the nonlinear actuator, three distinct response regions are identified – linear, near saturation, and highly saturated. The near saturation region features intermittent rate limiting, but the overall response remains quasi-linear. The highly saturated region, however, is characterized not only by the input command frequency, but also by the maximum rate and amplitude of the input. That is, the nonlinear response is both amplitude and frequency dependent. Comparing the simplified model with a high order actuator model from a high-performance aircraft verified the utility of the simplified approach for the study of pilot-vehicle system interactions including PIO.

Next, a generalized exact describing function-based method and associated describing function approximations are introduced to identify the gain attenuation and added phase lag associated with control surface rate limiting that can lead to pilot-induced oscillations and subsequent loss of control. The generalization was achieved using a normalized ratio of the linear to nonlinear control surface actuator time constants, where the nonlinear time constant is a function of the actuator maximum rate and the input command amplitude. This method provides an accurate measure of the phase lag due to rate limiting using easily obtained parameters. Associated with this work, an inverse describing technique was reintroduced to the community that allows for the prediction of PIO including the frequency of oscillation. Fundamentally, rate limiting introduces

added phase lag into the response of the aircraft. This alone can be sufficient to lead to PIO, depending upon the characteristics of the aircraft. Flight 1-1-5 of the X-15 provides a perfect example of this effect, wherein an aircraft configuration that had good predicted handling qualities by linear system measures, still had a severe Category II PIO due to the control surface actuator rate limiting. For Category II PIO cases where the rate limiting occurs in series with an otherwise linear system, inverse describing function techniques are used to predict the limit cycle or PIO frequency. In the X-15 example used in this thesis, the PIO frequency was significantly reduced from the linear neutral stability frequency, thus displaying the profound impact of actuator rate limiting. This result takes on added significance in light of the inability of the linear criteria and metrics to identify the PIO susceptibility of this configuration.

Building on the comprehension and analysis methods associated with nonlinear PIO that involves control surface rate limiting, Part II: Category II PIO Mitigation Methods develops two novel PIO mitigation techniques. The first method, the Smart-Cue/Smart-Gain, provides the means to alert, constrain and thereby alleviate loss of control associated with unfavorable pilot-vehicle systems interactions including PIO that are often present in high gain, closed-loop operations. Here, "ideal" pilot to surface relationships were used to measure the impact of control system effects, such as control surface rate limiting, that distort the actual control system response. The resulting Position Error measure of this "dynamic distortion" was used to develop; 1) a command path gain adjustment mechanism, a Smart-Gain, and 2) active alerting and constraining proprioceptive and tactile feedback cues to the cockpit controller, a Smart-Cue, when predetermined dynamic distortion boundaries, the Position Lag metric, are exceeded. The Smart-Gain and Smart-Cue concepts were developed and refined via piloted simulation. Flight test evaluations with test pilots from NASA and industry were then conducted using the Calspan Learjet variable stability in-flight simulator. When used together the Smart-Gain and Smart-Cue were found to enhance flight safety by significantly reducing pilot-vehicle system loss of control incidents.

From the Smart-Cue/Smart-Gain, evolved the SAFE-Cue concept. Over the last two decades, many novel adaptive flight control systems that provide a means to safely operate an air vehicle in the presence of damage or failures were introduced. While these systems show great promise, integration of exemplar systems in flight test aircraft at (U.S.) National Aeronautics and Space Administration Armstrong Flight Research facility revealed the potential for unfavorable pilot-vehicle coupling including pilot-induced oscillations. To address this issue directly, the Smart Adaptive Flight Effective Cue or SAFE-Cue system was developed that features an adaptive command path gain to mitigate oscillation tendencies and an inceptor force feedback cue to alert the pilot that the system is active. SAFE-Cue generalizes the Smart-Cue/Smart-Gain, such that a flight control system error computed from a model-based ideal system response that is compared with the actual system response is used to activate SAFE-Cue. Flight test evaluations were again conducted with the Calspan Learjet using NASA and industry test pilots. The pilots preferred and responded best to the linear or nearly linear SAFE-Cue mechanizations that resulted in a more predictable aircraft response. In the presence of a nonlinear failure, several gain only and gain plus force feedback SAFE-Cue configurations resulted in performance that approached that of the baseline healthy aircraft for each pilot. While the focus featured an adaptive controller, the SAFE-Cue concept is completely general and can be applied to any fly-by-wire flight control system implementation as a means to mitigate loss of control.

In Part III: PIO Detection, the Inceptor Peak Power-Phase (IPPP) PIO metric is introduced and validated using the Smart-Cue/Smart-Gain flight test database. The IPPP metric can be used for

analytical prediction or real-time identification and features the use of novel wavelet scalogram-based methods that consider the time-varying peak pilot input power as a function of the controlled element phase at the frequency of the peak power, all of which are elements of the PIO signature, defined in Part I. The utility of the metric was explored using a flight test database that featured 26 cases, three evaluation tasks, three evaluation test pilots, and a full range of assigned PIO tendency ratings. Before applying the metric, characteristics of the PIO signature were applied to define a normalizing term for the inceptor peak power term. Initial PIO/no-PIO boundaries were established, and the effectiveness of these boundaries was assessed using the 26 flight test cases. The results of the assessment initially found that 23 of the 26 cases were correctly identified as a PIO or no-PIO case based on the assigned PIO tendency ratings. Further analysis of the three "missed" cases revealed that the metric was working as intended and no modifications to the current boundaries were needed.

The results of this research provide the means and methods to detect and evaluate PIO tendencies that may be concealed in complex fly-by-wire flight control system designs. Describing functions based on simplified nonlinear models of the control surface actuator can be used to identify the impact of rate limiting including estimation of the added phase lag that can lead to a flying qualities cliff. The IPPP metric can be used as either an analysis or real-time flight test control room tool. In terms of mitigation, the Smart-Cue/Smart-Gain system can be used minimize the impact of the nonlinear rate limiting of an isolated control surface actuator, while the SAFE-Cue system can be used to minimize the deleterious nonlinear effects of a wider flight control system response.

Building upon this research, the next generation of control designers can address the challenging PIO cases that not only involve nonlinear system behavior, but also transitions between flight control system modes. This may prove to be significant for the emerging class of electric vertical takeoff and landing (eVTOL) rotorcraft that will almost certainly feature highly augmented vehicle dynamics and flight control modes that engage as a function of airspeed. In these cases, three or more mode transitions may occur as the vehicle accelerates from hover to cruise. For this class of vehicles as well as any other future piloted aviation system, application of appropriate PIO analysis methods, detection schemes, and mitigation approaches must be included as part of the design process from the assessment of computer simulation models, piloted simulation evaluations, and finally flight test.

NOTATION AND ABBREVIATIONS

Notations

A	Actuator command input amplitude
A_i	Sum-of-sinewave amplitude at the frequency i
a_n	Normal acceleration
E	Magnitude of actuator model error signal
E	Actuator model error signal ($e = \delta_c - \delta$)
e_L	Saturation Point
F_{as}	Lateral control stick force, also F_{LAT}
F_{cue}	Inceptor force feedback cue
F_{es}	Longitudinal control stick force, also F_{LON}
F_s	Control stick force
F_{δ_s}	Feel system spring force
f_p	Feel system preload force
f_s	Feel system coulomb friction force
G	Linear system
G	Gravity constant
H	Altitude
I_{eff}	Effective feel system inertia
I	Pilot-vehicle system input
K^*	Rate limiting element ratio of triangle output amplitude to sinusoidal maximum input amplitude (x_o/x_{imax})
K_c	Effective vehicle attitude response controlled element gain
K_f	Hydraulic servo flow rate gain
K_p	Pilot describing function gain
K_s	Feel system spring force gain
K_{SOS_c}	Sum-of-Sines command gain
K_v	Hydraulic servovalve gain

M	Mach number
M	Pilot-vehicle system output
N	Nonlinear system
P	Roll rate
Q	Pitch rate
q_{err}	Pitch rate system error
q_{Nom}	SAFE-Cue nominal system pitch rate
$\bar{q}$	Dynamic pressure
$P(\omega,t)$	Wavelet-based scalogram
$P_{max}(t)$	Wavelet-based scalogram peak power at time t
p_{err}	Roll rate system error
S	Laplace domain complex variable
T	Linear system time constant (actuator model, $T = 1/\omega_a$)
T_{LAG}	Time lag
T_{NL}	Nonlinear system actuator model indicial response time constant
T	Time
t_D	Rate limiting element phase difference between triangle output and sinusoidal input ($t_D = t_o - t_i$)
t_i	Rate limiting element time to maximum input amplitude
t_o	Rate limiting element time to maximum output amplitude
V_i	Indicated airspeed
V_L	Actuator rate limit
V_{max}	Maximum surface limit
V_V	Vertical speed
x_i	Rate limiting element sinusoidal input amplitude
$\dot{x}_i$	Rate limiting element sinusoidal input rate
x_{imax}	Rate limiting element maximum sinusoidal input amplitude
x_o	Rate limiting element triangle output amplitude
$\dot{x}_o$	Rate limiting element sinusoidal output rate

$Y_{c_{effective}}$	Effective attitude response transfer function
Y_c	Controlled element describing function
Y_p	Pilot describing function
α	Angle-of-attack
β	Angle-of-sideslip
$\Delta\phi$	Additional phase lag due to rate limiting
δ	Surface position
$\dot{\delta}$	Surface actuator rate
δ_a	Aileron position
δ_{as}	Lateral control stick position
δ_c	Surface command
$\delta_c^{'}$	Surface command after SAFE-Cue gain
δ_{err}	Smart-Cue/Smart-Gain position error
δ_h	Horizontal stabilizer position
$\dot{\delta}_h$	Horizontal stabilizer rate
δ_{h_c}	Horizontal stabilizer position command
δ_{LAG}	Position lag
δ_p	Pilot command input
δ_{PE}	Position error
δ_s	Control stick position
$\dot{\delta}_s$	Control stick rate
$\ddot{\delta}_s$	Control stick acceleration
δ_v	Hydraulic servovalve position
ϕ	Roll attitude
ϕ_i	Actuator input phase angle
$\phi_{max}(t)$	Controlled element phase lag at the wavelet-based scalogram frequency at which the maximum power occurs for time t

$\hat{\phi}_{\max}(t)$	Weighted controlled element phase lag for time *t*
θ	Pitch attitude
θ_c	Pitch attitude command
θ_e	Pitch attitude error
τ_e	Effective delay
τ_{p_ϕ}	Roll attitude phase delay
τ_{p_θ}	Pitch attitude phase delay
ω	Frequency
ω_a	Actuator bandwidth frequency
ω_a^*	Actuator nonlinear bandwidth frequency
$\omega_{BW\phi}$	Roll attitude bandwidth frequency
ω_{BW_θ}	Pitch attitude bandwidth frequency
ω_i	Actuator input frequency
ω_{LCO}	Limit cycle oscillation frequency
$\omega_{\max}(t)$	Wavelet-based scalogram frequency at which the maximum power occurs for time *t*
$\hat{\omega}_{\max}(t)$	Weighted wavelet-based scalogram frequency for time *t*
ω_{onset}	Actuator saturation onset frequency
ω_s	Actuator saturation frequency
ζ	Damping ratio

Abbreviations

AFB	(U.S.) Air Force Base
AIAA	American Institute of Aeronautics and Astronautics
AirSTAR	Airborne Subscale Transport Aircraft Research
AVGSTB	(F-14) Average stabilizer position
BUFCM	(F-14) Back Up Flight Control Module
BW	Bandwidth
DF	Describing Function
DFA	Describing Function Approximation
DOF	Degrees of Freedom
DSP	(Calspan Learjet) Digital Signal Processor
EP	Evaluation Pilot
FAA	Federal Aviation Administration
FBW	Fly-By-Wire
FCS	Flight Control System
FFT	Fast Fourier Transform
FWD	Forward
HQR	(Cooper-Harper) Handling Qualities Rating
IPPP	Inceptor Peak Power-Phase
KIAS	Knots Indicated Airspeed
LOCATS	Loss of Control Analysis Tool Set
LOCIS	Loss of Control Inhibition System
LOSPOSIN	(F-14) Longitudinal stick position in inches
MOA	(U.S.) Military Operations Area
MRAC	Model Reference Adaptive Control
NACA	(U.S.) National Advisory Committee for Aeronautics
NASA	(U.S.) National Aeronautics and Space Administration
NAWCAD	(U.S.) Naval Air Warfare Center, Aircraft Division
NRC	(Canada) National Research Council

PAC	Phase Aggression Criterion
PIO	Pilot-Induced Oscillation
PIOR	Pilot-Induced Oscillation (tendency) Rating
PIOS	Pilot-Induced Oscillation Suppression filter
RHO/MSLS	Receding Horizon Optimal (controller)/Modified Sequential Least Squares
RL	Rate Limit
RMS	Root Mean Square
ROVER	Real-time Oscillation Verifier
SAFE-Cue	Smart Adaptive Flight Effective Cue
SAS	Stability Augmentation System
SoS	Sum-of-Sines
SP	Safety Pilot
STI	Systems Technology, Inc.
TED	Trailing Edge Down
TEU	Trailing Edge Up
VISTA	(X-62A) Variable Stability Flight Simulator Test Aircraft
VSS	(Calspan Learjet) Variable Stability System
VSST	(NASA) Vehicle Systems Safety Technology (program)

1. Introduction

It surprised me, it really shocked me... I thought something had broken and I didn't see any [warning] lights...

Thomas Morgenfeld, Test Pilot, "Report Pinpoints Factors Leading to YF-22 Crash," Michael A. Dornheim, Aviation Week and Space Technology, November 9, 1992

Parts of this chapter have been published as:

Title	Identifying a Pilot-Induced Oscillation Signature: New Techniques Applied to Old Problems
Journal	Journal of Guidance, Control, and Dynamics, vol. 31, no. 1, pp. 215-224, 2008
Authors	D. G. Mitchell and D. H. Klyde

1.0 INTRODUCTION

1.1 Pilot-Induced Oscillations and the First Century of Powered Flight

On December 17, 1903 Wilbur and Orville Wright successfully conducted the world's first powered flight at Kill Devil Hills in North Carolina. Though not recognized at the time, the Wrights also introduced the world to the phenomenon of pilot-induced oscillations. Detailed definitions are provided in the next section, but in short, a pilot-induced oscillation or PIO is an out-of-phase oscillation observed between the control inputs of the pilot and the response of the vehicle to that input. For the Wright Flyer, the out-of-phase oscillations resulted from the attempt of the pilot to control an airframe that was statically and dynamically unstable in the longitudinal axis. In their flight dynamics study of the 1903 Wright Flyer configuration [1, page 537], Jex and Culick noted that "*The strongly unstable pitching characteristic of the 1903 Flyer is arguably its worst feature… The large negative static margin (-20%) and limited control trim range meant that the airplane was barely controllable.*" In a related paper [2, page 43], these authors noted that pilot-induced oscillations "*were likely a problem for the 1903 Flyer, as shown by photographs in which the canard is fully deflected fully up or down.*"

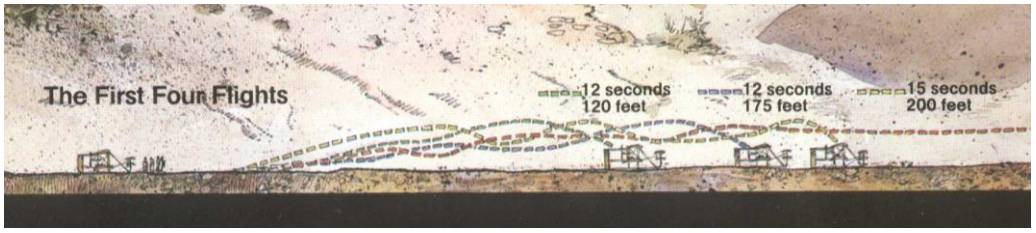

(a) Illustration of first four flights with observed flight path oscillations (from the United States National Park Service Brochure for the Wright Brothers National Memorial, North Carolina)

(b) Site of the first four flights as observed 100 years later

Figure 1.1: *The first four powered flights conducted by the Wright Brothers on Dec. 17, 1903.*

From the Wright Flyer to fly-by-wire, the phenomenon of pilot-induced oscillations has persisted, evolving with the complexity of the airframes and their associated flight control systems. Though

airframe designers have long recognized the threat posed by PIO, each generation has been forced to address the issue whether identified in developmental flight test (for example, the YF-16 [3]), operational flight test (for example, F-14 [4]), or mission operations (for example, C-17 [5]). A desired outcome of the research presented herein is that these occurrences may be minimized in the second century of powered flight through enhanced comprehension and mitigation methods.

Since its founding in California in 1957, Systems Technology, Inc. has participated in the search for comprehension and solutions to the PIO phenomenon as a core activity. The research described in this thesis began in the 1990's after a series of high profile PIO events occurred that featured control surface actuator rate limiting as a key element. Since such events almost always result in severe PIO, funding for research in this area became available and was sustained for the next several decades beginning with the United States Air Force Unified PIO Program [6,7,8,9,10] and continuing to the European Union ARISTOTEL Program (Aircraft and Rotorcraft Pilot Couplings – Tools and Techniques for Alleviation and Detection) [11], which concluded in 2013.

1.2 The PIO Signature[1]

The United States Department of Defense Interface Standard for Flying Qualities of Piloted Airplanes, MIL-STD-1797A [12] contains a concise definition of PIO: it consists of "sustained or uncontrollable oscillations resulting from efforts of the pilot to control the aircraft." It has been suggested that the word "unintentional" be added before "sustained," to distinguish from intentional oscillatory behavior. This recognizes the important fact that in a PIO the pilot is not seeking the out-of-phase oscillatory pilot-vehicle system behavior, but the PIO is instead a deleterious effect resulting from unfavorable pilot-vehicle system coupling.

Taken literally, the MIL-STD-1797A definition means that any oscillation that occurs during manual, piloted control may be classified as a PIO. Yet many times this oscillation is nothing more than a result of pilot overcontrol in an otherwise normal circumstance. For example, to the outsider the typical ballooning in flight path that any student pilot encounters during landing training may appear to be a PIO. This ballooning is simply part of standard pilot compensation and is usually no more than one or two cycles, with no threat of developing into a life-threatening PIO event. Indeed, visual inspection of the time history records from even the experienced pilot in the landing flare with a known good airplane may often reveal small corrections that might appear to be signs of a PIO. These are not what MIL-STD-1797A is referring to, nor are they to be feared.

[1] The material in this section has been adopted from a paper written by the author of this thesis and longtime collaborator David Mitchell wherein the key elements of PIO, that is, the PIO signature was defined. [Mitchell, D. G. and D. H. Klyde, "Identifying a Pilot-Induced Oscillation Signature: New Techniques Applied to Old Problems," *Journal of Guidance, Control, and Dynamics*, vol. 31, no. 1, pp. 215-224, 2008.]

There is a certain appeal to declaring every unintentional oscillation a PIO. A sure way to raise eyebrows in a full-scale development flight program is for a pilot in a post-flight debrief to hint that the aircraft in question exhibits PIO tendencies. This may result in an overreaction by the test team, even if the pilot clearly states that the oscillations were extremely minor, resulted from very high-bandwidth manual control, and could easily be terminated. When emotion is removed from the equation, the pilot can be asked about the frequency, amplitude, tendency to diverge, etc., for the event in question, and the handling qualities experts can then determine if there is real cause for concern. This would then lead to a systematic method for quantitative analysis of the event and an investigation of its causes. Quantitative analysis of PIO is a major theme of this thesis and the reference [13] paper.

Residual oscillations that continue even if the pilot is no longer attempting to control the aircraft are not PIO. Typically, these residual oscillations are the result of lightly damped modes. To complicate the interpretation, lightly damped modes can result in PIO if flight control system failures result in zero damping. Many of the PIOs recorded in older (1950s and earlier vintage) aircraft are traceable directly to low inherent damping of the short period or Dutch roll modes. To eliminate any potential confusion, PIO as stated in [12] results from "efforts of the pilot to control the aircraft." Since the PIO is evidence of an undamped closed-loop, pilot-vehicle oscillation, then there must exist during the PIO at least one measurable aircraft state that is 180 degrees out of phase with at least one pilot control. This leads to the following proposed definition from [13, page 217]: "*A PIO exists when the airplane attitude, angular rate, normal acceleration, or other quantity derived from these states, is approximately 180 degrees out of phase with the pilot's control inputs.*" Of course, there can be many occurrences of 180 degree out of phase oscillations within the context of a pilot-vehicle system. With this in mind, an important element of the PIO signature is that the out of phase oscillations must be at an amplitude and frequency to impact the task. Therefore, the high frequency, small amplitude out of phase oscillations that often occur are of no consequence to PIO.

There are many, perhaps hundreds, of time traces in the open literature that illustrate the two precepts for PIO introduced so far: 1) oscillatory time responses; and 2) out-of-phase behavior. The literature reveals that PIOs can occur in all aircraft including high performance military aircraft, commercial transports, business jets, and rotorcraft [13]. Some aircraft have also experienced ground handling PIO that can occur during high-speed rollout after landing [14]. As an illustration, consider three rather well-known sets of traces in Figure 1.2. They are the pilot control stick inputs (force or position) and angular attitude outputs for the YF-22 low-altitude pitch PIO [15] at Edwards AFB in 1992; the roll PIO of an MV-22 near a ship [16] in 1999; and a pitch PIO of an F-14 [4], operating on its backup flight control module or BUFCM, while attempting an in-flight refueling in 1990. While there is evidence of high-frequency control activity on all control stick traces in Figure 1.2, a lower-frequency, sinusoidal oscillation is evident as well. Angular attitude is approximately 180 degrees out of phase with pilot control stick inputs at the start of the oscillations, and in all cases is more than 180 degrees out of phase by the end of the traces.

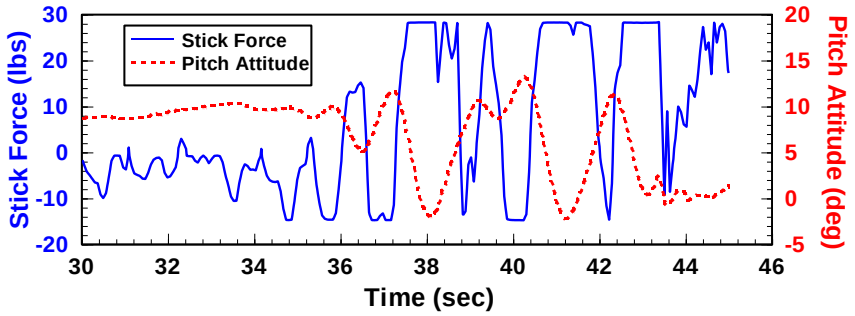

(a) YF-22 (1992)

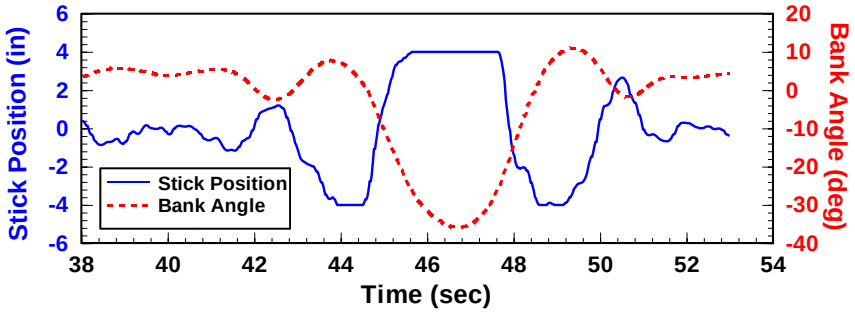

(b) MV-22 (1999)

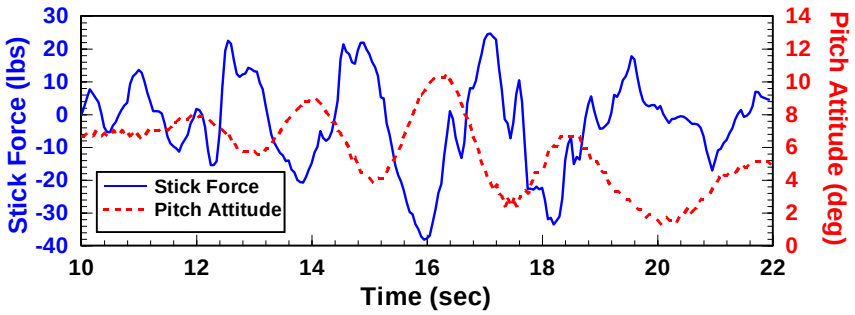

(c) F-14 BUFCM (1990)

Figure 1.2: *Input-output pairs for three example PIO events demonstrate out-of-phase oscillatory characteristics.*

Because of the critical importance of distinguishing between a potentially catastrophic PIO and nuisance oscillations, one solution is to change the definition of PIO. The primary emphasis is to make a distinction between closed-loop pilot/aircraft oscillations that are a side effect of the pilot's tracking effort and those that have a potential for loss of control. These oscillations may look identical on recorded data, and only the pilot involved can properly make this crucial distinction.

One way of viewing the crucial distinction between oscillations resulting from degraded handling and those that can result in a divergent PIO is to note that in the former case the pilot drives the oscillation, whereas in a "real" PIO (as defined here) the pilot is driven by the oscillation. If the oscillation requires that the pilot redirects efforts away from the primary task by a noticeable amount, such that a new task has been created (for example, stop the oscillation). In such cases the pilot is being driven by the oscillation and is therefore forced to do a new task. In extreme cases (for example, YF-22 [15]), the pilot thought that he had experienced a flight control system failure, and that the new task was to cope with that failure.

One important way to characterize PIO is by the amplitude of the pilot's input and the aircraft's response. If both input and output are below a certain threshold, one should not care if the first two definitions (oscillations and out-of-phase) are met, because the pilot will not even see it, or it will appear to be nothing more than a minor nuisance. Thus, to be a real "PIO," the input, or output, or both, must be large enough to be noticed.

In summary, the signature of PIO is defined by:

- The presence of an oscillation.
- A pilot control input that is 180 degrees out-of-phase with a vehicle response (typically attitude, angular rate, or linear acceleration).
- Oscillations that are large enough to be noticed by the pilot and have an impact on task performance.

1.3 PIO Categories

In 1997, a summary report by a United States National Research Council (NRC) Committee on the Effects of Aircraft-Pilot Coupling on Flight Safety was published [17]. The NRC Committee separated PIOs by Category per earlier reported work first published in [18] and further detailed in [6]. The categories depend essentially on the degree of nonlinearity in the event:

- Category I: Linear pilot-vehicle system oscillations. These PIOs result from identifiable phenomena such as excessive time delay, excessive phase loss due to filters, improper control/response sensitivity, etc. They are the simplest to model, understand, and prevent. They are also the least common in operational flying.
- Category II: Quasi-linear events with some nonlinear contributions, such as rate or position limiting. For the most part, these PIOs can be modeled as linear events, with an identifiable nonlinear contribution that may be treated separately. The most common nonlinear contribution is the subject of this thesis: rate limiting of a control effector actuator. These are the most common severe PIO events.
- Category III: Nonlinear PIOs with transients. Such events are difficult to recognize and rarely occur but are always severe. Mode switching that cannot be represented by a quasi-linear equivalent is the common culprit.

The pilot-vehicle oscillations in Category I may be casual, easily repeatable, readily eliminated by loosening control (that is, lowering pilot gain), and are generally non-threatening. With a major triggering input, however, the oscillations may be quite severe and catastrophic. More often than not, these situations involve aircraft configurations that are characterized by excessive lags. Analyses of Category I oscillation possibilities can reveal the oscillatory frequencies consistent with a presumed type of pilot behavior (for example, compensatory or synchronous), pilot gain levels, and nominal high-gain pilot-vehicle system bandwidths. These events are far and away the dominant PIO category found in flight research.

Category II PIOs are very similar to those of Category I except for the dominance of key lag-introducing series nonlinearities. They are invariably severe PIOs, whereas Category I covers both small and large amplitude levels. Rate limiting, either as a series element or as a rate-limited surface actuator, modifies the Category I situation by adding an amplitude-dependent lag and by setting the limit cycle magnitude. Other simple nonlinearities (for example, stick command shaping and aerodynamic characteristics) may also be present.

Category III PIOs can be much more complicated to analyze in that they intrinsically involve transitions in either the pilot or the effective controlled element dynamics. Thus, there are a minimum of two sets of effective pilot-vehicle characteristics involved: pre- and post-transition. When these differ greatly, very severe PIOs can occur. The shifts in controlled element dynamics may be associated with the size of the pilot's input, or may be due to internal changes in either control system or aerodynamic/propulsion configurations, mode changes, etc. Pilot transitions may be shifts in dynamic behavioral properties (for example, from compensatory to synchronous), from modifications in cues (for example, from attitude to load factor), or from behavioral adjustments to accommodate task modifications (for example, from target tracking to boundary avoidance tracking).

The categories defined above do not differentiate as to PIO severity (that is, large-amplitude severe PIOs can occur in all categories). They also have little if anything to say about the subjective and emotional aspects of a severe PIO. The pilot involved cares not at all whether his or her encounter was a Category I, II, or III event! For the analyst, on the other hand, such details are essential to develop understanding of the event and determine corrective actions.

1.4 Problem Statement

1.4.1 Research Goal

Prior to the work of this thesis, which was conducted over several decades, past research into PIO was typically proceeded by high profile PIO events that then led to additional funding. High profile PIO events involving the T-38 [19], F-4 [20], and X-15 [21] led the PIO work conducted by STI in the 1960's that was summarized in [22]. The next set of high profile PIO events were associated with the introduction of fly-by-wire flight control systems that included the YF-16 Flight 0 [3] and Space Shuttle [23]. Research at this time, in general, focused primarily on addressing handling qualities of higher order systems on not specifically PIO. The collected work was released by the U.S. Department of Defense in the interface standard, MIL-STD-1797A, that featured new criteria such as Neal-Smith, Airplane Bandwidth, and others [12]. High profile PIO

events again occurred in the late 1980's and early 1990's. These severe PIO events included the C-17 [5], YF-22 [15], V-22 [16], and JAS-39 Gripen [24] and all featured control surface actuator limiting, the focus of this thesis. These events resulted in the Unified PIO Theory research introduced earlier in this chapter including the work that initiated the research described in this thesis. Given that modern PIO phenomena are dominated by the presence of control surface actuator rate limiting, the goals of this thesis are as follows:

To address Category II PIO, the goals of this thesis are to
Provide enhanced comprehension and analysis methods, in-flight mitigation methods, and wavelet-based detection methods.

The theories, analyses, mitigation, and detection methods featured in this thesis are designed to be general and are therefore not tied to a particular aircraft type, flight control system architecture, or cockpit inceptor configuration.

1.4.2 Approach and Scope of Thesis

The primary inspiration for what became the work of a career and the foundation of this thesis are a handful of pages found in the Appendix of the classic PIO reference by Ashkenas, Jex, and McRuer [22], the "founding fathers" of Systems Technology, Inc. The career work began with the research conducted as part of the Unified PIO Theory program that was sponsored by the United States Air Force [6]. The objective of this research was to understand the nature of control surface actuator rate limiting and its role in Category II PIO. The Appendix pages describe a simplified model of a rate limited servo along with describing function approximations for the near saturation and highly saturated model conditions. It also alludes to an exact describing function solution that can be used to describe the system for a given set of model and input conditions. This served as the launching point for the research of this thesis that addresses the following topics.

- A generalized describing function representation of a rate limited control surface actuator is defined that allows for the resulting added phase lag and gain attenuation to be computed given the command input amplitude and frequency and the actuator maximum rate.
- An inverse describing function analysis method based on this generalized describing function and a simplified rate limiting element representation are used to provide a prediction of the pilot-induced oscillation limit cycle frequency.
- A pilot-induced oscillation mitigation method is developed and tested that features an active inceptor cue that alerts the pilot of potential pilot-induced oscillation onset and an adaptive command path gain that mitigates the jump resonance [25], the sudden transition from one amplitude of oscillation of another, associated with control surface rate limiting. The resulting "Smart-Cue" and "Smart-Gain" were refined via piloted

simulation and validated in flight by experienced test pilots using the Calspan Learjet In-Flight Simulator aircraft.

- Building upon the success of the Smart-Cue and Smart-Gain innovations, the concept was reimagined to mitigate the deleterious effects of adaptive control approaches that were shown in flight test at NASA and elsewhere to create unfavorable pilot-vehicle interactions including pilot-induced oscillations in the presence of failures. This more general Smart Adaptive Flight Effective Cue (SAFE-Cue) was also refined via piloted simulation and validated in flight by experienced test pilots again using the Calspan Learjet In-Flight Simulator aircraft.
- Using wavelet-based techniques that allow for time-varying frequency responses, a new pilot-induced oscillation detection metric is defined and validated using the data from the Smart-Cue/Smart-Gain flight test database.

Taken together, this research provides a holistic approach to Category II PIO wherein the results provide enhanced comprehension, improved analysis methods, on-board mitigation techniques, and new wavelet-based detection metrics that can be used to identify PIO.

With its focus on Category II PIOs, the scope of this work does not address the largely solved comprehension and mitigation methods associated with Category I PIOs, that is, essentially linear system oscillations, see, for example, [10, 11, 17]. Further, this work does not address Category III PIO with its focus on mode transitions within the flight control system and/or pilot-vehicle system. These transitions are typically design dependent and are therefore difficult to generalize. Nonetheless, new research in this area is clearly needed as advanced air mobility vehicles, many featuring electric propulsion and highly augmented fly-by-wire flight control laws that transition as a function of speed, enter operation.

1.5 Guidelines for the Reader

The chapters of this thesis have been organized into three parts. Chapters 2 – 4 comprise Part I: Comprehension and Analysis and cover the comprehension of Category II PIO with control surface actuator rate limiting. Chapters 5 – 10 comprise Part II: Category II PIO Mitigation Methods and cover the use of active inceptor force cueing and command path gain adjustments to mitigate Category II PIO. Finally, Chapters 11 – 12 comprise Part III: PIO Detection and cover the development and application of a wavelet scalogram-based PIO detection method. The content of each chapter is comprised primarily of previously published journal and conference papers. Source material is identified in the introduction of each chapter. As such, each chapter can be read independently though the intention is that each of the three parts tells a complete story. An appendix is included that derives the wavelet-based scalograms that are used as an analysis tool and a key element of the PIO detection method.

1.6 References

1. Jex, H. R., and F. E. C. Culick, "Flight Control Dynamics of the 1903 Wright Flyer," AIAA 85-1804-CP presented at the *AIAA 12th Atmospheric Flight Mechanics Conference*, Snowmass, CO, August 19-21, 1985.

2. Culick, F. E. C., and H. R. Jex, "Aerodynamics, Stability and Control of the 1903 Wright Flyer," published in *Proceedings of the Symposium on the 80th Anniversary of the Wright Brothers First Flight*, Smithsonian Institution, December 16, 1983.

3. Smith, J. W., *Analysis of a Lateral Pilot-Induced Oscillation Experienced on the First Flight of the YF-16 Aircraft*, NASA TM-72867, September 1979.

4. Niewoehner, R., LCDR USN, and S. Minnich, "F-14 Dual Hydraulic Failure Flying Qualities Evaluation," *Thirty-Fifth Symposium Proceedings*, Society of Experimental Test Pilots, September 1991, pp. 4-15.

5. Weltz, G. L, K. M. Shweyk, and D. M. Murray, "Application of New and Standard Pilot-Induced Oscillation (PIO) Analysis Methods to Flight Test Data of the C-17 Transport Aircraft," AIAA-2007-6387 presented at *Atmospheric Flight Mechanics Conference*, Hilton Head, SC, 2-23 August 2007.

6. Klyde, D. H., D. T. McRuer, and T. T. Myers, *Unified Pilot-Induced Oscillation Theory Volume I: PIO Analysis with Linear and Nonlinear Vehicle Characteristics, Including Rate Limiting*, WL-TR-96-3028, Dec. 1995.

7. Preston, J. D., J. Hodgkinson, J. Buckley, K. Citurs, D. G. Mitchell, and R. H. Hoh, *Unified Pilot-Induced Oscillation Theory, Volume II: Pilot-Induced Oscillation Criteria Applied to Several McDonnell Douglas Aircraft*, WL-TR-96-3029, Dec. 1995.

8. Anderson, M. R., and A. B. Page, *Unified Pilot-Induced Oscillation Theory, Volume III: PIO Analysis Using Multivariable Methods*, WL-TR-96-3030, Dec. 1995.

9. Bailey, R. E., and T. J. Bidlack, *Unified Pilot-Induced Oscillation Theory Volume IV: Time-Domain Neal-Smith Criterion*, WL-TR-96-3031, Dec. 1995.

10. Mitchell, D. G., and R. H. Hoh, *Development of Methods and Devices to Predict and Prevent Pilot-Induced Oscillations*, AFRL-VA-WP-TR-2000-3046, Dec. 2000.

11. Pavel, M. D., *Aircraft and Rotorcraft Pilot Couplings – Tools and Techniques for Alleviation and Detection*, ARISTOTEL 266073, Final Publishable Summary, July 8, 2014.

12. Anon., *Department of Defense Interface Standard, Flying Qualities of Piloted Aircraft*, MIL-STD-1797A, Jan. 1990; Notice of Change, 28 June 1995.

13. Mitchell, D. G. and D. H. Klyde, "Identifying a Pilot-Induced Oscillation Signature: New Techniques Applied to Old Problems," *Journal of Guidance, Control, and Dynamics*, vol. 31, no. 1, pp. 215-224, 2008.

14. Klyde, D. H., T. T. Myers, R. E. Magdaleno, and J. G. Reinsberg, "Identification of the Dominant Ground Handling Characteristics of a Navy Jet Trainer," *J. Guidance, Control, and Dynamics*, Vol. 25, No. 3, 2002, pp. 546-552.

15. Dornheim, M. A., "Report Pinpoints Factors Leading to YF-22 Crash," *Aviation Week & Space Technology*, 9 Nov. 1992, pp. 53-54.

16. Rudzis, J. D., and Seymour, C., "Unique Tiltrotor Handling Characteristics Encountered During MV22 Sea Trials Tests," *Forty Fourth Symposium Proceedings*, Society of Experimental Test Pilots, Lancaster, CA, Sept. 2000, pp. 67-79.

17. Anon., *Aviation Safety and Pilot Control*, prepared by the National Research Council Committee on the Effects of Aircraft-Pilot Coupling and Flight Safety, National Academy Press, Washington, D.C., 1997.

18. McRuer, D. T., *Pilot-Induced Oscillations and Human Dynamic Behavior*, NASA CR-4683, Dec. 1994.

19. Jex, H. R., *Summary of T-38 PIO Analyses*, STI-TR-239-1, Systems Technology, Inc. Hawthorne, CA, Jan. 1963.

20. McPherson, T. M., and E. J. Hogan, Jr., *Low Altitude High Speed Flight Evaluation of the F-4A/B (F4H-1F/-1) Airplane*, NATC-RAD32-103, 2 April 1963.

21. Matranga, G. J., *Analysis of X-15 Landing Approach and Flare Characteristics Determined from the First 30 Flights*, NASA TN-D-1057, July 1961.

22. Ashkenas, I. L., H. R. Jex, and D. T. McRuer, *Pilot-Induced Oscillations: Their Cause and Analysis*, Norair Report NOR-64-143, Northrop Corporation, July 24, 1964.

23. Teper, G.L., R.J. DiMarco, I.L. Ashkenas, and R.H. Hoh, *Analysis of Shuttle Orbiter Approach and Landing Conditions*, NASA CR-163108, July 1981.

24. Kullberg, E., and P.O. Elgerona, "SAAB Experience with PIO," *Flight Vehicle Integration Panel Workshop on Pilot Induced Oscillations*, AGARD-AR-335, February 1995, pp. 9-1 to 9-9.

25. Graham, D., and D. McRuer, "Retrospective Essay on Nonlinearities in Aircraft Flight Control," *J. Guidance*, Vol. 14, No. 6., Nov.-Dec. 1991, pp. 1089 – 1099.

Part I: Comprehension and Analysis Methods

2. The Nature of Control Surface Actuator Rate Limiting

At its most insidious, rate limiting phenomena can cause the sudden, dramatic onset of substantial incremental shift in the phase lag, which is instantly manifested by a change in pilot gain or command.

Committee on the Effects of Aircraft-Pilot Coupling on Flight Safety, National Research Council, 1997

Parts of this chapter have been published as:

Title	Pilot-Induced Oscillation Analysis and Prediction with Actuator Rate Limiting
Journal	Journal of Guidance, Control, and Dynamics, vol. 20, no. 1, Jan.-Feb. 1997, pp. 81 – 88
Authors	D. H. Klyde, D. T. McRuer, and T. T. Myers
Title	Investigating the Role of Rate Limiting in Pilot-induced Oscillations
Journal	Journal of Guidance, Control, and Dynamics, vol. 27, no. 5, Sept.-Oct. 2004, pp. 804-813
Authors	D. H. Klyde and D. G. Mitchell

2.0 THE NATURE OF CONTROL SURFACE ACTUATOR RATE LIMITING

The material in this chapter has been taken largely from two references [1,2] that explore the nature of control surface actuator rate limiting. As mentioned in Part 1, the material herein was inspired by the work of Ashkenas, Jex, and McRuer as found in the Appendix of their classic PIO report from the 1960's [3]. This work inspired the further development of the rate limiting describing function analyses of [4] that was conducted as part of the United States Air Force Unified PIO Theory Program of the mid 1990's.

2.1 Introduction

Throughout the first 100 years of powered flight, aircraft handling qualities has been addressed as a secondary consideration of the design process that is typically dominated by performance and cost requirements. Because of their often catastrophic nature, however, nothing brings attention to handling qualities like a high profile PIO. Traditionally, the occurrence of such an event has led to research activities that are intended to alleviate the problem once and for all. Despite significant technical advances in this area, PIOs continue to occur with both flight test and operational aircraft.

The focus of the Comprehension and Analysis Methods sections of this thesis is on the role of rate limiting in PIO. The earliest well-documented PIO event that featured rate limiting was the first flight of the X-15 aircraft in 1959. This event, which is discussed in more detail in Chapter 4 of this thesis, is one of the most analyzed of all PIO events. Among the earliest is the analysis documented in [3] that features the development of describing function approximations for a rate limited actuator and an inverse describing function technique used to predict limit cycle oscillations and their frequencies. Attention to the effects of rate limiting and other system nonlinearities surfaced again in conjunction with the severe PIOs that occurred with the YF-12 aircraft during aerial refueling. An excellent description of the nonlinear analysis of these events was done at NASA by Smith and Berry [5].

More recent highly documented PIO events that involved rate limiting include the YF-22 [6] and JAS-39 [7] events. These events that resulted in significant damage to the YF-22 and the loss of two JAS-39 aircraft inspired a new thrust in handling qualities research that emphasized comprehension, prevention, and alleviation of the nonlinear effects associated with rate limiting. Specifically, the YF-22 event led to the Air Force Unified PIO Program described in Chapter 1 of this thesis, while the JAS-39 events led SAAB to develop a patented control scheme [7] designed to alleviate the effects of rate limiting.

For PIO to occur, there must be a trigger [8,9]. Following the well-publicized crashes of the YF-22 and the JAS-39 aircraft in the early 1990's, it was speculated, on the other hand, that rate limiting was a trigger for most PIOs on fly-by-wire aircraft. After the research efforts of the 1990's including the Unified PIO Program, it was concluded that rate limiting can be a trigger for PIO. Sometimes PIO can also be the cause of the rate limiting. Further, it is possible to encounter severe rate limiting without a PIO. Comprehension of these possible outcomes is

important if Category II PIOs are to be mitigated in design or via on-board counter measures such as the PIO suppression filter used on the Space Shuttle [10].

2.2 A Simplified Actuator Model with Rate Limiting

2.2.1 Simplified Model Description

A block diagram of a simplified rate limited servo actuator model [1,2,4] is presented in Figure 2.1. As shown in the figure, the input surface command (δ_c) produces an output surface deflection (δ). The output deflection is fed back to the command to produce an error signal, $e = \delta_c - \delta$. In the forward path the error signal serves as the input to the nonlinear saturation block. The saturation block is characterized by two design parameters: 1) a gain equivalent to the linear actuator closed-loop bandwidth or more simply referred to as the linear bandwidth (ω_a) and 2) a saturation value equivalent to the actuator rate limit (V_L). From Figure 2.1, it is clear that the saturation point (e_L) can be defined in terms of these design parameters by $e_L = V_L/\omega_a$. The output from the saturation block is the surface rate ($\dot{\delta}$). This signal is then integrated to produce the surface deflection (δ).

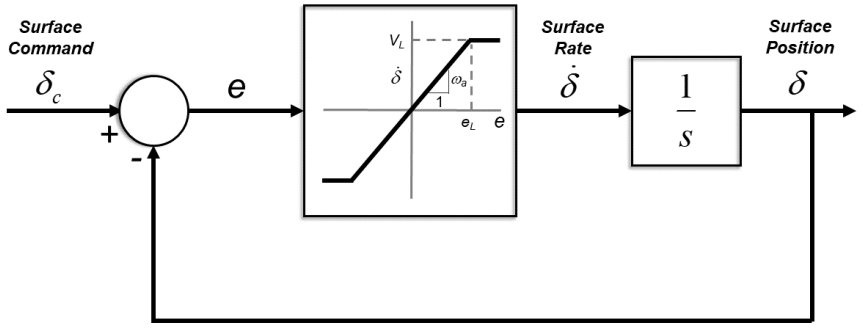

Figure 2.1: *Simplified control surface actuator model [3].*

The model has three distinct operating ranges. First, when $e < e_L$, the model is linear with a closed-loop response characterized by a simple first order lag with a time constant, $T = 1/\omega_a$. These first order features are exemplified in the Bode plot and step time response of Figure 2.2. Here, everything is characterized by the time constant. Interpreted in the frequency domain, T is the inverse of the linear bandwidth (that is, the frequency at which the output/input is down 3 dB from the value at zero frequency) as shown in Figure 2.2(a). In the time domain the step response is governed completely by the time constant. For example, the Figure 2.2(b) exponential response exhibits a series of subtangents that again reflect T. The time constant also corresponds to a "system rise time" of the indicial response that is determined by the time to reach the maximum (final) surface displacement at the maximum output velocity. One or more of these characteristics is fundamentally changed when the input amplitude exceeds the linear region saturation point.

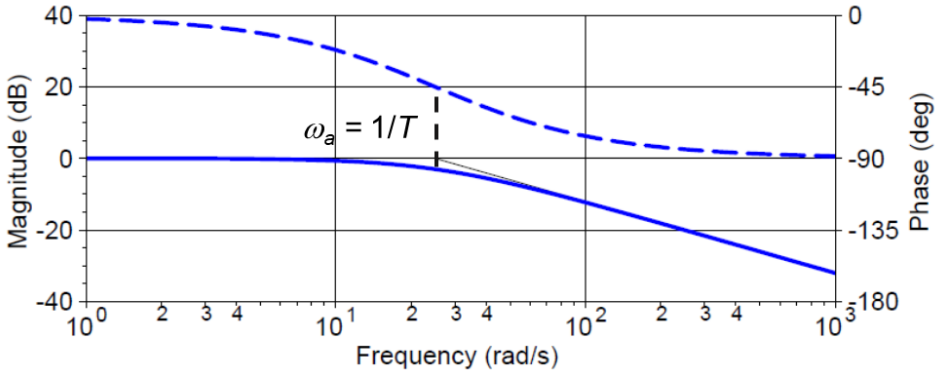

(a) Bode frequency response

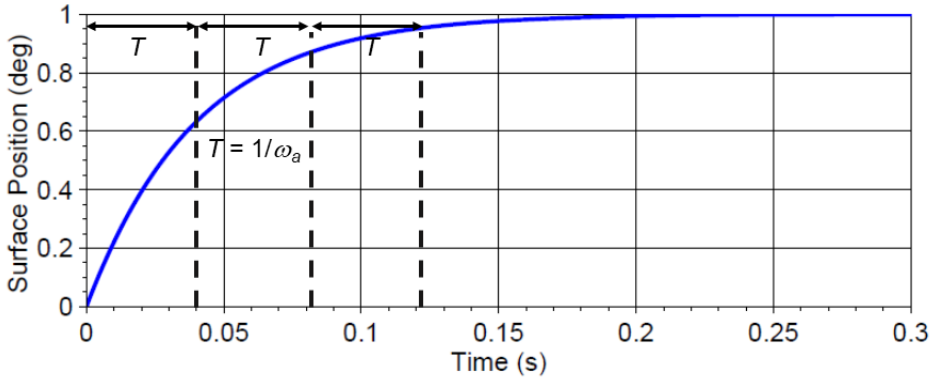

(b) Step response

Figure 2.2: *Linear control surface actuator Bode plot and step time response.*

The second operating range is the near saturation range that occurs when the maximum error exceeds e_L by a small amount. This region is characterized by a quasi-linear response that is only intermittently rate limited. Thus, the nonlinear amplitude effects in this region are imperceptible to the pilot.

The third operating range is fully nonlinear and is characterized by an output rate that equals the actuator rate limit, $\dot{\delta} = V_L$, for most of the time. In this region the presence of the nonlinearity makes both the frequency and time responses amplitude dependent. For the step response, the system rise time (T_{NL}) will be the magnitude of the step input divided by the velocity limit as shown in Figure 2.3. For sinusoidal inputs with amplitudes that are large enough to keep the system velocity at limit values most of the time, the limiter approaches a bang-bang characteristic. As illustrated later, this type of closed-loop system can be characterized by describing functions

that can be expressed in simple analytical terms. The bang-bang idealization is a very useful limiting case that is valid when the linear bandwidth is very large when contrasted to the effective bandwidth of the nonlinear system. This "rise time" is completely independent from that for the linear system. Thus, for this fully nonlinear case, the closed-loop frequency and time response characteristics are totally defined by the rate limit and the input amplitude, independent of the linear system time constant.

In the transition near saturation regime between the essentially linear and the essentially nonlinear, the system responses will depend on the linear time constant, the velocity limit, and the input amplitude. Although this situation defies a straightforward analytical treatment, the quasi-linear nature of the system response permits the use of nonlinear computer simulation models to generate time responses and with some effort (for example, by using fast Fourier transform techniques applied to the output time histories) corresponding frequency responses.

2.2.2 Time Response Surveys

The following discussion provides three example cases that span the ranges of interest (that is, linear, near saturation, and highly saturated). For all cases the design parameters ω_a and V_L were held constant at 20 rad/s and 40 deg/s, respectively. The input sine wave frequency (ω_i) was held constant at 5 rad/sec. Thus, the input amplitude, $\delta_c = A$, was varied to obtain responses within the three desired model ranges of interest. When the design parameters are held constant at the above stated values, the system will not saturate until e = 2 deg.

2.2.2.1 Linear Range

Figure 2.4 presents the closed-loop actuator model time responses for a linear range case with an input magnitude of 5 deg. As shown in the figure the error signal always remains below the 2 deg saturation point. The linearity of the response is further exemplified by an actuator rate that is always well below the 40 deg/s rate limit. In Figure 2.5, the output actuator position is compared to the input command. The noticeable lag in the output response results from the first order closed-loop time constant as previously identified in Figure 2.2. The phase lag due to the effective first-order time constant is $\tan^{-1}(T\omega)$. For the conditions illustrated, this phase lag is well approximated by the argument. Thus, for input frequencies much less than the actuator bandwidth frequency, the output response is shifted from the input by T seconds as indicated in Figure 2.2.

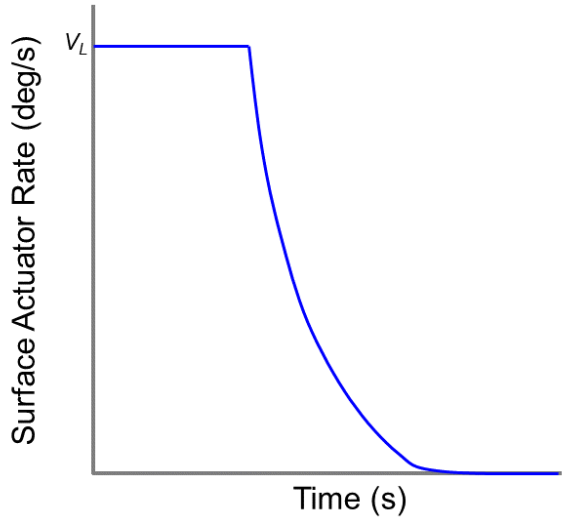

(a) Surface actuator rate

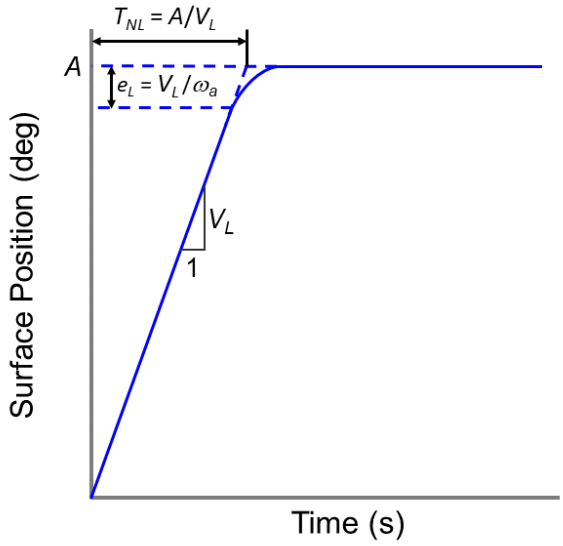

(b) Surface position

Figure 2.3: *Nonlinear closed-loop actuator response to a step input of amplitude A.*

2.2.2.2 Near Saturation Range

Figure 2.6 presents the closed-loop actuator model time responses for a near saturation case with an input magnitude of 9 deg. As shown in the figure the error signal intermittently exceeds the 2 deg saturation point. These excursions into the nonlinear range are more evident in the actuator rate response that becomes clipped at the 40 deg/s rate limit. In Figure 2.7, the output actuator position is compared to the input command. The figure illustrates an output position response that remains effectively linear even though the saturation point has been clearly exceeded. The nearly linear nature of the output actuator position is further exemplified by a phase lag that remains consistent with the linear time constant.

2.2.2.3 Highly Saturated Range

Figure 2.8 presents the closed-loop actuator model time responses for a saturation case with an input magnitude of 15 deg. As shown in the figure, the error signal consistently exceeds the 2 deg saturation point although it still appears more or less sinusoidal. The nonlinear nature is more evident in the actuator rate response that appears "box car-like" for this highly saturated case. Thus, the actuator operates as a bang-bang (that is, maximum-to-maximum) controller. In Figure 2.9, the actuator output position is compared to the input command. The figure displays a triangle wave output response that reverses when equal to the input (that is, when the error signal passes through zero). It should be noted that, unlike the indicial response discussed earlier, the phase lag for this more generalized case is *not* consistent with T_{NL} (that is, the phase lag $\neq \omega T_{NL}$). In the analyses that follows in subsequent chapters, it is shown that the T_{NL} parameter still plays a significant role in characterizing the nonlinear system.

2.3 Applicability of the Simplified Model

Before proceeding further, it is important to verify the low order nonlinear actuator model of Figure 2.1 has utility for the study of Category II PIO. A high order aileron control surface actuator model for the NASA F/A-18 High Alpha Research Vehicle was derived from parameters provided in [11] and its references. In general, higher order electrohydraulic actuator models feature not only dynamics for the position control loop, but also the servovalve loop and the current loop as well as various filters. A Bode plot for the high order model is shown in Figure 2.10(a). A low order approximation that emphasizes the dominant position loop dynamics is shown in Figure 2.10(b). In both cases, the solid line represents the magnitude response and the dashed line represents the phase response. The two cases are directly compared in Figure 2.10(c) and (d). Note that when the frequency region of the pilot-vehicle system control is considered, that is, frequencies less than 20 rad/s, the low order model is shown to well represent the dynamic response of the high order model. This example therefore illustrates the utility of pursuing Category II PIO analysis investigations using a low order actuator model.

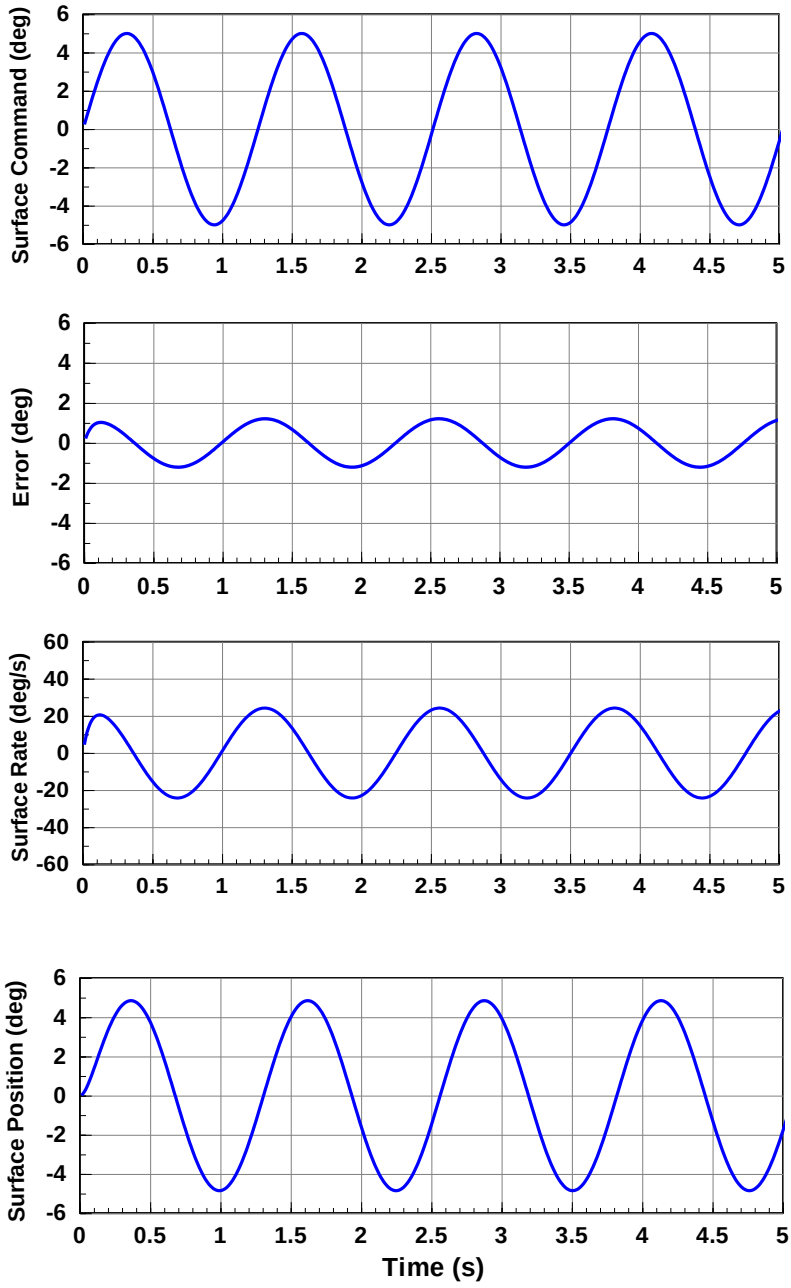

Figure 2.4: *Linear actuator model time responses.*

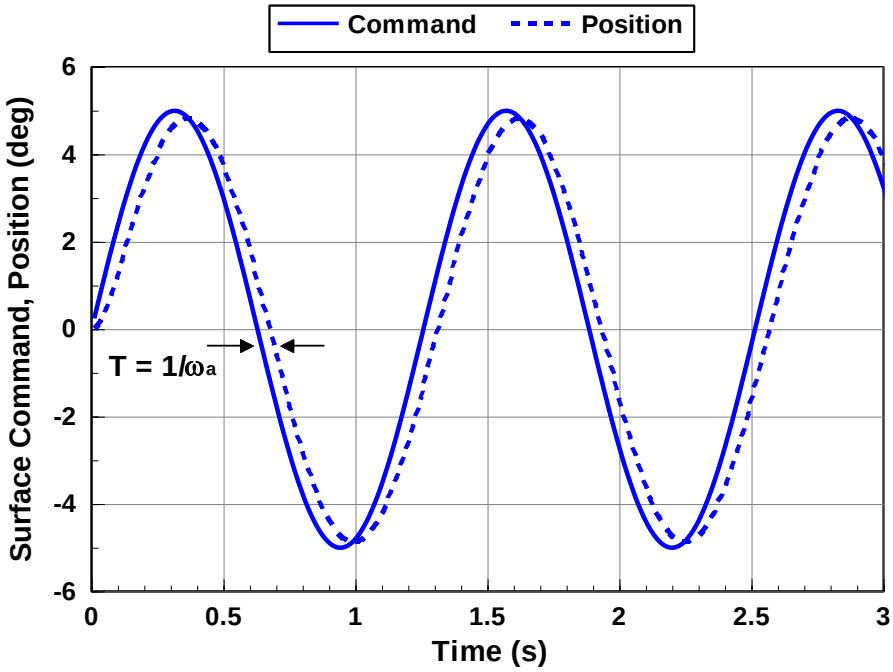

Figure 2.5: *Linear actuator model input command and output position time responses.*

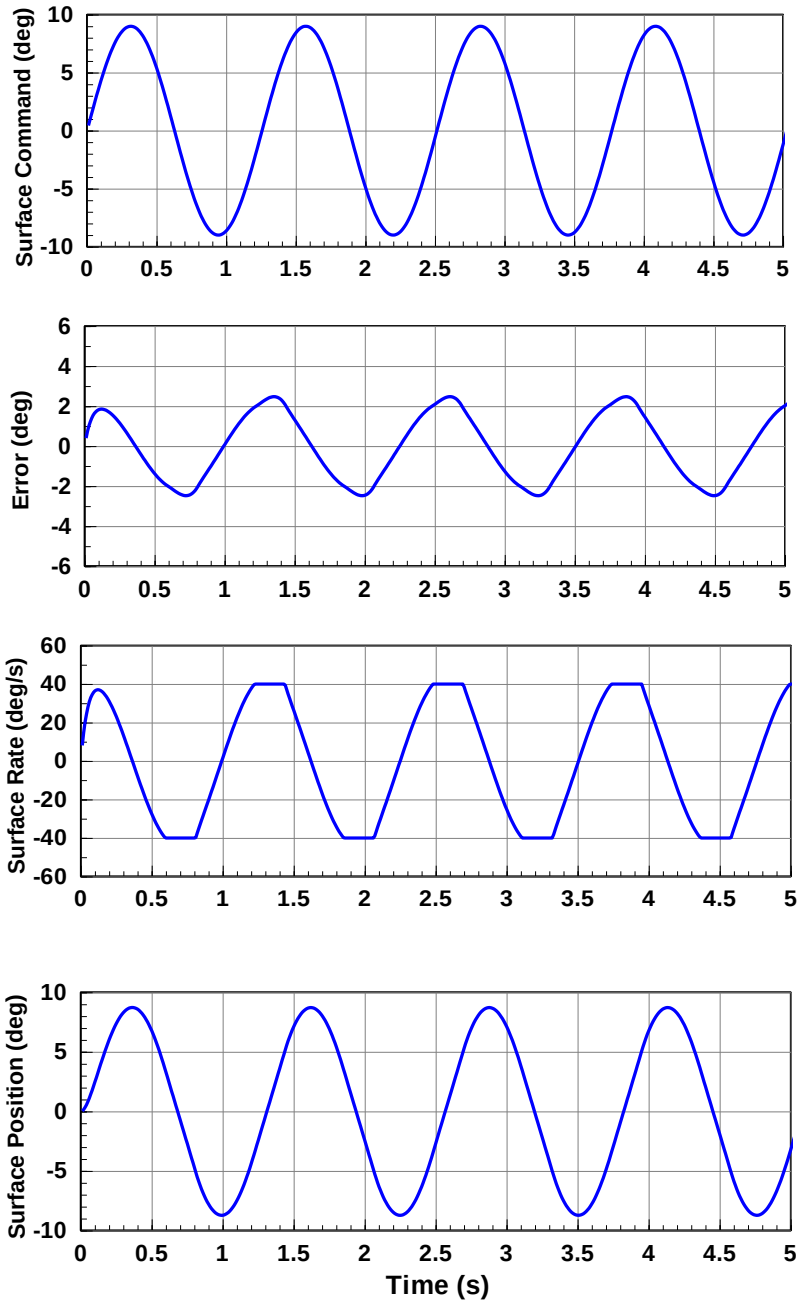

Figure 2.6: *Near saturation actuator model time responses.*

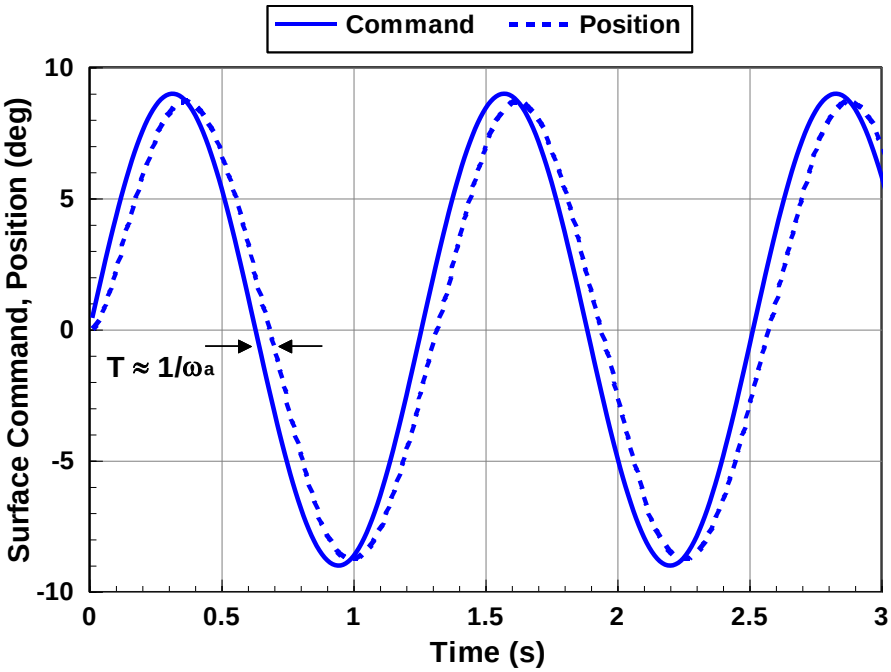

Figure 2.7: *Near saturation actuator model input command and output position time responses.*

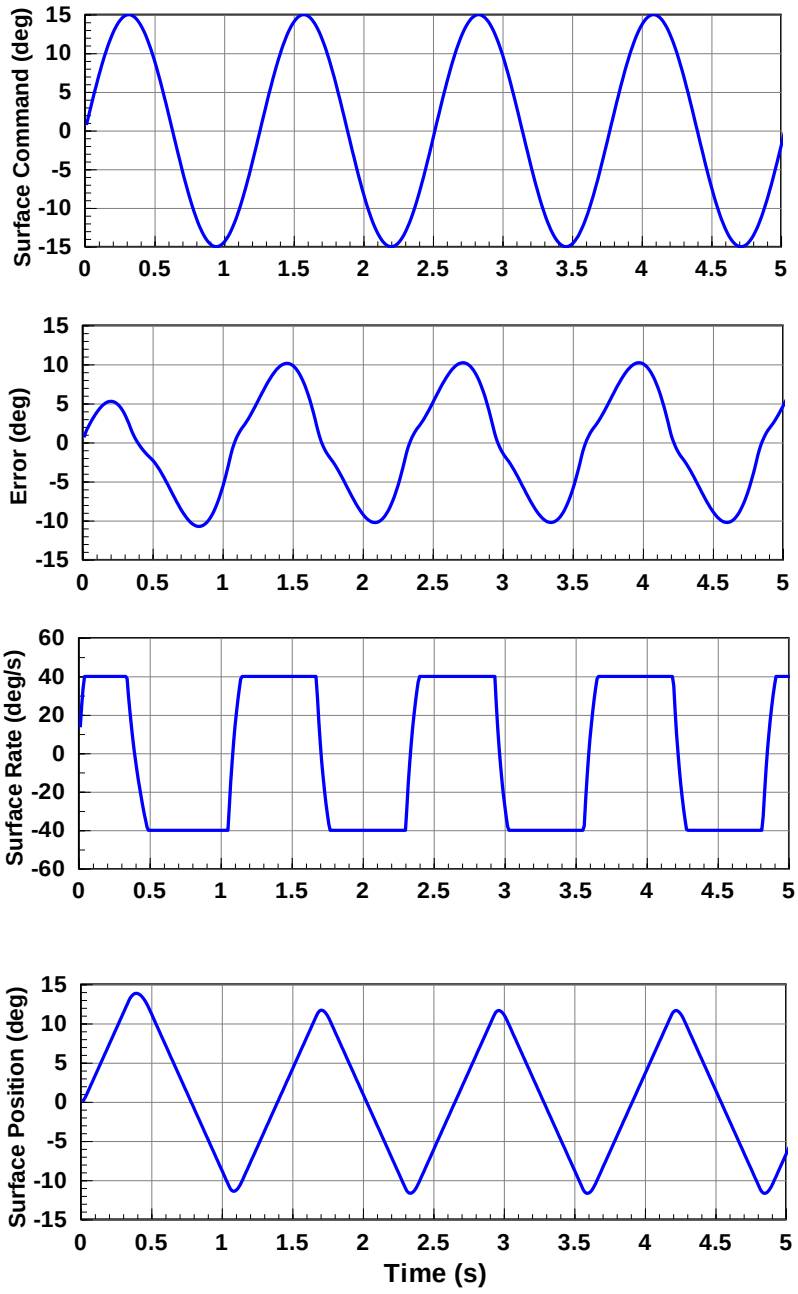

Figure 2.8: *Highly saturated actuator model time responses.*

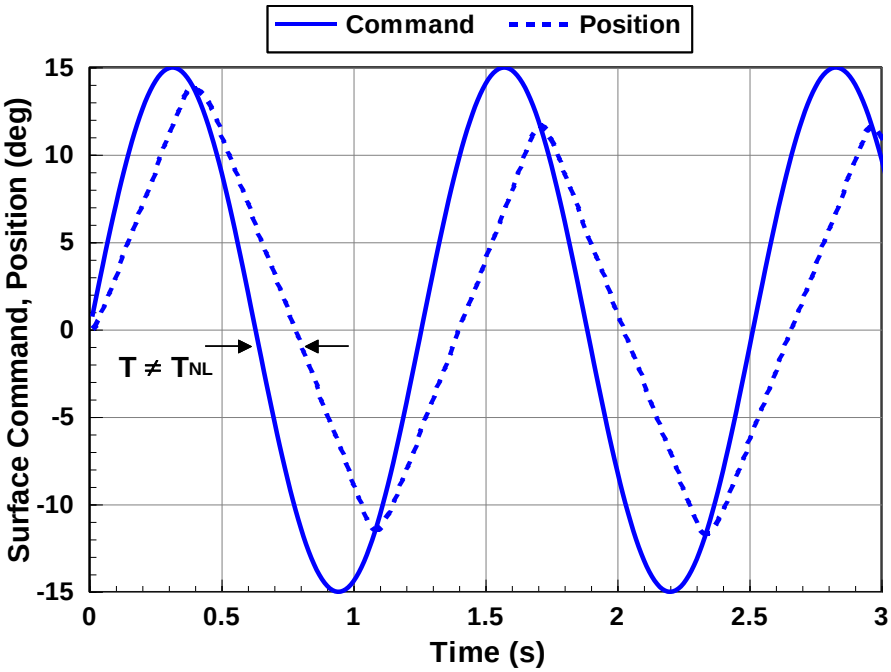

Figure 2.9: *Highly saturated actuator model input command and output position time responses.*

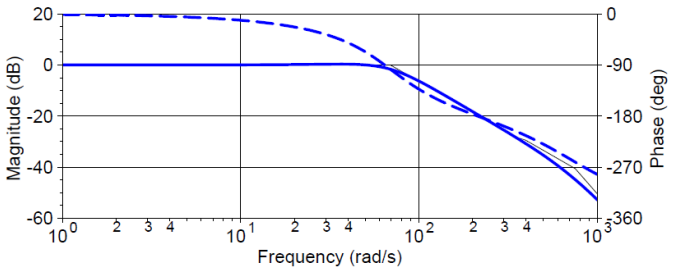

(a) High order model

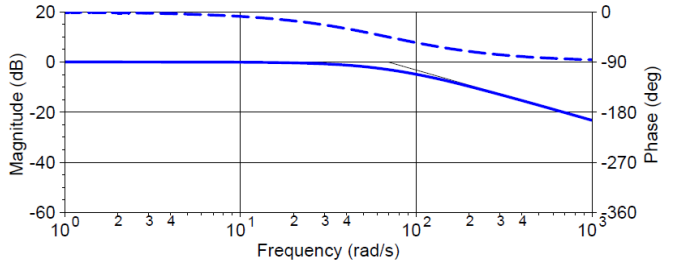

(b) Low order model

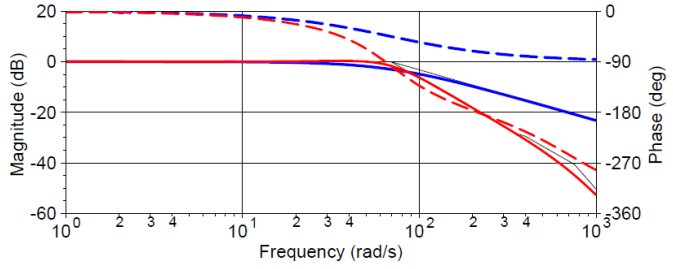

(c) Combined models

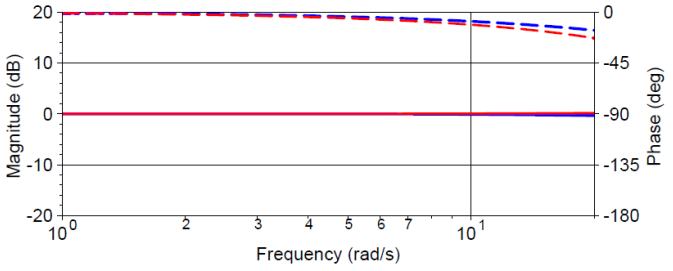

(d) Combined models, region of pilot control

Figure 2.10: *Comparison of high and low order control surface actuator model Bode plots (δ/δ_c).*

2.4 Conclusions

In this chapter, a simplified model of a control surface actuator was introduced to study the nature of rate limiting. Using this simple model, the linear characteristics of the actuator response are completely defined in terms of its time constant, T, or bandwidth frequency, ω_a, wherein $T = 1/\omega_a$. As such, the linear response is frequency dependent. Three distinct actuator response regions were identified – linear, near saturation, and highly saturated. The near saturation region features intermittent rate limiting, but the overall response remains quasi-linear. The highly saturated region, however, is characterized not only by the input command frequency, but also by the maximum rate and amplitude of the input. That is, the nonlinear response is both amplitude and frequency dependent. Comparing the simplified model with a high order actuator model from a high-performance aircraft verified the utility of the simplified approach for the study of pilot-vehicle system interactions including PIO.

2.5 References

1. Klyde, D. H., D. T. McRuer, and T. T. Myers, "Pilot-Induced Oscillation Analysis and Prediction with Actuator Rate Limiting," *J. Guidance, Control, and Dynamics*, Vol. 20, No. 1, Jan. – Feb. 1997, pp. 81 – 88.

2. Klyde, D. H., and D. G. Mitchell, "Investigating the Role of Rate Limiting in Pilot-induced Oscillations," *J. Guidance, Control, and Dynamics*, Vol. 27, No. 5, Sept.-Oct. 2004, pp. 804-813.

3. Ashkenas, I. L., H. R. Jex, and D. T. McRuer, *Pilot-Induced Oscillations: Their Cause and Analysis*, Norair Report NOR-64-143, Northrop Corporation, July 24, 1964.

4. Klyde, D. H., D. T. McRuer, and T. T. Myers, *Unified Pilot-Induced Oscillation Theory Volume I: PIO Analysis with Linear and Nonlinear Vehicle Characteristics, Including Rate Limiting*, WL-TR-96-3028, Dec. 1995.

5. Smith, J. W., and D. T. Berry, *Analysis of Longitudinal Pilot-Induced Oscillation Tendencies of YF-12 Aircraft*, NASA TN D-7900, Febuary 1975.

6. Dornheim, M. A., "Report Pinpoints Factors Leading to YF-22 Crash," *Aviation Week and Space Technology*, 9 November 1992, pp. 53-54.

7. Rundqwist, L., and R. Hillgren, "Phase Compensation of Rate Limiters in JAS 39 Gripen," AIAA-96-3368 presented at the *Atmospheric Flight Mechanics Conference*, San Diego, CA, 29-31 July 1996.

8. McRuer, D. T., *Pilot-Induced Oscillations and Human Dynamic Behavior*, NASA CR-4683, Dec. 1994.

9. Anon., *Aviation Safety and Pilot Control*, prepared by the National Research Council Committee on the Effects of Aircraft-Pilot Coupling and Flight Safety, National Academy Press, Washington, D.C., 1997.

10. Smith, J. W., and J. W. Edwards, *Design of a Nonlinear Adaptive Filter for Suppression of Shuttle Pilot-Induced Oscillation Tendencies*, NASA TM-81349, 1980.

11. Brenner, M. J., *Aeroservoelastic Modeling and Validation of a Thrust-Vectoring F/A-18 Aircraft*, NASA TP 3647, Sep. 1996.

3. The Exact Describing Function and Approximations

Jump resonance, the entrainment of frequency, and chaos need to be studied by flight control engineers only enough to precude their appearance in our systems.

Graham and McRuer from their "Retrospective Essay on Nonlinearities in Aircraft Flight Control," 1991

Parts of this chapter have been published as:

Title Pilot-Induced Oscillation Analysis and Prediction with Actuator Rate Limiting

Journal Journal of Guidance, Control, and Dynamics, vol. 20, no. 1, Jan.-Feb. 1997, pp. 81 – 88

Authors D. H. Klyde, D. T. McRuer, and T. T. Myers

Title Investigating the Role of Rate Limiting in Pilot-induced Oscillations

Journal Journal of Guidance, Control, and Dynamics, vol. 27, no. 5, Sept.-Oct. 2004, pp. 804-813

Authors D. H. Klyde and D. G. Mitchell

3.0 THE EXACT DESCRIBING FUNCTION AND APPROXIMATIONS

The material in this chapter has been taken largely from two references [1,2] that develop a generalized exact describing function of a nonlinear control surface actuator based on the model described in the previous chapter. The analysis examples were taken from material created by the author of this thesis as part of the short course "Pilot-Induced Oscillations: From the Wright Flyer to Fly-by-Wire" that is taught to industry and government agencies with co-author David Mitchell.

3.1 Introduction

With constantly increasing computing power available, simulation remains the tool of choice for analyzing nonlinear systems. Although powerful, computer simulation results are specific to the given set of model parameters. In this way, the nonlinear simulation serves as a system performance verification tool. Describing function techniques provide an analytical alternative to computer simulation. There are important reasons to exercise describing function techniques, the most important of which with respect to the analysis of Category II PIO is that describing function results can be generalized. Describing functions also provide extensions of linear graphical procedures. In this chapter describing functions that apply to the simplified model introduced in Chapter 2 are developed.

3.2 Literal Approximate Describing Functions

Literal approximate describing functions are those that can be represented in a symbolic, parameter-based form as distinguished by those that are represented in numerical form.

3.2.1 Open-Loop

A sinusoidal input generally approximates the actuator commands for PIO incidents [3]. That is, using the model structure of Figure 3.1, $\delta_c = A\sin(\omega_i t + \phi_i)$, where δ_c is the actuator command input, A is the command amplitude, ω_i is the input frequency, and ϕ_i is the input phase angle. This suggests approximating the saturation nonlinearity within the feedback loop with a sinusoidal describing function. Saturation is a "simple" nonlinearity (Ref. 4) such that a sinusoidal describing function is a real number invariant with input frequency. It is given by the ratio of the Fourier fundamental of the output to that of the input. To use this describing function to model the closed-loop system of Figure 3.1, it must be assumed that the error is approximately sinusoidal. This assumption is justified below. Because of the complex nature of the saturation Fourier fundamental, approximations are necessary to achieve a literal solution. The material presented in this section is based on analytical work that was originally presented in Ref. 5, but it is included here for completeness as it is a step to the exact sinusoidal describing functional results that follow.

The first step in developing an approximate describing function is to assume that the error signal in Figure 3.1 can be represented by a sinusoid, $e = E\sin(\omega t + \phi)$. By examining the error signal time response in Figure 3.2, a highly saturated case, this is shown to be a reasonable assumption.

In the linear range up to the saturation point ($E \le e_L$), the effective gain of the nonlinearity is ω_a. Further, ω_a sets the bandwidth frequency of the linear closed-loop δ/δ_c response. In the highly saturated range, however, the effective gain of the saturation nonlinearity with the feedback loop open is related to the saturation Fourier fundamental by the following equation[2] as defined in Figure 4-10c of [4]:

$$\omega_a^* = \frac{2\omega_a}{\pi}\left[\sin^{-1}\left(\frac{e_L}{E}\right)+\left(\left[\frac{e_L}{E}\right]\right)\sqrt{1-\left(\frac{e_L}{E}\right)^2}\right] \tag{3.1}$$

One can see that as the magnitude of the input (E) to the nonlinear element increases, the effective nonlinear gain (ω_a^*) further decreases with respect to the linear bandwidth (ω_a). In fact, $\omega_a^*/\omega_a \rightarrow 0$ as $E/e_L \rightarrow \infty$.

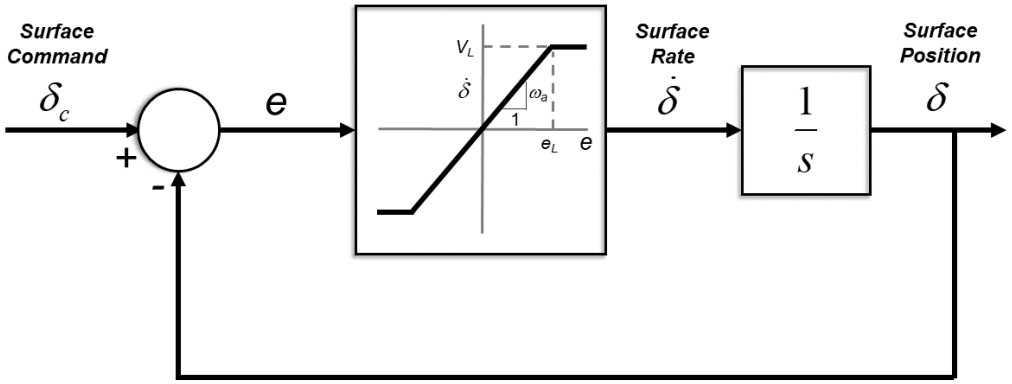

Figure 3.1: *Simplified control surface actuator model.*

By using series expansions for the arcsine and square root terms in Eqn. 3.1 and by retaining only the linear terms, the following approximation is obtained:

$$\omega_a^* = \frac{4}{\pi}\frac{V_L}{E}\left[1-\frac{1}{6}\left(\frac{V_L}{\omega_a E}\right)^2-\cdots\right] \approx \frac{4}{\pi}\frac{V_L}{E} \tag{3.2}$$

[2] Note that the equation from [4] was written in terms of the $e_L = V_L/\omega_a$ substitution.

As shown in [5], the first order approximation of Eqn. 3.2 represents an approximation of the saturation output with a square wave. Such a square wave will have a fundamental $4/\pi$ times the saturation rate. By examining the rate signal of Figure 3.3, it is evident that the square wave approximation is indeed appropriate for the highly saturated range.

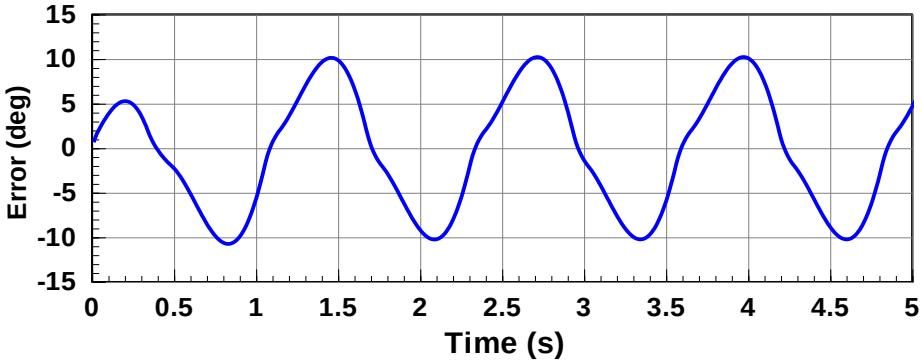

Figure 3.2: *Simplified actuator error signal time response for highly saturated case.*

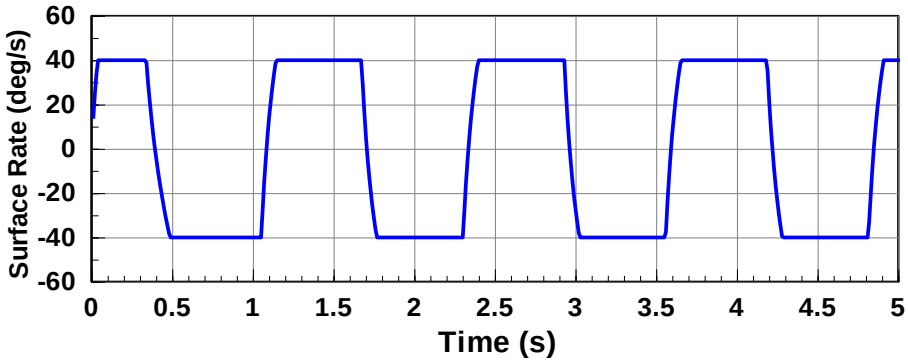

Figure 3.3: *Simplified actuator rate signal time response for highly saturated case.*

In the near saturation range an approximation of the effective nonlinear gain is made by the following equation:

$$\omega_a^* \approx \frac{V_L}{E} \tag{3.3}$$

Eqn. 3.3 represents the case displayed in Figure 3.4 where the slightly clipped output rate is still well represented by a sinusoid whose amplitude is approximated by the magnitude of the rate limit.

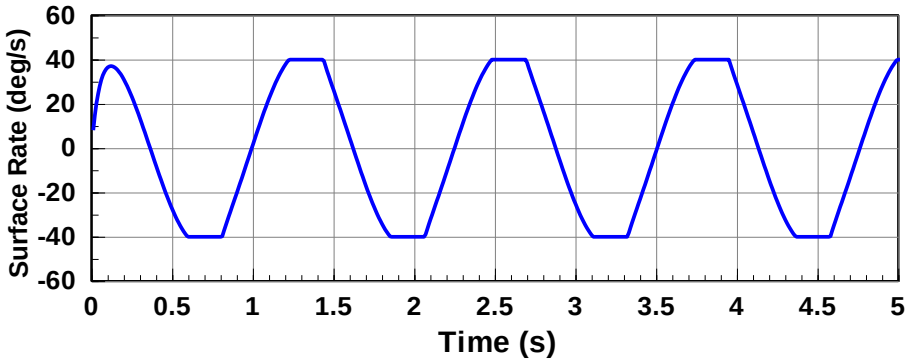

Figure 3.4: *Simplified actuator rate signal time response for near saturation case.*

For the open-loop describing functions [5], the two approximations bound the exact result. This feature is revealed in Figure 3.5 where the describing function approximations of Eqns. 3.2 and 3.3 are compared to the exact describing function of Eqn. 3.1 for the open-loop case. Specifically, the plots are the nonlinear open-loop gain normalized by the linear closed-loop bandwidth (ω_a^*/ω_a) versus the error amplitude (E) normalized by the saturation point (e_L). To obtain the displayed hyperbolic curves, substitute $V_L = \omega_a e_L$ in Eqns. 3.2 and 3.3 and then solve in terms of the normalized parameters. The linear range is represented by a normalized gain value of 1 for $E/e_L \leq 1$. The nonlinear bandwidth decreases as the actuator rate limit becomes more highly saturated. In the near saturation region, the Eqn. 3.3 describing function provides an adequate representation of the normalized gain as E/e_L approaches 1^+. The normalized gain for the highly saturated describing function, on the other hand, remains at a value of 1 until $E/e_L = 4/\pi$. Thus, it provides a poor approximation in the near saturation range. For $E/e_L >> 1$, however, the highly saturated describing function provides an excellent approximation of the open-loop nonlinear bandwidth.

3.2.2 Closed-Loop

To obtain a closed-loop sinusoidal describing function, the approximations for the nonlinear bandwidths (i.e., Eqns. 3.2 and 3.2) must be defined in terms of the system input and output variables, δ_c and δ, respectively. First, simple block diagram algebra is used with Figure 3.1 to define an error signal transfer function in terms of the input command (for $e \leq e_L$):

$$\frac{e(s)}{\delta_c(s)} = \frac{1}{1+\frac{\omega_a}{s}} \tag{3.4}$$

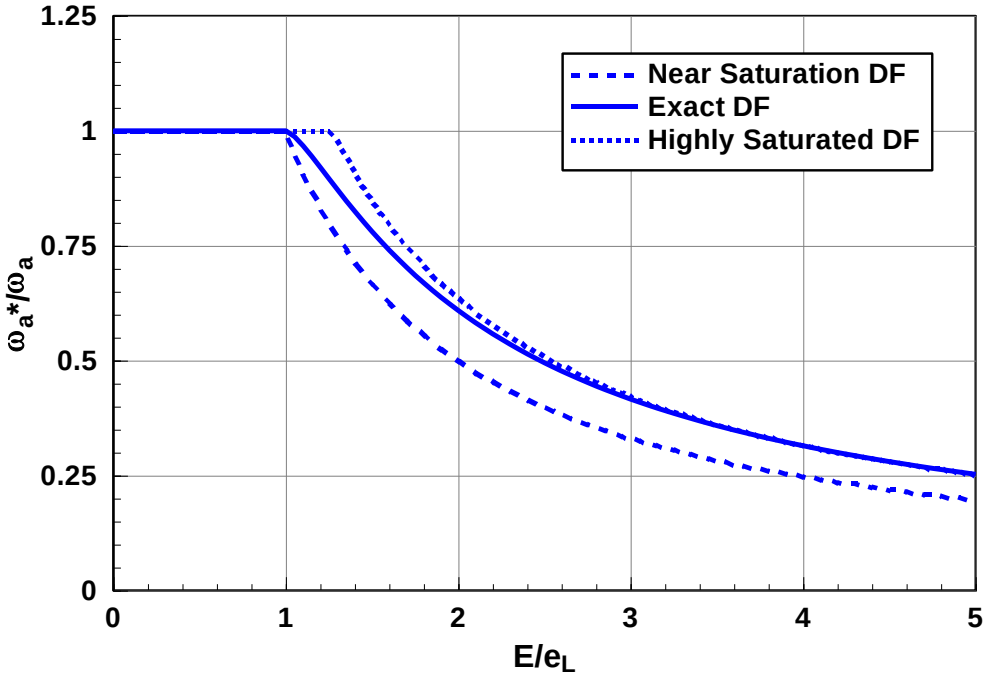

Figure 3.5: *Open-loop describing function representation of the nonlinear gain.*

The next step is to substitute $j\omega$ for s and ω_a' for ω_a in Eqn. 3.4 and then solve for the describing function magnitude. This yields the following equation:

$$\left|\frac{e(j\omega)}{\delta_c(j\omega)}\right| = \frac{\omega}{\sqrt{\omega^2 + \left(\omega_a^*\right)^2}} = \frac{E}{A} \tag{3.5}$$

At this point either Eqn. 3.2 or 3.3 can be used to provide a substitution for E in Eqn. 3.5. Eqn. 3.2 is used here since the highly saturated range is more relevant to the analysis of Category II PIOs. Thus, the next step is to substitute the following relation for E, obtained from Eqn. 3.2, into Eqn. 3.5:

$$E = \frac{4}{\pi}\frac{V_L}{\omega_a^*} \tag{3.6}$$

The final step is to then solve for ω_a'. After performing some algebra, the following equation is obtained:

$$\omega_a^* = \frac{1}{\sqrt{\left(\frac{\pi}{4}\frac{A}{V_L}\right)^2 - \left(\frac{1}{\omega}\right)^2}} \quad \text{or} \quad \frac{\omega}{\sqrt{\left(\frac{\pi}{4}\frac{A\omega}{V_L}\right)^2 - 1}} \tag{3.7}$$

The closed-loop response for the linear, near saturation, and highly saturated regions is determined from basic block diagram relationships to be:

$$\frac{\delta(j\omega)}{\delta_c(j\omega)} = \frac{1}{\frac{j\omega}{\omega_a^*} + 1} \tag{3.8}$$

In the linear range, where $\omega_a{}^* = \omega_a$, Eqn. 3.8 reduces to a simple first order lag.

Magnitude $\left(\sqrt{\frac{1}{1+\left(\omega/\omega_a^{'}\right)^2}}\right)$ and phase $\left(-\tan^{-1}\left(\omega/\omega_a^*\right)\right)$ responses for the approximate closed-loop system describing function are determined by substituting $\omega_a{}^*$as defined in Eqn. 3.7 into Eqn. 3.8. For the *highly saturated* case this yields the following:

$$\left|\frac{\delta(j\omega)}{\delta_c(j\omega)}\right| = \frac{4}{\pi}\frac{V_L}{A\omega} \tag{3.9a}$$

$$\angle\frac{\delta(j\omega)}{\delta_c(j\omega)} = -\tan^{-1}\left[\sqrt{\left(\frac{\pi}{4}\frac{A\omega}{V_L}\right)^2 - 1}\right] \tag{3.9b}$$

When the *near saturation* approximation of Eqn. 3.3 is used in the previous derivation the following frequency response equations are obtained:

$$\left|\frac{\delta(j\omega)}{\delta_c(j\omega)}\right| = \frac{V_L}{A\omega} \tag{3.10a}$$

$$\angle\frac{\delta(j\omega)}{\delta_c(j\omega)} = -\tan^{-1}\left[\sqrt{\left(\frac{A\omega}{V_L}\right)^2 - 1}\right] \tag{3.10b}$$

3.2.3 Saturation Frequency

As defined in Eqn. 3.1, the effective gain, from which the near saturation and highly saturated describing function approximations were derived, only applies in the post saturation region. Thus, to obtain the complete rate limited actuator frequency response approximation, a combination of the linear, near saturation, and highly saturated region results must be employed. In the *linear* region the magnitude and phase as a function of normalized frequency (ω/ω_a) are given by:

$$\left|\frac{\delta(j\omega)}{\delta_c(j\omega)}\right| = \sqrt{\frac{1}{(\omega/\omega_a)^2+1}} \tag{3.11a}$$

$$\angle\frac{\delta(j\omega)}{\delta_c(j\omega)} = -\tan^{-1}(\omega/\omega_a) \tag{3.11b}$$

For constant input amplitude and constant actuator design parameters, there is a specific frequency at which the actuator just saturates. A literal form for the saturation frequency (ω_s) is obtained from Eqn. 3.5 by substituting $e_L = E$ (at saturation) and then solving for frequency. This results in the following:

$$\omega_s = \frac{\omega_a}{\sqrt{\left(\frac{A}{e_L}\right)^2 - 1}} \tag{3.12}$$

This result is further reduced by substituting $e_L = V_L/\omega_a$, and then solving for a normalized saturation frequency as shown by:

$$\frac{\omega_s}{\omega_a} = \frac{1}{\sqrt{\left(\frac{A\omega}{V_L}\right)^2 - 1}} = \frac{1}{\sqrt{\left(\frac{T_{NL}}{T}\right)^2 - 1}} \tag{3.13}$$

In Figure 3.6 the normalized saturation frequency is plotted as a function of the time constant ratio (T/T_{NL}) with identified linear and post saturation regions. This curve indicates that, as expected, the frequency required to saturate becomes larger as the time constant ratio approaches 1. The Figure 3.6 result is, therefore, used to analytically establish if the system has saturated for a given time constant ratio.

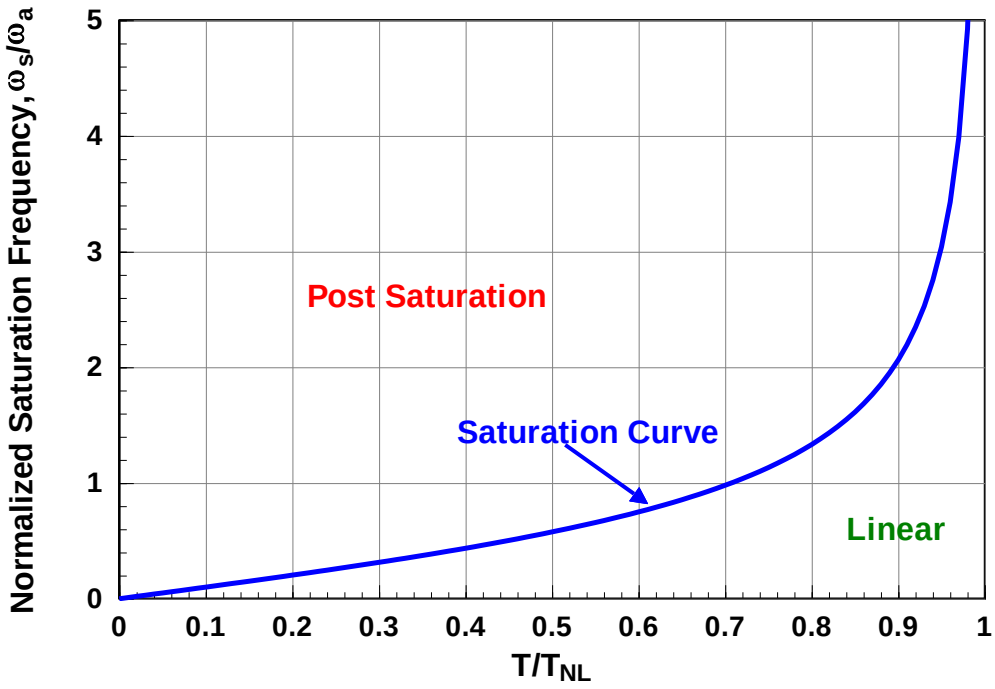

Figure 3.6: *Saturation frequency as a function of the time constant ratio.*

3.2.4 Normalized Closed-Loop Frequency Response Approximations

For time constant ratios of 1^-, the *near saturation* describing function (Eqn. 3.10) applies as given by the following normalized frequency magnitude and phase equations:

$$\left|\frac{\delta(j\omega)}{\delta_c(j\omega)}\right| = \frac{V_L}{A\omega_a}\frac{1}{(\omega/\omega_a)} = \frac{T}{T_{NL}}\frac{1}{(\omega/\omega_a)} \tag{3.14a}$$

$$\angle\frac{\delta(j\omega)}{\delta_c(j\omega)} = -\tan^{-1}\left[\sqrt{\left(\frac{T_{NL}}{T}\frac{\omega}{\omega_a}\right)^2 - 1}\right] \tag{3.14b}$$

Note that when Eqn. 3.14a applies, the resulting magnitude variation with frequency takes the form of an integrator, that is, a -20 dB/decade "k/s-like" asymptotic slope.

For inverse time constant ratios (T_{NL}/T) approximately greater than 2, the *highly saturated* describing function approximation applies as given by the following normalized frequency magnitude and phase equations:

$$\left|\frac{\delta(j\omega)}{\delta_c(j\omega)}\right| = \frac{4}{\pi}\frac{T}{T_{NL}}\frac{1}{(\omega/\omega_a)} \tag{3.15a}$$

$$\angle\frac{\delta(j\omega)}{\delta_c(j\omega)} = -\tan^{-1}\left[\sqrt{\left(\frac{\pi}{4}\frac{T_{NL}}{T}\frac{\omega}{\omega_a}\right)^2 - 1}\right] \tag{3.15b}$$

Note that when Eqn. 3.15a applies, the resulting magnitude also falls along a -20 dB/decade asymptotic slope.

3.3 The Exact Sinusoidal Describing Function

3.3.1 Fourier Integrals

The limitations of the literal describing function approximations, as described above, are their inability to provide an exact phase and gain reduction match to the nonlinear result. This is especially critical for the phase match as the added phase loss due to control surface actuator rate limiting is a key feature of Category II PIO [6]. To yield this desired match numerically, an exact sinusoidal describing function is obtained by first computing the Fourier integrals for the simplified model input and output fundamentals [4] using the following equations:

$$a_1 = \frac{2}{P}\int_{-P/2}^{P/2} f(t)\cos(\omega_{in}t)\,dt \tag{3.16a}$$

$$b_i = \frac{2}{P}\int_{-P/2}^{P/2} f(t)\sin(\omega_{in}t)\,dt \tag{3.16b}$$

In the preceding equations, $f(t)$ is the input or output periodic forcing function that for this case is a sine wave of period P. For sinusoidal input describing functions the a_1 term for the input is always zero. Thus, the a and b terms of Eqn. 3.16 are then used to define the describing function magnitude and phase [4] as shown by:

$$\left|\frac{\delta(j\omega)}{\delta_c(j\omega)}\right| = \frac{\sqrt{a_{1_{out}}^2 + b_{1_{out}}^2}}{b_{1_{in}}} \tag{3.17a}$$

$$\angle\frac{\delta(j\omega)}{\delta_c(j\omega)} = -\tan^{-1}\left(\frac{a_{1_{out}}}{b_{1_{out}}}\right) \tag{3.17b}$$

3.3.2 Generalized Results

A nonlinear simulation of the Figure 3.1 system was amended to compute the Fourier integrals of Eqn. 3.16 as well as the magnitude and phase from Eqn. 3.17. In Figure 3.7, the exact sinusoidal describing function actuator output response is compared with the nonlinear simulation for the highly saturated example case. As shown in the figure, the describing function provides an exact phase match to the simulation result once the initial transient has passed. This exact phase match occurs because for a sinusoidal input, only the Fourier fundamental is required to completely define the input and output phase. That is, the higher harmonic terms all share the same phase with the fundamental. The magnitude, however, will in general not be matched unless the remnant harmonic terms are also included. In the Figure 3.7 example, the describing function peak magnitude falls short of the true nonlinear magnitude by approximately 15%. For full saturation, when the output wave is triangular, the peak of the complete output will be simply $\pi^2/8$ that of the fundamental. It should be noted that the actual peak value of the output wave is irrelevant for stability analyses, whereas the fundamental is essential.

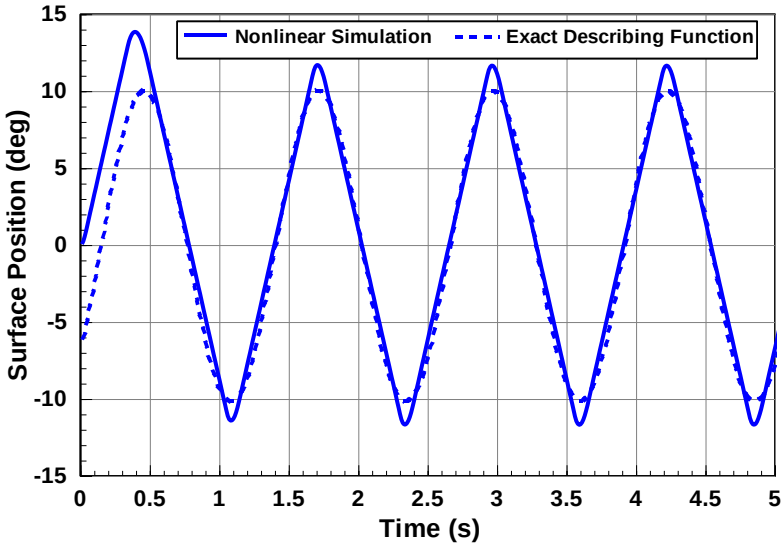

Figure 3.7: *Exact sinusoidal describing function time response comparison with nonlinear simulation.*

Equation 3.16 was evaluated numerically to generate the magnitude and phase curve families displayed in Figure 3.8(a) and Figure 3.8(b), respectively. Both sets of curves are plotted as a function of the normalized frequency (ω/ω_a) and the linear to nonlinear time constant ratio (T/T_{NL}). Thus, the two plots display the describing function magnitude and phase of the nonlinear system in terms of the actuator design parameters (V_L and ω_a) and the actuator model input parameters (A and ω_i), all known quantities.

There are several observations to note from the plots. First, the T/T_{NL} = 1 curve represents the linear case. A second observation is that the more highly saturated cases are represented by the smaller time constant ratio curves; these curves depart from the linear curve at a normalized frequency that is equivalent to their time constant ratio. For example, the T/T_{NL} = 0.1 curve departs from the linear curve at a normalized frequency of 0.1. Another, more significant result is that known design and input parameters can be used to exactly identify the added phase lag due to a rate limiting actuator. The magnitude and phase plots of Figure 3.8(a) and Figure 3.8(b), respectively, represent the difference between the exact sinusoidal describing function and the linear system. As expected, the more highly saturated cases have larger phase differences. It should also be noted that since the maximum first order phase lag is 90°, $\Delta\phi \rightarrow 0$ for all of the curves as $\omega/\omega_a \rightarrow \infty$.

3.3.3 Nonlinear Bandwidth

A primary interest in the frequency responses of the describing functions is a search for a useful extension of the linear system bandwidth metrics to the nonlinear case. For the linear first order system, the asymptotic breakpoint of $|\delta/\delta_c|$, ω_a, is a common linear system bandwidth metric. Equation 3.8 suggests that even the nonlinear cases can be characterized by a first order form. Thus, ω_a^* becomes an obvious candidate for a nonlinear bandwidth metric. As shown in Figure 3.8(a), the magnitude frequency response curves for the exact sinusoidal describing function display a "first order-like" character in that there is a distinct break frequency defined by the intersection of high (-20 dB/decade) and low (0 dB/decade) frequency asymptotes. This break frequency is near ω_a^*. From the figure it is also evident that ω_a^* decreases as T/T_{NL} decreases, and $\omega_a^* = \omega_a$ for the T/T_{NL} = 1, that is, the linear case.

To obtain a literal rather than a graphical representation for the nonlinear bandwidth, the describing function approximations must be used. As stated earlier, however, the nonlinear magnitude responses of Eqns. 3.14a and 3.15a have "k/s-like" frequency responses that do not allow for a first order lag bandwidth to be defined. This occurs because these are effectively high frequency approximations that are only valid for $\omega > \omega_s$. The corresponding nonlinear phase relations of Eqns. 3.14b and 3.15b do not, however, have the flat character of a "k/s-like" frequency response and thus do provide a basis for defining the nonlinear bandwidth.

In the following discussion approximations are given for the nonlinear closed-loop actuator bandwidth (ω_a^*) that are based on the previously developed sinusoidal input describing function approximations. As shown by Eqn. 3.1, the rate limited actuator is approximated in the highly saturated region by a first order system with a nonlinear bandwidth that was defined in Eqn. 3.7. This equation can be written in terms of the normalized frequency and the time constant ratio as shown by:

$$\frac{\omega_a^*}{\omega_a} = \frac{\omega/\omega_a}{\sqrt{\left(\frac{\pi}{4}\frac{T_{NL}}{T}\frac{\omega}{\omega_a}\right)^2 - 1}} \approx \frac{4}{\pi}\frac{T}{T_{NL}} \tag{3.18}$$

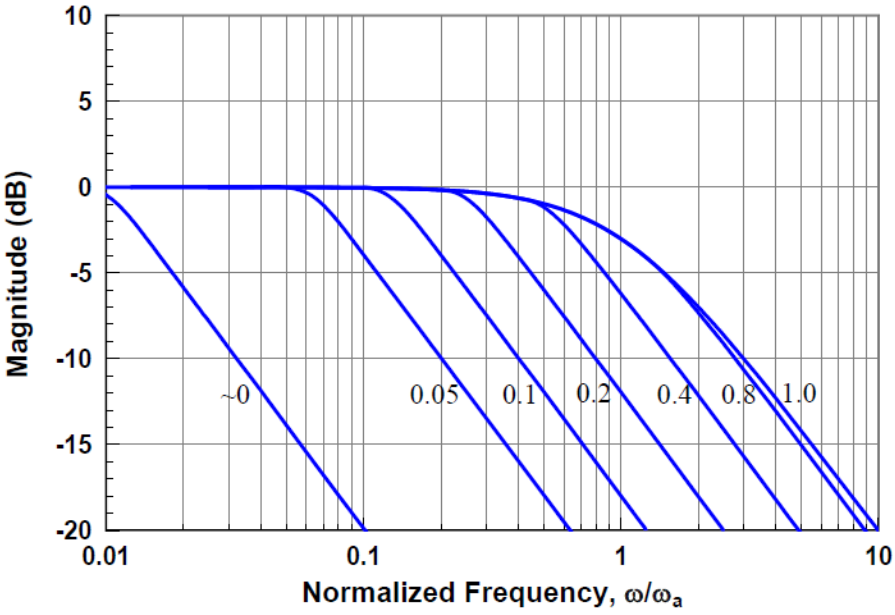

(a) Magnitude

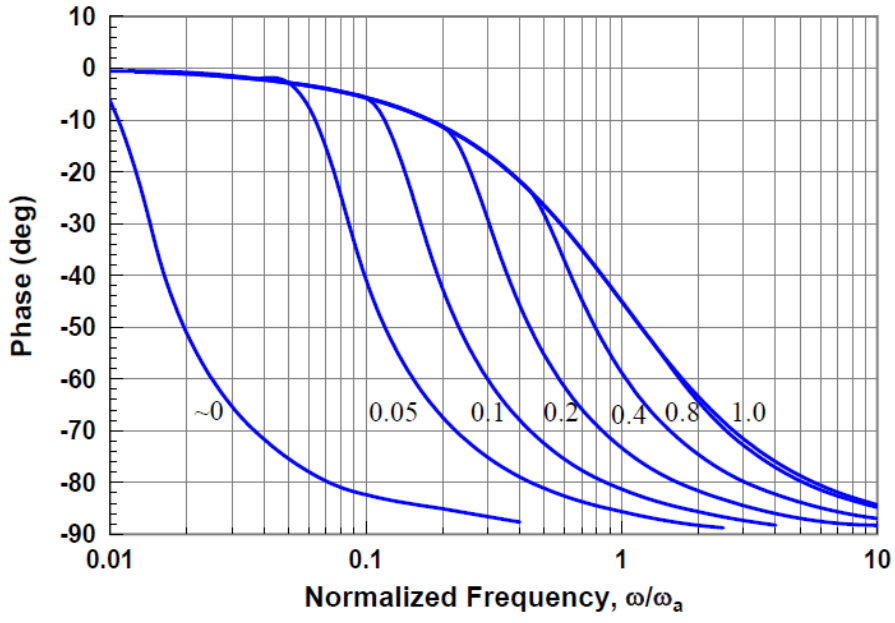

(b) Phase

Figure 3.8: *Generalized exact sinusoidal describing function frequency response.*

The simplified form of Eqn. 3.18 applies when the inverse of the time constant ratio (T_{NL}/T) is much greater than 1 ($T_{NL}/T >> 1$). By applying the $\omega_a = 1/T$ identity to the simplified form of Eqn. 3.18, the nonlinear bandwidth is shown to be approximated by a constant with a value near 1 ($4/\pi = 1.273$) times the inverse of the nonlinear time constant. Thus, in the highly saturated region, there is still an analogy to the linear case, that is, $\omega_a^* \approx \frac{4}{\pi}\frac{1}{T_{NL}}$.

A similar result is obtained for the near saturation region case when the Eqn. 3.3 approximation is used to define the nonlinear bandwidth. This results in the following equation when the inverse of the time constant ratio approaches 1, $T_{NL}/T \rightarrow 1^+$:

$$\frac{\omega_a^*}{\omega_a} = \frac{\omega/\omega_a}{\sqrt{\left(\frac{T_{NL}}{T}\frac{\omega}{\omega_a}\right)^2 - 1}} \approx \frac{T}{T_{NL}} \quad \text{or} \quad \omega_a^* = \frac{1}{T_{NL}} \tag{3.19}$$

Since $T_{NL}/T \approx 1$, the simplified form given in Eqn. 3.19 applies when $\omega/\omega_a >> 1$. As shown by a review of the Figure 3.8(a) magnitude plot, this corresponds to near saturation cases that fall along the high frequency asymptote. By applying the $\omega_a = 1/T$ identity to the simplified form of Eqn. 3.19, the nonlinear bandwidth is shown to be approximated by the inverse of the nonlinear time constant. Thus, as expected in this region, there is a direct analogy to the linear case.

The saturation frequency defined in Eqn. 3.13 can also be written in terms of the nonlinear bandwidth as shown by the following:

$$\frac{\omega_S}{\omega_a} = \frac{1}{\sqrt{\left(\frac{T_{NL}}{T}\right)^2 - 1}} \frac{1}{\left(\omega_a^{'}/\omega_a\right)} \tag{3.20}$$

Since the highly saturated case is of most interest here, the simplified form of Eqn. 3.18 can be substituted into Eqn. 3.20 for $T_{NL}/T >> 1$ to yield:

$$\frac{\omega_s}{\omega_a} = \frac{\pi}{4} \tag{3.21}$$

When highly saturated, the nonlinear bandwidth is approximated by a constant factor of $4/\pi$ times the saturation frequency.

As described above, the nonlinear actuator model displays a “first order-like” character. Thus, the nonlinear bandwidth can be defined graphically in terms of classical first order system measures. In addition to the intersection of the high and low frequency asymptotes, these also include the frequency at a phase of -45° and at a magnitude of -3 dB. For a linear system these

measures, of course, all yield the same bandwidth frequency. As shown in Figure 3.9, this is not the case for nonlinear systems. The Figure 3.8 exact sinusoidal describing function plots were used to obtain the bandwidth frequencies as a function of T/T_{NL} for the above three measures. The resulting curves are shown in the figure along with the highly saturated and near saturation nonlinear bandwidth approximations of Eqns. 3.18 and 3.19. The figure reveals that the nonlinear bandwidths indicated by the -45° and -3 dB curves overlay and are larger than those indicated by the asymptote intersection curve. The figure also reveals that the nonlinear bandwidth approximations (Eqns. 3.18 and 3.19) bound the asymptote intersection curve. When the approximations are directly compared to the asymptote intersection curve, the highly saturated approximation provides an excellent match for $T/T_{NL} \leq 0.4$ and a good match for $0.4 < T/T_{NL} \leq 0.6$. The near saturation approximation, on the other hand, provides a reasonable match to the asymptote intersection curve for $T/T_{NL} \geq 0.9$. There may be some debate as to which curve appropriately defines the nonlinear bandwidth. Since the asymptote intersection yields a lower frequency, it is the conservative case. Thus, in the appropriate T/T_{NL} regions the approximations can be used to attain a conservative estimate of the nonlinear bandwidth.

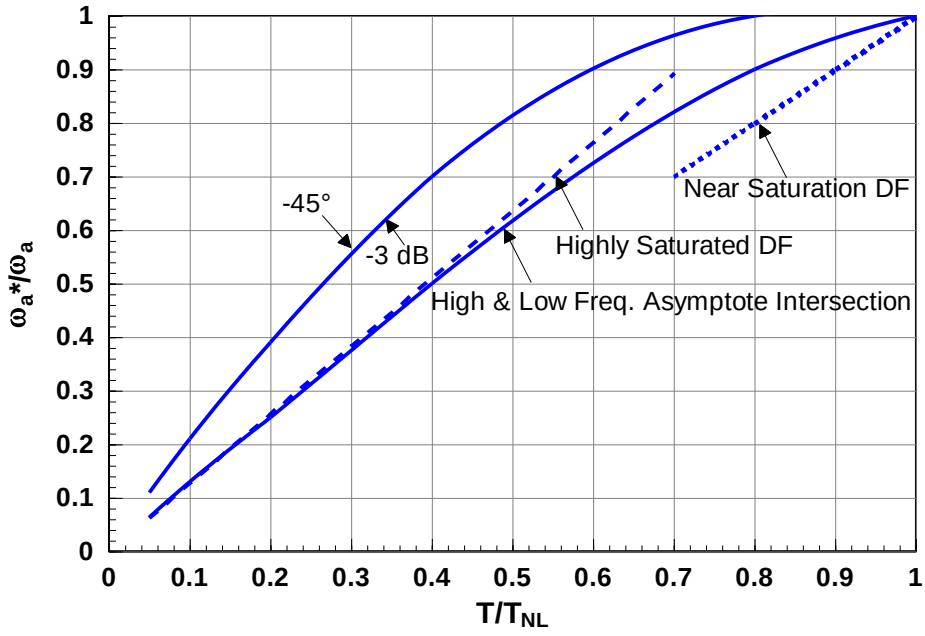

Figure 3.9: *Nonlinear bandwidth variation.*

3.4 The Rate Limiting Element

Often times software rate limits are placed in series with an actuator to ensure that the actual physical limit is not encountered, thus preventing potential damage to the flight hardware. It is not unusual for these nonlinearities to be found in the feedback path as well. The primary difference between the software limit and the hardware limit as described in [3] is the significant

loss in actuator bandwidth that accompanies the hardware limit when saturated. A software rate limit can be represented by the simplified actuator model where the bandwidth is effectively infinite (i.e., $T/T_{NL} \rightarrow 0$). Although Figure 3.8 displays both an amplitude reduction and added phase lag due to rate limiting, it is the added phase lag that is the dominant effect. Thus, when encountered in an automatic control system or a pilot-vehicle system, the primary effect of actuator or software rate saturation is to consume available phase margin that can then lead to loss of control and PIO.

A describing function approximation of a software rate limiting element can be obtained by assuming a sinusoidal input/triangle output rate limiting element as was done by Hanke [7] and shown in Figure 3.10. This method does not consider the servo loop explicitly, since only the wave forms of the input and output of the rate limiting element are considered. It does, however, implicitly take into account the servo loop by requiring a reversal of the output whenever the servo error, $e = x_i - x_o$, becomes zero. This nonlinear element model is exact when applied to a control system software limiter that contains no dynamics. It is also used to approximate an infinite bandwidth actuator (i.e., $\omega_a >> \omega$). Further, it can be used as a second describing function approximation for the highly saturated case.

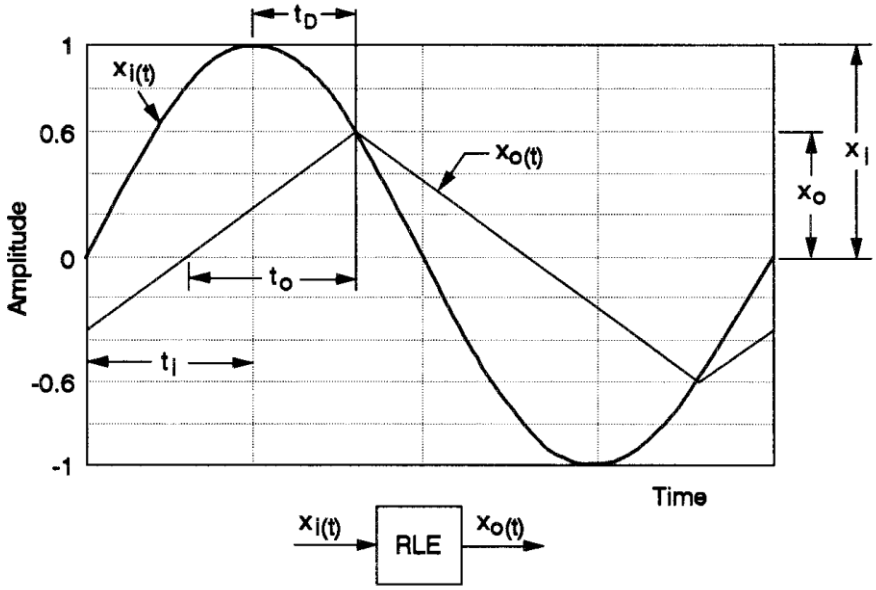

Figure 3.10: *Rate limiting element output time response for a sinusoidal input (from Ref. 7).*

Input and output time responses are shown in Figure 3.10 for the Ref. [7] model with the variables related to this derivation identified. Since the periods for the input and output are the same in the steady state, the times to peak amplitude or quarter periods (t_i and t_o, respectively) are also equivalent. The sinusoidal input, that is, command position, is defined by the following equation:

$$x_i(t) = x_{i_{max}} \sin(\omega t) \tag{3.22}$$

and the input rate is therefore:

$$\dot{x}_i(t) = x_{i_{max}} \omega \cos(\omega t) \tag{3.23}$$

Eqn. 3.23 can be written in terms of t_i by substituting $\omega = 2\pi/T$, where the period, $T = 4t_i$. The maximum input rate, that is, $\cos(\omega t) = 1$), is thus:

$$\dot{x}_{i_{max}} = \frac{\pi}{2} \frac{x_{i_{max}}}{t_i} \tag{3.24}$$

The peak magnitude of the triangle wave output is equal to x_o. The constant output rate is therefore:

$$\dot{x}_o = \pm \frac{x_o}{t_0} \tag{3.25}$$

The actual output/input magnitude is defined by taking the ratio of the constant output to maximum input rates and then solving for x_o/x_{imax}. Defining K^* as x_o/x_{imax}, this yields the following result:

$$K^* = \frac{x_o}{x_{i_{max}}} = \frac{\pi}{2} \frac{\dot{x}_o}{\dot{x}_{i_{max}}} \tag{3.26}$$

This result can be written in terms of the Figure 3.1 variables, as shown below by recognizing that the output rate when saturated is V_L and the maximum input rate is $A\omega$:

$$K^* = \frac{\pi}{2} \frac{V_L}{A\omega} \tag{3.27}$$

The K^* parameter is next used to define the describing function magnitude and phase. The describing function magnitude is obtained by multiplying K^*, which represents the actual peak magnitude of the triangle wave, by the Fourier fundamental of the triangle wave (i.e., $8/\pi^2$) as shown by:

$$\left| \frac{\delta(j\omega)}{\delta_c(j\omega)} \right| = \frac{8}{\pi^2} K^* = \frac{4}{\pi} \frac{V_L}{A\omega} \tag{3.28}$$

Note that this is identical to the highly saturated sinusoidal input describing function approximation magnitude with the same "k/s-like" frequency response.

The phase difference between the output and input is represented by t_D in Figure 3.10. It is also noted in the figure that the input and output amplitudes are equal at $t = t_i + t_D$. Thus, to obtain t_D, set the input relation of Eqn. 3.22 equal to the output and use the above substitution for t to produce the following:

$$x_{i_{max}} \sin\left[\omega\left(t_i + t_D\right)\right] = x_o \tag{3.29}$$

This equation is simplified by substituting K^* for x_o/x_{imax}, expanding $\sin[\omega(t_i + t_D)]$ and noting that $\omega t_i = \pi/2$. This results in:

$$\cos\left(\Delta\phi\right) = K^* \tag{3.30}$$

where $\Delta\phi = \omega t_D$ is the phase angle between the input and output. Finally, the phase difference ($\Delta\phi$) is obtained by solving for the argument:

$$\Delta\phi = \cos^{-1}\left(K^*\right) \tag{3.31}$$

The K^* parameter also provides a measure of the severity of the rate limiting, where $0 \leq K^* \leq 1$. As $K^* \rightarrow 1$, rate limiting diminishes and the nonlinear system becomes increasingly linear. As $K^* \rightarrow 0$, rate limiting increases and the corresponding amplitude reduction and added phase lag also increase as shown in Figure 3.11.

3.5 Analysis Examples

3.5.1 Analysis Steps

Using the tools provided in this chapter, the impact of control surface actuator rate limiting using the simplified model can be determined via the four steps defined below.

- Step 1: Identify Key System Parameters
    - Actuator bandwidth, ω_a
    - Maximum Rate, V_L
- Step 2: Select Actuator Command Input Frequency (ω_i) and Amplitude (A). To fully explore the nature of rate limiting, it is important to investigate the effects of varying actuator command amplitudes and frequencies.
- Step 3: Select Describing Function(s)
    - Exact Describing Function Simulation

- Near Saturation and Highly Saturated Describing Function Approximations (DFA)
- Software Rate Limiting Element Describing Function

- Step 4: Compute Gain Attenuation and Added Phase Lag

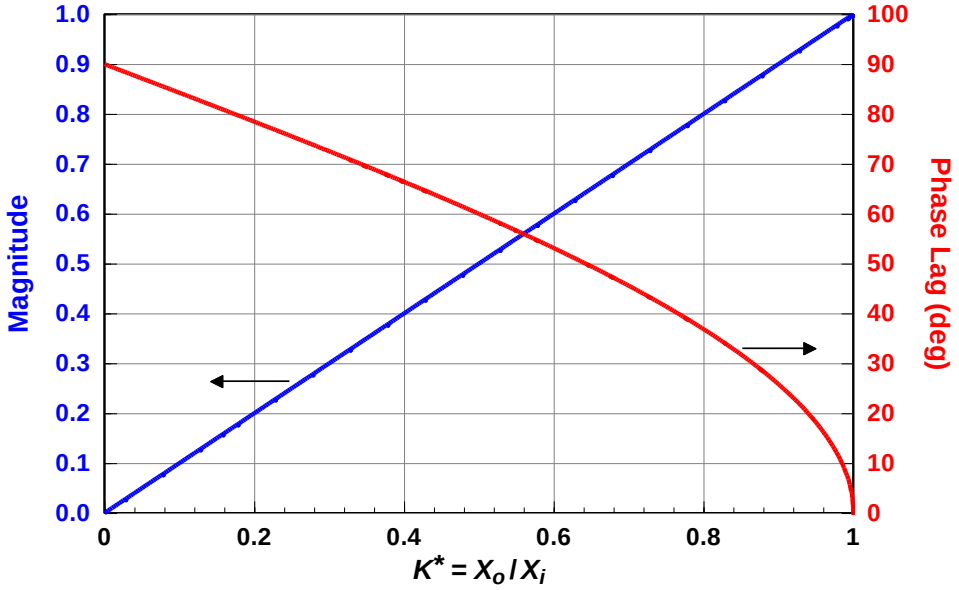

Figure 3.11: *Sinusoidal input/triangle output describing function.*

3.5.2 Level of Saturation Example Cases

Referring to Chapter 2, the three cases that were used to exemplify the linear, near saturation, and highly saturated cases are examined here to illustrate the impact of rate limiting in terms of gain attenuation and added phase lag. Step 1 is to identify the key system parameters. For these cases the simplified actuator model is characterized by a bandwidth of ω_a = 20 rad/s and a maximum rate of V_L = 40 deg/s. For Step 2, the input sinusoidal command frequency is ω_i = 5 rad/s and the input command amplitude is varied to achieve the three actuator ranges: Linear: A = 5 deg; Near Saturation: A = 9 deg; and Highly Saturated: A = 15 deg. With these parameters identified, the time constant ratios and saturation frequencies for each case are as follows: Linear: T/T_{NL} = 0.4 and ω_s = 8.73 rad/s; Near Saturation: T/T_{NL} = 0.22 and ω_s = 4.56 rad/s; and Highly Saturated: T/T_{NL} = 0.13 and ω_s = 2.69 rad/s. For Step 3, the nonlinear simulation and the two actuator describing function approximations are used to compute the analysis results shown in Figure 3.12.

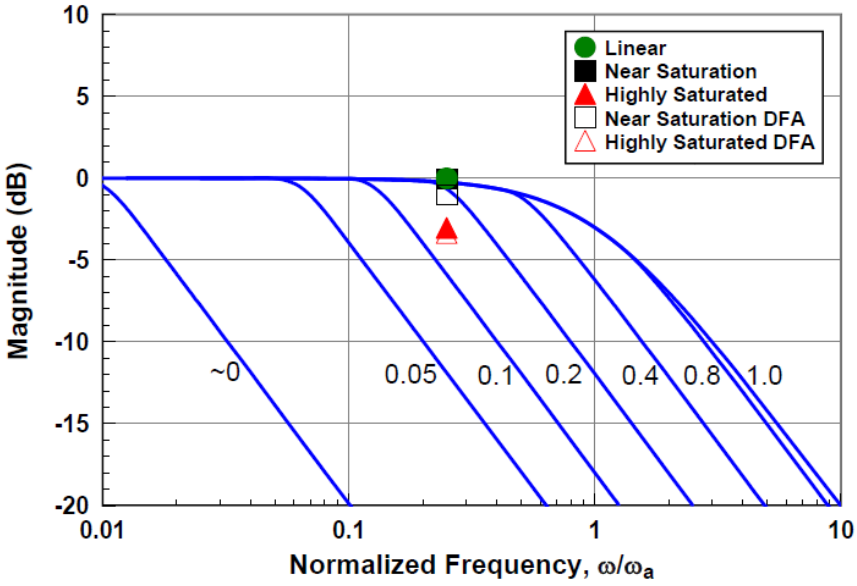

(a) Magnitude

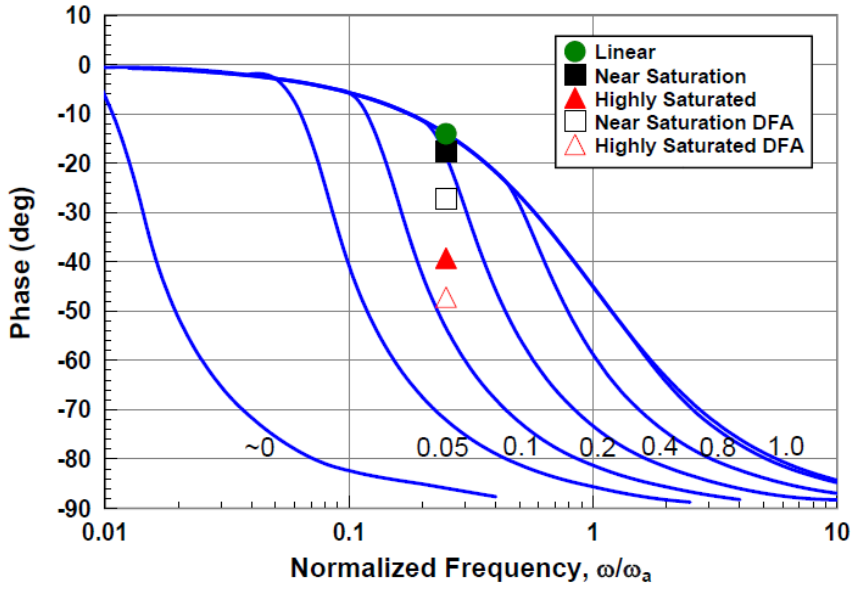

(b) Phase

Figure 3.12: *Generalized exact sinusoidal describing function frequency response analysis results for linear, near saturation, and highly saturated example cases.*

The solid symbols in Figure 3.12 represent the analysis results for the exact describing function that were computed using nonlinear simulation. First, note that the linear results fall along the linear $T/T_{NL} = 1.0$ magnitude and phase curves. As expected, the near saturation cases fall just off the linear curve indicating empirically the quasi-linear nature of this region. While the magnitudes observed for the linear and near saturation cases are essentially equivalent, there is a small, but notable added phase lag for the near saturation case. For the highly saturated case, there is an approximately 25 deg added phase lag when compared to the linear case. In the high gain pilot tasks most often associated with PIO, this added phase lag may be enough to consume all available pilot-vehicle system phase margin. The open symbols plotted on Figure 3.12 represent the near saturation and highly saturated describing function approximation results. In both cases, the approximations over predict the gain attenuation and added phase lag when compared to the exact describing function results. For quick "back of the envelope" computations, the describing function approximations at least provide a conservative result.

3.5.3 Rate Limiting Element Example Case

The same example cases can be explored using the rate limiting element. Here, the sinusoidal input/triangle output describing function only applies to the highly saturated case. Using the parameters defined for this case in the previous section and Eqn. 3.23, a K^* value of 0.84 is computed. The describing function magnitude attenuation and added phase lag results are shown in Figure 3.13. Like the highly saturated describing function approximation results, these are also conservative when compared to the exact describing function results in that the added phase lag is over predicted by approximately 8 deg. That is, the exact describing function predicts an added phase lag of approximately 25 deg, while the sinusoidal input/triangle output describing function predicts an added phase lag of 33 deg as shown in Figure 3.13.

3.6 Conclusions

In this chapter, describing function methods were derived that can be used to characterize the nature of rate limiting with a focus on the linear, near saturation, and highly saturated regions of performance. Using a simplified nonlinear model of a control surface actuator with rate limiting, it has been shown that a closed-loop rate limited actuator is characterized by not only an added phase lag but also a significant reduction in actuator bandwidth. Further, the sudden onset of these characteristics can be brought about by only small changes in input command amplitudes, especially when the pilot is operating in a high-gain closed-loop task. By using the exact describing function analysis methods described in the chapter, the characteristics associated with actuator rate limiting that can lead to PIO were quantified in terms of known command input and actuator design parameters. Further, more easily computed describing function approximations were defined in terms of these command input and design parameters. Using example cases for all three regions, the describing function results were shown to be conservative, that is, the added phase lag due to the rate limiting was over predicted when compared to the exact describing function case.

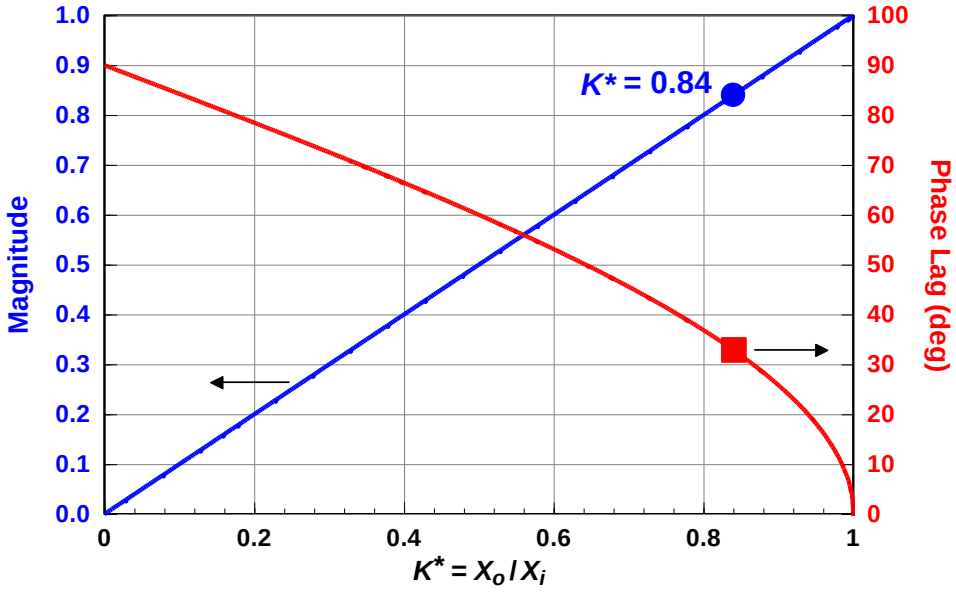

Figure 3.13: *Sinusoidal input/triangle output describing function with highly saturated example.*

3.7 References

1. Klyde, D. H., D. T. McRuer, and T. T. Myers, "Pilot-Induced Oscillation Analysis and Prediction with Actuator Rate Limiting," *J. Guidance, Control, and Dynamics*, Vol. 20, No. 1, Jan. – Feb. 1997, pp. 81 – 88.

2. Klyde, D. H., and D. G. Mitchell, "Investigating the Role of Rate Limiting in Pilot-induced Oscillations," *J. Guidance, Control, and Dynamics*, Vol. 27, No. 5, Sept.-Oct. 2004, pp. 804-813.

3. Klyde, D. H., D. T. McRuer, and T. T. Myers, *Unified Pilot-Induced Oscillation Theory Volume I: PIO Analysis with Linear and Nonlinear Vehicle Characteristics, Including Rate Limiting*, WL-TR-96-3028, Dec. 1995.

4. Graham, D. and D. McRuer, Analysis of Nonlinear Control Systems, John Wiley and Sons, Inc., New York, 1961. (Also Dover, 1971).

5. Ashkenas, I. L., H. R. Jex, and D. T. McRuer, *Pilot-Induced Oscillations: Their Cause and Analysis*, Norair Report NOR-64-143, Northrop Corporation, July 24, 1964.

6. Anon., *Aviation Safety and Pilot Control*, prepared by the National Research Council Committee on the Effects of Aircraft-Pilot Coupling and Flight Safety, National Academy Press, Washington, D.C., 1997.

7. Hanke, D., "Handling Qualities Analysis on Rate Limiting Elements in Flight Control Systems," *Flight Vehicle Integration Panel Workshop on Pilot Induced Oscillations*, AGARD-AR-335, February 1995.

4. PIO Limit Cycle Prediction using the X-15 as a Case Study

Crossfield was an extraordinary test pilot, but at the end of the first flight, a seemingly simple power-off glide on June 8, 1959, the airplane tested him.

Peter Garrison, Air and Space Magazine, November 2007

Parts of this chapter have been published as:

Title	Pilot-Induced Oscillation Analysis and Prediction with Actuator Rate Limiting
Journal	Journal of Guidance, Control, and Dynamics, vol. 20, no. 1, Jan.-Feb. 1997, pp. 81 – 88
Authors	D. H. Klyde, D. T. McRuer, and T. T. Myers
Title	Investigating the Role of Rate Limiting in Pilot-induced Oscillations
Journal	Journal of Guidance, Control, and Dynamics, vol. 27, no. 5, Sept.-Oct. 2004, pp. 804-813
Authors	D. H. Klyde and D. G. Mitchell

4.0 PIO LIMIT CYCLE PREDICTION USING THE X-15 AS A CASE STUDY

The approximate and exact describing functions for rate limiting provide a complete tool kit for the analysis of Category II PIO. The material in this chapter has been taken largely from two references [1,2] that feature the famous X-15 PIO as a case study. Additional details were taken from material created by the author of this thesis as part of the short course "Pilot-Induced Oscillations: From the Wright Flyer to Fly-by-Wire" that is taught to industry and government agencies with co-author David Mitchell.

4.1 Inverse Describing Function Techniques

A key motivation for developing the describing functions (approximate and exact) defined in the previous chapter is to predict closed-loop pilot-vehicle system limit cycles [3] referred to here as Category II PIO. A synchronous pilot longitudinal closed-loop system with a rate limited actuator nonlinear element in series with linear elements is shown in Figure 4.1. For this synchronous behavior, it has been demonstrated that when sinusoidal inputs appear in pilot-vehicle systems, a pilot can essentially duplicate the sinusoid with no phase lag up to frequencies of about 3 Hz (about 20 rad/sec) [4]. For these synchronous cases, the pilot can be represented by a pure gain (K_p) as shown in the Figure 4.1 block diagram.

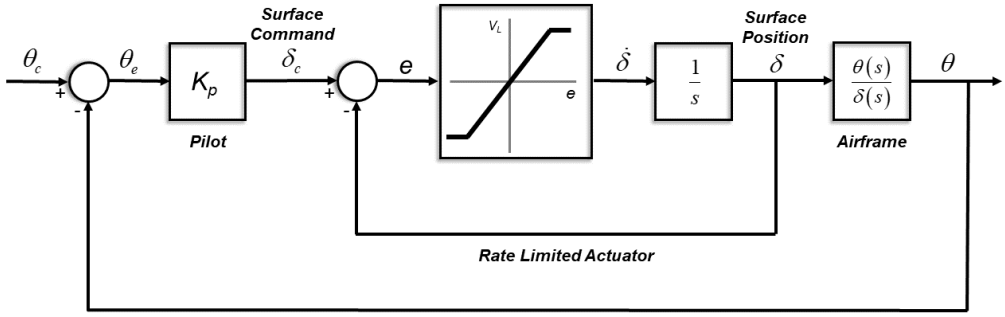

Figure 4.1: *Synchronous pilot closed-loop system with nonlinear actuator.*

The criterion for a neutrally damped oscillation is simply that the open-loop amplitude ratio is 1.0 (0 dB) and the phase is -180°. For an oscillation to persist in the Figure 4.1 example, the synchronous pilot-vehicle system with a series nonlinear element must satisfy the following equation:

$$G(j\omega)N(j\omega, A) = -1 \tag{4.1a}$$

or

$$G(j\omega) = \frac{-1}{N(j\omega, A)} \tag{4.1b}$$

In the equation $G(j\omega)$ represents the frequency dependent linear elements (K_p and θ/δ in Figure 4.1) and $N(j\omega,A)$ represents the frequency and amplitude dependent nonlinear element (the describing function δ/δ_c in Figure 4.1).

A simple analysis technique is possible when the describing function can be separated from the linear elements as in the Figure 4.1 example. First, the negative inverse describing function, that is, the right hand side of Eqn. 4.1b is plotted on a standard Nichols or gain-phase chart. The linear portion, that is, the left hand side of Eqn. 4.1b is then plotted. An intersection of the two curves satisfies Eqn. 4.1b and provides the frequency and amplitude of the limit cycle. This is a prediction of the PIO frequency for the synchronous pilot example.

The most straightforward version of this kind of analysis for rate limiting conditions applies for series command rate limiters or single effectors where $\omega_a >> \omega_u$, since the nonlinearity is then only a function of K^*. In this case the inverse describing function magnitude and phase are defined from Eqns. 4.2 (as derived in Chapter 3).

$$K^* = \frac{\pi}{2}\frac{V_L}{A\omega};\ \Delta\phi = \cos^{-1}\left(K^*\right) \tag{4.2}$$

The Nichols chart plot for this case is shown in Figure 4.2. Once again, the limit cycle frequency is defined by an intersection of the linear transfer function, $G(j\omega)$, with the Figure 4.2 curve.

For effectors where ω_a is not necessarily much larger than ω_u, a more elaborate inverse describing function procedure is required. In Figure 4.3, the inverse exact sinusoidal describing function curves are plotted on a Nichols chart for various time constant ratios, that is, T/T_{NL} = 1.0, 0.8, 0.4, 0.2, 0.1, 0.05, and ~0. It should be noted that each curve is a function of amplitude $(\dot{\delta}_c / V_L)$, time constant ratio (T/T_{NL}), and normalized frequency (ω/ω_a). It should be noted that $\dot{\delta}_c = A\omega$. The time constant ratio for each curve is identified on the plot. Thus, to find the appropriate intersection, the normalized limit cycle frequency as defined by the linear transfer function must match the normalized frequency of the inverse describing function. The details of applying these methods are illustrated by the X-15 examples considered next.

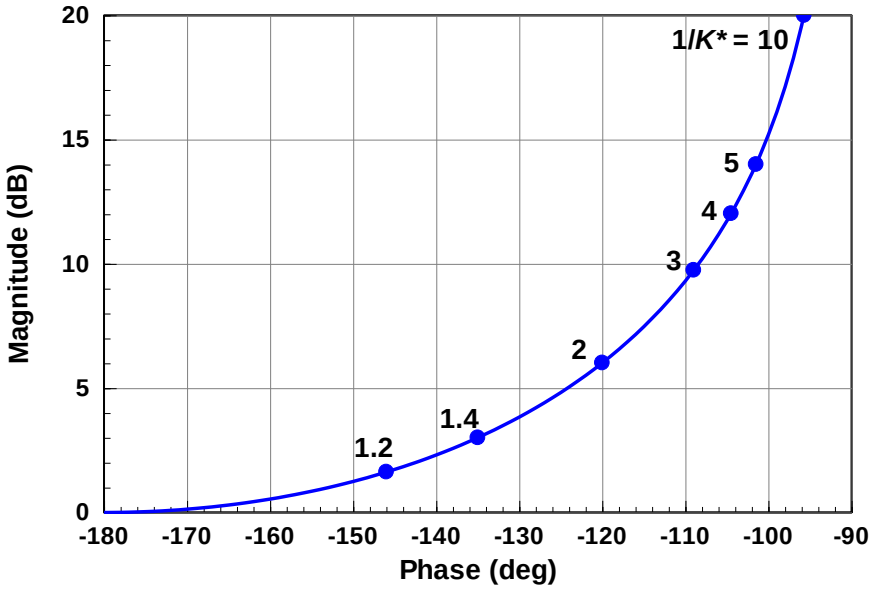

Figure 4.2: *Sinusoidal input/triangle output inverse describing function.*

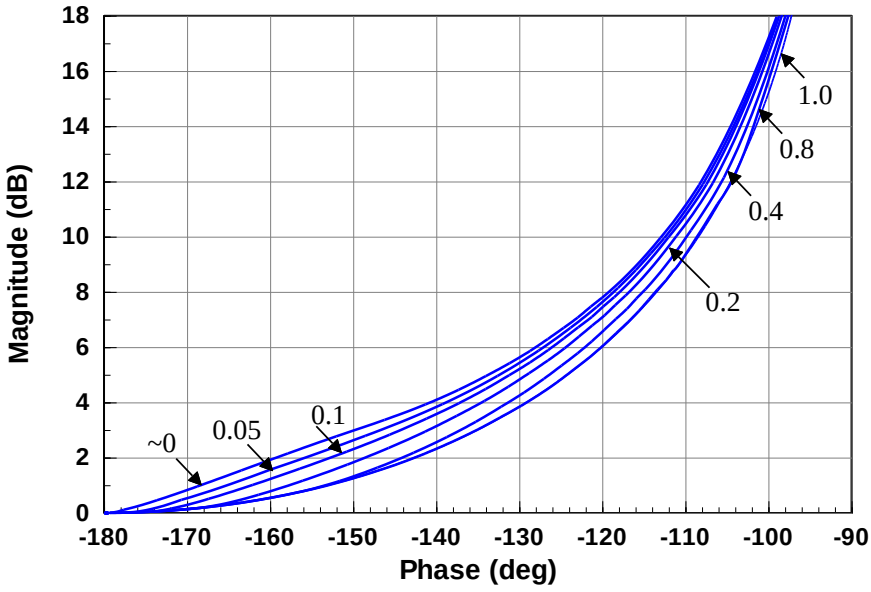

Figure 4.3: *Exact sinusoidal inverse describing function.*

4.3 The X-15 PIO

4.3.1 Program Description

The X-15 program began in 1952 as a joint venture between the U.S. military and the National Advisory Committee for Aeronautics (NACA), the predecessor to NASA, to investigate the basic problems associated with human space flight. As described in [5], the objectives of the aircraft program were to investigate aerodynamic forces, heating, stability and control, reentry characteristics, and human physiology at extremely high speeds and altitudes. The North American Aviation built X-15 aircraft, shown in Figure 4.4, was released from a B-52 carrier vehicle at 45,000 ft. The aircraft would accelerate to speeds from Mach 2 to 6 and achieve altitudes as high as 350,000 ft. The program concluded in 1968 after almost 200 flights that provided over 18 hours of high speed research. First flight of the X-15 was designated for North American pilot Scott Crossfield, a distinguished test pilot whose achievements included the first Mach 2 flight.

Figure 4.4: *X-15 aircraft and pilot Scott Crossfield is strapped in for first flight (NASA Photos).*

4.3.2 Flight 1-1-5 Landing Flare PIO

The X-15 landing flare PIO occurred on 8 June 1959 with pilot Scott Crossfield at the controls. This first flight (designated as Flight 1-1-5) was an unpowered glide flown using the side-located controller and with the pitch damper off. Additional details of the flight and subsequent changes to the aircraft are provided in [6]. As shown in the flare time history traces of Figure 4.5, severe longitudinal oscillations developed near the end of the flap cycle and rate limiting is clearly evident in the horizontal stabilizer angle (δ_h) trace. The "triangle-wave" response of the δ_h time trace in the PIO region indicates that the actuator was operating in the highly saturated region. From the pitch rate (q) trace, a PIO frequency of approximately 3.3 rad/s is measured. For this flight the maximum control surface rate was limited to 15 deg/s.

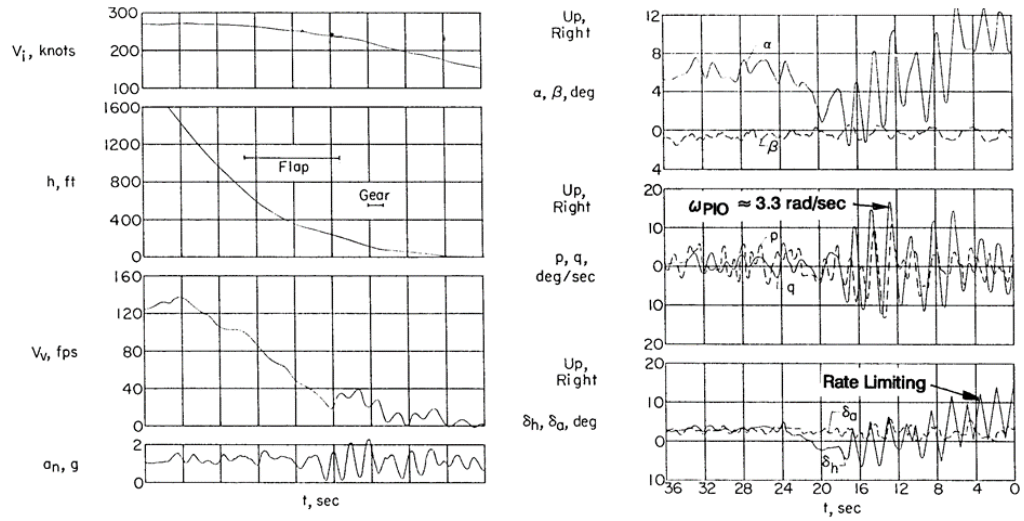

Figure 4.5: *Time histories of the X-15 Aircraft flight 1-1-5 landing flare [6].*

4.3.3 Linear System Survey

Since the PIO occurred with the pitch stability augmentation system (SAS) off, the X-15 bare airframe data [7] were used to generate relevant longitudinal transfer functions. Corrections to the data were made to accommodate the PIO flight condition and aircraft weight. A first order model for the horizontal stabilizer actuator (ω_a = 25 rad/sec) was obtained from [8]. Using these data, the Bode and Nichols frequency response survey of Figure 4.6 for the θ/δ transfer function was generated, where δ is the horizontal stabilizer. The transfer function in Figure 4.6 is displayed in the short hand format introduced and long used by Systems Technology, Inc., that is, $a(s+b)[s^2+2\zeta\omega s+\omega^2]=a(b)[\zeta,\omega]$.

The transfer function gain was arbitrarily set so that the frequency response would pass through 0 dB at –110 deg of phase. Several key Category I PIO indicators, that is, Airplane Bandwidth/Phase Delay [9], and Average Phase Rate [10], are identified on the plots. Not only do all the applied Category I criteria indicate that the X-15 would not be susceptible to PIO, but also the aircraft was found to be Level 1 for the applied handling qualities measures. Figure 4.6 also indicates that the instability frequency for the linear system with a synchronous pilot loop closure is 5.31 rad/sec. This is almost twice that of the observed PIO frequency of 3.3 rad/sec.

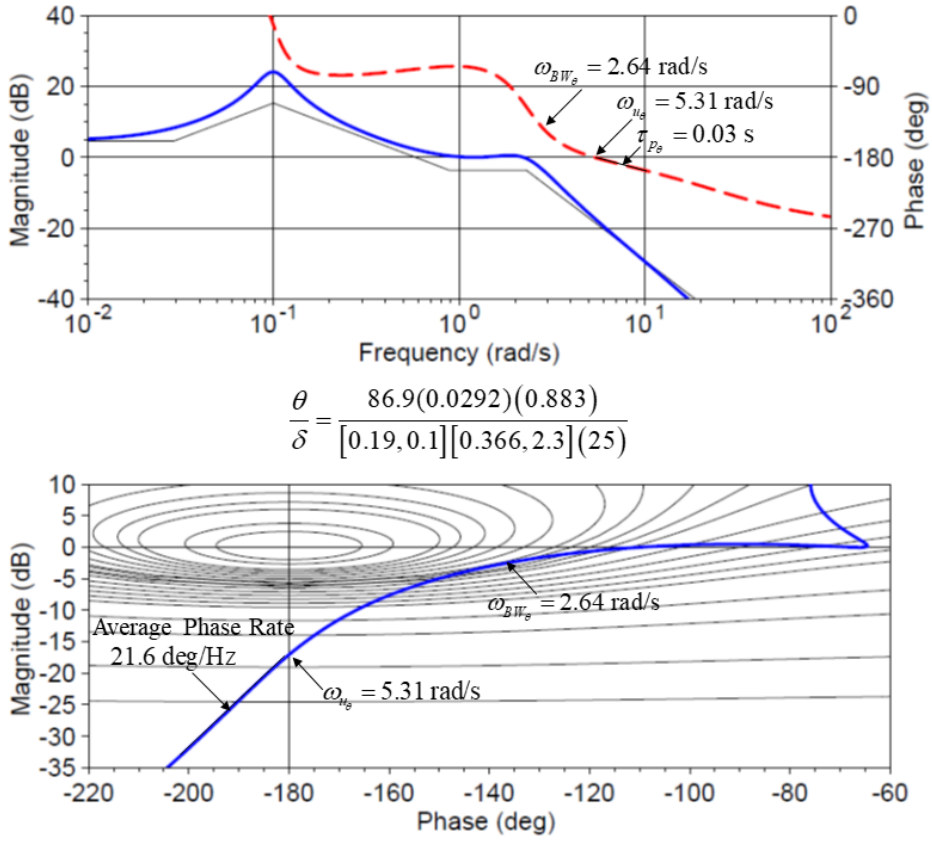

Figure 4.6: *Linear system Bode and Nichols chart frequency response survey of the X-15 at the first flight (Flight 1-1-5) landing flare condition.*

4.4 PIO Prediction

4.4.1 Sinusoidal Input/Triangle Output Inverse Describing Function Analysis

Inverse describing function techniques are used for single effector series nonlinearities to predict limit cycle frequencies and associated added phase lags and magnitude reductions. The X-15 example is used here to demonstrate the technique. The sinusoidal input/triangle output describing function applies for series rate limiting elements and for cases where the effector actuator bandwidth is much larger than the PIO frequency. Because this describing function is only a function of K^*, a significant simplification exists when one of these conditions is met. The X-15 has a 25 rad/s actuator bandwidth, so it is reasonable to assume that this frequency will be significantly larger than limit cycle frequencies that typically vary from 1.4 to 8 rad/s [11].

Figure 4.2 displays the sinusoidal input/triangle output inverse describing function on a Nichols chart with specific values of $1/K^*$ called out. To determine the limit cycle frequency, the gain of the bare airframe X-15 transfer function is adjusted assuming a synchronous pure gain pilot model until the curve is just tangent with the inverse describing function curve. The result is shown in Figure 4.7 where the X-15 transfer function is the solid line and the inverse describing function is the dashed line. At the tangent point a limit cycle frequency of 2.64 rad/s is identified. This is within 20% of the actual PIO frequency identified in Figure 4.5, and clearly demonstrates that the identified rate limiting effects are in the right direction. At the tangency point the nonlinearity provides an added phase lag of -44.8 deg and a magnitude reduction of -2.96 dB.

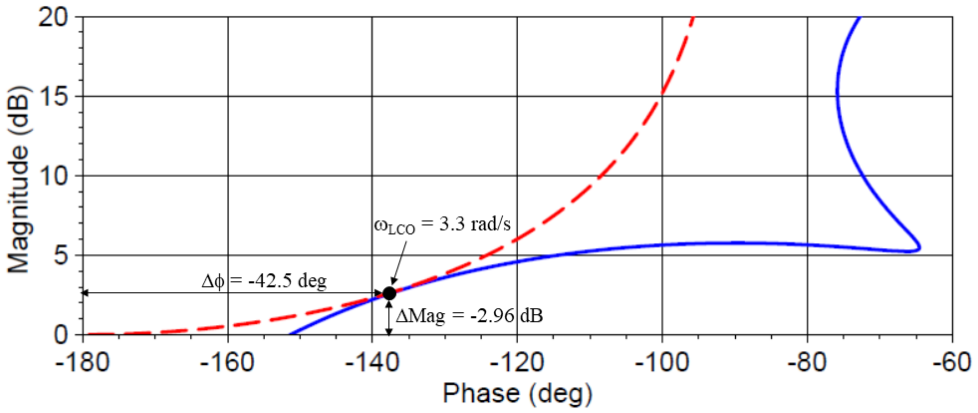

Figure 4.7: *Limit cycle frequency identification using the sinusoidal input/triangle output inverse describing function for the X-15 example case with a synchronous pilot.*

The inverse describing function method can be used to expand the analysis beyond the pure gain synchronous pilot case of Figure 4.7. Given a PIO frequency estimated of 3.3 rad/s as shown in Figure 4.5, it can be assumed that the pilot was adding compensation to achieve a frequency higher than the synchronous pilot case. An increase in PIO frequency is indicative of lead compensation by the pilot near the short period frequency, which is 2.3 rad/s for the X-15. With an assumed pilot response delay of 0.25 s, the following pilot transfer function when combined with the X-15 θ/δ transfer function yields a PIO frequency of 3.3 rad/s:

$$Y_p = 0.835(s+1.375)e^{-0.25s} \tag{4.3}$$

The resulting compensatory pilot-vehicle system finds the inverse describing function at a limit cycle oscillation frequency of 3.3 rad/s. which is equivalent to the measured PIO frequency. Note the impact of the lead compensation is to produce a slight reduction in the gain attenuation and added phase lag due to the control surface actuator rate limiting.

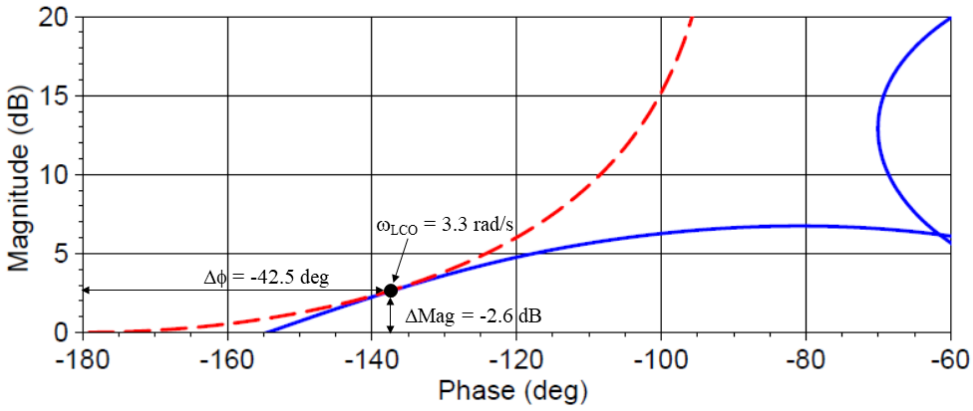

Figure 4.8: *Limit cycle frequency identification using the sinusoidal input/triangle output inverse describing function for the X-15 example case with a compensatory pilot.*

4.4.2 Exact Inverse describing Function Analysis

The X-15 analysis is repeated here using the exact inverse describing function. For the sinusoidal input/triangle output inverse describing function analysis example, it was assumed that the linear 25 rad/s actuator bandwidth of the X-15 was significantly larger than the limit cycle frequency, that is $\omega_a >> \omega_{LCO}$. This assumption reduced the problem to a single inverse describing function curve that was only a function of amplitude, that is, K^*. When using the exact inverse describing function, the methods apply regardless of the linear actuator bandwidth. The first step is to identify the normalized frequency variation on a Nichols chart for the θ/δ transfer function. To accommodate possible intersections with the inverse describing function, it is only necessary to identify normalized frequencies for phase angles less than or equal to -90° as shown in Figure 4.9. These normalized frequencies correspond most closely to the T/T_{NL} = 0.05 curve from Figure 4.13.

To determine the limit cycle frequency, the synchronous pilot gain that is multiplied by the X-15 θ/δ transfer function is adjusted until the curve is just tangent with the inverse describing function curve. The result is shown in Figure 4.11. At the tangent point a limit cycle frequency of 2.69 rad/s is identified via the linear transfer function and corresponding values of added phase lag (-42.7°) and magnitude reduction (-4.22 dB) are read from the plot. Note that the added phase lag and predicted synchronous pilot limit cycle oscillation frequency from the exact inverse describing function case match well with the results displayed in Figure 4.7 for the sinusoidal input/triangle output inverse describing function. Given that this is a highly saturated example, these results were not unexpected. There were more noticeable differences in the gain attenuation predictions with the exact describing function result yielding the larger, more conservative result. While not shown here, the exact inverse describing function analysis can be repeated with a compensatory pilot-vehicle system model for this example case to yield a closer match to the X-15 PIO frequency.

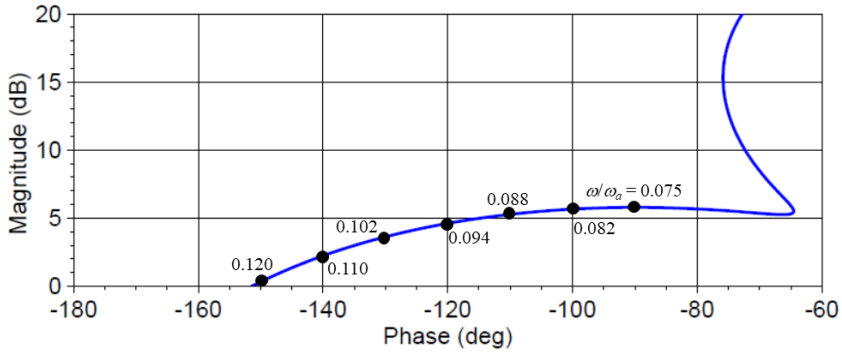

Figure 4.9: *Normalized frequency variation for the X-15 θ/δ linear transfer function.*

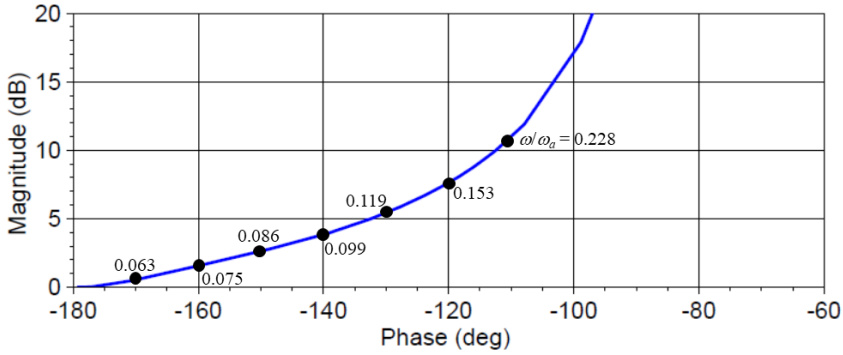

Figure 4.10: *Normalized frequency variation for T/T_{NL} = 0.05 exact inverse describing function curve.*

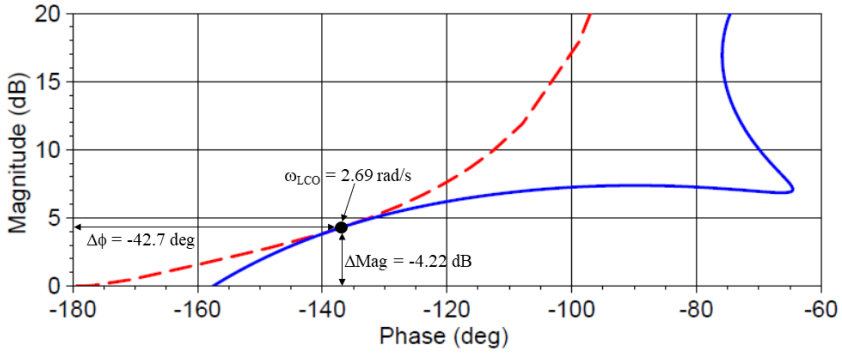

Figure 4.11: *Limit cycle frequency identification using the exact inverse describing function for the X-15 example case with a synchronous pilot.*

4.4.3 Increasing Pilot Gain

Inverse describing function analysis provides a limit cycle frequency estimate at the point of tangency. As the pilot gain is increased beyond this point, several intersections can occur as shown in Figure 4.12, however, only the intersections that result in stable limit cycles, that is, sustained oscillations, are of interest when evaluating PIO susceptibility. The question then arises as to how to determine the stability at the point of intersection. A complete discussion of limit cycle stability is provided in [12]. First, identify the direction of increasing frequency on the linear transfer function and increasing amplitude on the inverse describing function. Next, place yourself as an observer moving along the linear curve in the direction of increasing frequency. As you pass through the point of intersection, if the direction of increasing amplitude along the inverse describing function is toward your right, the limit cycle is stable. If, on the other hand, the direction of increasing amplitude is toward your left, then the limit cycle is unstable. This method was used to identify the stability of the two intersections shown in Figure 35.

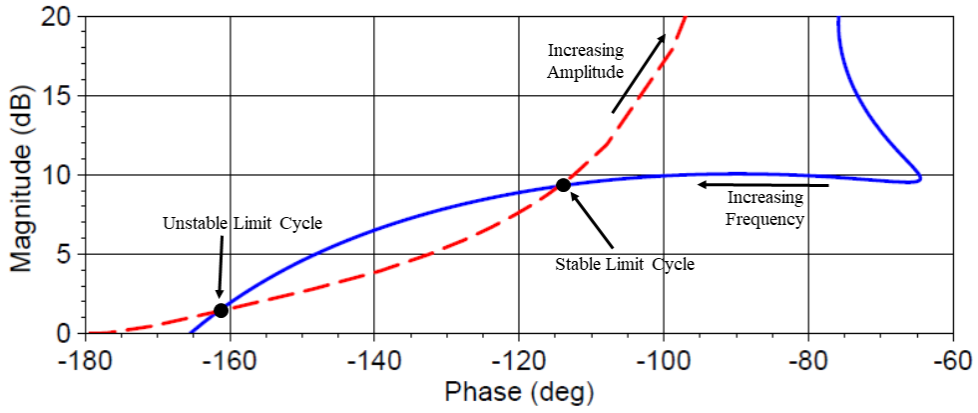

Figure 4.12: *Determining limit cycle stability as pilot gain increases.*

4.5 The Impact of Rate Limiting

4.5.1 Rate Limited Actuator Approximation

To provide additional insight, a quasi-linear describing function for the effective aircraft at (or near) the PIO condition is developed. The added phase lag and synchronous pilot limit cycle frequency, that is, 2.64 rad/s, are first used to define a first order lag representing the rate limited actuator, $\omega_a^* = 2.37$ rad/s. This lag is then combined with the bare airframe X-15 dynamics to define a new effective vehicle linear system model. A Bode frequency response for the "new" vehicle is shown in Figure 4.13. When this response is compared with the linear response of Figure 4.6, there is significant reduction in bandwidth frequency, a large increase in phase delay, and the unstable frequency is, as expected, equal to the predicted synchronous pilot limit cycle frequency.

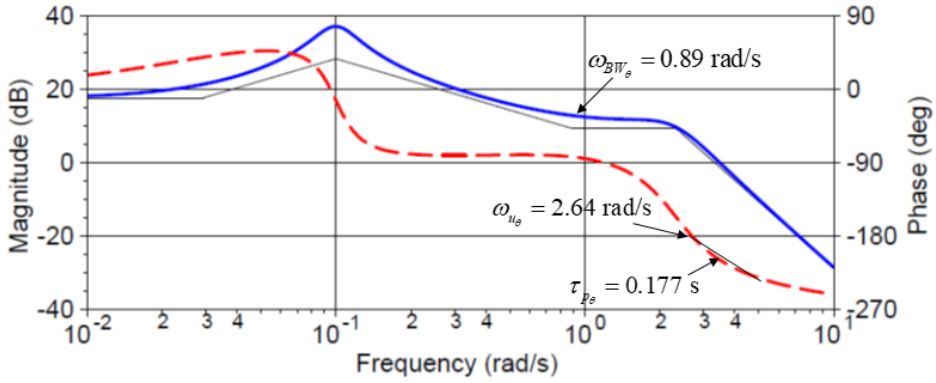

Figure 4.13: *Frequency response Bode plot for the X-15 synchronous pilot example case with a first order lag representation of the highly saturated actuator.*

4.5.2 The Impact of Rate Limiting on Aircraft Bandwidth

As described in Chapter 3, rate limiting will occur when the input frequency exceeds the "saturation frequency" or what reference [13] refers to as the onset frequency, which can be defined in terms of the K^* parameter:

$$\omega_{onset} = \frac{2K^*}{\pi}\omega_i \tag{4.4}$$

Noting that K^* is a function of input amplitude, A, and maximum rate, V_L, onset frequencies were computed for the X-15 example where V_L = 15 deg/sec, ω_i = 3.3 rad/sec, that is, the PIO frequency, and A = 3, 6, 9, 12, and 15 degrees. The results are plotted in Figure 4.14 with a simplified version of the aircraft bandwidth/phase delay PIO boundaries included [9].

When A = 3 deg, the onset frequency is above the PIO frequency and no rate limiting occurs. Thus, the bandwidth and phase delay parameters represent the linear system values for this case. As the input amplitude increases to 6 deg, the onset frequency moves below the PIO frequency. As described in Chapter 2, this falls in the near saturation region and the effect of the rate limiting is minimal as evident by the small shift up and to the left in the bandwidth/phase delay parameter plane. For the remaining three input amplitude cases, the aircraft has entered the highly saturated region and is clearly susceptible to PIO. Note the significant jump, a jump resonance [14], in phase delay for these points that results from the significant added phase lag from the rate limiting. Beyond A = 9 deg the bandwidth frequency is determined by the gain margin frequency [9], and thus also shows a dramatic shift. The impact of the rate limiting is to greatly reduce bandwidth frequency and increase phase delay, both contributing factors to a poor handling aircraft that is also highly susceptible to PIO.

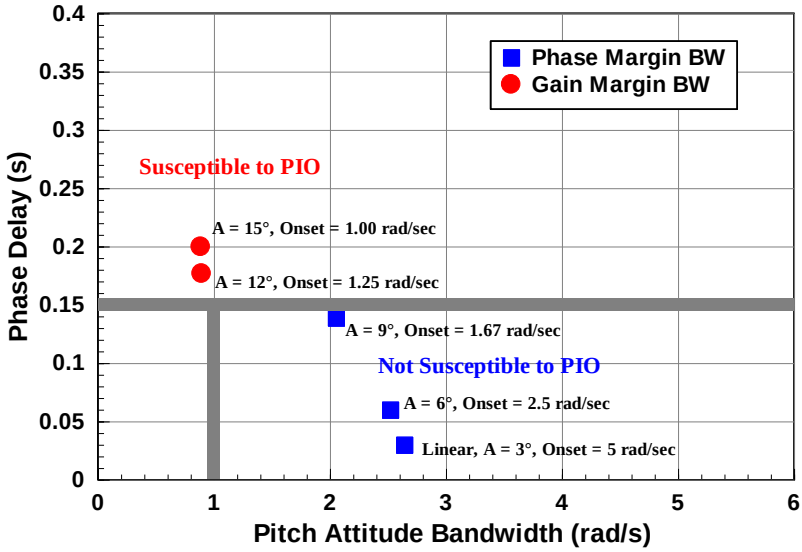

Figure 4.14: *X-15 example bandwidth/phase delay variations with increasing rate saturation.*

4.6 Conclusions

Rate limiting of control surface actuators can have dire effects on handling qualities and PIO. The magnitude of the effects depends on three basic factors: (1) how long the actuator is rate-limited; (2) how much more the pilot-vehicle system demands of the airplane; and (3) the consequences on aircraft dynamics of encountering the limit. Fundamentally, rate limiting introduces added phase lag into the response of the aircraft. This alone can be sufficient to lead to PIO, depending upon the characteristics of the aircraft. Flight 1-1-5 of the X-15 provides a perfect example of this effect, wherein an aircraft configuration that had good predicted handling qualities by linear system measures, still had a severe Category II PIO due to the control surface actuator rate limiting. For Category II PIO cases where the rate limiting occurs in series with an otherwise linear system, inverse describing function techniques are used to predict the limit cycle or PIO frequency. In the X-15 example used here, the PIO frequency was significantly reduced from the linear neutral stability frequency, thus displaying the profound impact of actuator rate limiting. This result takes on added significance in light of the inability of the linear criteria and metrics to identify the PIO susceptibility of this configuration.

4.7 References

1. Klyde, D. H., D. T. McRuer, and T. T. Myers, "Pilot-Induced Oscillation Analysis and Prediction with Actuator Rate Limiting," *J. Guidance, Control, and Dynamics*, Vol. 20, No. 1, Jan. – Feb. 1997, pp. 81 – 88.

2. Klyde, D. H., and D. G. Mitchell, "Investigating the Role of Rate Limiting in Pilot-induced Oscillations," *J. Guidance, Control, and Dynamics*, Vol. 27, No. 5, Sept.-Oct. 2004, pp. 804-813.

3. Ashkenas, I. L., H. R. Jex, and D. T. McRuer, *Pilot-Induced Oscillations: Their Cause and Analysis*, Norair Report NOR-64-143, Northrop Corporation, July 24, 1964.

4. McRuer, D. T., *Pilot-Induced Oscillations and Human Dynamic Behavior*, NASA CR-4683, Dec. 1994.

5. Wallace, L. E., *Flights of Discovery: 50 Years at the NASA Dryden Flight Research Center*, NASA SP-4309, NASA History Office, Washington, D.C., 1996.

6. Matranga, G. J., *Analysis of X-15 Landing Approach and Flare Characteristics Determined from the First 30 Flights*, NASA TN-D-1057, July 1961.

7. Heffley, R. K., and W. F. Jewell, *Aircraft Handling Qualities Data*, NASA CR-2144, December 1972.

8. Taylor, L. W., Jr., and J. W. Smith, *An Analysis of the Limit-Cycle and Structural-Resonance Characteristics of the X-15 Stability Augmentation System*, NASA TN D-4287, December 1967.

9. Mitchell, D. G., and R. H. Hoh, *Development of Methods and Devices to Predict and Prevent Pilot-Induced Oscillations*, AFRL-VA-WP-TR-2000-3046, December 2000.

10. Gibson, J. C., *Development of a Methodology for Excellence in Handling Qualities Design for Fly by Wire Aircraft*, Delft University Press, The Netherlands, 1999.

11. Mitchell, D. G. and D. H. Klyde, "Identifying a Pilot-Induced Oscillation Signature: New Techniques Applied to Old Problems," *Journal of Guidance, Control, and Dynamics*, Vol. 31, No. 1, 2008, pp. 215-224.

12. Graham, D. and D. McRuer, Analysis of Nonlinear Control Systems, John Wiley and Sons, Inc., New York, 1961. (Also Dover, 1971).

13. Hanke, D., "Handling Qualities Analysis on Rate Limiting Elements in Flight Control Systems," *Flight Vehicle Integration Panel Workshop on Pilot Induced Oscillations*, AGARD-AR-335, Febuary 1995.

14. Graham, D., and D. McRuer, "Retrospective Essay on Nonlinearities in Aircraft Flight Control," *J. Guidance*, Vol. 14, No. 6., Nov.-Dec. 1991, pp. 1089 – 1099.

Part II: Category II PIO Mitigation Methods

5. Historical Precedents for Inceptor Cueing

The artificial feel system is relatively alterable, especially when fully-powered, irreservable controls are used. Thus the control system designer is faced with the task of achieving the desired complete pilot-airframe system response by a prudent design of the artificial feel system.

BuAer Report AE 61-4, Volume V, The Artificial Feel System, May 1953

Parts of this chapter have been published as:

Title	Development of Smart-Cue and Smart-Gain Concepts to Alleviate Pilot-Vehicle System Loss of Control
Journal	Journal of Guidance, Control, and Dynamics, vol. 32, no. 5, Sept.-Oct. 2009, pp. 1409-1417
Authors	D. H. Klyde and D. T. McRuer

5.0 HISTORICAL PRECEDENTS FOR INCEPTOR CUEING

Having identified the deleterious effects of control surface actuator rate limiting in Part I of this thesis, Part II explores the use of Category II pilot-induced oscillation (PIO) mitigation methods based on novel active inceptor cueing methods. While the effective aircraft dynamic properties involved in PIO events have been extensively studied and understood including via the Unified PIO and ARISTOTEL programs identified in Chapter 1, similar scrutiny has not been paid to the many aspects of the primary manual control system that converts the pilot control inputs to motions of the control surfaces. It has often been tacitly assumed that the adoption of fly-by-wire systems has eliminated the primary manual control link as an important player in loss of control situations. Consequently, the impact of static and dynamic control system effects that distort "ideal" pilot to surface relationships, the near absence of manipulator tactile cues for some fly-by-wire systems, as well as the total elimination in fly-by-wire systems of some favorable cues present in traditional hydro-mechanical systems have not received detailed attention. To this end, this chapter, largely based on the material in [1], explores the historical precedents for inceptor cueing to alert and, if necessary, constrain pilot actions to preserve controlled flight. Successful implementation of these mechanisms inspired and informed the PIO mitigation methods that are the focus of Part II.

5.1 Some Historical Precedents

5.1.1 Inceptor Force Cueing

For many years, designers of manual primary control systems used various devices attached to the cockpit controls to cue the pilot. In the simplest and most primitive systems, the cockpit controls are mechanical, comprising cables, push-pull rods, etc. that connect the controls directly to the control surface – a reversible control system. Thus, the pilot applies to the cockpit controls all the forces required to move the control surface. Here, the controller cues reflect the aerodynamic forces on the surface. There may also be some acceleration-sensitive cues due to effective mass imbalances in the control system. These may be deliberate to provide a bobweight effect that modifies the stick force/g, or inadvertent. In the latter instance they can sometimes create inappropriate stick forces, for instance during a catapult takeoff. Parasitic effects, such as cable friction, free play, etc. are minimized by rigging adjustments.

As speed regimes and size of the aircraft increased, the corresponding forces required by the pilot to move the surfaces also increased. To provide the pilot with some assistance the cockpit controls were aided by various gearing-like devices, such as ratio changers or connecting the cockpit controls directly to a tab or servo tab that recruited aerodynamic forces to apply moments to the main control surfaces. Tabs were used on numerous designs including the Boeing B-17 bomber and the Lockheed Constellation transport. Then came power boost systems. Here, the pilot retained a direct connection with the surfaces with the power boost operating in parallel to provide additional force.

The next stage in the evolution of manual control systems amounted to a watershed. In the 1940's Northrop Aircraft, Inc. developed a series of flying wing aircraft, starting with the N9M as a small experimental version and progressing to the large XB-35 and YB-49 bombers, which had wing

spans identical to the Northrop B-2 that came along decades later. The early N9M experimental craft showed an alarming tendency for elevon hinge moment reversal at high angles of attack. This provided the motivation for the development of so-called fully-powered surface actuation systems to completely separate the pilot from the control surfaces – the irreversible control systems. This solved the basic problem intended and also introduced two very important side effects. The first was that the manual control system configuration inboard of the fully-powered surface actuators made it somewhat easier to introduce small actuators as series links into the control path. This made possible the first *Stability Augmentation Systems* (SAS) to correct some of the dynamic deficiencies in aircraft stability and control properties. By virtue of the series installation, the pilot was unaware of the actions of the SAS, while the limited authority made it possible for the pilot to readily override any hardover SAS failures. These were the days of single thread SAS systems, so such provisions were critical safety issues. Because aircraft stability and control dynamic deficiencies were becoming rampant, this "side effect" of fully-powered manual control systems was welcomed by flight control system designers charged with the development of systems to remedy the dynamic deficiencies.

The second side effect was also of profound importance. With the isolation of the pilot came a loss of the proprioceptive and tactile cues associated with direct connection of the cockpit inceptors with their corresponding control surfaces. This created a requirement for the development of artificial feel devices to provide surrogates for the missing cues. It also created an opportunity for the introduction of other force and position cueing that had no direct parallel with those exhibited by conventional mechanical manual control systems. In essence, the newly required force producers could, in principle, feed back various appropriate dynamic variables as artificial feel system force cues. Then, when the pilot responded to these, the effective closed-loop pilot-vehicle system dynamics were improved just as with the SAS. Thus, the artificial feel system became a *Force Stability Augmentation* system [2]. The difference between this and the conventional (motion) *Stability Augmentors* is that the latter are always available, whereas the Force Stability Augmentor requires the pilot to be active in the pilot-vehicle system loop to provide the stabilizing function. The similarity in the two categories of stability augmentation system is often overlooked and the awkward "Force Stability Augmentor" phrase is simply not competitive with the easier "Artificial Feel System."

In the several generations of aircraft equipped with fully-powered control systems, artificial feel to simulate the cues found in reversible mechanical systems has been introduced in a number of ways, some of which are listed below:

- Dynamic pressure ($\bar{q}$) bellows – In longitudinal control systems on aircraft such as the Northrop flying wings and the Northrop F-89, $\bar{q}$ -bellows provided a stiffness force proportional to dynamic pressure. The systems often used a dead center linkage to trim. The system as used on the Northrop XB-35 flying wing is illustrated in Figure 5.1.
- Springs – In lateral control systems, springs were used to provide artificial feel. Preloaded springs were often used to help center the cockpit controller and to minimize hysteresis effects.

- Down spring – In longitudinal control systems a preloaded spring that tended to push the stick down was used to modify the stick force per speed characteristic. Down springs were also used on reversible systems.
- Stick Pushers – These devices were used to introduce controller forces proportional to Mach number to cope with the "tuck under" characteristic wherein the nose will pitch downward as the airflow in the vicinity of the wing reaches supersonic speeds.
- Bobweights – These are used to modify the stick force per g characteristic. Bobweights are sensitive to local acceleration, so favorable locations were a critical design feature. They were most often located at or near the pilot location. They were often integrated with $\bar{q}$ -bellows trim.
- Dual bobweights – These were most commonly found on Grumman aircraft such as the F-14. They were designed to give an effective favorable bobweight location and, with so called "sprash pots," provide forces that were proportional to rate.
- Stick shakers – This device was designed to mimic the natural tactile cue associated with the vibrations felt on a reversible manual control system inceptor as the aircraft approached stall. The device uses an angle-of-attack detector and provides a vibration on the stick near stall.

Several of the devices described above were originally used in conventional, reversible manual control systems.

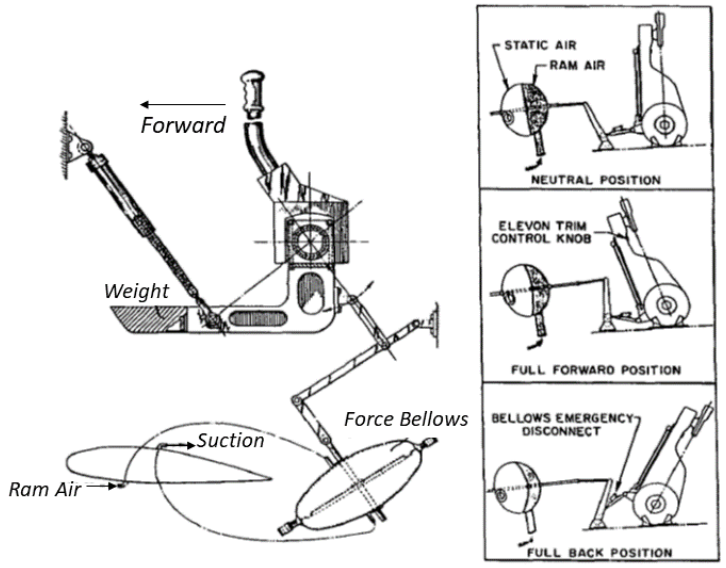

Figure 5.1: *Northrop XB-35 pitch axis artificial feel system with dynamic pressure bellows [3].*

For fly-by-wire (FBW) systems that employ force sensing inceptors such as the General Dynamics (now Lockheed Martin) F-16, artificial feel system cues have been all but eliminated. Most FBW systems have, however, maintained position sensing control inceptors that feature significant range of motion. Some FBW systems such as that employed on the Boeing 777 restore artificial feel via a back driven control column and yoke. Furthermore, the Lockheed Martin F-35 Joint Strike Fighter features a fully programmable sidestick controller.

5.1.2 Command Path Gain Reduction

Command path gain reduction concepts are also not without precedent. Methods for mitigating PIO on the Space Shuttle were investigated by NASA. Reference [4] describes the PIO suppression (PIOS) filter that was designed to reduce pilot gain when potential for PIO is high, while minimizing any additional phase lag. To achieve the desired gain reduction, the filter modifies the stick shaping function as a function of the amplitude and frequency of the pilot's input, thereby reducing the amount of rate limiting. In essence, the filter attenuates the pilot input at all frequencies. The PIOS filter was implemented in the Shuttle control laws, and no pitch PIOs have been reported in the open literature since the 1977 ALT-5 event [5].

5.2 Fundamental Understanding – Key Underlying Factors Related to Cockpit Inceptors

When means such as inceptor force cueing are considered to alleviate loss of control due to PIO, there is a fundamental starting point from which new approaches can be developed. That is, by virtue of having encountered, analyzed, and solved many pilot-associated loss of control situations in the past, there is an excellent understanding of many of the key factors involved. For example, for the very severe set of PIO problems the understanding of the key underlying factors is excellent [6,7]. Essentially all PIO situations that have occurred in the past involve:

- The pilot as an essentially continuous controller element in a very high gain (for example, unstable or neutrally stable) closed-loop pilot-vehicle system.
- Fundamental mismatches between desired and actual effective aircraft characteristics.

In this scenario, the pilot's characteristics have been largely unchanged through aviation's recent history, although they have been differentially affected by the evolving nature of the pilot's means of imposing control, that is, the evolving cockpit inceptors. The airplane-centered mismatches have tended to be era-sensitive. In early era aircraft, directly connected pilot-surface primary control system PIO were sometimes encountered due to aircraft stability and control deficiencies such as unstable short period and rapidly diverging spiral modes. PIO were very rare for stable aircraft with adequate flying qualities, although nonlinearities including those induced by mis-rigging phenomena could occasionally lead to PIO problems.

In larger early aircraft that required some clever mechanical gearings, such as geared or servo tabs, to convert pilot-generated control forces to levels adequate for the movement of large control surfaces, the lags introduced between the pilot's direct control of a tab and the actual surface movement could significantly change the effective vehicle lags. PIO were then quite often

exhibited in high precision tasks such as tightly controlled approach and landing. Pilots were able, with substantial training and experience, to compensate for these essentially linear system lags.

When the first fully-powered hydraulic actuating systems were introduced (e.g., on the Northrop flying wings and Northrop F-89, as well as somewhat later on the North American F-86 and similar fighters) the developmental problems of the surface actuators themselves played important roles. The most notable were associated with achieving a sufficiently high maximum surface rate, a high degree of effective linearity between pilot command and surface response, and aircraft dynamic sensitivities that did not require extremely careful pilot adjustment and variation of his gain while engaged in tight closed-loop tasks. The notable lessons learned during this period were associated with:

- Extreme sensitivity especially when associated with rapidly varying aircraft gain. An important example was the Northrop XP-89, where in a dive from, say, M = 0.8, with a stick force/g near 70 lbs/g, the aircraft was converted to M = 0.76, with a stick force/g near 4-5 lbs/g that required a bobweight to reach those values from 3 lbs/g. After learning to cope with these changes, and occasional momentary PIO, the airplane was considered "sensitive," and went on to an operational career of over two decades.
- Sluggish actuation system dynamics and extreme maneuvers. The far-famed "JC Maneuver," a name coined for the handling qualities cliff by the upset test pilot of an early North American F-86, was an example of some of the first sustained and very exciting PIO.
- Insufficient maximum control surface rates. Most control system designers of early fighters experimented extensively, searching for minimum "magic" values of control surface rate that always insured adequate and precise control. Minimum surface rate has an important impact on the hydraulic system power supply requirements and hence aircraft weight. Only under somewhat unusual circumstances did actual aircraft have to put up with insufficiencies. A notable example resulted in the North American X-15 PIO [8].

These encounters and experiences equipped designers with practical data and considerations to avoid these particular causes in most, if not all, of the later, so-called, century series fighters. The primary control systems still had direct connections from the pilot to the hydraulic valves directly controlling the surfaces, with appropriate intermediaries such as force producers, preloads for centering and reduction of hysteresis, etc. to achieve a sufficient degree of system quasi-linearity.

Then came the modern era of fly-by-wire, with the ideal being a complete lack of mechanical connection between the pilot and the surface actuation systems. Given the simplified mechanical designs, why does the PIO phenomena persist? With fly-by-wire the pilot's manipulator can be a sidestick, and the control signals could be either force or displacement depending on the stick travels allowed by the detailed design. The earliest systems, for example, the F-16, were basically force sensing sticks, and a number of PIO inevitably followed [9]. With force sticks:

- Cues related to trim state and actual surface position provided to the pilot from the stick forces and displacement are absent, that is, the inceptor has lost its proprioceptive feedback display function.
- There is no stick force indication of control surface rate limiting or even when the surface is on its stops. The mechanical forces imposed on the pilot are defined by a force gradient and a major force buildup when encountering the stick stops.
- Determining and adjusting the sensitivity range can be a very time consuming and expensive matter. For example, Appendix C of [10] investigated 19 configurations with 34 pilots to arrive at compromises for the General Dynamics (now Lockheed Martin) F-16.

On fly-by-wire transport aircraft there is currently a major philosophical difference in pilot inceptor design. Airbus uses passive sidestick controllers, while Boeing uses back-driven wheel/columns. With the back-driven installations many of the cues removed by virtue of the mechanical design of sidesticks can be re-inserted. Because the control wheel/columns are coupled and moving, again acting as a "proprioceptive display," trim state, pilot-copilot interaction and joint situation awareness are also brought back to an earlier era. Further, the employment of active side stick inceptors in military aircraft such as the F-35 and CH-53K and commercial aircraft such as the Gulfstream G500 points to a trend towards re-introduction of haptic feedback.

5.3 Mechanisms for Eliminating Unfavorable Pilot-Vehicle Interactions

To quote the late John Gibson, a leading flying qualities engineer from the UK, the best way to eliminate unfavorable pilot-vehicle interactions is "by design" and many of his design guidelines can be found in his TU Delft Ph.D. thesis [11]. As described above, the causes of unfavorable pilot-vehicle interactions are well understood. Thus, this knowledge base of analysis techniques and criteria must be applied throughout the design process. Note, however, that the application of criteria to provide a simple "black box" Go/No Go answer is a dangerous practice. The next mechanism to eliminate unfavorable pilot-vehicle interactions is flight test. To successfully uncover potential "handling qualities cliffs," appropriate evaluation tasks that force the pilot to interact with the aircraft in a closed-loop, high gain manner are required. Example tasks include precision offset landings, aerial refueling, formation flying, etc.

The last line of defense against unfavorable pilot-vehicle interactions are on-board systems that include PIOS filters, rate limiting phase compensators, and various detection schemes/warning devices. PIOS filters such as those used on the Space Shuttle [5] modify the stick input as a function of command amplitude and frequency of the pilot's input to reduce the amount of rate limiting. Rate limiting phase compensation schemes, such as those employed on the SAAB Gripen [12] and the Boeing F/A-18 E/F [13], attempt to minimize the added phase lag associated with rate limiting by reversing the actuator when the commanded rate is of the opposite sign. These schemes appear to work reasonably well although the handling qualities of the aircraft are often still degraded while the alleviation schemes are active. Furthermore, there is no feedback cue to the pilot when the scheme is active. Various on-board PIO detection schemes have also been development. These include a Neural Net-based technique developed by Accurate

Automation Corp. [14], the Real-time Oscillation Verifier (ROVER) concept of Hoh Aeronautics, Inc. [15], and the wavelet-based Loss of Control Analysis Tool Set (LOCATS) [16] from Systems Technology, Inc. The objective of these detection schemes is to provide ample warning to the pilot of impending PIO or loss of control. Because the schemes designed to detect the oscillatory nature of PIO need at least some fraction of the initial PIO cycles to positively detect the condition, ample warning may not be possible.

Note that these "fix-it" approaches presume that the control system elements work as intended by the designer. Yet departures from the design ideals, ranging from inadequate surface rates or mis-rigging of control system elements to faulty design are often root causes of unfavorable pilot-vehicle characteristics. The recognition that this can be the case in practice was one of the factors leading to the Loss of Control Inhibition System (LOCIS) concept of A'Harrah (US Patents #7,285,932 [17] and #7,285,933 [18]) that inspired some of the activities of the work described herein. This, in turn, leads to a somewhat more general view that "dynamic distortions" that result in the departures of the actual system from the ideal can be key factors. This is explored next in Chapter 6.

5.4 Conclusions

In a review of historical examples, it was shown the aircraft designers have long used inceptor artificial feel mechanisms to restore or provide cues to the pilot when flying aircraft with indirect flight control systems. Further, it was shown that the fundamental understanding of PIO is sufficient to devise mitigation methods. Whether a suppression filter or a control surface actuator rate limiting compensation scheme, the industry has introduced mechanisms through which the deleterious effects of rate limiting can be mitigated at least partially, but often at the expense of handling qualities and pilot-vehicle system task performance. The challenge addressed in the subsequent chapters of Part II is to devise new methods that can not only mitigate PIO susceptibility due to rate limiting but also maintain desirable handling qualities and task performance.

5.5 References

1. Klyde, D. H., and D. T. McRuer, "Development of Smart-Cue and Smart-Gain Concepts to Alleviate Pilot-Vehicle System Loss of Control," *J. of Guidance, Control, and Dynamics*, Vol. 32, No. 5, Sept.-Oct. 2009, pp. 1409-1417.

2. Anon., *The Artificial Feel System*, U.S. Navy Bureau of Aeronautics (BuAer) Report AE-61-4V, May 1953.

3. Ashkenas, I. L., "Northrop Flying Wing, A Design Experience," presented as part of the *AIAA Distinguished Lecture Series*, 1990-1992.

4. Smith, J. W., and J. W. Edwards, *Design of a Nonlinear Adaptive Filter for Suppression of Shuttle Pilot-Induced Oscillation Tendencies*, NASA TM-81349, 1980.

5. Teper, G.L., R.J. DiMarco, I.L. Ashkenas, and R.H. Hoh, *Analysis of Shuttle Orbiter Approach and Landing Conditions*, NASA CR-163108, July 1981.

6. McRuer, D. T., *Pilot-Induced Oscillations and Human Dynamic Behavior*, NASA CR-4683, Dec. 1994.

7. Anon., *Aviation Safety and Pilot Control*, prepared by the National Research Council Committee on the Effects of Aircraft-Pilot Coupling and Flight Safety, National Academy Press, Washington, D.C., 1997.

8. Matranga, G. J., *Analysis of X-15 Landing Approach and Flare Characteristics Determined from the First 30 Flights*, NASA TN-D-1057, July 1961.

9. Smith, J. W., *Analysis of a Lateral Pilot-Induced Oscillation Experienced on the First Flight of the YF-16 Aircraft*, NASA TM-72867, September 1979.

10. Garland, M. P., M. K. Nelson, R. C. Patterson, D. W. Peterson, *F-16 Flying Qualities with External Stores*, AFFTC-TR-80-29, Feb. 1981.

11. Gibson, J. C., *Development of a Methodology for Excellence in Handling Qualities Design for Fly by Wire Aircraft*, Delft University Press, The Netherlands, 1999.

12. Rundqwist, L., and R. Hillgren, "Phase Compensation of Rate Limiters in JAS 39 Gripen," AIAA-96-3368 presented at the *Atmospheric Flight Mechanics Conference*, San Diego, CA, 29-31 July 1996.

13. Donley, S. T., G. L. Gross, J. L. Koper, "Actuator Rate Saturation Compensator," United States Patent Number 4866361, 12 September 1989.

14. Cox, C. J., and C. E. Lewis, "Pilot-Induced Oscillation Detection and Compensation Apparatus and Method," *United States Patent Number 5935177*, 10 August 1999.

15. Mitchell, D. G., and R. H. Hoh, Development of Methods and Devices to Predict and Prevent Pilot-Induced Oscillations, AFRL-VA-WP-TR-2000-3046, Dec. 2000.

16. Thompson, P. M., D. H. Klyde, E. N. Bachelder, and T. J. Rosenthal, *On-Line Loss of Control Detection Using Wavelets*, NASA CR-2005-212873, July 2005.

17. A'Harrah, R. C., "Method and Apparatus for Loss of Control Inhibitor Systems," *United States Patent*, US Patent #7,285,932, Oct. 23, 2007.

18. A'Harrah, R. C., "Method and Apparatus for Loss of Control Inhibitor Systems," *United States Patent*, US Patent #7,285,933, Oct. 23, 2007.

6. Dynamic Distortion

The distortion of the pilot's input to control surface output relationship is an effective metric of anomalous control system behavior, which can contribute to loss-of-control accidents and incidents.

Ralph A'Harrah, NASA Headquarters, 2004

Parts of this chapter have been published as:

Title	Development of Smart-Cue and Smart-Gain Concepts to Alleviate Pilot-Vehicle System Loss of Control
Journal	Journal of Guidance, Control, and Dynamics, vol. 32, no. 5, Sept.-Oct. 2009, pp. 1409-1417
Authors	D. H. Klyde and D. T. McRuer

6.0 DYNAMIC DISTORTION

This chapter explores the concept of dynamic distortion that is largely based on the material in [1]. The analysis of the F-14 database was conducted as part of the NASA-sponsored work that informed the development of pilot-induced oscillation (PIO) mitigation techniques described in Part II of this thesis.

6.1 Introduction

At present the aircraft flying qualities community has sufficient understanding of pilot-vehicle systems in general to make the case that effective vehicle dynamic characteristics for a given design can be considered to be either ideal or good enough. Departures from these nominally ideal properties can then be labeled as "distortions" that may underlie pilot-vehicle system problems. A common example is control surface rate limiting that is the focus of this thesis, where deviation from ideal or desirable values has been shown to lead to PIOs in some circumstances. Another example is mis-rigging of control system elements, such as mechanical maladjustments leading to control system backlash or excessive hysteresis.

The common theme is that the actual manual flight control system is in some way deviating from an ideal system. The pilot is expecting one type of response, typically a linear response that has predictable characteristics, but the actual system is behaving differently because of the distortion. Within this general context, Ralph A'Harrah while at NASA Headquarters proposed the "Loss of Control Inhibition System" (LOCIS) wherein distortions are detected, and appropriate cues are then introduced to the pilot by way of compensation to mitigate the distortions (U.S. Patents #7,285,932 and #7,285,933). It was recognized at the time that this was still a general concept that had yet to be made concrete or specific. It served as a motivation for the work reported in this part of the thesis to attempt to quantify such conceptual terms as "distortions" and "idealized systems" as innovative and unifying principles underlying the development of corrective measures in the form of controller cues. To advance this generalized theme, concrete examples were needed. Thus, the critical distortion involving control surface rate limiting as the key factor in Category II PIO [2] and subsequent loss of control was selected for the work described herein.

6.2 The Concept of Dynamic Distortion

Dynamic Distortion, as defined herein, is characterized by the departure of the actual primary manual control system from an idealized system. This requires consideration of potential "ideal system characteristics" and the varieties of potential "distortions." For manual control system departures from the ideal, the distortions are somewhat different for classical hydro-mechanical systems, discussed first, and fly-by-wire systems.

Many of the sources of distortion, including their corrective techniques, are reflected in the much simplified Figure 6.1. Some are fundamentally parasitic, such as control system and hydraulic valve friction and any backlash or free play in joints. Others are the consequence of design, such as flow rate limiting and valve bottoming, when the servovalve movement reaches its physical limit. Others are corrective procedures, such as preloads to load out backlash or to counter the

effects of friction. Recall that the actual distortions are not the specific sources themselves but rather the residual effect left from inadequate or imprecise compensation. The impact of these unfavorable properties on the stability of the pilot-vehicle system can be assessed by their describing functions [3].

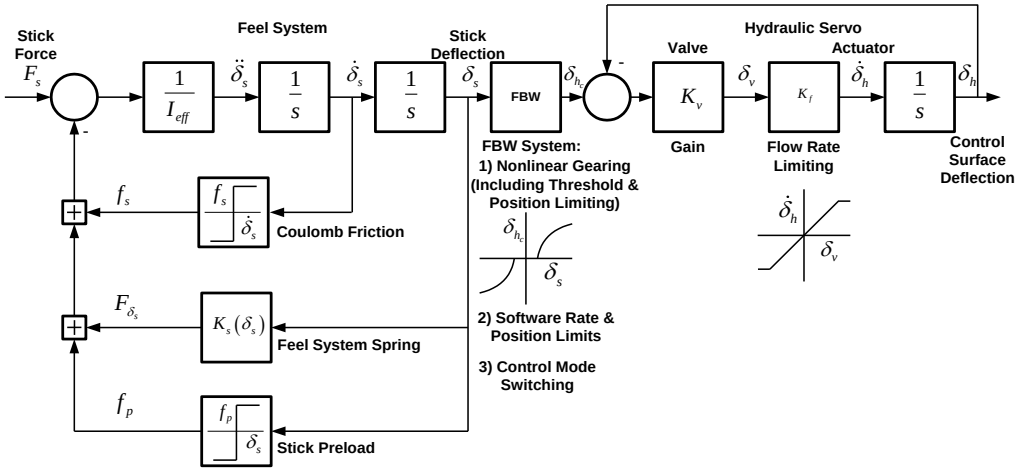

Figure 6.1: *Common manual control system nonlinearities.*

In classical manual control system departures from ideal system properties – referred to here as "dynamic mismatch from the ideal" – can be classified in terms of their fundamental dynamic effects. The impact of these unfavorable properties on the stability of the pilot-vehicle system can be assessed by their describing functions [3]. Describing functions related to control surface actuator rate limiting were described previously in Chapters 3 and 4. A cross section of relevant inverse describing functions is shown in Figure 6.2, adapted from [4].

Graded in terms of their unfavorable consequences, these properties include:

- Introduction of unwanted thresholds and hysteresis, for example, from uncompensated wear at joints, increased friction, mismatched preload/friction adjustments, etc. Here, threshold refers to a minimum control surface input that must be exceeded before the output responds, while hysteresis refers to control system friction wherein the output lags behind the input. There is always some threshold and/or hysteresis in a mechanical system – the "ideal" here is simply to maintain it within viable bounds. The describing function for a threshold is an amplitude ratio increase with the size of the input (see pg. 109 of [3]). This approaches the amplitude ratio of the linear system as the input size increases. Hysteresis contributes both a phase lag and an amplitude ratio decrease, see again [3]. Considerable efforts are often taken in primary control systems to convert hysteresis to threshold via preloads as described further in [5], detents, etc.

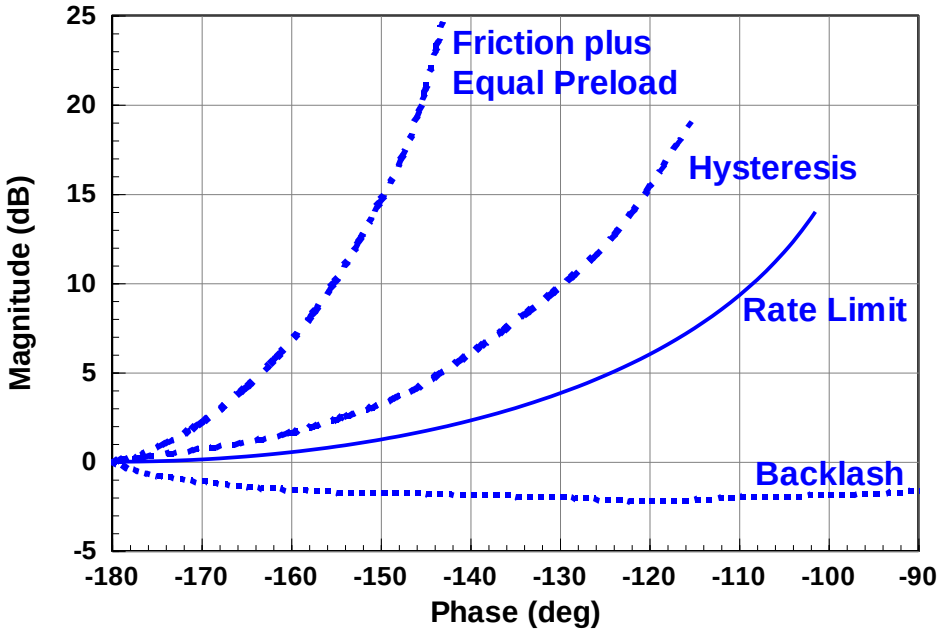

Figure 6.2: *Inverse describing functions for common flight control system nonlinearities from [4].*

- Introduction of backlash, for example, free play, inappropriately preloaded joints and/or gearing) because of its extremely unfavorable dynamic properties, that is, the describing function characteristic combines increased amplitude ratio with increased phase lag, "backlash" per se is never acceptable in a manual control system. When present, it is always rigged out with preload and converted to at least a hysteresis and ideally to a threshold property.
- Deteriorated effector dynamics, for example, reduced effector bandwidth resulting from system pressure reduction due to partial loss of power sources or overloaded conditions, contaminated hydraulic oil, and other flow discrepancies including loss of fluid effects reduce actuator effectiveness.
- Inoperable or jammed effector, for example, servo valve jam, foreign object jamming primary control chain, fluid loss, etc. not only reduce actuator effectiveness, but also can lead directly to loss of control.

In a modern FBW system, several of these effects no longer apply. Indeed, their elimination as a source of primary control system problems in rigging and maintenance has long been one of the major practical arguments for FBW systems, for example, Boeing 757 and 767 spoiler systems, rather than some of the more esoteric and academic justifications. Unfortunately, FBW mechanizations have introduced new static and dynamic mismatch sources. Some notable examples include:

- Manipulator mismatches, for example, between pilot and co-pilot for those systems without coupled, back-driven manual controllers.
- Mismatches between segments of mechanically uncoupled surfaces, for example, flap, spoiler, or elevon segments.
- Inadvertent or premature changes in system dynamics, for example, primary control system gain changes intended to be functions of aircraft configuration actually introduced when the configuration change is commanded rather than when it is executed. A notable example of a "premature" change is a longitudinal system gain change that coincides with the pilot's movement of a flap system manipulator rather than when the flaps actually achieve the commanded position. Similarly, an example of an "inadvertent" change has occurred in the same flap system when a mismatch between flap segments occurred via asymmetric gust loading in the course of flap deflections, thereby locking the flaps in an intermediate position as intended in the control system to avoid a serious asymmetric flap situation. But, the actual flap position was arbitrarily determined by when the gust hit rather than any pre-conceived situations, with the consequence that the primary control system gain was quite inappropriate for the actual effective aircraft dynamics.

Control surface actuator rate limiting plays a significant role in producing dynamic distortion in both classical and modern fly-by-wire flight control systems. In fact, rate limiting has been present in almost every severe PIO that has occurred with operational and flight test aircraft since the North American X-15 event in 1959 [2].

6.3 Exploring Dynamic Distortion from a Flight Test Database

6.3.1 F-14 Simulated Dual-Hydraulic Failure Flight Test Program Overview

The F-14 aircraft featured a dual hydraulic system wherein each system features a pump that is powered by one of the two engines. The titanium hydraulic lines were susceptible to resonance frequency failures. As described in [6], problems with the F-14 hydraulic system began with the second flight during full scale development testing. On this flight both primary hydraulic systems failed as did a valve in the backup hydraulic system. The aircraft was lost just prior to touchdown. Much later, from October 1990 to March 1991, the U.S. Navy conducted a flying qualities evaluation of the F-14 with simulated dual hydraulic failure [6] to better understand the pilot-vehicle system characteristics when using the back-up flight control module or BUFCM. In this study, the BUFCM was evaluated to define areas of operation for in-flight refueling and landing. The BUFCM has two modes that are available to the pilot. The BUFCM-HIGH mode features a maximum stabilator rate of 10 deg/s, while BUFCM-LOW has a 5 deg/s maximum rate. Although the aircraft demonstrated good handling qualities using the BUFCM in formation flight with a tanker, a number of PIOs were encountered during in-flight refueling, drogue tracking, and offset field landings.

Because the F-14 was fully instrumented, a valuable Category II PIO database was inadvertently created. To support the analysis herein, the Naval Air Warfare Center, Aircraft Division

(NAWCAD) provided selected flight test data from the F-14 Dual Hydraulic Failure flight test program with corresponding documentation. These high-quality data included a subset of the flight test runs and a number of frequency sweep runs that were generated as part of the flight test program [6]. An analysis of this database was reported in [7].

6.3.2 Description of the Data

The F-14 database are described in Table 6.1. The run numbers and configurations identified in the table correspond to those identified in the NAWCAD data package. The altitude, airspeed, and Mach numbers provided here were taken directly from the data files. In Table 6.1, the aerial refueling cruise configuration runs used herein are identified by wing sweep and flap positions, flight condition, that is, altitude, speed in knots indicated airspeed, and Mach number as recorded at the start of a run, and flight control system mode, that is, SAS-On, SAS-Off, or BUFCM-High.

Table 6.1: *Run log of aerial refueling cases.*

Run No.	Config.*	Task	Flight Control System ID	Altitude (ft)	Airspeed (KIAS)	Mach No.	HQR
J_01	Cruise-20-0	Hook-Up	SAS-On	14,000	262	0.51	4
J_03	Cruise-20-0	Hook-Up	SAS-Off	20,000	307	0.67	8
J_04	Cruise-20-0	Hook-Up	SAS-Off	20,000	200	0.44	5
J_05	Cruise-20-0	Hook-Up	BUFC M-High	19,000	200	0.42	10
J_06	Cruise-20-0	Hook-Up	BUFC M-High	19,000	200	0.42	10
J_07	Cruise-35-0	Hook-Up	SAS-On	17,000	256	0.53	3
J-08	Cruise-35-0	Hook-Up	SAS-Off	17,000	252	0.52	4
J_09	Cruise 35-0	Tracking	BUFC M-High	16,000	256	0.52	10

* Configuration Cruise-XX-YY denotes landing gear retracted, wing sweep at XX deg, and flaps at YY deg

6.3.3 Longitudinal Flight Control System Characteristics of the F-14

For the F-14A, longitudinal control is provided by symmetric application of the horizontal stabilizers. Pushrods and bellcranks transmit the cockpit control stick motion to tandem stabilizer actuators. The nonlinear stick position-to-stabilizer gearing for the nominal cruise configuration is shown in Figure 6.3. The gearing is uniformly adjusted upward for various flap configurations. This relationship will represent the "ideal" control system characteristic from which dynamic distortion will be identified in the analysis conducted below.

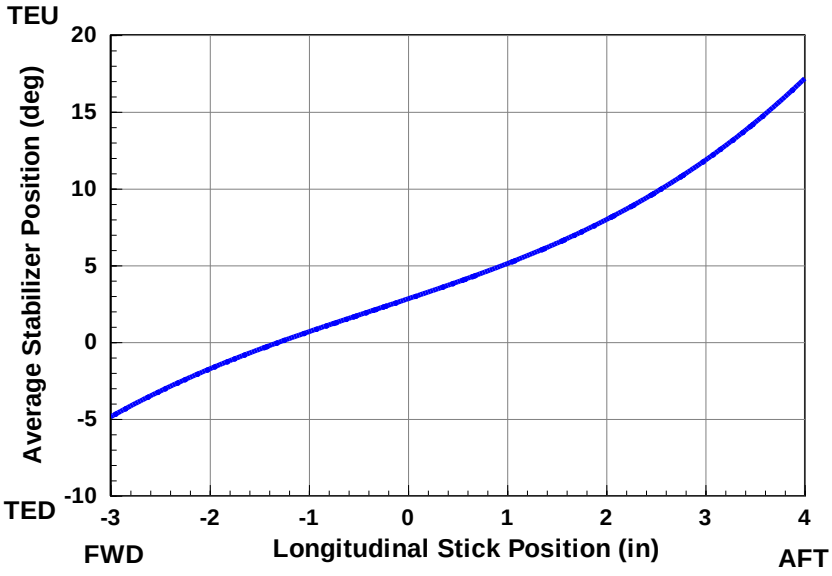

Figure 6.3: *F-14 longitudinal control system stabilizer gearing.*

6.3.4 Time History Comparisons

Longitudinal stick position and average stabilizer position for the cruise, 20 degree wing sweep configurations identified in Table 6.1 are shown in Figure 6.4 for the SAS-On, SAS-Off, and BUFCM-High cases. All runs were high gain hook-up tasks. Thus, there is a noticeable increase in the stick command and corresponding stabilizer output as the probe approaches the drogue. For the SAS-On case of Figure 6.4(a) and the second SAS-Off case, Figure 6.4(c), the task was demanding but successful for this precision, high gain task as reflected in the assigned Level 2 pilot ratings listed in Table 6.1. Although only a qualitative assessment can be made from a review of the time histories, these cases appear essentially linear and the observed lags between the input and output positions are small. For the BUFCM-High cases of Figure 6.4(d) and Figure 6.4(e), the responses are very different. First, the input and output magnitudes are much higher and the "triangle-like" output response associated with rate limiting is evident. Furthermore, the observed lag between the output and input time series is much larger than that observed in the essentially

linear cases. Both cases resulted in severe PIO that forced the pilot to abandon the task to regain control of the aircraft. The SAS-Off case of Figure 6.4(b) displays increased input and output amplitudes perhaps due to reduced system damping, but no significant rate limiting.

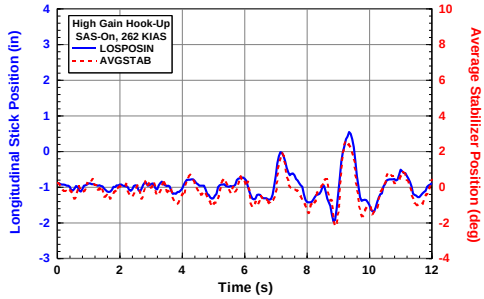

(a) SAS-On high gain hook-up (Run J_01)

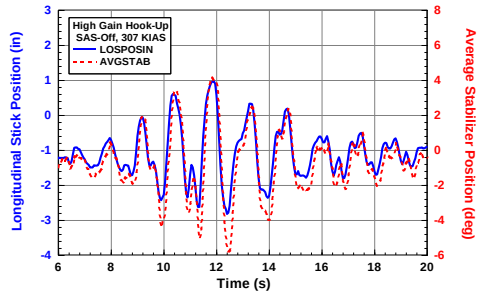

(b) SAS-Off high gain hook-up (Run J_03)

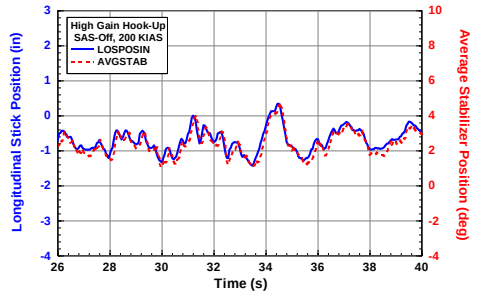

(a) SAS-Off high gain hook-up (Run J_04)

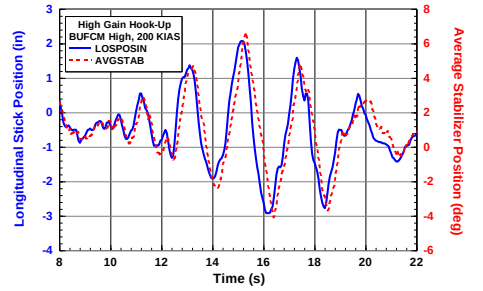

(d) BUFCM-High high gain hook-up (Run J_05)

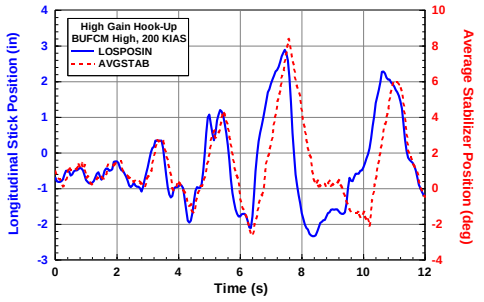

(e) BUFCM-High high gain hook-up (Run J_06)

Figure 6.4: *Cruise-20-0 longitudinal stick position and average stabilizer position time history comparisons for five aerial refueling hook-up cases.*

Longitudinal stick position and average stabilizer position for the cruise, 35 degree wing sweep configurations identified in Table 6.1 are shown in Figure 6.5 for the SAS-On, SAS-Off, and

BUFCM-High cases. Unlike the 20 degree wing sweep cases, however, the pilot tasks are not equivalent. For the SAS-On and SAS-Off cases, the high gain hook-up task was again used, while a drogue tracking task was used for the BUFCM-High task. Both are representative of high gain, precision tracking tasks even though the drogue tracking is a much longer task, roughly 60 seconds compared to the 12-14 second hook-ups.

In the 35 degree wing sweep cruise configuration, both the SAS-On and SAS-Off high gain, hook-ups were essentially routine. As reflected in the Cooper-Harper Handling Qualities Ratings (HQR) pilot ratings of HQR 3 and HQR 4, respectively, the pilot was able to attain desired performance, although the SAS-Off case required somewhat higher workload. The time responses are quite similar to those discussed above for the corresponding 20 degree wing sweep cases in terms of magnitudes and apparent linearity, that is there is no "triangle-like" average stabilizer responses observed for the SAS-On and SAS-Off cases. If the dynamic distortion concept has merit, one would not expect to see much evidence of distortion in these cases.

The drogue tracking run is of particular interest, because as identified in [7] it features intermittent pilot-induced oscillations. That is, there is an initial PIO that occurs between 5 and 22 seconds, followed by a quiescent period up to 42 seconds or so, when a second PIO of smaller amplitude occurs. In the two PIO regions, Figure 6.5(d) and Figure 6.5(e), the rate limiting associated with the BUFCM-HIGH configuration is clearly visible in the triangle wave-like output evident in the stabilizer response. Because of the sustained time on the rate limit, one would expect to see significant evidence of dynamic distortion in this run.

6.3.5 Evidence of Dynamic Distortion

The series of runs introduced in the previous section provide a wide range of exposure to the effects of rate limiting – from essentially linear to highly saturated response characteristics. To search for evidence of dynamic distortion, the actual average stabilizer position versus longitudinal control stick position as measured in flight is compared with the "ideal" response defined in Figure 6.3. The ideal curve from Figure 6.3 is a steady state response, so any dynamic response will distort from this ideal. The degree of the distortion can, however, provide insight into the predictability of response for the pilot wherein a highly distorted response will be indictive of a less predictable controlled element. Figure 6.6 provides a comparison of the actual and ideal longitudinal control system characteristics for the cruise, 20 degree wing sweep cases. The SAS-On comparison plot is shown in Figure 6.6(a). Although there is a small, essentially constant offset from the ideal curve, for this case there is no evidence of distortion. This is not the case for the SAS-Off cases shown in Figure 6.6(b). First, the J_04 run almost mirrors the SAS-On case in that there is a small offset from the ideal curve, but no significant distortion. The result is quite different for the J_03 run. This was the SAS-Off case discussed previously that appeared to suffer from reduced damping at the higher speed. Here, the degraded system (rated HQR 8 by the evaluation pilot) clearly displays some distortion from the ideal response. It is the two BUFCM-High cases shown in Figure 6.6(c), however, that display significant distortion.

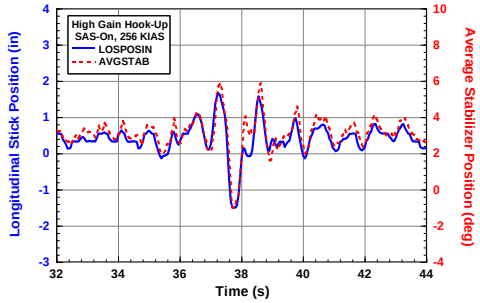

(a) SAS-On high gain hook-up (Run J_07)

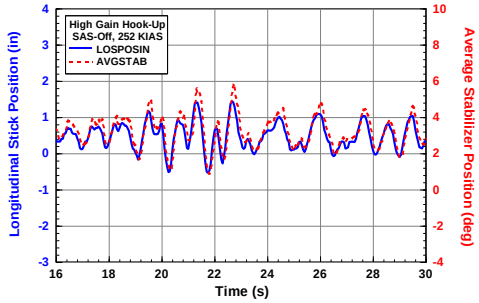

(b) SAS-Off high gain hook-up (Run J_08)

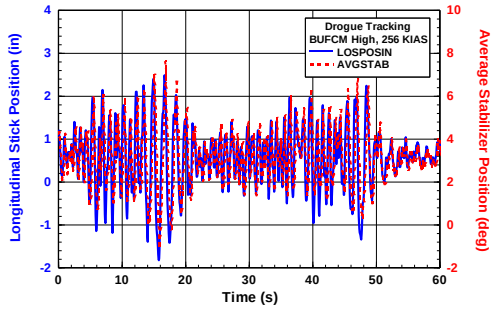

(c) BUFCM-High tracking (Run J_09)

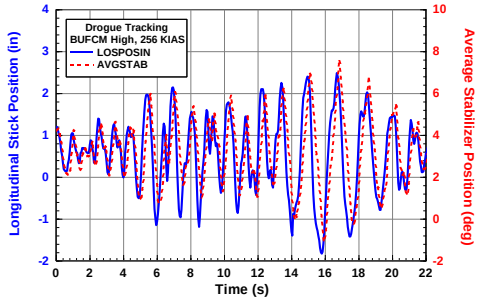

(d) BUFCM-High tracking (PIO1)

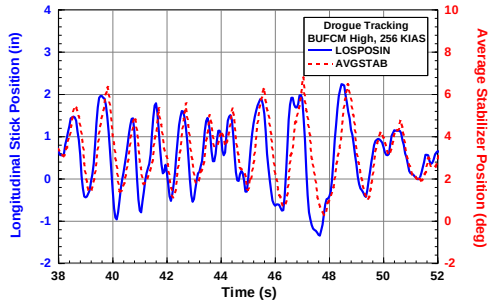

(e) BUFCM-High tracking (PIO2)

Figure 6.5: *Cruise-35-0 longitudinal stick position and average stabilizer position time history comparisons for two aerial refueling hook-up cases and three drogue tracking cases.*

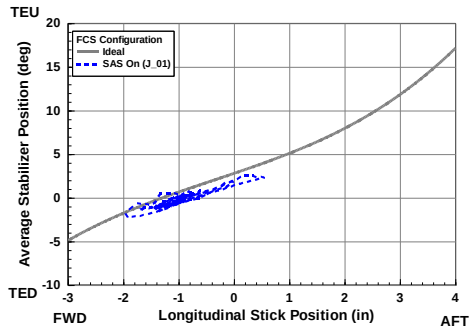

(a) SAS-On (Run J_01)

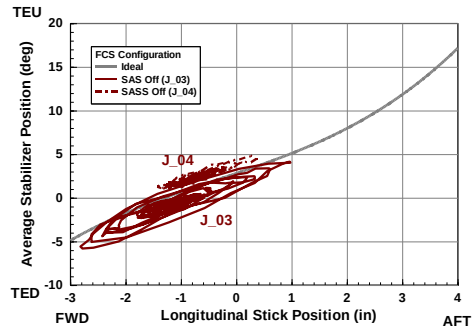

(b) SAS-Off (Runs J_03 and J_04)

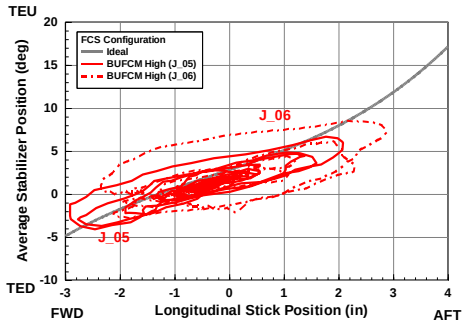

(c) BUFCM-High (Runs J_05 and J_06)

Figure 6.6: *Comparison of actual and ideal longitudinal control system characteristics for Cruise-20-0 cases (SAS-On, SAS-Off, and BUFCM-High).*

Figure 6.7 provides a comparison of the actual and ideal longitudinal control system characteristics for the cruise, 35 degree wing sweep cases. The SAS-On comparison shown in Figure 6.7(a) provides a result similar to that seen for the 20 degree wing sweep SAS-On case. Here, the SAS-Off case, Figure 6.7(b), displays little difference from the SAS-On Case. Following the trend established with the previously discussed BUFCM-High cases, the drogue tracking example shows in Figure 6.7(c) the significant distortion associated with rate limiting.

In the examples shown herein, it was expected that the dynamic responses associated with high gain maneuvering would “distort” from the ideal responses that were represented by the steady state flight control system gearing. While the distortions were represented well visually in these example cases, an improved measure of dynamic distortion was needed to support the development of a successful mitigation method, as any dynamic element in the flight control system response such as a command path filter will result in distortions when compared to the steady state response. Such a measure was identified and is the focus of Chapter 7.

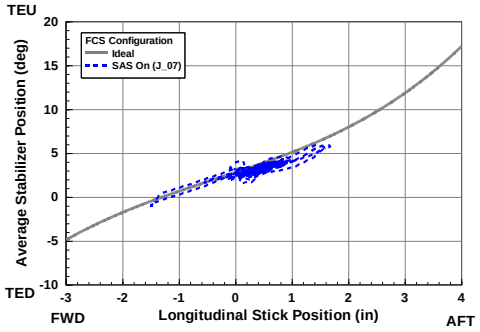

(a) SAS-On (Run J_07)

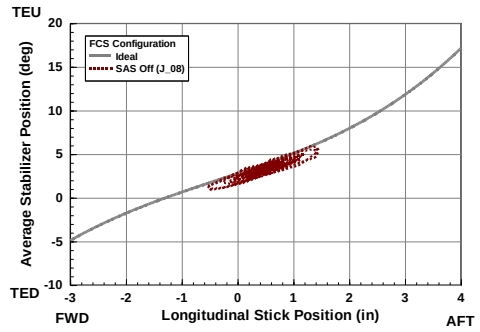

(b) SAS-Off (Run J_08)

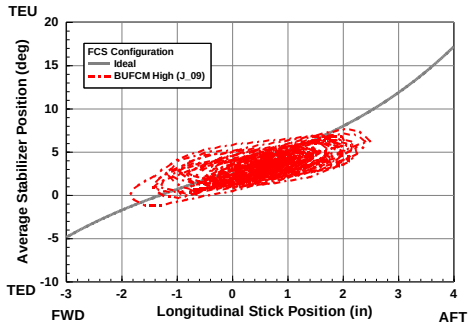

(c) BUFCM-High (Run J_09)

Figure 6.7. *Comparison of actual and ideal longitudinal control system characteristics for Cruise-35-0 Cases (SAS-On, SAS-Off, and BUFCM-High).*

6.4 Conclusions

The analysis of the F-14 flight test data provided the following findings and observations. Although the concept of dynamic distortion was initially somewhat ill-defined, it was nonetheless shown to be an effective means of identifying key flight control system nonlinearities such as rate limiting. When dynamic distortion was defined in terms of a simplified ideal linear system represented by the steady state system characteristics, rate limiting distortions were identified particularly well; however, the concept as defined in these terms was not a “catch all” for all of the items that can lead to unfavorable pilot-vehicle interactions such as PIO, for example, poor aircraft dynamics, inappropriate control stick sensitivity, etc. Furthermore, command path filters that are commonplace in modern systems, also result in a dynamic distortion when compared to the steady state gearing. The results of this analysis thus demonstrated that an “idealized system” response that can provide a more robust measure of dynamic distortion was still needed.

6.5 References

1. Klyde, D. H., and D. McRuer, "Development of Smart-Cue and Smart-Gain Concepts to Alleviate Pilot-Vehicle System Loss of Control," *J. of Guidance, Control, and Dynamics*, Vol. 32, No. 5, Sept.-Oct. 2009, pp. 1409-1417.

2. Klyde, D. H., and D. G. Mitchell, "Investigating the Role of Rate Limiting in Pilot-induced Oscillations," *J. Guidance, Control, and Dynamics*, Vol. 27, No. 5, Sept.-Oct. 2004, pp. 804-813.

3. Graham, D., and D. McRuer, Analysis of Nonlinear Control Systems, John Wiley & Sons, Inc., New York, NY, 1961.

4. Graham, D., and L. G. Hofmann, *Investigation of Describing Function Technique*, AFFDL-TR-65-137, Wright-Patterson Air Force Base, August, 1965.

5. Crane, H. L., *Analog-Computer Investigation of Effects of Friction and Preload on the Dynamic Longitudinal Characteristics of a Pilot-Airplane Combination*, NASA TN D-884, May 1961.

6. Niewoehner, R., LCDR USN, and Minnich, S., "F-14 Dual Hydraulic Failure Flying Qualities Evaluation," *Thirty-Fifth Symposium Proceedings*, Society of Experimental Test Pilots, Lancaster, CA, Sep. 1991, pp. 4-15.

7. Klyde, D. H., and D. G. Mitchell, "Extraction of Pilot-Vehicle Characteristics in the Presence of Rate Limiting," AIAA 99-1069 presented at *37th Aerospace Sciences Meeting and Exhibit*, Reno, NV, Jan. 11-14, 1999.

7. An Idealized Manual Control System Paradigm

A hydraulic servo actuator which includes a predominantly open center type valve is characterized by considerable position error when operating under load.

BuAer Report AE-61-4, Volume IV, The Hydraulic System, May 1953

Parts of this chapter have been published as:

Title Development of Smart-Cue and Smart-Gain Concepts to Alleviate Pilot-Vehicle System Loss of Control

Journal Journal of Guidance, Control, and Dynamics, vol. 32, no. 5, Sept.-Oct. 2009, pp. 1409-1417

Authors D. H. Klyde and D. T. McRuer

7.0 AN IDEALIZED MANUAL CONTROL SYSTEM PARADIGM

Building on the material from Chapter 6, an idealized manual control system concept is defined in this chapter to quantify the concept of dynamic distortion and introduce the Smart-Cue and Smart-Gain concepts to mitigate Category II pilot-induced oscillations (PIO). The material presented is largely based on that found in [1].

7.1 Nonlinear System Description

To give some perspective to the approach of this work to define an ideal manual control system, first return to the "ancient" history of fully-powered surface actuation systems. As noted previously, the main stream began in the 1940's at Northrop Aircraft, Inc. when requirements for an irreversible, power-enhancing, surface actuation system became apparent from flight tests on early Northrop flying wings. The power-enhancement requirement stemmed from the very size and speed of such aircraft as the Northrop XB-35 and YB-49 bombers. In principle, this could have been accommodated in other ways, such as power-boost, servo-tabs, etc. However, the need for the irreversible feature was central because the hinge moment gradients reversed at high angles of attack, thereby presenting the pilot with very difficult if not impossible handling and control problems. A fully-powered (in contrast to power-boosted) surface actuator assures the complete separation of the pilot from the forces associated with the control surface.

The development of successful fully-powered systems was probably the most important and long-lasting accomplishment in primary manual control systems in the two decades from about 1942 to 1962 when almost all high-performance aircraft were so equipped. Although fully-powered systems are now ubiquitous, their perfection was a major achievement that required many exceptional engineering and technical breakthroughs. Major problems in mechanical and hydraulic system design, actuator system stability, and flying qualities, many at the margins of the then state-of-the- art, had to be surmounted. Ultimately the systems became technologically mature and operationally effective and have since served several generations of high performance aircraft. Still, fully-powered manual hydro-mechanical primary control systems are not perfect, but an understanding of the nature of both their favorable and unfavorable features suggests concepts that can lead to more ideal systems in today's fly-by-wire technology.

7.2 A Potential Ideal System Paradigm

Figure 7.1 shows an idealized version of a single channel of a fully-powered system typical of the end of the initial era in these developments [2]. These are exemplified on such aircraft as the Northrop F-89D interceptor that served operationally for over two decades starting about 1954. In this system, the pilot's inceptor (stick, control column, or pedals), restrained by an artificial feel system, is mechanically connected to a hydraulic servo valve via a combination of push-pull rods, cables, etc. The valve housing is integral with a hydraulic cylinder. A pilot command input, $\delta_p = x_i$, moves the valve from its neutral position and creates an actuator system error ($x_e = x_i - x_s$) that ports hydraulic fluid to the cylinder. The valve-cylinder flow pathway(s) are arranged so that the cylinder housing, x_s, moves to reduce the valve displacement from neutral, thereby driving the actuator system error to zero. In the integral valve-cylinder configuration shown, the lags within the closed-loop actuator system are absolute minimums as the position feedback is

inherent in the physical arrangement. The ultimately evolved successful versions are high bandwidth actuators that add only a small lag and very light valve friction forces to the hydro-mechanical control chain. As a consequence, the evolved systems have minimum to no impact on the dynamics of the overall pilot-vehicle closed- system in even the most extreme conditions of pilot control.

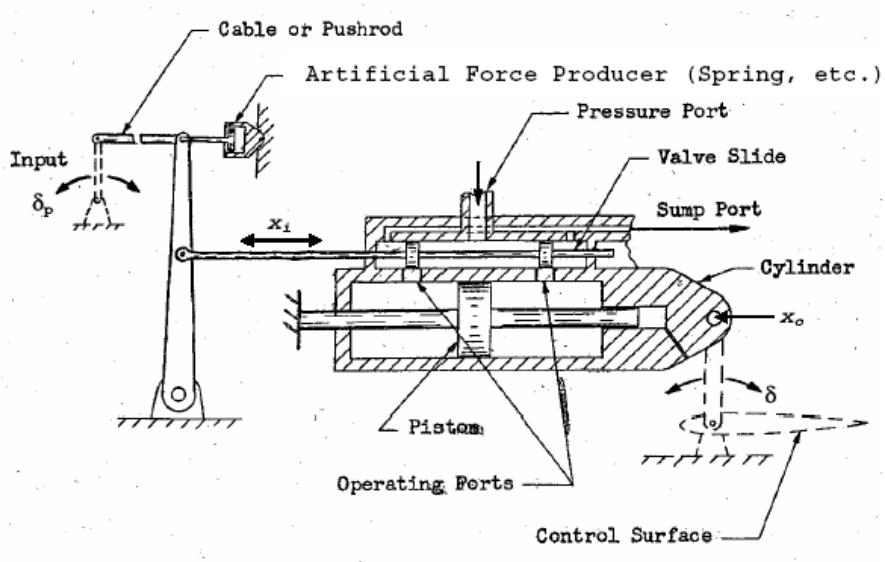

Figure 7.1: *Idealized longitudinal control system [2].*

Such systems exhibit:

- Sufficiently high maximum surface rates;
- Minimum effective actuation system lags inserted into the manual control system (by virtue of high-bandwidth actuation system dynamics); and
- High degree of effective linearity between the pilot command and the control surface deflection.

For those aircraft where all these conditions were satisfied there appear to be no unfavorable pilot-vehicle interactions, for example, PIO present in the flight record. It is for this reason that the actuation system illustrated in Figure 7.1 embodies potentially ideal paradigms useful for the current work. There were, of course, many PIO events leading to the above assertion. These encounters and the technical advances leading to their subsequent correction were steps along the way to the technologically mature actuation systems that provide the essential features listed.

Unfavorable pilot-vehicle system interactions such as PIO appeared to become more common as high-performance aircraft advanced into the fly-by-wire era [3,4]. Whether this apparent increase

was actual, or just an artifact of closer attention, or more extensive sensitivity to what are always unusual events is not at issue here – suffice to say that essentially every new high-performance aircraft equipped with a fly-by-wire flight control system has exhibited PIO at one time or another. These were, typically, linked to specific causes, most often associated with actuator rate limiting or excessive pilot-vehicle system lags. The contributing features have, in the main, been corrected for each specific aircraft after the appearance of the unfavorable events.

In the process of dealing with the PIO specifics of many different aircraft, some specialists with a historical bent looked back to earlier days when, for some reason or other, the aircraft systems seemed to have been essentially PIO-free. Thus, the justification for the return to the past in proposing the Figure 7.1 system is to rediscover some potentially "ideal" properties. Just what these might be stems from looking at the differences between it and the more advanced fly-by-wire systems that have not been initially PIO-free.

7.3 Differences between Modern and Classic Manual Control Systems

The most profound difference between the manual control channels of modern fly-by-wire systems and that depicted in Figure 7.1 is the replacement of all the mechanical features up to and including the servo valve with electro-hydraulic and or electro-mechanical components. This replacement has many beneficial effects. Major differences between fly-by-wire and the idealized control system include:

- Elimination of parasitic nonlinear features due to mechanical elements such as frictions, hysteresis, backlash, etc.;
- Consequent elimination of the mechanical contrivances deliberately introduced to counter the unfavorable parasitic nonlinearities (e.g., preloads to provide stick-centering in the presence of distributed cable system friction or to modify backlash to a hysteresis effect);
- Possible use of an essentially non-movable manipulator for mechanical sticks or columns (as on the General Dynamics, now Lockheed Martin, F-16 [5]); and
- Possible use of moving manipulators with prescribed back-drive characteristics (as with the Boeing 777 [3]).

Another somewhat more subtle difference occurs for circumstances where the pilot's command inputs are large and very rapid, as typically is present in a so-called Category II PIO where rate-limiting is a central feature in the PIO [3,6]. In the Figure 7.1 "old" system, rate limiting coincides with valve bottoming and a consequent direct physical cue to the pilot that the controls are against a solid, albeit moving, stop. In these conditions the control surface is essentially directly connected with the pilot while the valve is bottomed and the pilot command and surface travels are intrinsically locked together. Thus, the surface position can never lag the pilot command by more than the surface travel equivalent of the maximum valve travel from neutral. In modern fly-by-wire systems, the pilot is not mechanically connected to the actuation system, so such direct cues and intrinsic restraints are not present. It is these differences that offered some key insights and opportunities that have been explored further in this work.

7.4 Time Lag and Position Lag

In large-amplitude rate-limited oscillations with the "ideal system" of Figure 7.1, the surface and pilot's positional commands, as noted above, are intrinsically linked between the fixed constraints provided by the stops defining the maximum valve displacements from neutral. The pilot's input essentially drives the valve back and forth from one stop to the other. In the course of such oscillations, the surface motion is going at maximum velocity (rate limit) after each input reversal. Consequently, the command input and the surface position are both essentially triangular waveforms, as idealized in the Figure 7.2 time traces. In this situation, the two displacements are separated by a time delay equal approximately to the maximum valve displacement from neutral divided by the actuator rate limit. In aircraft manual control system parlance this quantity is called the *Time Lag*, T_{lag}. This is a nonlinear system characteristic that is in no way to be confused with the more conventional effective time delay that defines the linear system properties of the hydraulic actuator closed loop system.

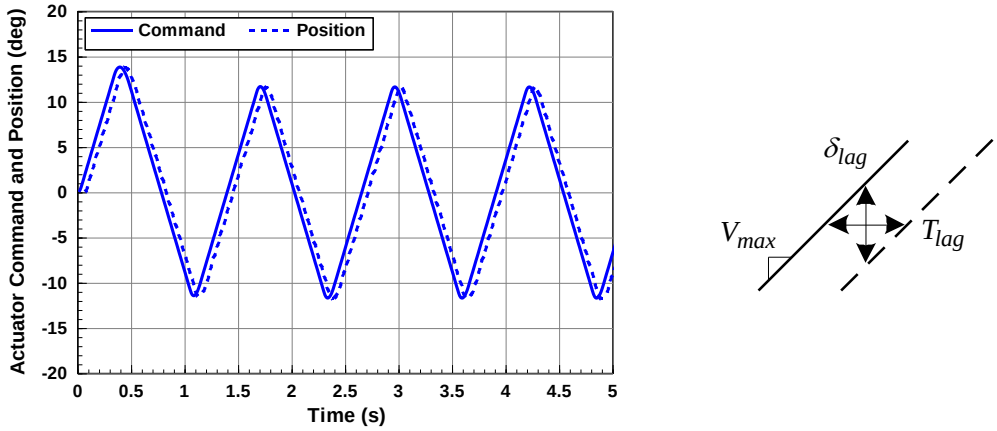

Figure 7.2: *Input/output comparisons for a valve bottoming actuator.*

The commanded and actual surface positions under these conditions are also tightly constrained. This is measured by the *Position Lag*. When expressed in terms of the surface position this is denoted as δ_{lag} and is measured in degrees. This is the amount of surface travel that corresponds to the maximum valve displacement from neutral and represents the maximum position increment that the surface may lag the pilot input command. The *Time Lag* and *Position Lag* are directly related via the maximum surface rate, that is, the rate limit. Thus, the *Time Lag*, T_{lag}, is the *Position Lag*, δ_{lag}, divided by the surface rate limit, V_{max}:

$$T_{Lag} = \frac{\delta_{Lag}}{V_{\max}} \tag{7.1}$$

It is important to note that the position lag is measured in position units and that pilot force inputs are not necessarily relevant. No matter how hard the pilot pulls or pushes, he or she can only

bottom the valve, which is a hard constraint. In fact, one reason that over-driven valves and other schemes ultimately replaced the hard limits implicit in the Figure 7.1 system was the occasional valve damage that over-active pilots exerted on the early systems.

When fully-powered systems were in their early phases of development, a great deal of analytical and experimental effort was spent to determine desirable values for the three key parameters: time and position lags and maximum surface rates. These quantities are among the central design and dynamic features of fully-powered actuators. Pilot control factors, including PIO tendencies, were major considerations. Remarkably, pilot preferences, especially fighter pilots and helicopter pilots, typically support far higher surface rates than are theoretically needed even in quite drastic maneuvers. Pilots tended to dislike the valve-bottoming cue and, to avoid it, demanded faster surface rates than an equivalent automatic system could effectively use. This is often the bane of surface actuator designers who are concerned with weight, volume, and power demands. On the other hand, there are several instances where a too-conservative "solution" that settled for lower surface rates resulted in a quite dramatic rate-limited PIO, for example, the North American X-15 first flight PIO [7]. Consequently, as a result of a great deal of experimentation on a large number of aircraft, some examples of desirable rates and lags have gradually emerged. For example, desirable surface rates for fighter aircraft are, from stop to stop: 1 second – elevator; ½ second – aileron; 1 second – rudder [8].

7.5 The Smart-Cue and Smart-Gain Concepts

7.5.1 The Smart-Cue

The basic idea in applying the ideal system concept is to restore a force feedback cue akin to the ideal valve-bottoming characteristics in a fly-by-wire system configuration. This is the heart of the Smart-Cue concept. Note that Smart-Cue can be applied to non- fly-by-wire manual control systems as well; however, the implementation may be more hardware intensive. As shown in Figure 7.3, the commanded surface position and actual surface position are used to define a Position Error via an ideal linear system that can be as simple as a unity gain. Comparisons of the Position Error with idealized manual control system characteristics, that is, Position Lag, will therefore reflect differences, due to distortions in the actual system. Cueing and corrective haptic forces, the Smart-Cue, are then presented to the pilot as a "proprioceptive display." Nominally the mechanization of this feature will be based on an inceptor with active back-drive capability. In principle, the back-drive mechanism is an adjustable spring gradient artificial feel system force producer that constitutes a proprioceptive display.

Consider, as the prime example, rate limiting in the control surface actuator. This is the most pervasive and awkward to handle manual control system distortion. As a source of Category II PIO, it is also probably the most commonly encountered controls-related pilot-vehicle system safety issue. In an ideal emulation, the spring gradient would be that appropriate to the particular control surface within the range of pilot-vehicle system linear operations. Then, when the pilot control input signal calls for surface rates that exceed the velocity limit, the force feedback will be increased and in the utmost implementation can simulate a valve-bottoming virtual stop. For the extreme case that emulates valve-bottoming, this has the following effects:

- The pilot is cued to the presence of dynamic distortion due to rate limiting;
- The pilot control input and the surface output are essentially locked together as long as the distortion persists;
- The control surface position lags the pilot command by the Position Lag (δ_{lag}); and
- The time delay between the pilot and the surface is constrained to be no more than the Time Lag (T_{lag}) as long as the distortion persists.

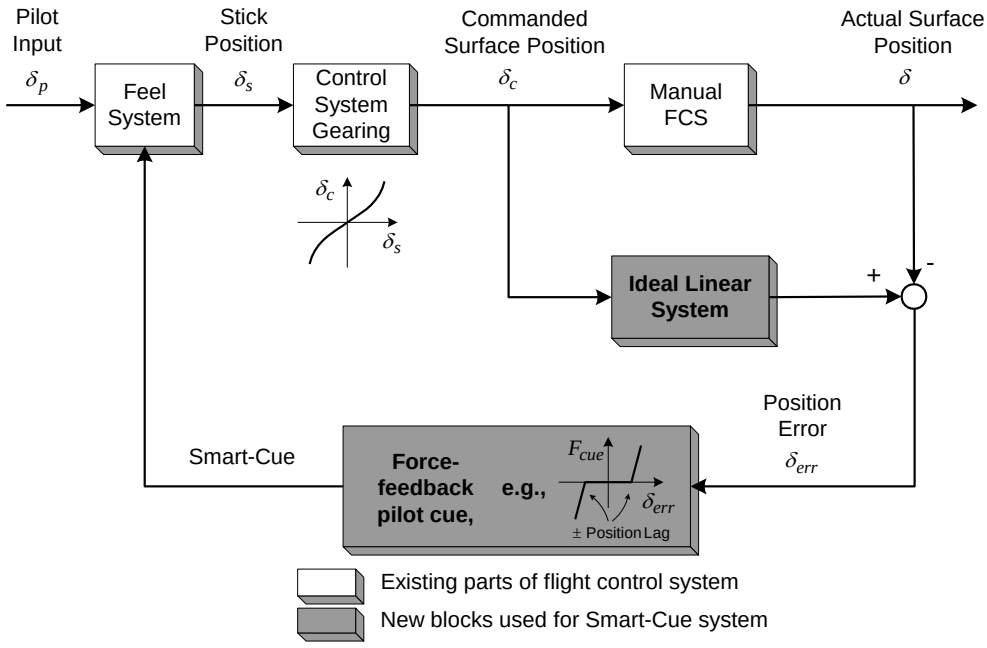

Figure 7.3: *Implementation of the Smart-Cue system.*

As a practical matter in the absence of an actual physical stop, it is difficult to mechanize exactly the essentially infinite spring gradient character of the virtual stop corresponding to valve bottoming. However, an extreme and sudden change in the effective gradient is entirely feasible. For example, increases in effective stick force gradient with adjustable force producers are commonplace.

Although the fundamental concept has remained fixed, many options remain regarding how the concept is mechanized and integrated within a modern flight control system that include the following:

- Design of the Alerting Function: This includes selecting Position Lag and related values and determining how to turn the force feedback on and off. This is the heart of the

mechanization issue that can mean the difference between a highly effective cue and a nuisance or worse.

- Design of the Constraining Function: This includes selecting the level of force feedback from gentle resistance to hard stops that emulate the valve-bottoming effect. Since the degree of force feedback will be a function of the amount of identified dynamic distortion as measured by the Position Error, variable force feedback gradients are possible as well.

The fundamental design concept – providing a force feedback cue to the pilot based on a measure of dynamic distortion, the *Smart-Cue*, – has thus been established.

Piloted simulation was used to evolve the Smart-Cue mechanizations that were eventually evaluated in flight. A number of feedback force options were considered individually and in various combinations. Options included a force that produced an effective spring gradient change, a coulomb friction force, and damping forces based on control stick velocity and the rate of change of position error. The gradient force was found to be effective for pitch axis evaluations, but high frequency oscillations associated with the limb-manipulator mode [9], a modified stick-arm neuromuscular mode, regularly occurred in the roll axis. No such oscillations accompanied the friction force in either axis. The damping forces did not yield useful results and were thus eliminated from the mix. Best results in the simulator were obtained in both axes for runs involving combined gradient and friction forces, see also [10].

7.5.2 The Smart-Gain

A second design concept that is also based on a measure of dynamic distortion, the *Smart-Gain*, evolved from the checkout flight process [11]. In short, the Calspan Learjet II In-Flight Simulator was used to conduct both the checkout flights and formal evaluations. In the checkout flight process, several Smart-Cue mechanizations were found to work well for the cruise evaluations. Results of the precision offset landing task were less certain. First, the evaluation pilot appreciated that the Smart-Cue gave an apparent “trough” in which it was safe to move the stick in the presence of control surface rate limiting. The impact of the trough was more pronounced when the cueing force was increased as a function of Position Error. A cueing force level could not be found, however, that allowed the pilot to comfortably make roll axis corrections without “fighting” the Smart-Cue forces. Still some improvements with the cueing were observed. These results led to a post flight debrief discussion of possible command path gain adjustments as an alternative to the high feedback forces.

Piloted simulation was used to rapidly prototype such a concept, the *Smart-Gain*. Past work including the PIO suppression filter [12] used on the space shuttle employs command path gain reduction techniques. Such techniques estimate the frequency of the pilot’s input, and then attenuate the input as a function of this frequency. This technique does not, however, take the response of the control system into consideration, so the pilot input is attenuated whether or not it is needed. With the Smart-Gain, the pilot input is attenuated as a function of the Position Error, the measure of dynamic distortion, as shown in Figure 7.4. A Position Lag metric is used to turn the Smart-Gain “on” and “off.” The Position Lag may be set independently to the values used for the Smart-Cue.

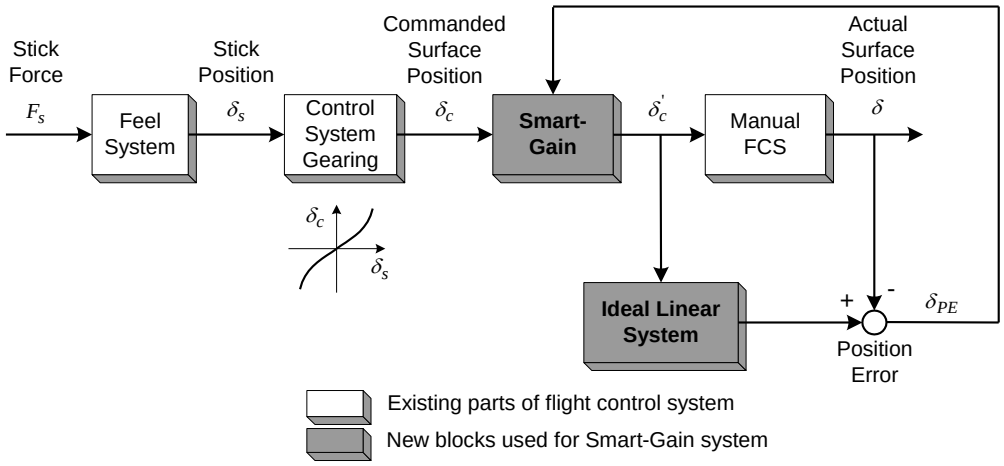

Figure 7.4: *Implementation of the Smart-Gain system.*

The Smart-Gain was found to be a critical innovation. As described in [11] and Chapter 8, repeated successful landings were accomplished during the formal evaluation process with best results coming from a Smart-Cue/Smart-Gain combination.

7.6 Exploring Position Lag and Position Error with the F-14 Flight Test Database

7.6.1 Database

The F-14 database introduced in Chapter 6 is reintroduced in Table 7.1. The run numbers and configurations identified in the table correspond to those identified in the data package provided by the U.S. Naval Air Warfare Center Aircraft Division (NAWCAD). The altitude, airspeed, and Mach numbers provided here were taken directly from the data files. In Table 7.1, the aerial refueling cruise configuration runs used herein are identified by wing sweep and flap positions, flight condition, that is, altitude, speed in knots indicated airspeed, and Mach number as recorded at the start of a run, and flight control system mode, that is, stability augmentation system on (SAS-On), stability augmentation system off (SAS-Off), or back-up flight control module in high rate mode (BUFCM-High), that is 10 deg/s.

7.6.2 Surveying the Data

The dynamic distortion concept including the ideal linear system parameters was investigated using the F-14 flight test database that featured evaluation runs with and without severe actuator rate limiting. Using the "idealized system" concept defined above, the F-14 flight test database is used here to assess Position Lag as a dynamic distortion metric. For each run a position error was computed (trim positions were estimated) and compared with a representative Position Lag of ±2 degrees. The resulting plots are shown in Figure 7.5 and Figure 7.6 for the Cruise-20-0 and

Cruise-35-0 cases, respectively. The position errors for the SAS-On and SAS-Off runs that exhibited little distortion and no PIO tendencies are plotted with solid lines, while dashed lines are used for the poor handling SAS-Off case and the BUFCM-High cases that all exhibited PIO. Note that the solid lines remain below the selected Position Lag boundary, while the dashed lines do not. These data suggest that a Position Lag less than 2° is consistent with the absence of PIO. Such values are also consistent with the early ad hoc tests conducted decades ago during the development of practical fully-powered actuation systems wherein the design guides then established called for Position Lags in the range of 1° to 2° of surface deflection [13].

Table 7.1: *Run log of aerial refueling cases.*

Run No.	**Config.***	**Task**	**Flight Control System ID**	**Altitude (ft)**	**Airspeed (KIAS)**	**Mach No.**	**HQR**
J_01	Cruise-20-0	Hook-Up	SAS-On	14,000	262	0.51	4
J_03	Cruise-20-0	Hook-Up	SAS-Off	20,000	307	0.67	8
J_04	Cruise-20-0	Hook-Up	SAS-Off	20,000	200	0.44	5
J_05	Cruise-20-0	Hook-Up	BUFCM-High	19,000	200	0.42	10
J_06	Cruise-20-0	Hook-Up	BUFCM-High	19,000	200	0.42	10
J_07	Cruise-35-0	Hook-Up	SAS-On	17,000	256	0.53	3
J-08	Cruise-35-0	Hook-Up	SAS-Off	17,000	252	0.52	4
J_09	Cruise 35-0	Tracking	BUFCM-High	16,000	256	0.52	10

* Configuration Cruise-XX-YY denotes landing gear retracted, wing sweep at XX deg, and flaps at YY deg

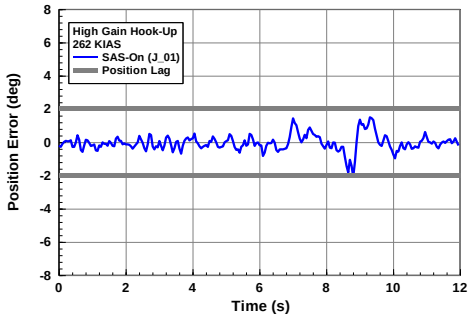

(a) SAS-On high gain hook-up (Run J_01)

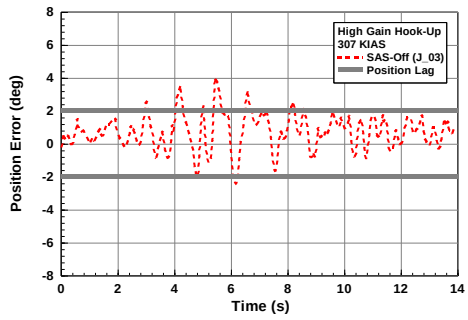

(b) SAS-Off high gain hook-up (Run J_03)

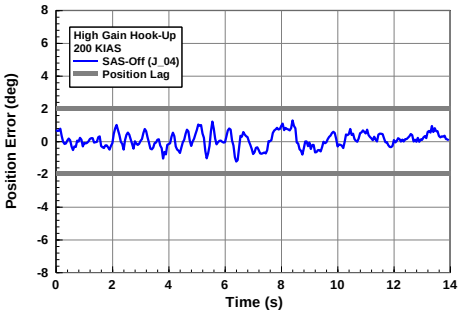

(c) SAS-Off high gain hook-up (Run J_04)

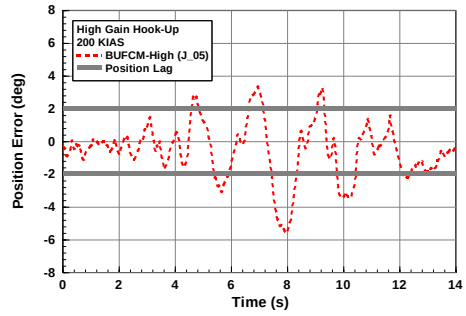

(d) BUFCM-High high gain hook-up (Run J_05)

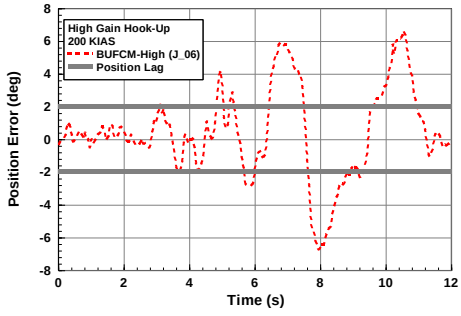

(e) BUFCM-High high gain hook-up (Run J_06)

Figure 7.5: *Exploration of position lag using the F-14 Cruise-20-0 cases.*

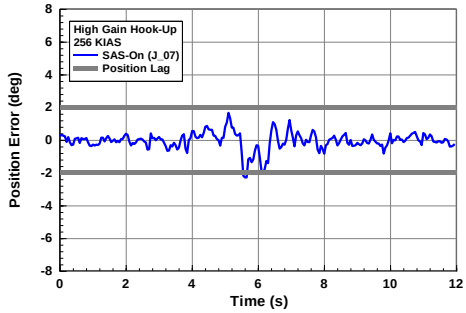

(a) SAS-On high gain hook-up (Run J_07)

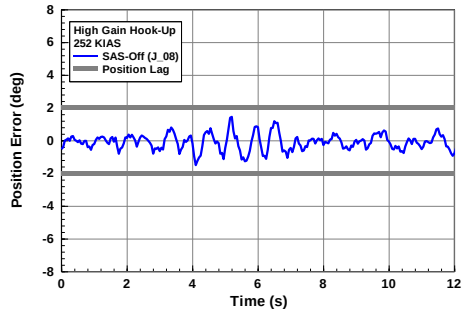

(b) SAS-Off high gain hook-up (Run J_08)

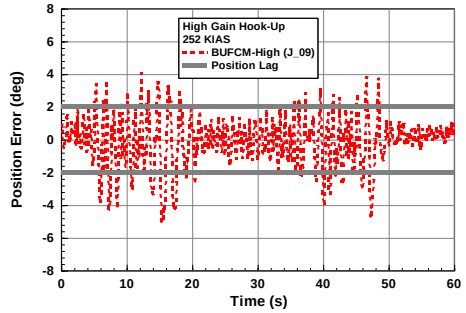

(c) BUFCM-High drogue tracking (Run J_09)

Figure 7.6: *Exploration of position lag using the F-14 Cruise-35-0 cases.*

7.7 Conclusions

This chapter described the development of an innovative means to alert, constrain and thereby alleviate loss of control associated with unfavorable pilot-vehicle systems interactions including pilot-induced oscillations that are often present in high gain, closed-loop operations. It has often been tacitly assumed that the adoption of fly-by-wire systems has eliminated the primary manual control link as an important player in loss of control situations. “Ideal” pilot to surface

relationships were used to measure the impact of control system effects, such as control surface rate limiting, that distort the actual control system response. The Position Error measure of this "dynamic distortion" was used to develop; 1) a command path gain adjustment mechanism, a Smart-Gain, and 2) active alerting and constraining proprioceptive and tactile feedback cues to the cockpit controller, a Smart-Cue, when predetermined dynamic distortion boundaries, the Position Lag metric, are exceeded. The Smart-Gain and Smart-Cue concepts were developed and refined via piloted simulation before ultimately being evaluated and refined via flight test as described in Chapter 8.

7.8 References

1. Klyde, D. H., and D. T. McRuer, "Development of Smart-Cue and Smart-Gain Concepts to Alleviate Pilot-Vehicle System Loss of Control," *J. of Guidance, Control, and Dynamics*, Vol. 32, No. 5, Sept.-Oct. 2009, pp. 1409-1417.

2. Anon., *Fundamentals of Design of Piloted Aircraft Flight Control Systems Volume IV: The Hydraulic System*, U.S. Navy Bureau of Aeronautics (BuAer) Report AE-61-4, May 1953.

3. Anon., *Aviation Safety and Pilot Control*, prepared by the National Research Council Committee on the Effects of Aircraft-Pilot Coupling and Flight Safety, National Academy Press, Washington, D.C., 1997.

4. Mitchell, D. G. and D. H. Klyde, "Identifying a Pilot-Induced Oscillation Signature: New Techniques Applied to Old Problems," *Journal of Guidance, Control, and Dynamics*, Vol. 31, No. 1, 2008, pp. 215-224.

5. Smith, J. W., *Analysis of a Lateral Pilot-Induced Oscillation Experienced on the First Flight of the YF-16 Aircraft*, NASA TM-72867, September 1979.

6. Klyde, D. H., and D. G. Mitchell, "Investigating the Role of Rate Limiting in Pilot-induced Oscillations," *J. Guidance, Control, and Dynamics*, Vol. 27, No. 5, Sept.-Oct. 2004, pp. 804-813.

7. Matranga, G. J., *Analysis of X-15 Landing Approach and Flare Characteristics Determined from the First 30 Flights*, NASA TN-D-1057, July 1961.

8. Glenn, J. E., "Manual Flight Control System Functional Characteristics," *IEEE Transactions on Human Factors in Electronics*, Vol. HFE-4, No. 1, Sep. 1963.

9. Mitchell, D. G., B. L. Aponso, and D. H. Klyde, *Effects of Cockpit Lateral Stick Characteristics on Handling Qualities and Pilot Dynamics*, NASA CR-4443, June 1992.

10. Klyde, D. H., C. Y. Liang, N. Richards, B. Cogan, "Use of Active Inceptor Cueing to Mitigate Pilot-Vehicle System Loss of Control," AIAA Paper No. 2012-4765 presented at the *Guidance, Navigation, and Control Conference*, Minneapolis, MN, 13-16 Aug. 2012.

11. Klyde, D. H., and C. Y. Liang, "Approach and Landing Flight Test Evaluation of Smart-Cue and Smart-Gain Concepts," *J. of Guidance, Control, and Dynamics*, Vol. 32, No. 4, July-Aug. 2009, pp. 1057-1070.

12. Smith, J. W., and J. W. Edwards, *Design of a Nonlinear Adaptive Filter for Suppression of Shuttle Pilot-Induced Oscillation Tendencies*, NASA TM-81349, 1980.

13. Anon., *Report of the First Piloted Aircraft Powered Surface Control System Symposium*, Bureau of Aeronautics Airborne Equipment Division, Department of the Navy, Washington D.C., Oct. 1949.

8. Approach and Landing Flight Evaluation of Smart-Cue and Smart-Gain Concepts

I have not felt a cliff where I thought there is PIO there. Everything felt very controllable without oscillations.

NASA Test Pilot, Smart-Cue/Smart-Gain Flight Test Evaluations, January 2007

Parts of this chapter have been published as:

Title	Approach and Landing Flight Test Evaluation of Smart-Cue and Smart-Gain Concepts
Journal	Journal of Guidance, Control, and Dynamics, vol. 32, no. 4, July-Aug. 2009, pp. 1057-1070
Authors	D. H. Klyde and C. Y. Liang

8.0 APPROACH AND LANDING FLIGHT EVALUATION OF SMART-CUE AND SMART-GAIN CONCEPTS

Under sponsorship from the U.S. National Aeronautics and Space Administration (NASA), flight test evaluations of the Smart-Cue and Smart-Gain were conducted by Systems Technology, Inc. using the Calspan Corporation Learjet In-Flight Simulator. The material in this chapter is largely from [1] and describes the approach and landing evaluations. Further descriptions of flight test results are found in companion references [2,3].

8.1 Introduction

At present the aircraft flying qualities community has sufficient understanding of pilot-vehicle systems in general to make the case that some effective vehicle dynamic characteristics can be considered to be either ideal or good enough. Departures from these nominally ideal properties can then be defined as "*distortions*" that may underlie pilot-vehicle system problems. A common example is control surface actuator rate limiting, where deviation from desirable values has been shown to lead to pilot-induced oscillations (PIO) in some circumstances. Another example is mis-rigging of control system elements, such as mechanical maladjustments leading to control system backlash or excessive hysteresis. The common theme is that the actual manual flight control system is in some way deviating from an ideal system. The pilot is expecting one type of response, but the actual system is behaving differently because of the distortion. Within this general context Ralph A'Harrah while at NASA Headquarters proposed the "Loss of Control Inhibition System" (LOCIS) wherein distortions are detected and appropriate cues are then introduced to the pilot by way of compensation (U.S. Patents #7,285,932 and #7,285,933). It was recognized that this was still a general concept that had yet to be made concrete or specific. It served as a motivation for the work reported in Part II of this thesis to attempt to quantify such conceptual terms as "*distortions*" and "*idealized systems*" as innovative and unifying principles underlying the development of corrective measures in the form of controller cues.

To advance this generalized theme, concrete examples were needed. In this work, the critical distortion examined involved control surface actuator rate limiting as a factor in Category II PIO [4]. The research evolved and successfully demonstrated conceivable mitigation means – herein referred to as the *Smart-Cue* and *Smart-Gain* that were defined in Chapter 7. Because rate limiting has been a contributing if not causal factor in the severe PIO loss of control events involving modern fly-by-wire (FBW) aircraft, this distortion remained the focus for the flight test program described herein. This chapter presents the approach and landing results from a flight test evaluation of the Smart-Cue and Smart-Gain concepts.

8.2 Learjet In-Flight Simulator Description

8.2.1 Capabilities Overview

The Calspan Corporation variable stability Learjets are modified Learjet Model 25 aircraft. The Lear II shown in Figure 8.1 was used in this program. The Learjets provide three degrees-of-freedom (3-DOF) in-flight simulation capabilities for advanced stability, control, and flying

qualities demonstrations and research [5]. They are also used to test/demonstrate advanced flight control systems concepts. The aircraft are used in these capacities to support flight test training of test pilots and flight test engineers around the world, as well as support new aircraft development programs.

Figure 8.1: *Variable stability Learjet 25 (Calspan photo).*

The right seats of the Learjets have been extensively modified to serve as the Evaluation Pilot (EP) crew station. The normal Learjet wheel/column has been removed. It is replaced with one of three experimental controllers; 1) centerstick, 2) sidestick, and 3) wheel/column. Each of these two axis control inceptors has programmable variable feel capability, allowing simulation and evaluation of a wide range of characteristics. The Learjet's aircraft rudder pedals have also been replaced with variable feel capability. Electrohydraulic servo actuators drive the aircraft's primary control surfaces in response to pilot inputs and the signals from the Variable Stability System (VSS). The Safety Pilot (SP), whose controllers remain mechanically connected to the Learjet control surfaces, via cables, occupies the left seat. Figure 8.2 shows the modified aircraft configuration with the incorporated VSS components.

8.2.2 Variable Stability System Description

This section reflects the Learjet systems circa 2006-2007. As described in [5], in-flight simulation is performed using control laws hosted in the VSS computers. These computers include the original hybrid digital/analog units and a fully digital unit. Each VSS computer system is comprised of two independent subsystems. The first, the variable feel system, provides the EP with tactile force cues from the pitch/roll controller and rudder pedals, that is, gradients, displacements, and nonlinearities such as breakout and friction. The second hosts the control laws, which augment the Learjet dynamics to represent those of the vehicle to be simulated.

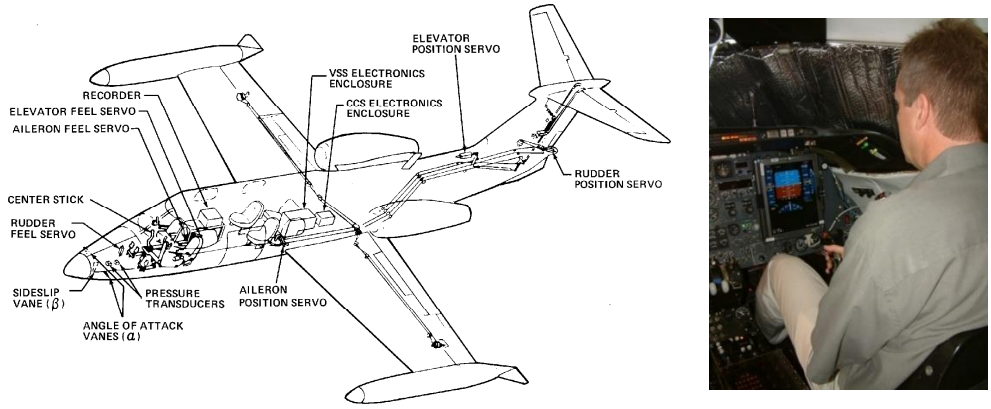

Figure 8.2: *Learjet configuration layout and cockpit in ground simulation mode with programmable head-down display.*

The all-digital unit consists of several Digital Signal Processors (DSPs) installed in a personal computer. The DSPs compute and control the feel system, input/output management, and augmentation control law algorithms. The host computer allows simulation control, passing data to and from the DSPs, data recording, and real-time plotting. The DSPs can be programmed directly in C or symbolically using MATLAB™ Simulink. This makes the VSS a useful tool for rapid prototyping and allows quick turnaround of desired system changes. The architecture of the analog sensor conditioning electronics and of the VSS computing equipment allows easy interface with sensors, augmentation control laws, feel systems, and cockpit displays, including the programmable head-down display shown in Figure 8.2.

The Learjets are equipped with onboard systems for recording test data. Data acquisition is controlled by the host computer interface at the test engineer console or by the SP via a hand-held keypad. Up to 512 channels of digital data may be recorded directly from the DSP computers and stored on removable flash memory. Selected parameters may be directed to the test engineer's computer displays for real-time monitoring. Audio and video information (from cameras, displays, and crew voices) is also recorded onboard using a DVD recorder. The aircraft also has provisions for telemetry transmission of data, audio, and video signals.

8.3 Method of Test

8.3.1 Experimental Design

The Calspan Learjet In-Flight Simulator was used to evaluate the Smart-Cue/Smart-Gain PIO mitigation system using both cruise flight and approach and landing evaluation tasks. The working area for the checkout and evaluation flights was along the southern shore of Lake Ontario with all approach and landing evaluations made at Niagara Falls airport. The crew for the checkout and evaluation flights consisted of a Calspan safety pilot, an evaluation pilot, a Calspan flight test engineer, and the STI flight test conductor. The evaluation pilots were exposed to the Smart-Cue and Smart-Gain mechanizations using the Learjet in a ground simulation mode prior

to formal flight test evaluations. This gave the pilots some sense of how the cues and gain reduction would engage in flight. Cruise evaluations flights were conducted first for all evaluation pilots.

The baseline configuration was designed to be PIO free, while the rate limited configurations were designed to be susceptible to PIO. While configured via the VSS, the baseline configuration was similar to the Learjet sans the VSS with its yaw damper engaged. Smart-Gain only and combined Smart-Cue and Smart-Gain cases were then introduced with the rate limited configurations to assess the effectiveness of the system in mitigating PIO. The configurations were "blind" to the evaluation test pilots, that is, the pilot did not know what configuration was being assessed run-to run. Upon touchdown, the safety pilot would take control and return the aircraft via a "touch and go" to the desired landing approach starting point wherein the evaluation pilot would again be given control of the aircraft. While the safety pilot was in control, the evaluation pilot would provide ratings and comments for the selected configuration. Given available flight test time, repeat runs of selected configurations were made at the discretion of the STI flight test conductor.

8.3.2 Lateral Axis Feel System

The lateral axis feel system dynamics for the stick are modeled as a second order system with nonlinearities. All parameters such as breakout, force gradients, and friction levels are fully configurable and variable in flight. The evaluation pilot applies a force on the stick which is measured and sent into the dynamic stick model to obtain the model stick position from the force. This position is then put through an inverse dynamic model of the physical stick and servo dynamics to obtain a command for the feel system servo that drives it to the position of the model.

Key feel system elements are shown in the Figure 8.3 block diagram. These include the dynamic characteristics of the control loader and the control system gearing. A summary of the selected baseline feel system characteristics used in this flight test program is provided in Table 8.1. As described previously, these characteristics can be easily varied from this baseline. The steady state stick force characteristics are shown in the right-side panel of Table 8.1 and the Bode frequency response is shown in Figure 8.4. The steady state characteristics were generated from the evaluation pilot station of Learjet 2 while operating in ground simulation mode. The frequency responses, on the other hand, were identified from frequency sweep data generated in flight. The lines on the Bode plot represent a transfer function fit using the Table 8.1 parameters with gain adjustments made to match the processed sweep data, solid line for magnitude and dashed line for phase. The resulting transfer function is shown in shorthand notation, where $a(s+b)[s^2+2\zeta\omega s+\omega^2]=a(b)[\zeta,\omega]$.

8.3.3 Approach and Landing Aircraft Configuration

The evaluation task for the approach and landing flight condition was the precision offset landing. Because of the limited number of available flight hours, Smart-Cue/Smart-Gain evaluations focused on the lateral axis. The longitudinal configuration was representative of a standard Learjet 25. The nominal approach speed was 140 knots with gear down and flaps set to 20

degrees. The approach speed was reduced at the discretion of the safety pilot as the fuel load decreased.

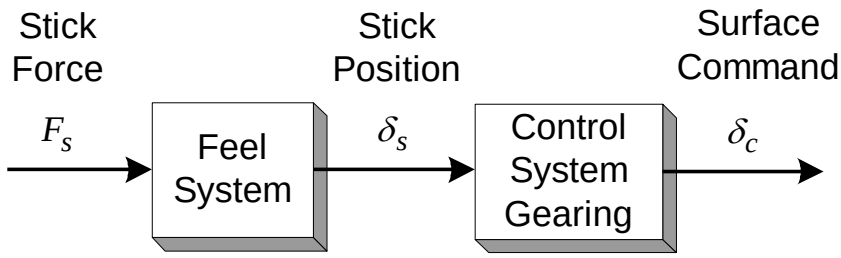

Figure 8.3: *Feel system elements.*

Table 8.1: *Lateral feel system characteristics.*

Parameter	Value
Spring Gradient (lb/in)	5.65
Damping (lb·s/in)	0.395
Natural Frequency (rad/s)	20
Damping Ratio	0.7
Inertia (lb·s^2/in)	0.0141
Breakout (lbs)	0.25
Travel (in)	±3.1
Control System Gearing (deg/in)	-12.3

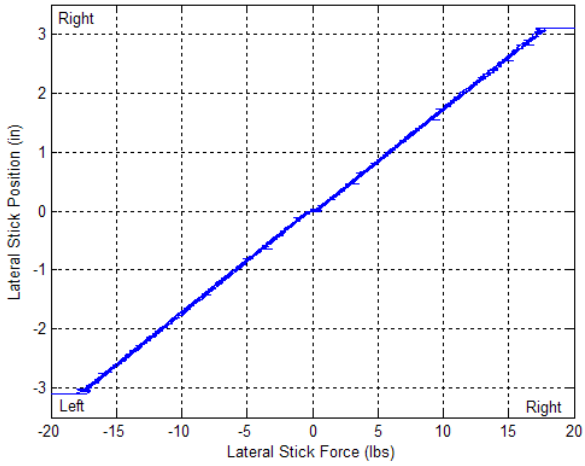

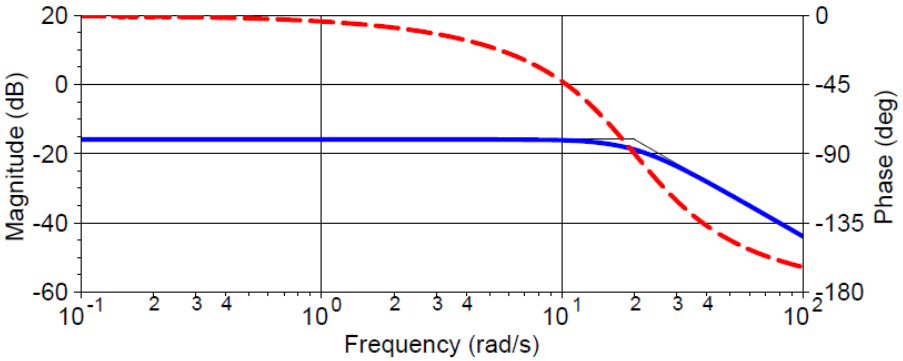

$$\frac{\delta_{as}}{F_{as}} = \frac{64.1}{[0.7, 20]}$$

Figure 8.4: *Lateral feel system Bode plot as identified from frequency sweep data.*

The baseline roll approach and landing configuration had characteristics similar to a nominal Learjet 25 with yaw damper engaged. The configuration is susceptible to PIO in the presence of significant rate limiting. A frequency response for the baseline roll configuration obtained from a checkout flight pilot generated frequency sweep is shown in Figure 8.5. Once again, the lines on the plot represent a transfer function fit using the known model dynamics where only the effective gain and delay were adjusted (solid line for magnitude and dashed line for phase). The resulting roll rate to lateral stick force transfer function in shorthand notation is as follows:

$$\frac{p}{Fas} = \frac{4.082e6(0)[0.335, 1.103]}{(-5.49e-3)[0.249, 1.25](1.324)[0.7, 20][0.7, 44]} e^{-0.125s} \qquad (8.1)$$

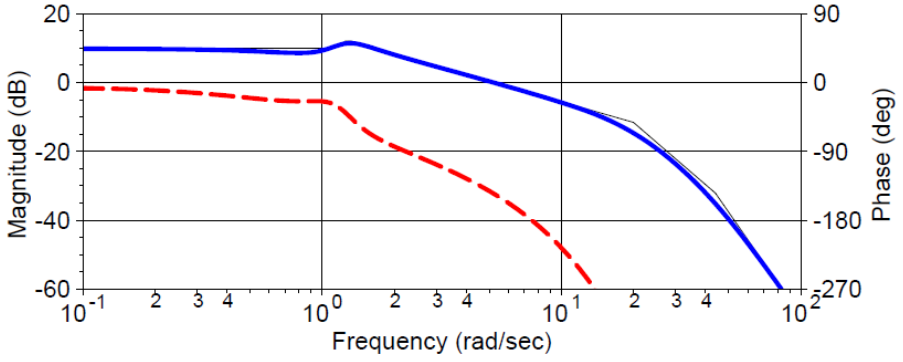

Figure 8.5: *Bode frequency response of the baseline roll axis approach and landing configuration.*

8.4 Flight Test Description

8.4.1 Test Procedures

The flight test evaluations were conducted as a formal handling qualities evaluation. To this end the following procedures were followed:

- Evaluation pilots were familiarized with the evaluation tasks using "good" aircraft configurations, that is, the baseline configuration described above, with no distortion inducing nonlinearities present.
- An appropriate level of familiarity was met when the pilot could routinely achieve desired performance with the selected evaluation task when presented the "good" configuration.
- Degraded configurations, the rate limit only configurations, were then presented to the pilot to evaluate before any force feedback Smart-Cues and command path Smart-Gains were introduced.
- For the approach and landing evaluations, the Smart-Gain was introduced first in isolation and then in combination with the Smart-Cues. Two Smart-Gain configurations were used in the flight test campaign: G1featured a more aggressive adaptive gain, while G2 = G1/1.5.
- Two types of Smart-Cues were introduced – a "friction-like" force cue and a "combined friction and spring gradient" force cue. Two friction cases, F1 and F3, and two combined cases, C1 and C2, were evaluated in flight. For the two friction cases, F3 had a more aggressive gradient than F1, where the gradient for F3 = 1.67*F1. For the combined friction plus gradient cases, both had the same gradient force, but C2 featured a less aggressive friction force, C2(friction) = C1(friction)/1.5. The pilot evaluated each force cue individually. The make up of these force feedback configurations is discussed in detail in Chapter 10.
- When conducting a formal evaluation, the pilot was asked to perform the selected evaluation task as many times as necessary (within reason) before providing pilot comments and ratings.
- Cooper-Harper handling qualities ratings [6], Figure 8.6, and PIO tendency ratings [7,8], Figure 8.7, were collected. Evaluation pilots were encouraged to talk through the rating scale decision trees as a means of extracting additional commentary.
- A detailed run log was taken and video with an over the evaluation pilot's shoulder view was recorded including audio commentary.

The purpose of the Smart-Cue and Smart-Gain is to provide protection from the flying qualities cliffs associated with dynamic distortion. The cue thus serves two functions: "alerting" and "constraining." The former annunciates the presence of a potential handling qualities cliff, while

the latter suppresses inputs that will lead to an encounter with that cliff. The purpose of the evaluation task used here was to simulate the types of closed-loop control scenarios that have produced such cliffs in operational and flight test aircraft. While task performance was important, the real evaluation was to determine if the Smart-Cue and Smart-Gain could serve as a protection from these cliffs. To this end, some sacrifice in task performance was anticipated when the cues were encountered.

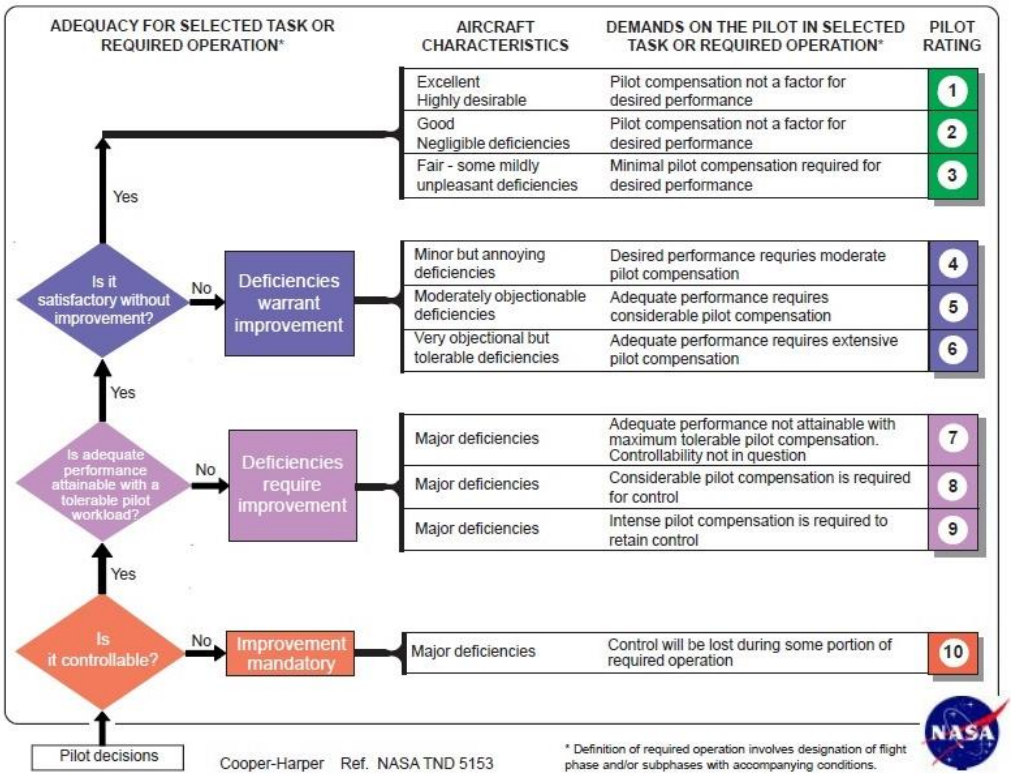

Figure 8.6: *Cooper-Harper Handling Qualities Pilot Rating Scale.*

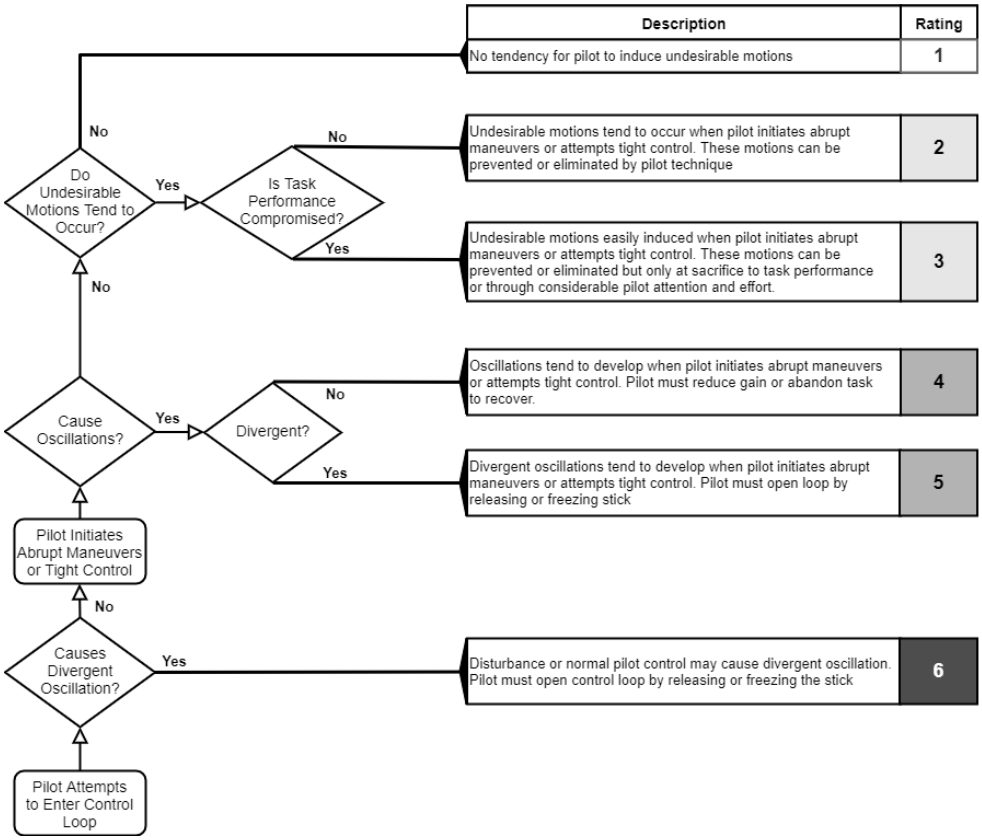

Figure 8.7: *Pilot-Induced Oscillation (PIO) Tendency pilot rating scale.*

8.4.2 Precision Offset Landing Task Description

All approach and landing evaluations were made at Niagara Falls International airport. The crew for the checkout and evaluation flights consisted of a Calspan SP, an EP, a Calspan flight test engineer, and the STI flight test conductor (the author of this thesis). The evaluation task was the precision offset landing task described below.

Task Objectives

- Evaluate ability to precisely control horizontal and vertical flightpath and airspeed.
- Evaluate ability to precisely control sink rate and attitude in the flare.
- Evaluate tendency for nose bobble or PIO.
- Evaluate control sensitivity and harmony in landing.

Task Description

The offset landing task consists of a visual approach during which the EP aligns the aircraft approximately 300 feet off the runway centerline (see Figure 8.8). At 150 to 200 feet above the ground, the EP corrects back to the centerline and attempts to touchdown within the desired parameters. The decision to correct is made by the SP. Offsets to the left or right can be used interchangeably; however, the direction of offset may often be dictated by the desire to turn away from civilian aircraft waiting in the hold short area. Typically, offsets were made to the right in this flight test program to take advantage of the drainage ditch visual cue located approximately 250-300 ft to the right of runway 28R (see Figure 8.8). Each landing was treated as a "must land" situation to ensure a high pilot gain. Desired and adequate performance requirements for the task are listed in Table 8.2.

During a typical landing pattern evaluation, the SP configures the aircraft for landing, selecting the proper flight control experiment, and engaging the VSS while on downwind. The EP begins the evaluation on base turn and lines up on final for the offset landing. The EP initiates the offset correction on his or her own or based on radar altitude calls from the SP. A precise flared landing is attempted using the instrument landing markers as the desired touchdown point. These markers are located 1,000 feet from the threshold. Upon touchdown, the SP takes control of the airplane and performs the takeoff and turn to downwind, while the EP provides comments and handling qualities ratings for that configuration. The head down display used for the task is shown in Figure 8.2. Example offset landing approach photos are shown in Figure 8.9.

Table 8.2: *Task performance requirements.*

Desired Performance	Adequate Performance
• Approach airspeed maintained within ± 5 kts. • Touchdown within 5 feet of centerline (main wheels on centerline). • Touchdown within ± 250 feet of aimpoint. • Sink rate – smooth touchdown. • No PIO.	• Approach airspeed maintained within -5 kts/+10 kts. • Touchdown within 25 feet of centerline. • Touchdown within ± 500 feet of aimpoint. • No PIO.

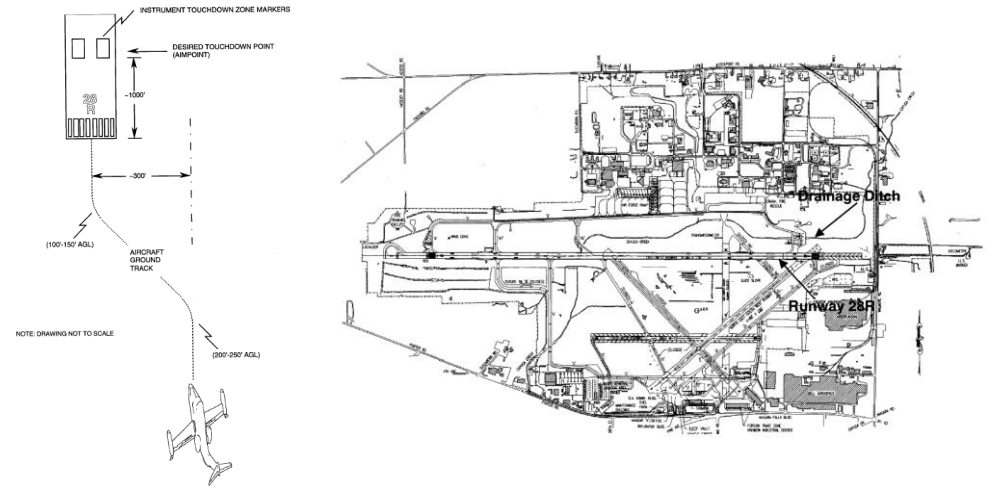

Figure 8.8: *Offset approach to Niagara Falls International airport and airport layout with key task visual cues (drainage ditch and Runway 28) identified.*

Figure 8.9: *Example offset landing approaches.*

8.5 Flight Test Results

8.5.1 Overview of the Test Program

Seven test pilots participated in this program. Pilots 1 and 2 served as safety pilots and did not conduct formal evaluations. All evaluation pilots were graduates of either the U.S. Air Force or U.S. Navy test pilot schools. Approach and landing flights were conducted with three of the five evaluation pilots. Pilots 3 and 4 did not conduct approach and landing evaluations due to poor weather conditions. Pilot 5 flew his approaches in nearly ideal conditions – calm air and good visibility. Under these conditions, the roll axis software rate limit needed to be reduced from 30 to 25 deg/sec, so that the handling qualities cliff could be properly exposed. Pilots 6 and 7, on the other hand, conducted their approach and landing evaluations in the presence of moderate

turbulence and crosswinds. No changes to the experimental procedures were required for these flights. The pilots and crews for the approach and landing evaluations are shown in Figure 8.10.

(a) Pilot 5 and Crew

(b) Pilot 6 and Crew

(c) Pilot 7 and Crew

Figure 8.10: *Pilots and flight test crews for the approach and landing evaluations.*

In the following discussion, three example runs were selected for each pilot to compare against the baseline: 1) the rate limited configuration, 2) the rate limited configuration with Smart-Gain, and 3) the rate limited configuration with Smart-Gain and Smart-Cue. Throughout the remainder of this section the following symbols are used: RL – rate limit, G – Smart-Gain, F – friction Smart-Cue, and C – combined gradient plus friction Smart-Cue. The number associated with the RL symbol is the magnitude of the rate limit in deg/s, while the number associated with the Smart-Gain and Smart-Cue symbol refers to particular configurations.

8.5.2 Pilot Ratings and Comments

For the roll axis approach and landing evaluations, the impact of the Smart-Gain was the dominant effect. The addition of the Smart-Cue, however, was an important and necessary performance benefit for two of the three pilots. For these pilots, the flights took place on a day with significant cross winds and turbulent air that added work load to the precision offset landing task. In these cases, the same gain reduction and feedback cue produced the best results for both pilots. The other pilot flew on a calm air day, which allowed him to use smoother pilot inputs and a lower gain technique. In this environment, the Smart-Gain alone did much of the work and only small Smart-Cue forces that may have been imperceptible to the pilot were ever present.

Cooper-Harper pilot handling qualities ratings (HQR) and pilot-induced oscillation tendency ratings (PIOR) were collected to compliment specific commentary in the qualitative assessment of the various configurations presented to the pilots. Summary PIOR versus HQR plots for each pilot are given in Figure 8.11. For Pilots 6 and 7, the baseline configuration that featured no rate limiting, BL, received Level 1 ratings with no PIO tendencies. Pilot 5 also noted no PIO tendencies with the baseline, but only achieved adequate performance. He noted that this was a reflection of his performance in the task more so than the actual handling qualities of the configuration. As mentioned earlier, a slightly lower rate limit was required for the evaluations of Pilot 5 due to the calm air day combined with a lower gain piloting technique.

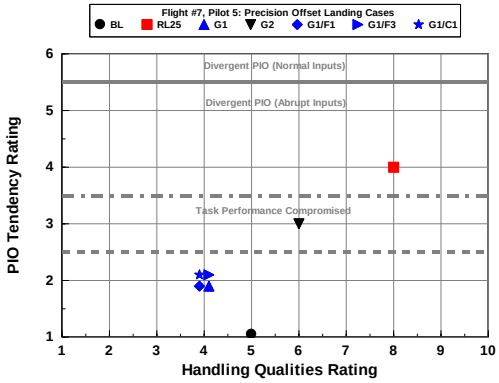

(a) Pilot 5

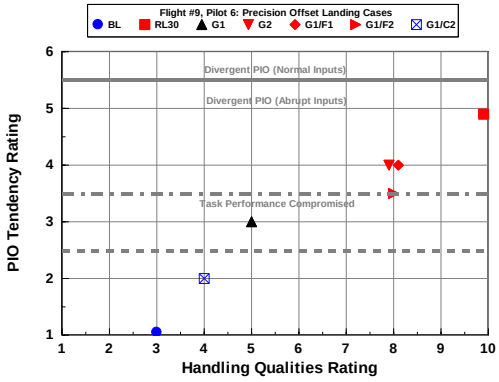

(b) Pilot 6

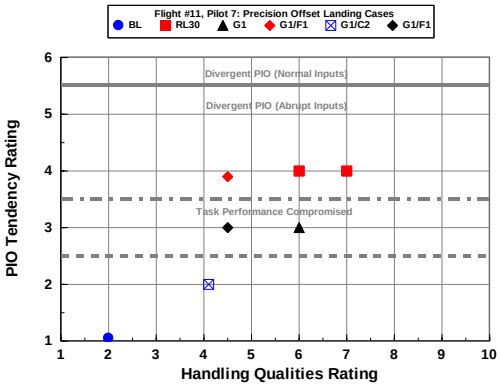

(c) Pilot 7

Figure 8.11: *Pilot ratings for the precision offset landing task.*

Nonetheless, all three pilots gave the rate limited configuration Level 3 pilot ratings (i.e., HQR ≥ 7) with observed PIO tendencies (i.e., PIOR ≥ 4). For Pilot 5, the G1 Smart-Gain made the greatest impact on his ratings to the extent that desired performance was attained. A more modest improvement was observed for Pilots 6 and 7. The G2 Smart-Gain configuration, defined by a less aggressive command path gain reduction compared to the G1 configuration, did not produce improved results. The presence of the Smart-Cues was not a factor in the qualitative evaluations of Pilot 5. For Pilots 6 and 7, both of which conducted their evaluations in moderate turbulence and crosswinds, the strongly preferred configuration was G1/C2. This Smart-Cue/Smart-Gain combination gave consistent performance (HQR 4/PIOR 2) over repeated runs for both pilots. Thus, the combined Smart-Cue/Smart-Gain combination led to the best overall results. A summary of pilot comments for the example run evaluations is provided in Table 8.3. The text colors were selected to match the assigned pilot ratings, that is, blue text for PIO tendency ratings of 1 or 2, black text for PIO tendency ratings of 3, and red text for PIO tendency ratings of 4 or higher.

Table 8.3: *Pilot ratings and comments for selected precision offset landing evaluations.*

Pilot	Configuration	HQR/PIOR	Pilot Comments
5	RL25	8+/4	I was fully devoted to trying to keep the wings level.
5	RL25 G1	4/2	I felt more connected. There was better predictability.
5	RL25 G1/C1	4/2	Doesn't look terribly different to me.
6	RL30	10/5	It wasn't divergent until I got in the loop.
6	RL30 G1	5/3	There are undesirable motions going on… but I am staying on task. I can meet performance, but with considerable compensation.
6	RL30 G1/C2	4/2	That wasn't a problem. That was easy. Performance was good.
7	RL30	7/4	No, I don't like this. As soon as I made the input I realized I wasn't getting what I wanted.
7	RL30 G1	6/3	More controllable, but still hard to make precise inputs. It was not nice right at the end. Probably wouldn't have seen it without the wind.
7	RL30 G1/C2	4/2	I have not felt a cliff where I thought there is a PIO there. Everything felt very controllable without oscillations.

8.5.3 Time Histories

Time history plots for the precision offset landing example runs from Table 8.3 are presented here. Plots for Pilots 5 are shown in Figure 8.12 through Figure 8.15, plots for Pilot 6 are shown in Figure 8.16 through Figure 8.19, and plots for Pilot 7 are shown in Figure 8.20 through Figure 8.22. Included in each example are time histories of the pilot's lateral stick input and the aircraft roll angle output. Also included are time histories of the force feedback Smart-Cue and the command path Smart-Gain. These signals are null for the rate limited only configuration and are therefore not included.

For Pilot 5 there is not a significant difference in the resulting aircraft roll angles associated with the large corrections back to the runway centerline with peak angles in the neighborhood of ±20°. The differences occur in the final, tightly controlled corrections to the runway centerline. Here, the rate limited configuration leads to a PIO, shown in Figure 8.13, that resulted in the safety pilot taking control after the third oscillation. Note also the increasing amplitude of the oscillatory pilot stick force inputs. No such oscillations are seen in the Smart-Gain alone and Smart-Cue/Smart-Gain configurations. The Smart-Gain is active whenever the command path gain is not equal to one. Although not necessarily consciously perceived by the Pilot 5, the presence of the Smart-Cue combined force reduced the amount of Smart-Gain activity when compared to the Smart-Gain alone example.

Both Pilots 6 and 7 employed a more aggressive technique due to natural tendencies and the presence of moderate turbulence and crosswinds. For Pilot 6 the initial correction to the runway centerline resulted in a bank angle of nearly 50°, compared to the 20° bank angle seen by Pilot 5 in his rate limit only run. Furthermore, a divergent PIO resulted from the final corrections and the safety pilot again took control as shown in Figure 8.17. With the Smart-Gain and Smart-Cue active, the resulting bank angle was less than 30° and no PIO was observed in the final corrections. The more aggressive technique of Pilot 6 resulted in a significantly more active Smart-Gain reduction, see Figure 8.18, however, the Smart-Gain activity is reduced when used with the combined force Smart-Cue as seen in Figure 8.19.

For Pilot 7 a distinct PIO tendency was observed in the initial correction to the centerline as well as in final corrections. His sensitivity to an impending flying qualities cliff, however, allowed him to avoid sustained oscillations, although the safety pilot did feel compelled to take control at touchdown. The pilot's high level of aggressiveness is further seen in the activity of the Smart-Gain and in the magnitude of the Smart-Cue force associated with the initial correction. Once again, the activity of the Smart-Gain is reduced in the presence of the Smart-Cue.

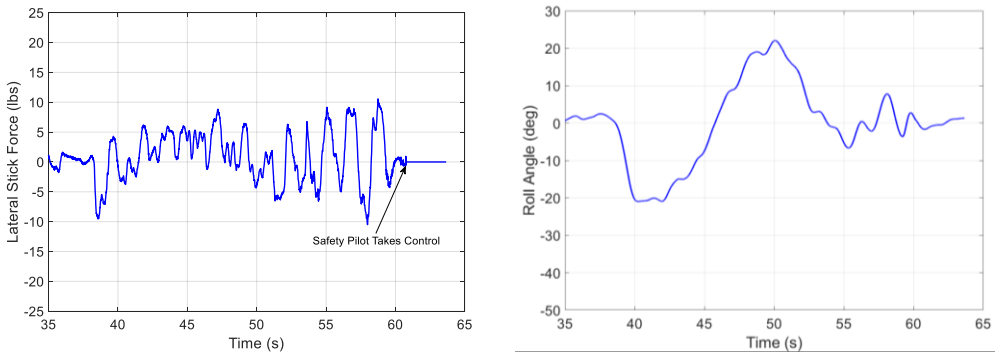

(a) Stick Force (b) Roll Angle (deg)

Figure 8.12: *Time histories for the Pilot 5 precision offset landing task, rate limited configuration RL25, pilot ratings – HQR 8+/PIOR 4.*

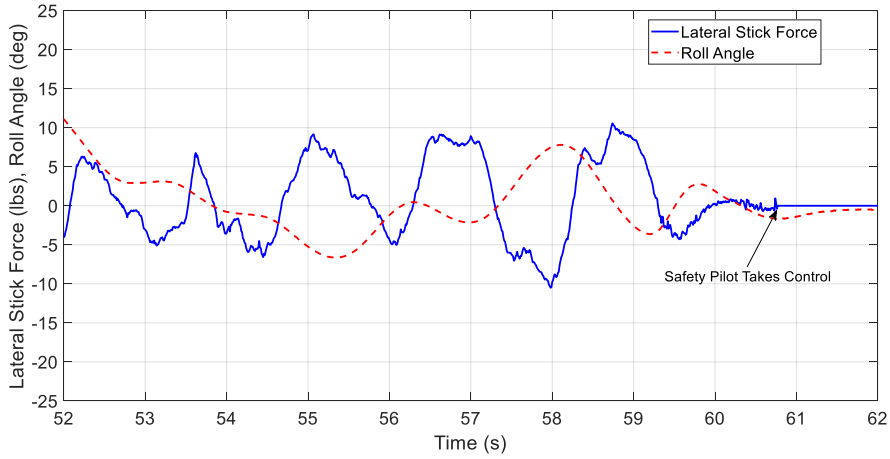

Figure 8.13: *Precision offset landing PIO, Pilot 5, rate limited configuration RL25, PIOR 4.*

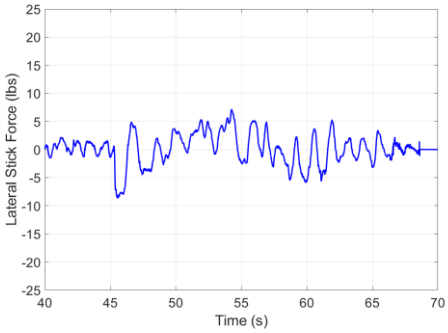

(a) Stick Force

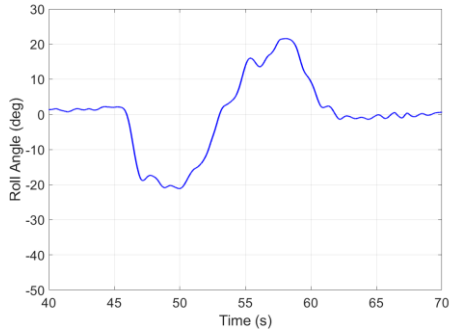

(b) Roll Angle (deg)

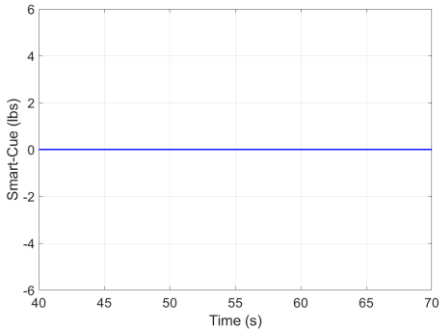

(c) Smart-Cue (lbs)

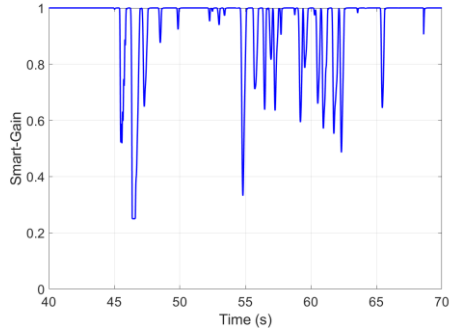

(d) Smart-Gain

Figure 8.14: *Time histories for the Pilot 5 precision offset landing task, rate limited configuration RL25 with Smart-Gain (G1), pilot ratings – HQR 4/PIOR 2.*

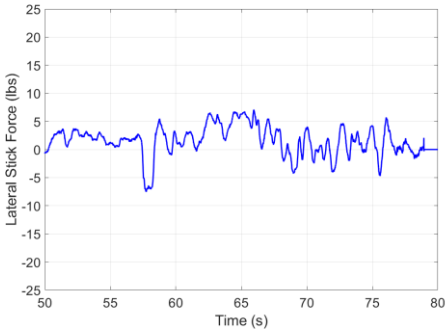

(a) Stick Force

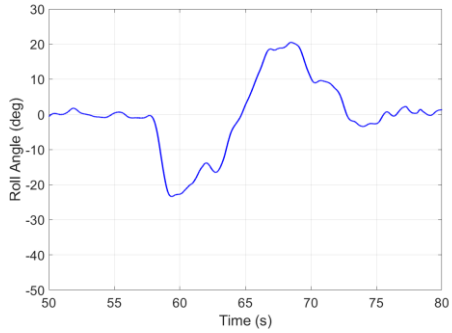

(b) Roll Angle (deg)

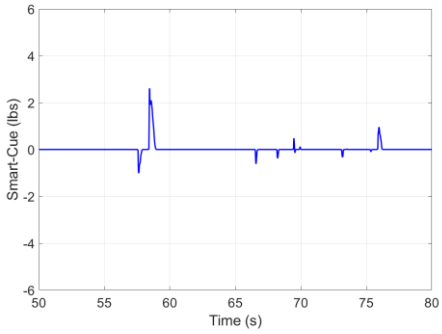

(c) Smart-Cue (lbs)

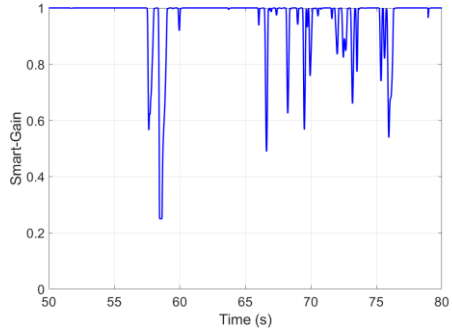

(d) Smart-Gain

Figure 8.15: *Time histories for the Pilot 5 precision offset landing task, rate limited configuration RL25 with Smart-Cue/Smart-Gain (G1/C1), pilot ratings – HQR 4/PIOR 2.*

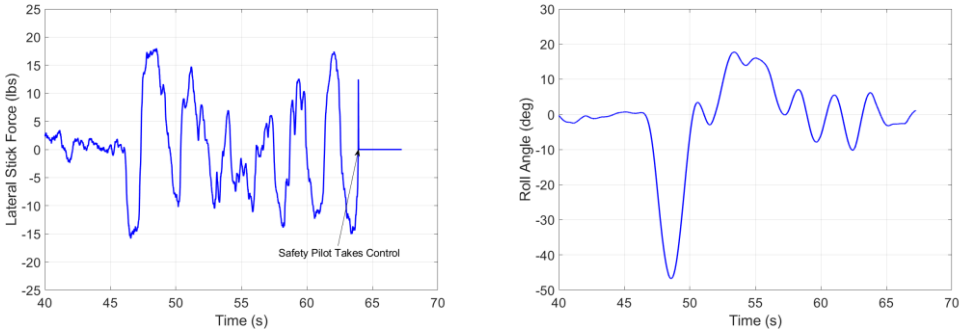

(a) Stick Force *(b) Roll Angle (deg)*

Figure 8.16: *Time histories for the Pilot 6 precision offset landing task, rate limited configuration RL30, pilot ratings – HQR 10/PIOR 5.*

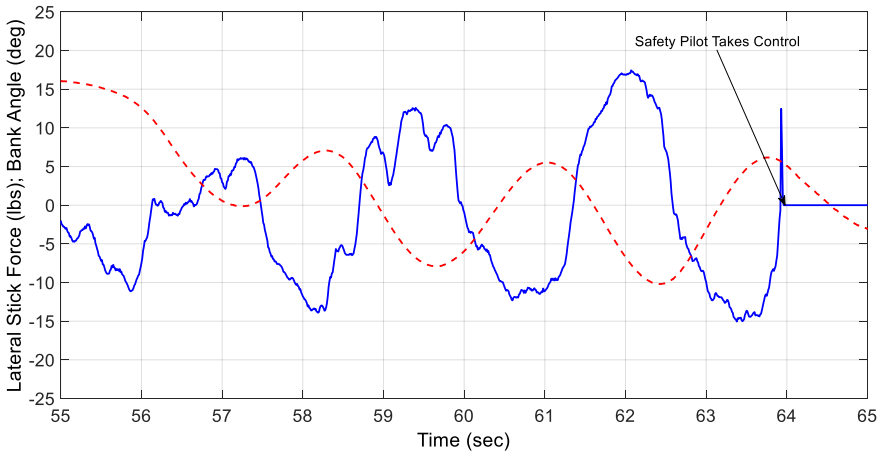

Figure 8.17: *Precision offset landing PIO, Pilot 6, rate limited configuration RL30, PIOR 5.*

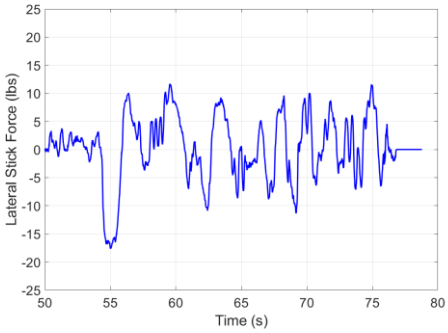

(a) Stick Force

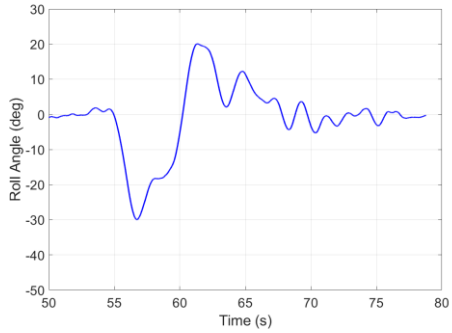

(b) Roll Angle (deg)

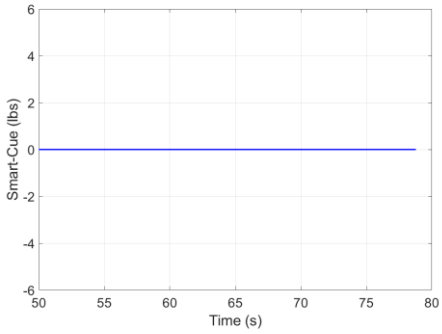

(c) Smart-Cue (lbs)

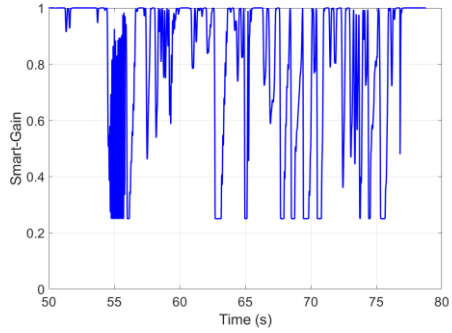

(d) Smart-Gain

Figure 8.18: *Time histories for the Pilot 6 precision offset landing task, rate limited configuration RL30 with Smart-Gain (G1), pilot ratings – HQR 5/PIOR 3.*

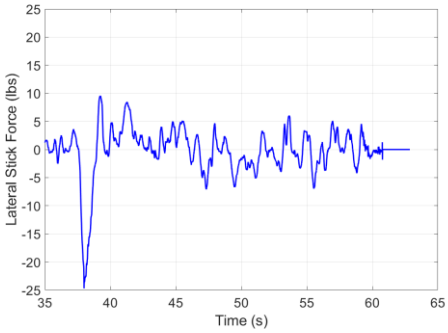

(a) Stick Force

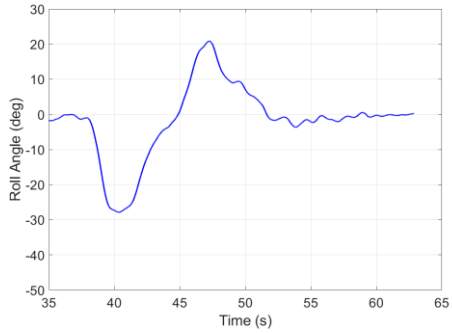

(b) Roll Angle (deg)

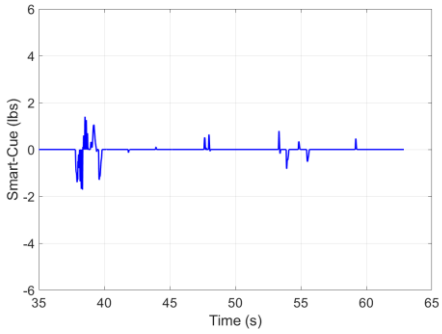

(c) Smart-Cue (lbs)

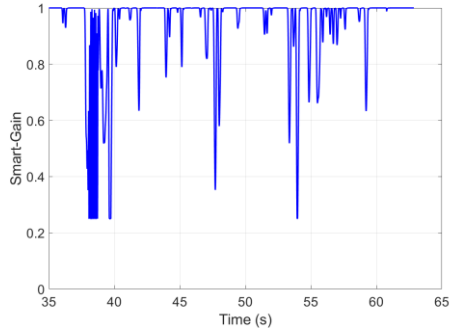

(d) Smart-Gain

Figure 8.19: *Time histories for the Pilot 6 precision offset landing task, rate limited configuration RL30 with Smart-Cue/Smart-Gain (G1/C2), pilot ratings – HQR 4/PIOR 2.*

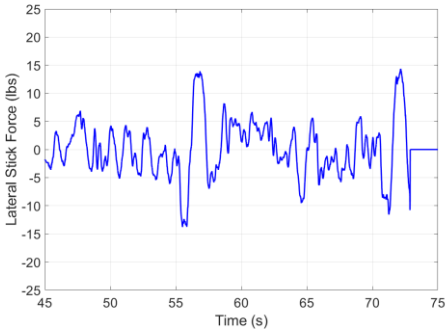

(a) Stick Force

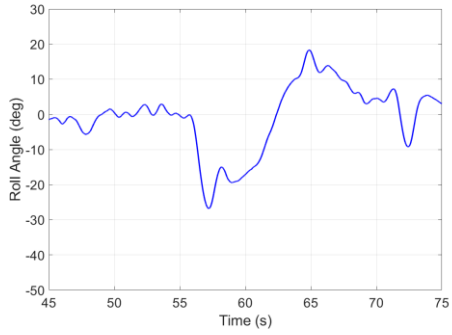

(b) Roll Angle (deg)

Figure 8.20: *Time histories for the Pilot 7 precision offset landing task, rate limited configuration RL30, pilot ratings – HQR 7/PIOR 4.*

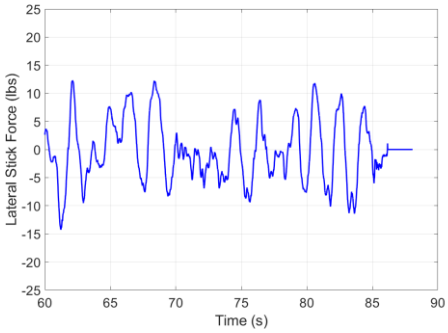

(a) Stick Force

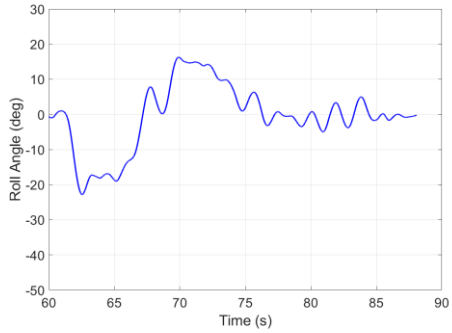

(b) Roll Angle (deg)

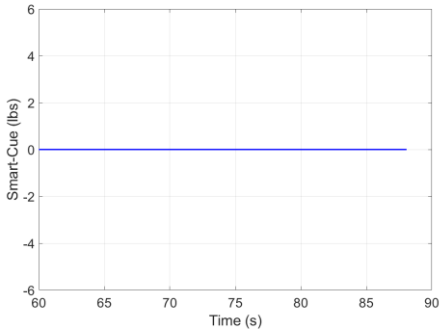

(c) Smart-Cue (lbs)

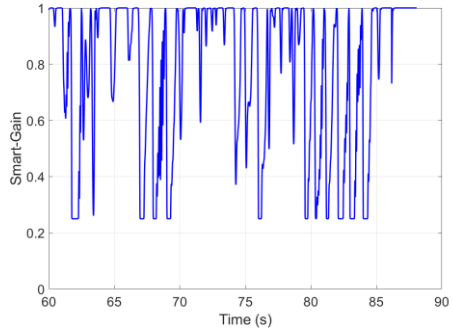

(d) Smart-Gain

Figure 8.21: *Time histories for the Pilot 7 precision offset landing task, rate limited configuration RL30 with Smart-Gain (G1), pilot ratings – HQR 6/PIOR 3.*

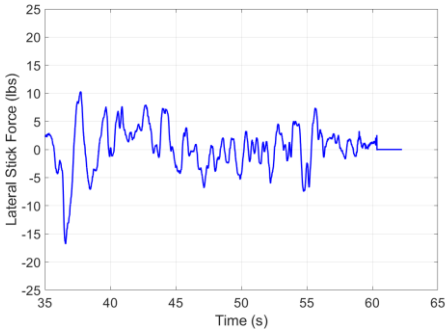

(a) Stick Force

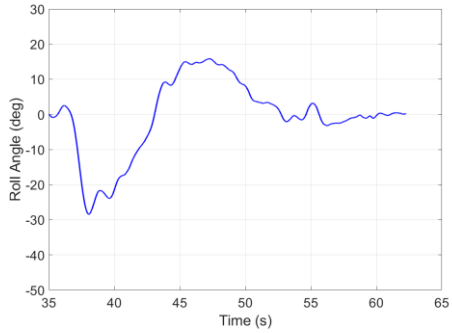

(b) Roll Angle (deg)

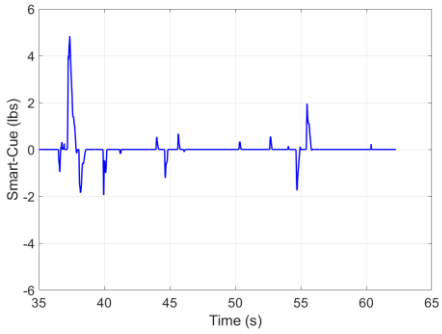

(c) Smart-Cue (lbs)

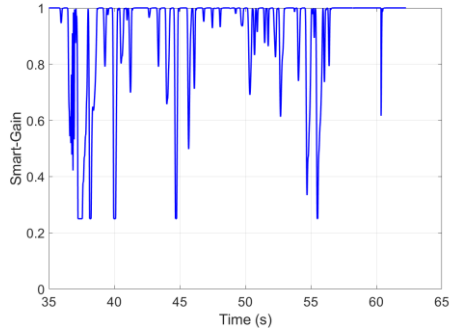

(d) Smart-Gain

Figure 8.22: *Time histories for the Pilot 7 precision offset landing task, rate limited configuration RL30 with Smart-Cue/Smart-Gain (G1/C2), pilot ratings – HQR 4/PIOR 2.*

8.5.4 Position Error Scalograms

The wavelet scalogram [9] not only identifies the peaks in signal power, but also when in time the peaks occurred. It is this characteristic that makes wavelets a powerful tool for detecting changes in time varying systems and it is this capability that is exploited for identifying from the flight test data system performance differences with the Smart-Cue and Smart-Gain active. In Appendix A, a description of wavelet-based scalograms as a means to assess time-varying systems is provided. Position Error, as described in Chapter 7, is the measure of dynamic distortion. Thus, if the methods are effective, there should be a significant reduction in Position Error with the Smart-Gain and/or Smart-Cue active. Scalograms offer a unique way to quantify this reduction.

Two-dimensional Position Error scalograms and corresponding Position Error time histories for the three precision offset landing example runs are shown in Figure 8.23, Figure 8.24, and Figure 8.25 for Pilots 5, 6, and 7, respectively. Scalograms, as described in Appendix A, are essentially time-varying power spectra density plots that not only show at what frequencies the peak power is occurring, but also at what point in time the peaks are occurring. In the two-dimensional scalogram plots, approximately 30 seconds of data, selected to capture the heart of the offset landing, are included in the plots shown here with the last time slice of the selected 30 seconds displayed as a series of red dots. Then, as time moves back to the earliest interval displayed on the plot, the solid "lines of persistence" change from a dark to light. Note that the same plot scales are used for the plots so both intra- and inter-pilot variations can be easily studied. The "absolute" power units for the scalogram of Position Error are $deg^2/(rad/s)$. Occasionally, a high frequency oscillation can be seen in the Position Error signal, around 55 seconds in Figure 8.24(b), that results from numerical computations within the Learjet VSS. This behavior, when it occurred, was not noticed by the pilots in the resulting Smart-Gain or Smart-Cue.

Because the Position Error is tied closely to the control activity of the pilot, the Position Error power occurs predominantly in the frequency range associated with pilot control (i.e., 0.1 to 20 rad/sec). For the Pilot 5 example cases, the peak power occurs during the PIO associated with the final correction of the rate limited example, see Figure 8.23(a). In this case the peak power closely correlates with the observed PIO frequency of 3.4 rad/sec. With the Smart-Gain and Smart-Cue active, the peak power is reduced by approximately a factor of 6. As noted previously, the Smart-Gain alone does much of the work for Pilot 5, although some further improvements are seen with the Smart-Cue active as well.

Comparing inter pilot results, the largest peak in Position Error power was seen in the Pilot 6 rate limited example case of Figure 8.24(a). This peak is associated with the divergent PIO that developed during the final corrections that was discussed earlier. For this pilot the addition of the Smart-Gain produces a reduction in Position Error power by a factor of 4.5, however, the Smart-Gain plus Smart-Cue results in a reduction by a factor of nearly 14. Although not as dramatic, similar trends are seen in the Pilot 7 results of Figure 8.25. For both Pilots 6 and 7 the combination of Smart-Gain and Smart-Cue was required to achieve the best results.

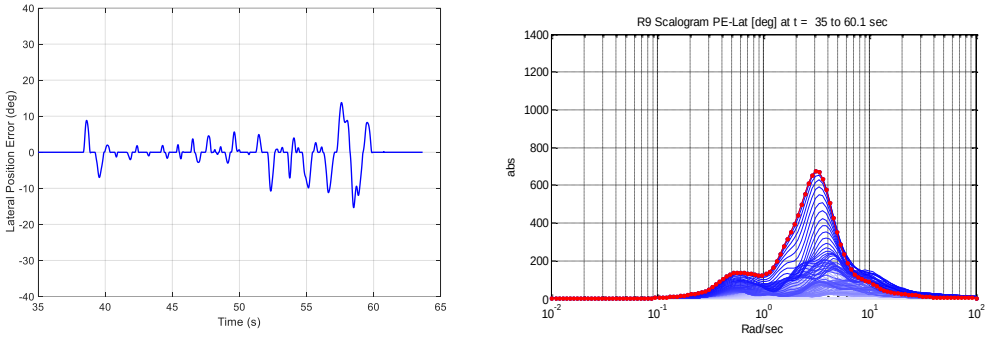

(a) RL25 – HQR 8+/PIOR 4

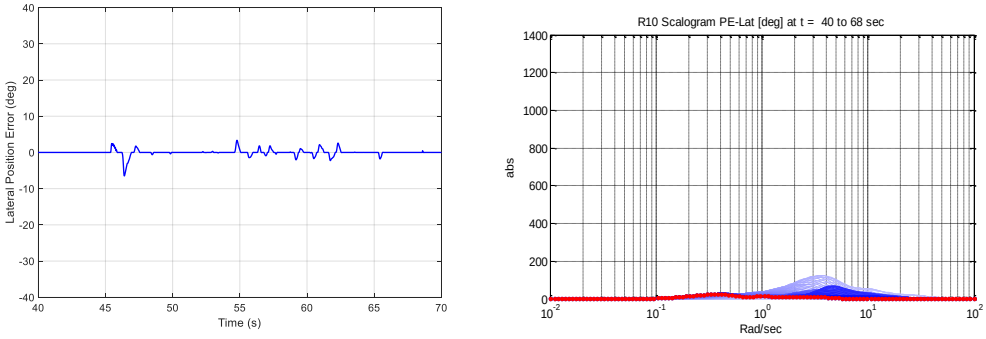

(b) RL25, Smart-Gain (G1) – HQR 4/PIOR 2

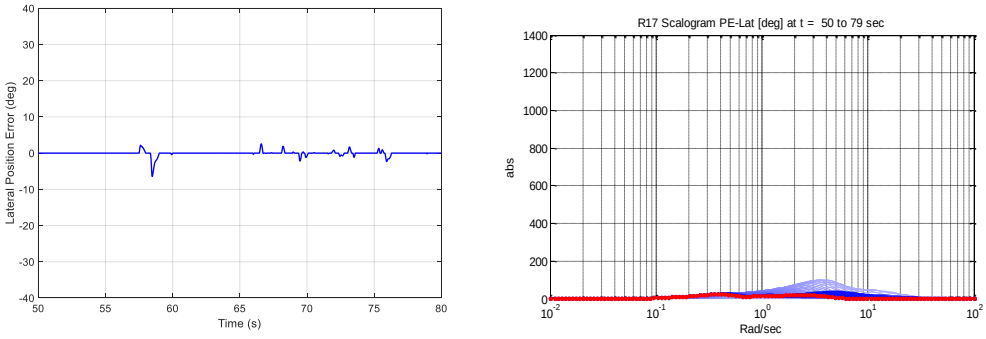

(c) RL25, Smart-Cue/Smart-Gain (G1/C1) – HQR 4/PIOR 2

Figure 8.23: *Lateral Position Error variations for the precision offset landing task, Pilot 5.*

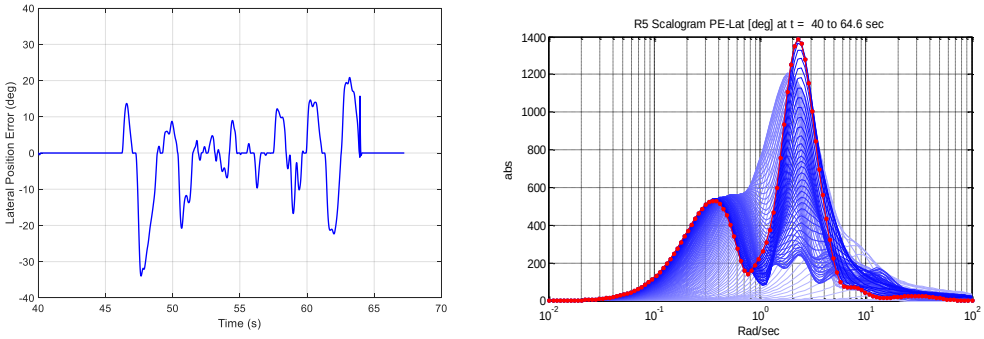

(a) RL30 – HQR 10/PIOR 5

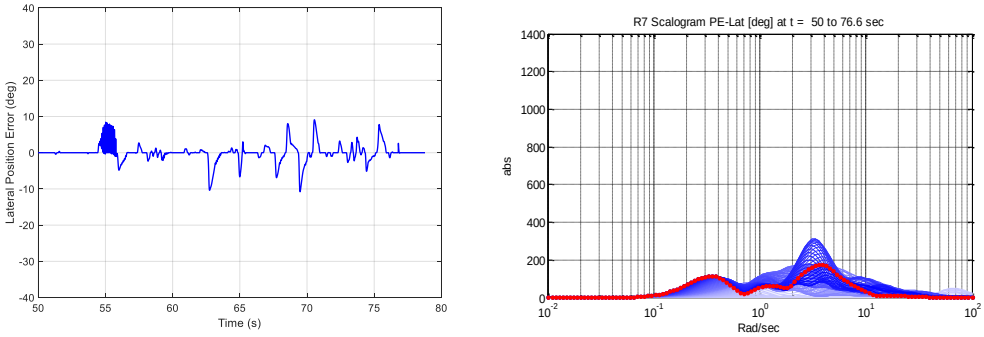

(b) RL30, Smart-Gain (G1) – HQR 5/PIOR 3

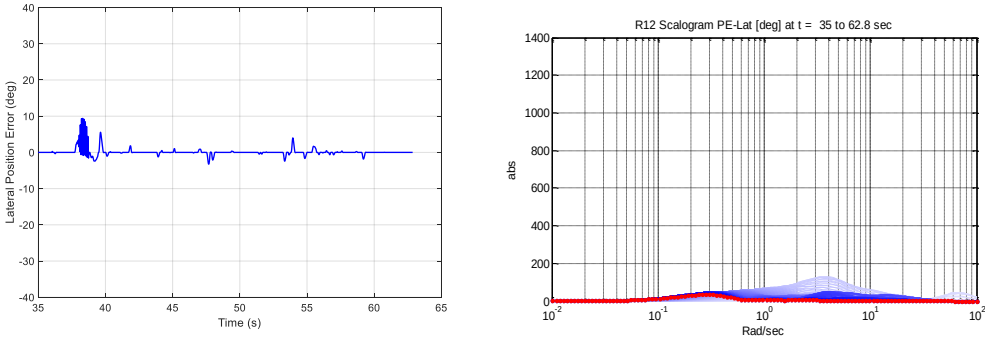

(c) RL30, Smart-Cue/Smart-Gain (G1/C2) – HQR 4/PIOR 2

Figure 8.24: *Lateral Position Error variations for the precision offset landing task, Pilot 6.*

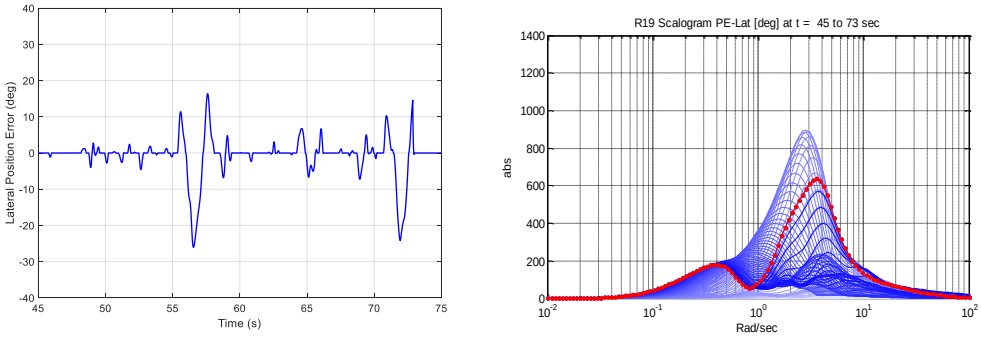

(a) RL30 – HQR 7/PIOR 4

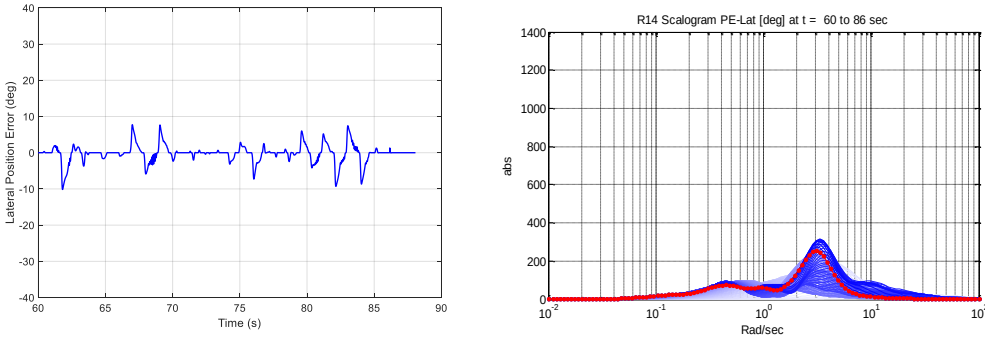

(b) RL30, Smart-Gain (G1) – HQR 6/PIOR 3

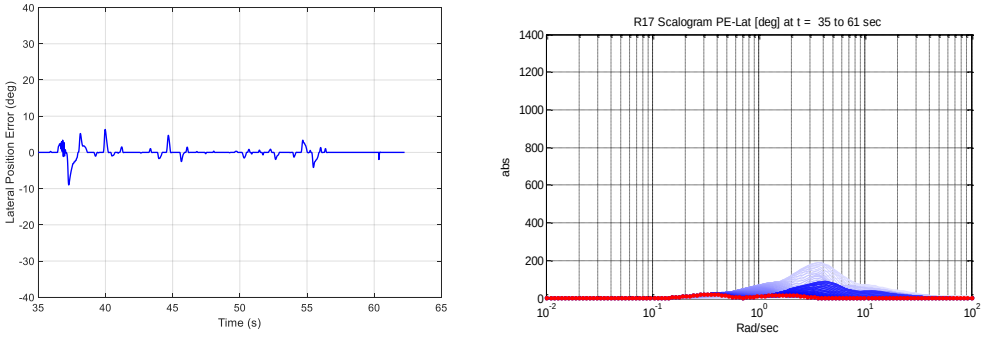

(c) RL30, Smart-Cue/Smart-Gain (G1/C2) – HQR 4/PIOR 2

Figure 8.25: *Lateral Position Error variations for the precision offset landing task, Pilot 7.*

8.6 Conclusions

In this Chapter, the Smart-Cue/Smart-Gain concept was evaluated by three test pilots using the Calspan Learjet In-Flight Simulator. The pilots evaluated four configuration variations with a precision offset landing task. The baseline configuration was found to be PIO resistant by all three pilots, while the rate limited only configuration was found to have PIO tendencies that in one case were divergent. Two Smart-Gain cases and two Smart-Cue/Smart-Gain cases were evaluated with the rate limited configuration. For the roll axis approach and landing evaluations, the impact of the Smart-Gain was the dominant effect. In the checkout flights it was difficult to achieve adequate landing performance with the rate limited configuration using the Smart-Cue alone. Addition of the Smart-Cue, however, was an important performance benefit for two of the three pilots, that is, Pilot 6 and Pilot 7. For these pilots, the evaluation flights took place on a day with significant cross winds and turbulent air that resulted in added work load for the precision offset landing task. The same Smart-Gain and combined force Smart-Cue produced the best results for both pilots. This combination consistently gave desired performance with no pilot-induced oscillation tendencies over repeated evaluations, which was significant considering that the wind conditions varied from run to run. The third pilot, Pilot 5, flew on a calm air day, which allowed him to use smoother pilot inputs associated with his lower gain technique. In this environment, the Smart-Gain alone did much of the work and only small Smart-Cue forces that may have been imperceptible to the pilot were ever present. When used together, the Smart-Gain and Smart-Cue were found to enhance flight safety in the approach and landing task by significantly reducing pilot-vehicle system loss of control incidents that routinely occurred with the rate limited alone configuration.

8.7 References

1. Klyde, D. H., and C. Y. Liang, "Approach and Landing Flight Test Evaluation of Smart-Cue and Smart-Gain Concepts," J. *of Guidance, Control, and Dynamics*, Vol. 32, No. 4, July-Aug. 2009, pp. 1057-1070.

2. Klyde, D. H., and C. Y. Liang, "Flight Assessment of Pilot Behavior with Smart-Cue and Smart-Gain Concepts Active," AIAA 2009-5606 presented at *Atmospheric Flight Mechanics Conference*, Chicago, IL, August 10-13, 2008.

3. Klyde, D. H., C. Y. Liang, and P. C. Schulze, "Applying Flight Test Lessons Learned 'On-the-Fly,'" AIAA 2009-5729 presented at *Atmospheric Flight Mechanics Conference*, Chicago, IL, August 10-13, 2008.

4. Klyde, D. H., and D. G. Mitchell, "Investigating the Role of Rate Limiting in Pilot-induced Oscillations," *J. Guidance, Control, and Dynamics*, Vol. 27, No. 5, Sept.-Oct. 2004, pp. 804-813.

5. Weingarten, N. C., "History of In-Flight Simulation at General Dynamics," *J. of Aircraft*, Vol. 42, No. 2, March-April 2005, pp. 290-298.

6. Cooper, G. E. and Harper Jr., R. P, *The Use of Pilot Rating in the Evaluation of Aircraft Handling Qualities*, AGARD Report 567; April 1969.

7. DiFranco, D. A., *Flight Investigation of Longitudinal Short Period Frequency Requirements and PIO Tendencies,* AFFDL-TR-66-163, June 1967.

8. Weingarten, N. C., and C. R. Chalk, *In-Flight Investigation of Large Airplane Flying Qualities for Approach and Landing*, AFWAL-TR-81-3118, Sept. 1981.

9. Thompson, P. M., D. H. Klyde, E. N. Bachelder, and T. J. Rosenthal, *On-line Loss of Control Detection using Wavelets*, NASA CR-2005-212873, July 2005.

9. Flight Test Evaluation of the Smart Adaptive Flight Effective Cue (SAFE-Cue)

It's pretty good, very similar to the baseline throughout. I kept my tracking accuracy. I think it was pretty good throughout.

Calspan Test Pilot, April 2013

Parts of this chapter have been published as:

Title Flight Test Evaluation of a Loss of Control Mitigation System

Journal Journal of Guidance, Control, and Dynamics, vol. 40, no. 4, April 2017, pp. 981-997

Authors D. H. Klyde, A. K. Lampton, N. D. Richards, and B. Cogan

9.0 FLIGHT TEST EVALUATION OF THE SMART ADAPTIVE FLIGHT EFFECTIVE CUE (SAFE-CUE)

Following the successful flight test evaluations of the Smart-Cue/Smart-Gain, as described in Chapter 8, approach to the mitigation of pilot-induced oscillations (PIO) in the presence of control surface actuator rate limiting, a more general approach was explored that focused on the overall system response. The work presented in this chapter was conducted under sponsorship of the National Aeronautics and Space Administration and resulted in the Smart Adaptive Flight Effective Cue (SAFE-Cue). The material in this chapter is largely taken from [1] and reports on the flight test evaluations of the SAFE-Cue system as an adaptive controller attempts to address simulated flight control system failures that include reduced control surface effectiveness and reduced control surface actuator rate limits. As will be shown in this chapter, these types of failures resulted in unfavorable pilot-vehicle interactions including PIO.

9.1 Introduction

9.1.1 Overview

NASA identified loss of control as a key ongoing safety issue for commercial aviation [2]. To this end, the Vehicle Systems Safety Technology (VSST) Project of NASA's Aviation Safety Program, as described on the NASA web page [3], *identifies risks and provides knowledge to avoid, detect, mitigate, and recover from hazardous flight conditions, and to maintain vehicle airworthiness and health*. Work in these areas has been presented to the aerospace community at large in a series of invited paper sessions at the American Institute of Aeronautics and Astronautics (AIAA) co-located Guidance, Navigation, and Control, Atmospheric Flight Mechanics, and Modeling and Simulation Technologies conferences and at the AIAA Science and Technology Forum and Exposition (SciTech). It is beyond the scope of this chapter to summarize the entirety of the loss of control related work presented in these forums, which includes many new concepts for pilot training, aircraft modeling, flight deck displays, and loss of control prediction and mitigation.

As part of the NASA VSST Project, a class of loss of control events associated with the pilot's attempt to tightly control the aircraft, often in response to some triggering event in the environment for example, turbulence or severe crosswinds, or changing aircraft dynamic response, for example, flight control system failures or unexpected transitions, was addressed in work reported herein that was conducted for NASA Armstrong Flight Research Center. While these incidents do not typically generate the same attention associated with upset loss of control events, a recent review conducted by the FAA found that pilot-vehicle system loss of control in the form of pilot-induced oscillations (PIO) continues to be a persistent problem in transport category aircraft often resulting in significant hull damage, injuries, and, more rarely, fatalities [4]. The result of the program is the Smart Adaptive Flight Effective Cue or SAFE-Cue system that is the focus of this chapter.

9.1.2 The Promise of Adaptive Control

Work in the area of learning neural networks for adaptive flight control was conducted by NASA as part the Integrated Resilient Aircraft Control and precursor programs [5,6,7,8,9]. Initially, an indirect adaptive control system was constructed and tested onboard a NASA F-15 research aircraft. This system consisted of a multilayer perception pre-trained neural network, online stability and control derivative identification, a dynamic cell structure online learning neural network, and a model-following control system based on the stochastic optimal feedforward and feedback technique [5]. This approach is "indirect" in that the plant model itself was updated in near real time with updated stability derivatives. Generally, indirect adaptation approaches include parameter update laws that are driven by model estimation errors whereas direct adaptation approaches are driven by controller tracking errors. In a piloted simulation, this adaptive online learning approach showed improvement in flying qualities as compared to a non-learning system.

The second generation of the above system consists of a direct adaptive learning neural network [7]. This system does not require any parameter identification and does not require knowledge of the nature or extent of the system change, that is, failure, or any uncertainty. The general control scheme of the so-called Gen 2 controller was based on an adaptive neural controller that cancels errors associated with the dynamic inversion of the model. Simulation results [7] showed neural network augmentation of the controller improves performance with aerodynamic and control surface failures in terms of tracking error and cross-coupling reduction.

In the mid-90's, Barron Associates led control design work for a series of Variable Stability In-Flight Simulator Test Aircraft (VISTA) F-16 flight tests that provided one of the first piloted validations of adaptive control where an adaptive controller was compensating for unforeseen control effector impairments as well as for changes in vehicle stability characteristics. Flight testing culminated in a smooth landing in a crosswind with a disabled, floating horizontal tail surface and destabilizing airframe effects consistent with what would be experienced with a missing control surface [10]. Barron Associates built on this success in the Retrofit Reconfigurable Control System program that demonstrated the ability of an adaptive system to recover the nominal handling qualities of an aircraft after an in-flight failure or damage. In piloted simulations, Boeing and Navy flight crews provided handling qualities rating (HQR) assessments for in-flight refueling, target tracking, and general maneuvering. The pilots stated that the nominal F/A-18 is an HQR 1 to 2 aircraft. Under aerodynamic surface failures, the production flight control system without the retrofit system performed poorly, receiving HQRs of 5 to 7. With the retrofit system in place, the ratings increased by 1/2 to 1 HQR point. A series of four successful flight tests were completed in 2006 at Patuxent River NAS [11].

Liu, Tang, and Tao from the University of Virginia and Joshi from NASA Langley [12] developed a method for adaptive failure compensation using asymptotic state tracking. The work focused on control failures, that is, rudder or aileron failure. If several control surfaces fail, this adaptive failure compensation scheme was shown to continue tracking a desired trajectory with a simulation model of a transport aircraft. This scheme works without knowledge of the failure or when it occurs. Simulation with a traditional fixed controller showed that control is not possible, thus some adaptive scheme was required. The addition of engine differential control inputs made

it possible for the model to continue to track the desired trajectory when failures of ailerons and rudders were present. Without the added engine control inputs, the desired tracking was not achievable.

Calise, Lee, and Sharma from the Georgia Institute of Technology [13] developed a reconfigurable flight control law for tailless aircraft using neural-networks. The advantage of this approach is the elimination of the need for parameter identification during the recovery from failures phase. The need for an accurate aerodynamic database for flight control design is significantly reduced as well. This overall approach was viewed as a direct path to reducing the cost associated with development of new aircraft. This technique was tested in a piloted simulation and also via flight test on the experimental X-36 aircraft.

The L1 adaptive control architecture pioneered by Dr. Naira Hovakimyan of the University of Illinois Urbana-Champaign is an extension of Lyapunov model reference adaptive control (MRAC) that decouples adaptation from robustness. This decoupling allows for fast adaptation while maintaining a robust system. The architecture was flown on the NASA Airborne Subscale Transport Aircraft Research (AirSTAR) system [14] and the Calspan Learjet In-Flight Simulator [15].

9.1.3 Unfavorable Pilot-Vehicle Interactions

While improvements in performance and stability in the face of failures and damage has been demonstrated with a variety of adaptive control approaches, unfavorable interactions of the human pilot with an adaptive system that can lead to loss of control have also been seen in flight test. One such example from a flight test program with the NASA NF-15B [9] is shown in Figure 9.1. Here, a roll axis PIO developed during a formation flying task with a simulated failed stabilator. Two test pilots participated in the flight test evaluations. It was noted in the reference that the PIO tendency was prevalent for one test pilot, but not to the other. This can often occur when unusual responses or nonlinearities are present. It was found that the pitch axis neural network was contributing to an unusual roll axis response.

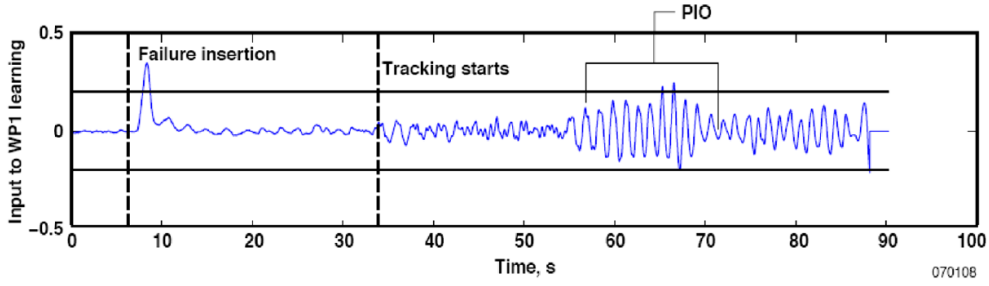

Figure 9.1: *Example Roll PIO with adaptive control system active [9].*

Depending on the nature of the failure or damage, the adaptive systems can be highly nonlinear. It is well understood that pilots perform best when the flight control system and resulting aircraft

responses are linear and predictable. Quoting earlier observations made by Graham and McRuer [16, page 1096], *Given a nonlinear system with features designed to give responses to some particular inputs or disturbances that are superior to those of a linear system, one can, with near certainty, find a foul input or disturbance that causes a very unfortunate response*. Thus, the adaptive system can improve upon the system response in the face of failures or damage; however, a human pilot can also with near certainty find a way to couple with the system in an unfavorable manner.

To reduce or eliminate these unfavorable interactions, the pilot must be provided with effective cues that: 1) indicate to the pilot that the dynamic system he or she is flying has changed, and 2) guide the pilot towards appropriate inputs. While some solutions may use a visual display warning or aural cues, these are often ignored or missed by the pilot, especially in a stressful environment. Another solution is to combine adaptive force feedback cues via the cockpit control inceptor with associated adaptive command path gain adjustments to alert the pilot of the control system adaptation and to guide the pilot towards a more predictable response.

9.2 The SAFE-Cue System

SAFE-Cue is a software system that is designed to be integrated with an existing flight control system. To use the system as intended, an active inceptor and tailored mechanizations of the software are required. The general composition of the SAFE-Cue mechanization structure is the same for both the pitch axis and the roll axis. Here, "mechanization" simply refers to the functions defining each component of the SAFE-Cue system. These component parts are briefly described in this section. The details of the component functions for the pitch and roll axis mechanizations are shown in later sections.

9.2.1 Concept Description

The SAFE-Cue system provides force feedback to the pilot via an active control inceptor with corresponding command path gain adjustments based on a measured system error between the adaptive controller response and a nominal system response [17]. The SAFE-Cue alerts the pilot that the adaptive control system is active, provides guidance via force feedback cues, and attenuates commands, thereby ensuring pilot-vehicle system stability and performance in the presence of damage or failures. While the focus herein is on an adaptive controller, the SAFE-Cue concept is completely general and can be applied to any fly-by-wire flight control system implementation to mitigate loss of control.

The adaptive controller is described in more detail in a companion paper related to this work [18]. In short, the system, as illustrated via the block diagrams of Figure 9.2, defines the magnitude of the adaptive command path gain and the intensity of the force feedback cue as a function of a pitch rate (as shown) or roll rate system error. Both systems can operate simultaneously. Thresholds on the system error are set so that there is no SAFE-Cue activity below these values. Above the threshold, the adaptive gain and force cue activate. The thresholds for the gain and force cue engage independently. The resulting force cue is a combination of a gradient-based force that approximates an effective feel system spring gradient change and a viscous friction-like force that is a function of the velocity of the inceptor motion as described further in Chapter

10 and [19]. There is only one nominal system model, so when the gain and force are both engaged, the input to the nominal system for the inceptor force feedback loop is $\delta_c^{'}$.

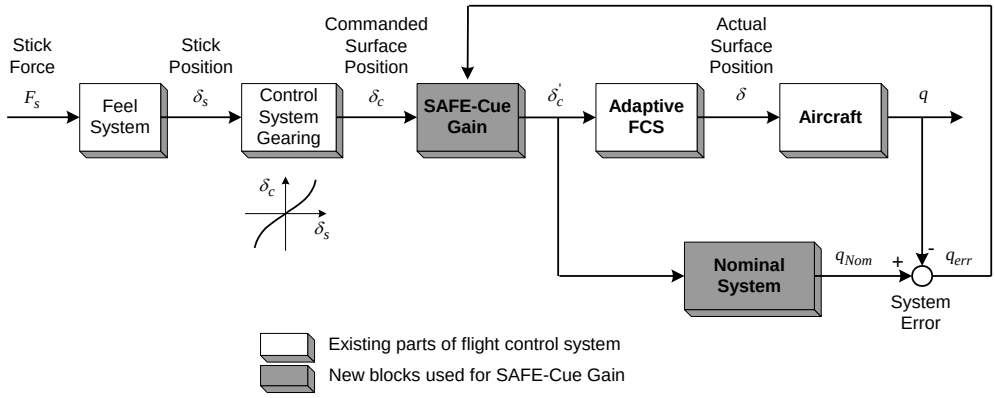

(a) Adaptive command path gain

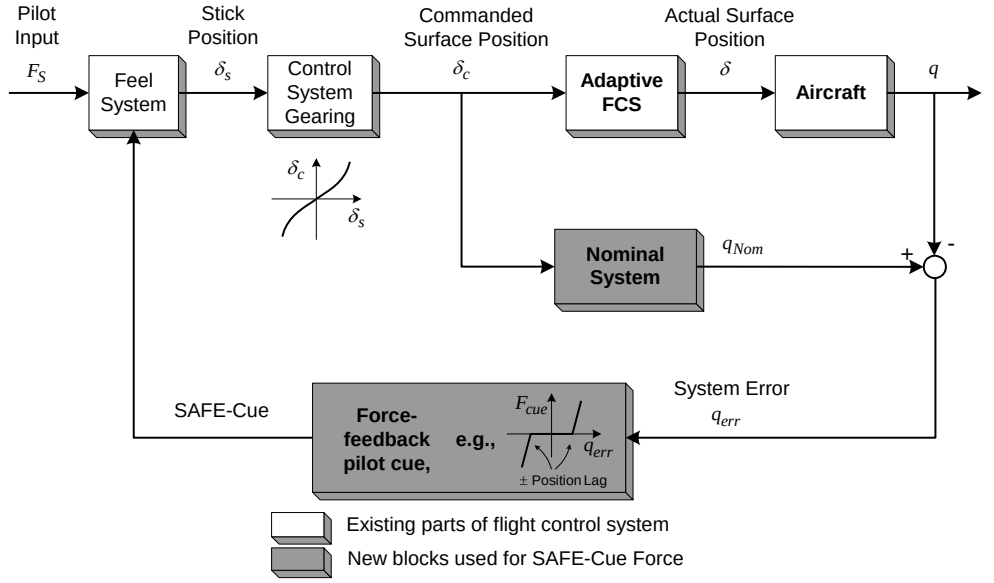

(b) Active force feedback cue

Figure 9.2: *SAFE-Cue system block diagrams.*

9.2.2 The SAFE-Cue Force

The SAFE-Cue Force mechanization combines a coulomb friction force, effectively acting as a viscous friction force, and a gradient force, or restraining force, which are comprised of three distinct structures or functions that are combined to form the total force cue sent through the inceptor and to the pilot. Further details regarding the creation of the combined force is provided in Chapter 10. These include structures for the magnitude of the friction force, a gain dictating the sign of the friction force, and the gradient force. The magnitude of the friction force and the gradient force are directly dependent on the system error, q_{err} or p_{err}, and are activated when the system error exceeds a prescribed threshold, which is not necessarily the same for the two components. The gain determining the sign of the friction force is a function of the cockpit inceptor velocity.

The original functions for the mechanization [17,19] have a linear relationship between the input and output for each structure. To add more versatility to the structures, the functions are generalized to a simple nonlinear equation in which the special case forms a linear function. Furthermore, several gains are added to the original equation for the total force cue to allow for quick manipulation of the magnitudes of the forces without manipulating the individual structures at a lower level.

This and the various other parameters that define the individual structures can be changed independently to create force cues that feel distinctly different to the pilot. This allows the engineer to create forces that are either friction force dominant, gradient dominant, or a balance of the two, whether they are complementary or antagonistic to each other. It was found in earlier studies [19, 20] that a balanced blending of the two mitigated the shortcomings and bolstered the benefits of each.

9.2.3 The SAFE-Cue Gain

The SAFE-Cue command path adaptive gain mechanization is comprised of one distinct structure or function that calculates the gain applied to the stick position input by the pilot [19]. The magnitude of the command path gain is directly dependent on the system error and is activated when the system error exceeds a prescribed threshold. The command path gain is then reduced until it reaches a prescribed minimum value. As for the structures defining the components of the SAFE-Cue force, the structure for the command path gain was also generalized to add versatility by including the option of a nonlinear function, and the parameters defining the structure can be manipulated to change the characteristics of the resulting system “feel.”

9.3 Method of Test

9.3.1 Indirect-Adaptive Controller

The adaptive controller used throughout the development and testing of the SAFE-Cue mechanizations was the Receding Horizon Optimal/Modified Sequential Least Squares (RHO/MSLS) algorithm [18] that was developed by Barron Associates, Inc. and is comprised of

a time-varying model of the current system dynamics using online parameter identification. It is robust to adverse conditions, low excitation, or correlated inputs. The identified model of the current system dynamics is used by the online control design module to predict future system states. Based upon this knowledge, the control design module computes a set of effector commands that will achieve stable responses that approach the desired responses as near as possible. This controller was selected as a representative adaptive system because of its past flight test successes [10,11]. Integration of other adaptive approaches with SAFE-Cue would require separate verification.

9.3.2 Test Aircraft Description

The flight test sorties were conducted in the Calspan Corporation Learjet 3 variable stability in-flight simulator shown in Figure 9.3. Details of the Calspan Learjet aircraft were provided in Chapter 8.

Figure 9.3: *Calspan Learjet 3 in-flight simulator (photo courtesy of Calspan Corporation).*

9.3.3 Checkout Flights

Three checkout flights were scheduled to evaluate the integration of the adaptive controller and the SAFE-Cue system into the variable stability system (VSS) in the Learjet In-Flight Simulator. The flights were conducted on March 14, March 15, and April 10, 2013, see Figure 9.4.

9.3.3.1 Baseline Configurations

In preparation for the formal flight test evaluations, three checkout sorties were conducted. The first flight assessed the baseline adaptive controller and associated failure scenarios, while the second and third flights focused on tuning of the SAFE-Cue mechanization parameters. Frequency sweeps were conducted to verify the dynamic characteristics of the baseline (BL) aircraft. The resulting pitch and roll axis frequency responses are shown in Figure 9.5(a) and Figure 9.6(a), respectively. Lines indicate transfer function fits (solid for magnitude and dashed for phase) to the resulting fast Fourier transform frequency response data (circles for magnitude and squares for phase). Only high coherence data points are shown, that is, coherence values of 0.66 or higher, where perfect linear correlation yields a coherence of 1.

Figure 9.4: *Calspan Learjet 3 readied for checkout flights (left), evaluation pilot (right).*

The frequency responses shown here were used to compute Airplane Bandwidth criteria parameters that were then compared against the latest handling qualities and PIO boundaries [21]. In Figure 9.5(b) the resulting pitch attitude criteria parameters are plotted against the up-and-away tracking requirements that were developed for tactical aircraft [22]. In the figure, the red lines represent the boundaries for Level 1, 2, and 3 handling qualities. The thicker blue lines, on the other hand, represent the PIO boundaries. The no PIO region is bounded in phase delay by the light blue line at 0.09 s and bandwidth frequencies above 1 rad/s. For bandwidth frequencies below 1 rad/s and phase delays below 0.09 s, moderate PIO is possible if the frequency domain pitch rate overshoot parameter, $\Delta G(q)$, is greater than 12 dB. As defined in [21,22], this parameter represents the frequency domain droop between the phugoid and short period mode as measured on a Bode plot. In the region between the phase delay values of 0.09 s and 0.14 s, moderate PIO is possible if the associated flight path bandwidth frequency is below 0.75 r/s. Note that this parameter is computed separately as defined in [22] and is not shown here. Finally, severe PIO is possible for phase delay parameters above 0.14 s as defined by the dark blue boundary. When using these boundaries, parameters are computed with the feel system excluded. Pitch attitude bobble are undesirable motions, not out of phase oscillations, that can occur when the pitch rate overshoot parameter is greater than 9 dB. Using these tracking task boundaries designed primarily for tactical aircraft because of limited availability of data for transport category aircraft, the baseline configuration is predicted to have a Level 2 handling qualities, but with no PIO susceptibility. In flight, the pilots found the pitch response to be desirable, a Level 1 transport category airplane, for the tracking task used herein.

For the roll axis bandwidth frequency and phase delay requirements, the red lines again define the handling qualities levels, while the thicker blue lines define the PIO tendency boundaries. Unfortunately, there are even fewer transport category supporting data for roll. Nonetheless, the baseline aircraft model was predicted to have borderline Level 1/Level 2 handling qualities, as shown in Figure 9.6(b), with no PIO susceptibility given that the control sensitivity was not too high. This prediction was verified in flight with the pilots, in general, finding the baseline roll response to be Level 1 as shown later in this chapter.

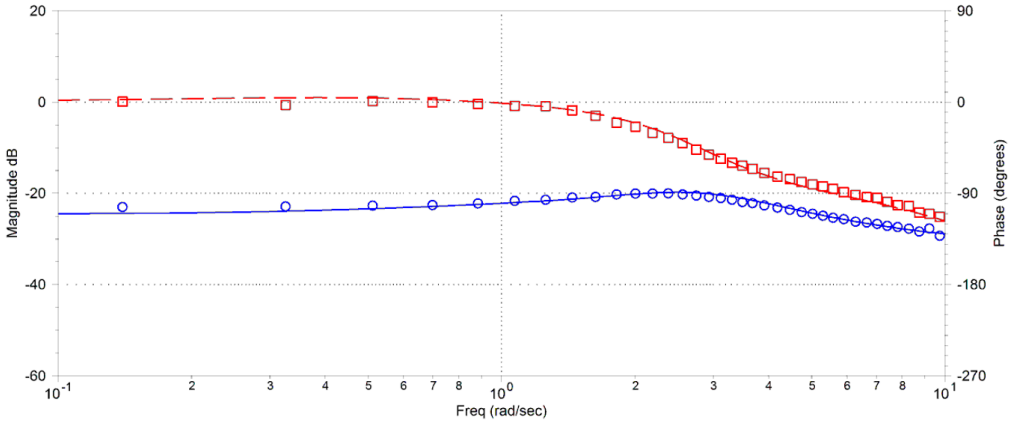

$$\frac{q}{\delta_{LON}} = \frac{-211.8(0.5328)(2)^2(7.5)}{(0.7646)(1.184)[0.5149, 2.833][0.7071, 88.61]} e^{-0.13s}$$

(a) Pitch rate to longitudinal stick position Bode plot

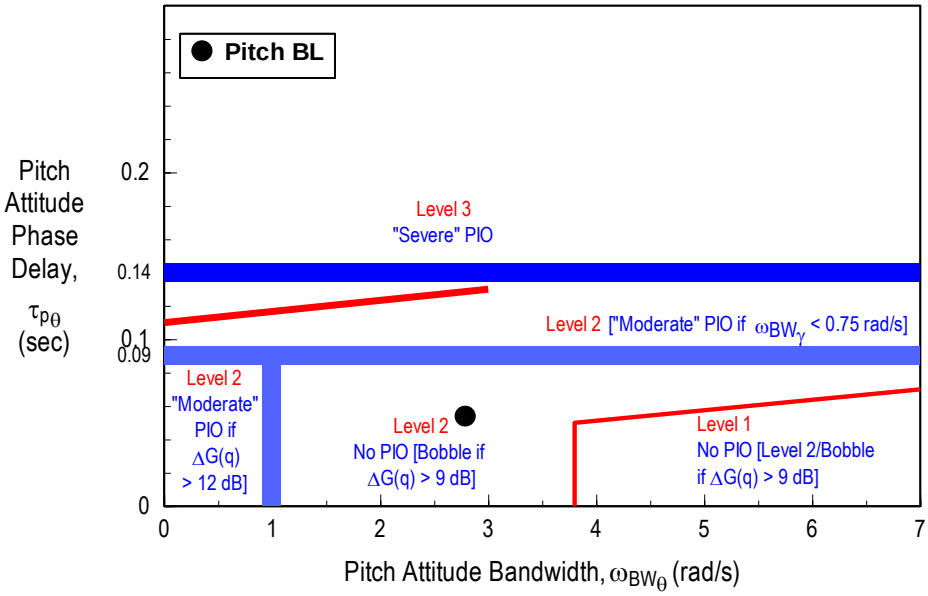

(b) Pitch attitude bandwidth

Figure 9.5: *Pitch axis baseline aircraft configurations.*

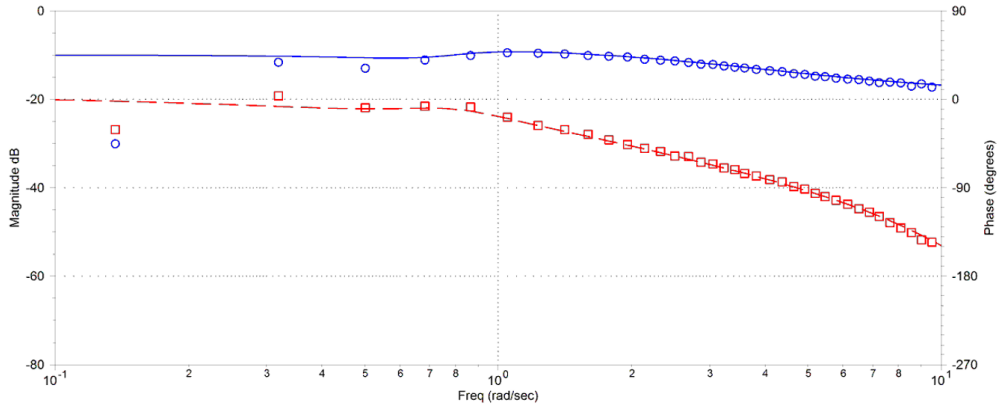

$$\frac{p}{\delta_{LAT}} = \frac{231(0)[0.3813, 0.7524](7.5)}{(0.004153)[0.3983, 0.8186](2.379)[0.7, 44]} e^{-0.19s}$$

(a) Roll rate to longitudinal stick position Bode plot

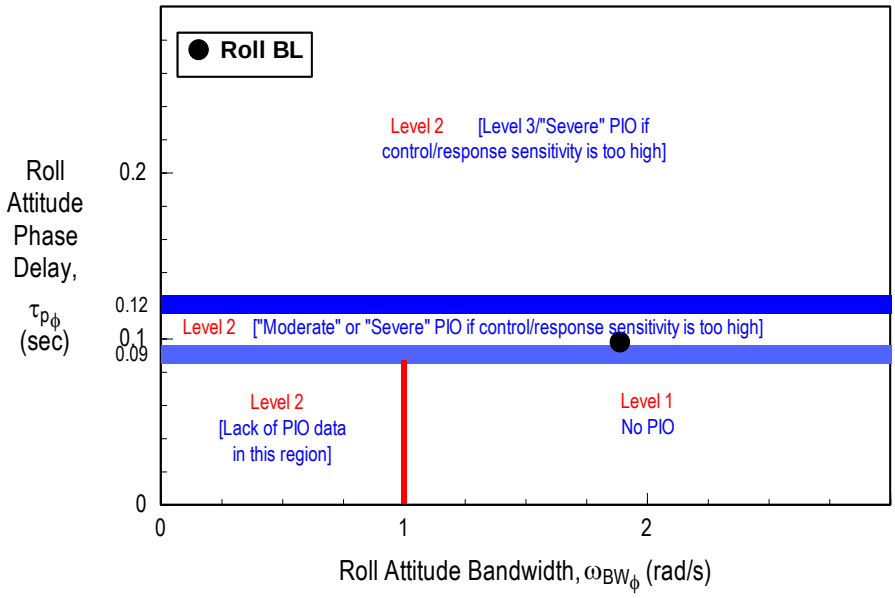

(b) Roll attitude bandwidth

Figure 9.6: *Roll axis baseline aircraft configurations.*

9.3.3.2 Failure Conditions

The goal in the checkout flight process was to create a pitch axis configuration that exercised the adaptive controller and was rated as a Level 2/Level 3 handling qualities aircraft. The failure used through the checkout flight was an elevator effectiveness reduction to 75% and a rate limit of 15 deg/sec. The failure selected for use in the remaining checkout flights and formal flight tests featured a reduction in elevator effectiveness from 100% effective to 75% effective and a reduction in control surface rate limit from 60 deg/sec to 15 deg/sec.

As part of the checkout flights, the pilot was also exposed to several roll axis failure scenarios. As with the pitch axis, the goal was to create a configuration that exercised the adaptive controller and was rated as a Level 2/Level 3 handling qualities aircraft. The failure first explored was an elevator effectiveness reduction to 75% and a rate limit of 30 deg/sec. This rate limit was found to be too low, aircraft controllability was found to be in question, so a value of 40 deg/sec was assessed and selected instead. The failure selected for use in the remaining checkout flights and formal flight tests featured a reduction in elevator effectiveness from 100% effective to 75% effective and a reduction in control surface rate limit from 100 deg/sec to 40 deg/sec.

9.3.4 SAFE-Cue Mechanizations

From the remaining checkout flights, two SAFE-Cue gain configurations and two force configurations for both longitudinal and lateral-directional axes were selected for the formal evaluation flights. The selected longitudinal configuration parameters are illustrated in Figure 9.7 and lateral-directional configurations in Figure 9.8. Note that these are used to create the SAFE-Cue mechanizations and do not reflect the baseline feel system characteristics. For both the pitch and roll axes, the Learjet center stick had a feel system natural frequency of 20 rad/s and a damping ratio of 0.7. The baseline pitch axis feel system gradient was 7.0 lbs/in, while the roll axis feel system gradient was 5.65 lbs/in.

The friction force consists of a gain that is a function of the stick velocity and a force that is a function of the system error. For the longitudinal axis cases, the G2 gain modified case and F2 force modified case were identified during the evaluation flights. Originally, both longitudinal friction force gains were the same as a function of stick velocity. The modification of F2 brought in the friction force gain more aggressively and resulted in an improved result for the last test pilot. There was no change in the F2 force as a function of the system error, only the gain. The gradient force component was the same for all longitudinal configurations. No such modifications were made in the lateral-directional axis following the checkout flights. For the lateral-directional axis, the friction force gain was the same for both configurations.

The primary differences between all configurations were in how rapidly the force or gain was applied as a function of the pitch rate (q_{err}) or roll rate (p_{err}) system error defined earlier in Figure 9.2. For the longitudinal gain configurations, the minimum gain reduction allowed also varied between a value of 0.5 (50% instantaneous gain reduction) and 0.25 (75% instantaneous gain reduction). Note that a gain term, not shown here, was also applied to the resulting combined friction plus gradient force to produce the resulting SAFE-Cue force that was presented to the pilot.

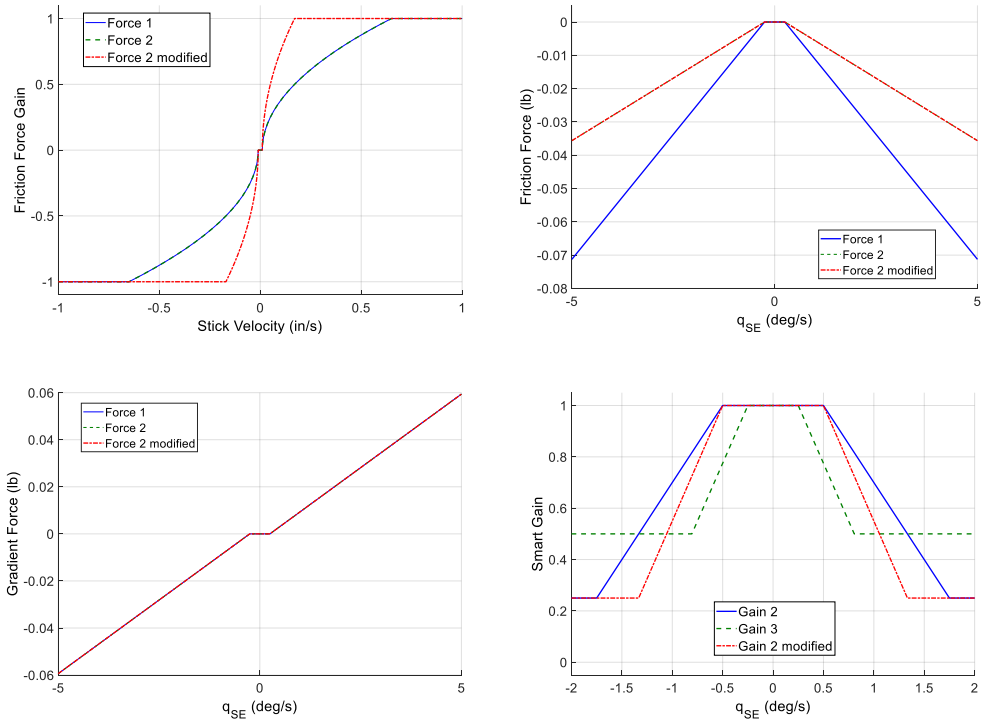

Figure 9.7: *Longitudinal axis mechanizations.*

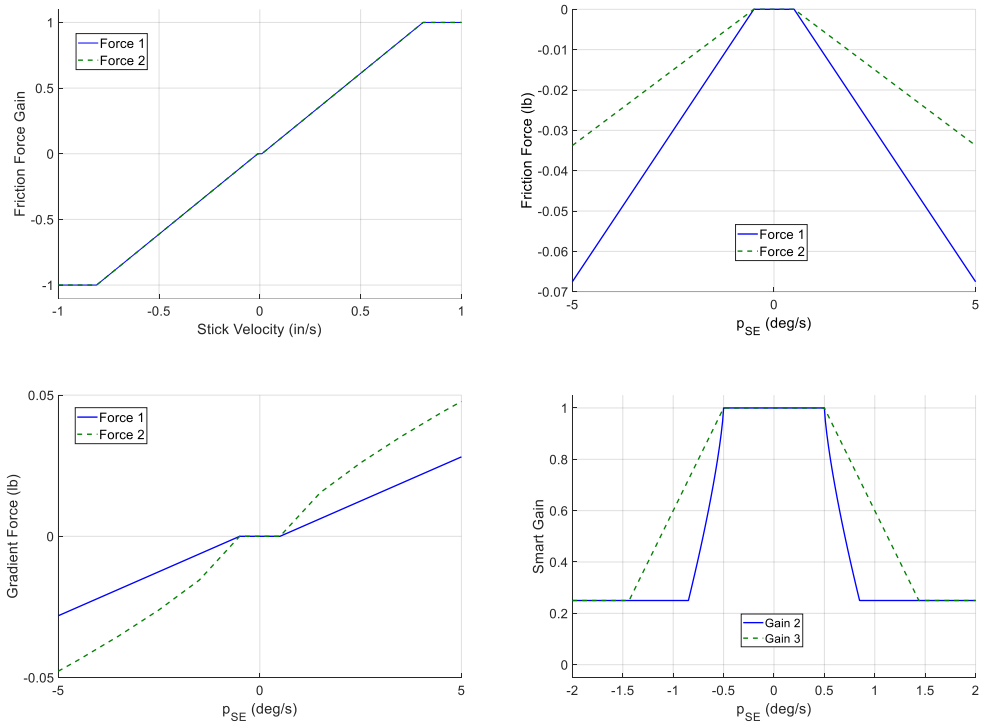

Figure 9.8: *Roll axis mechanizations.*

9.3.5 Evaluation Flights

All flight test sorties originated from the Calspan facility at the Niagara Falls International Airport in Niagara Falls, NY. Evaluations maneuvers were conducted in the MISTY Military Operations Area (MOA) special use airspace along the southern shore of Lake Ontario at an altitude of 15,000 ft and an airspeed of 250 KIAS (see Figure 9.9). The duration of each sortie was just under 2 hours with approximately 1.5 hours of evaluation time. While ratings and comments were taken in both flights, the first flight was considered a familiarization flight as described in an earlier section. In this sortie, the pilots were given verbal descriptions of the various configurations as they were introduced. The second flight featured “blind” evaluations, that is, the pilot had no knowledge of the various configurations as they were introduced. Three test pilots served as evaluators herein referred to as Pilot A, Pilot B, and Pilot C. Sorties for Pilot A were flown on Saturday, April 13. His second flight was cut short due to an aircraft mechanical issue. Flights for Pilot B were flown on April 17, while Pilot C completed his flights on April 18.

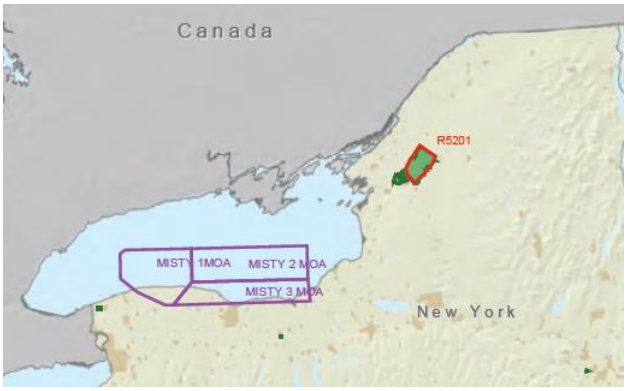

Figure 9.9: *MISTY Military Operations Area (MOA).*

(a) Pilot A *(b) Pilot B* *(c) Pilot C*

Figure 9.10: *Evaluation pilots in the Learjet.*

9.3.6 Evaluation Tasks

9.3.6.1 Pitch and Roll Sum-of-Sines Tracking

Tracking a computer-generated command signal produces a highly repeatable, precise task from which measures of pilot performance and handling qualities can be obtained. Figure 9.11 shows time histories for the pitch and roll attitude command signals. The task time for both command sets is 78 seconds consisting of the following: 10 seconds of warm-up (non-scored time); 63 seconds of scoring time; and 1.25 seconds of cool-down (non-scored time). The cool-down time was 5 seconds in the flight test. The form of the sum-of-sines command is as shown in the following equation with parameters defined in Table 9.1:

$$X_c = \sum_{i=1}^{n} A_i \sin\left(\omega_i t + \phi_i\right) \tag{9.1}$$

Table 9.1: *Sum-of-sines command signal parameters.*

Sine-wave No.	Pitch Attitude A_i (deg)	Pitch Attitude No. Cycles	Pitch Attitude ω_i (r/s)	Roll Attitude A_i (deg)	Roll Attitude No. Cycles	Roll Attitude ω_i (r/s)
1	-1	2	0.19947	-8	3	0.2992
2	1	5	0.49867	-8	4	0.39893
3	1	9	0.8976	8	7	0.69813
4	0.5	14	1.39626	4	18	1.79519
5	-0.2	24	2.39359	-1.6	30	2.99199
6	0.2	42	4.18879	-1.6	40	3.98932
7	-0.08	90	8.97597	0.64	70	6.98131

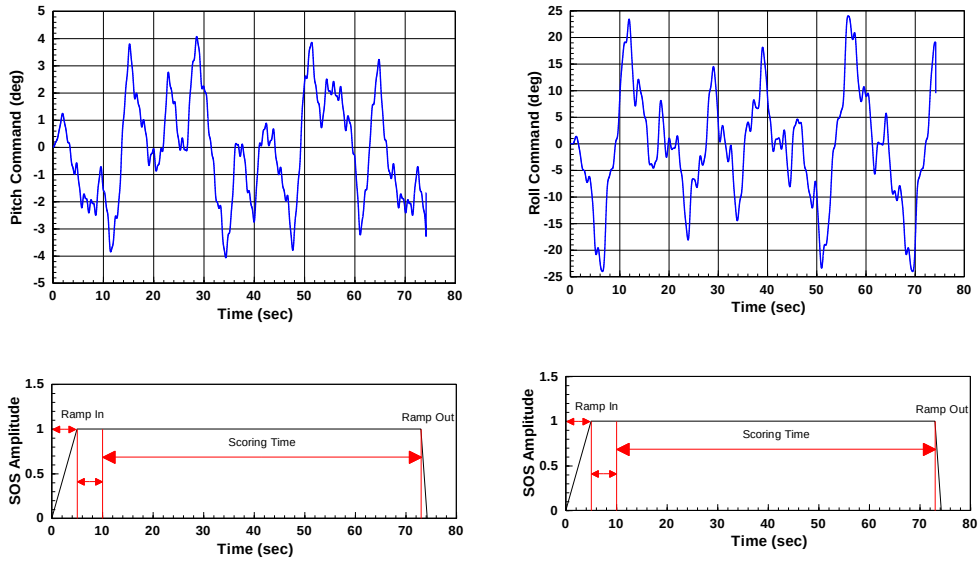

Figure 9.11: *Pitch and roll attitude Sum-of-Sines (SoS) command signals.*

9.3.6.2 Task Description

The pitch and roll attitude sum-of-sines tracking tasks are defined by the following objectives, description, and performance requirements. The desired and adequate performance requirements

for the roll axis differ from the pitch axis because of the significantly larger maximum command amplitudes in the roll axis, that is, ± ~4° in pitch versus ± ~24° in roll.

Task Objectives:

- Evaluate handling qualities in a tight, closed-loop tracking task.
- Evaluate feel system and control sensitivity characteristics.
- Identify bobble or PIO tendencies.

Description:

Aggressively track the displayed pitch or roll tracking signal, the orange command bar on the Learjet head down display shown in Figure 9.12, and attempt to keep errors within the specified tolerances. For pitch evaluations, the green reticle on Learjet head down display had a radius of ±2°, which gave the pilots a direct reference to perceive adequate performance, while desired performance was estimated. For roll evaluations, the "hats" at the end of the orange command bar produced a 7° angle with the center "dot" of the command bar. Thus, the pilots could use the green bar, which displayed the actual roll attitude, to estimate performance. Desired performance was represented by roll attitudes that remained just below the tip of the command bar "hats," while adequate performance was estimated by roll attitudes that remained just above the command bar "hats." The pilot thus attempted to minimize the attitude error represented by the difference between the command bar and actual aircraft attitude.

Pitch Desired Performance:

- ±1° in pitch 50% of the time.
- ±5 kts deviation in airspeed.

Roll Desired Performance:

- ±5° in roll 50% of the time.
- ±5 kts deviation in airspeed.

Pitch Adequate Performance:

- ±2° in pitch 50% of the time.
- ±10 kts deviation in airspeed.

Roll Adequate Performance:

- ±10° in roll 50% of the time.
- ±10 kts deviation in airspeed.

(a) Learjet head-down pitch tracking display

(b) Learjet head-down roll tracking display

Figure 9.12: *Attitude tracking task displays.*

9.3.7 Procedures

The first flight for each pilot was a familiarization flight in which the pilot was methodically led through the baseline configuration, the failure scenario, and the SAFE-Cue mechanizations for each axis. The flight test engineer explained what the pilot could expect before each run including how the SAFE-Cue system would affect the pilot. The pilot was asked to give a handling qualities rating (HQR) and a pilot-induced oscillation rating (PIOR) after each run and could request a repeat of the case if needed. The second flight of the evaluation was a 'blind' test. The baseline configuration, failure only case, and SAFE-Cue mechanizations were randomly ordered for each axis. The pilot was asked to fly and rate each without knowledge of the aircraft configuration or the SAFE-Cue mechanization. As before the pilot could request to redo a case if needed.

9.4 Flight Test Results

9.4.1 Pilot B Assessments

When conducting the flight evaluations with Pilot B, it was clear that he had an adverse physiological response with typical motion sickness symptoms to the pitch tracking tasks, which then impacted the roll tracking tasks that followed. This is illustrated herein via a direct comparison with Pilot C. When examining the pilot stick force inputs and the resulting bank angle responses of Figure 9.13 and Figure 9.14, differences between the two cases are clearly seen. Beginning with Pilot C, continuous control inputs of varying frequencies are seen with peak amplitudes between ±5 lbs. The resulting roll angle response reflects the tracked sum-of-sines input. For Pilot B, on the other hand, the time series reveal a much different pilot command, a "bang-bang" command that fixates on a single frequency and grows in intensity as the run progresses with peak magnitudes of ±10 lbs. The resulting bank angle response reflects the sum-of-sines command but with significant oscillations that persist throughout the run. The magnitude of these oscillations varies from ±5° to ±10°. With this piloting technique, all configurations tended to look the same to the pilot, and this was reflected by mostly similar pilot ratings. Therefore, the quantitative results for Pilot B should be interpreted with caution.

9.4.2 Task Performance

Each evaluation run started with the baseline configuration in pitch or roll. The failures were introduced approximately 20 seconds after the start of the tracking tasks (10 seconds into the scoring time). On the plots included herein, the solid red vertical lines indicate the task scoring time and the red dashed line indicates the failure insertion time. The solid line indicates the achieved pitch attitude/bank angle, while the dashed line indicates the SOS pitch attitude/bank angle command.

Task performance figures are shown in Figure 9.15 for four Pilot C example configurations in pitch: linear failure (LF, 75% control surface effectiveness), nonlinear failure (NLF, 75% control surface effectiveness + control surface rate limit of 15 deg/sec), Gain 2 (G2), and Gain 2 Force 1 (G2F1). Note that with the linear failure case, the RHO/MSLS adaptive controller restores aircraft performance such that it is not differentiable to the pilots when compared to the baseline [18].

There is a drastic difference between the pilot's performance with the linear failure and the nonlinear failure, Figure 9.15(a) and Figure 9.15(b), respectively. With the nonlinear failure present, the pilot was unable to complete the task as the aircraft oscillations grew too large and tripped the safety system returning control of the aircraft to the safety pilot. This is reflected in the quantified performance values, that is, RMS error, percent desired, percent adequate, and overall performance) listed in these two subfigures. The two cases with SAFE-Cue system engaged, as seen in Figure 9.15(c) and (d), show nearly complete mitigation of the unfavorable characteristics of the nonlinear failure. The pilot is able to stay in the loop, perform the task, and approach and/or match baseline performance levels.

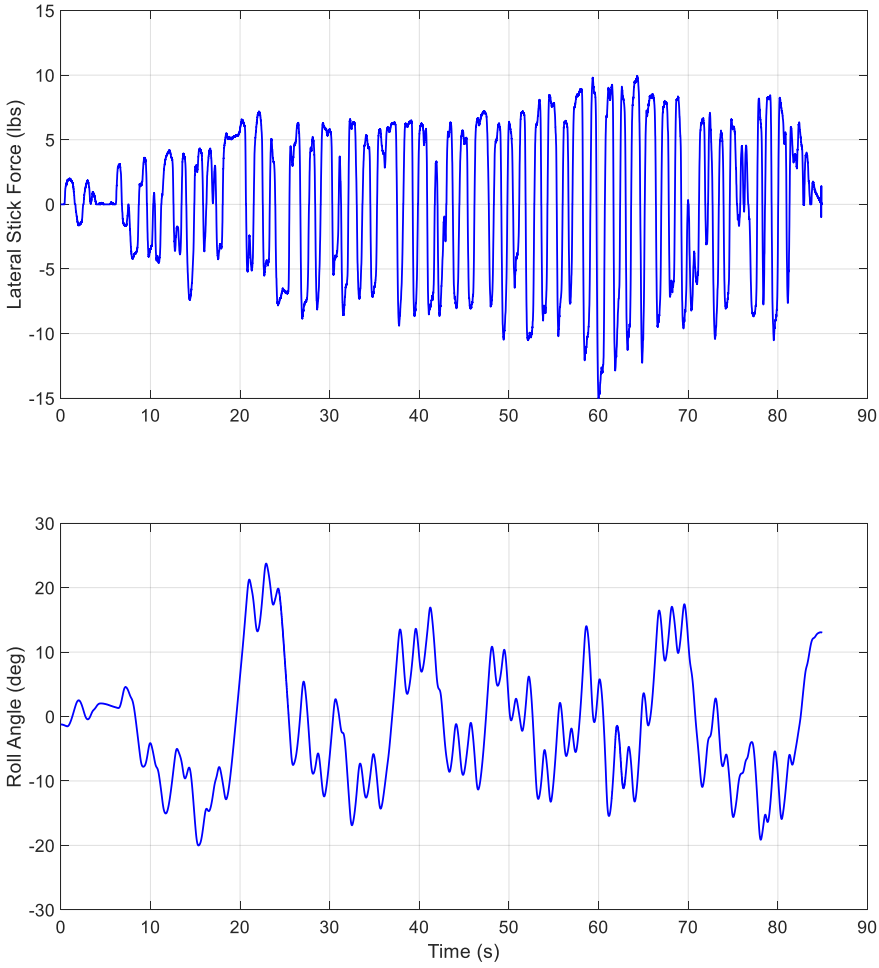

Figure 9.13: *Lateral stick force and roll angle time series for a baseline configuration run of Pilot B.*

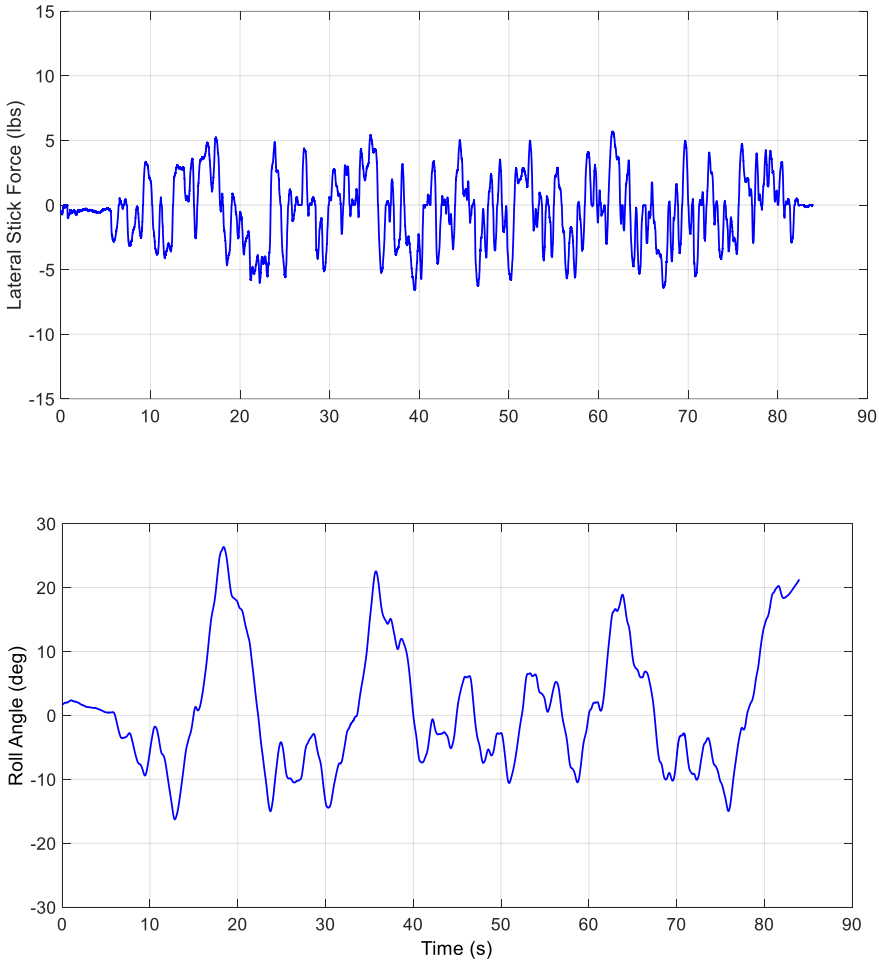

Figure 9.14: *Lateral stick force and bank angle time series for the baseline configuration run of Pilot C.*

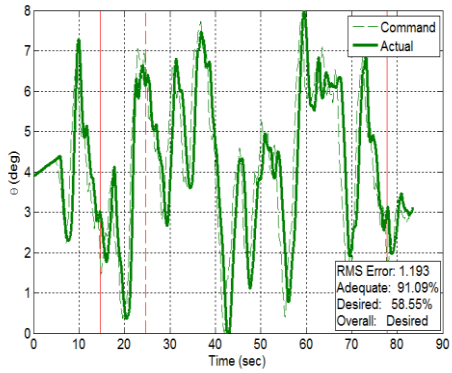

(a) Linear Failure (LF)

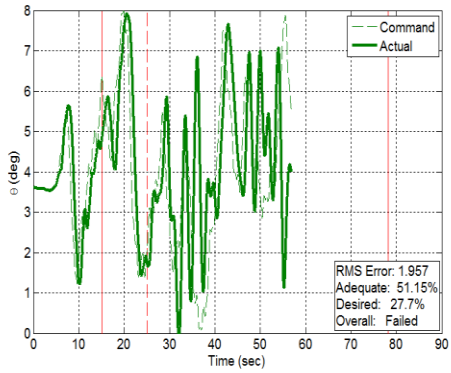

(b) Nonlinear Failure (NLF)

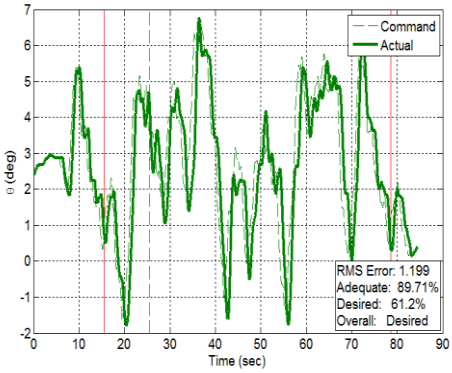

(c) Gain 2 (G2)

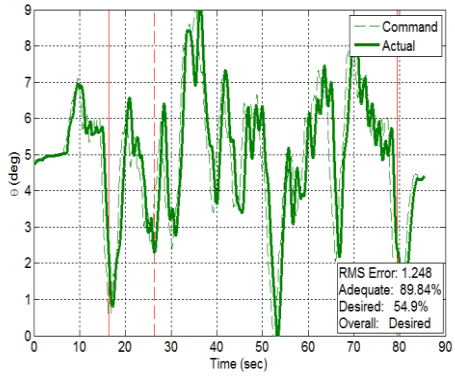

(d) Gain 2-Force 1 (G2F1)

Figure 9.15: *Pitch sum-of-sines tracking performance examples for Pilot C.*

Task performance figures are shown in Figure 9.16 for four Pilot C example configurations in roll: baseline (BL), nonlinear failure (NLF, 75% control surface effectiveness + control surface rate limit of 40 deg/sec), G2, and G2F2. As was seen in pitch, there is a drastic difference between the pilot's performance with the baseline and the nonlinear failure such that the pilot is unable to complete the task in the presence of the nonlinear failure. The two cases with SAFE-Cue system engaged, as seen in Figure 9.16(c) and (d), again show a marked improvement in performance. There are some qualitative differences between these cases and the baseline case in that the SAFE-Cue cases do not have the same level of tight control, but the quantitative values listed in the figures show that the pilot is able to approach performance levels achieved with the baseline configuration.

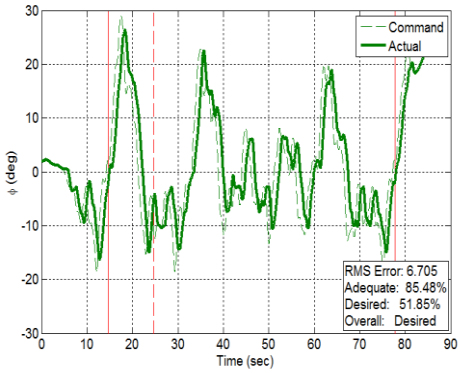

(a) Baseline (BL)

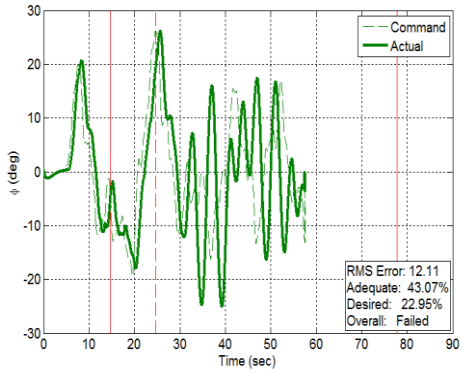

(b) Nonlinear Failure (NLF)

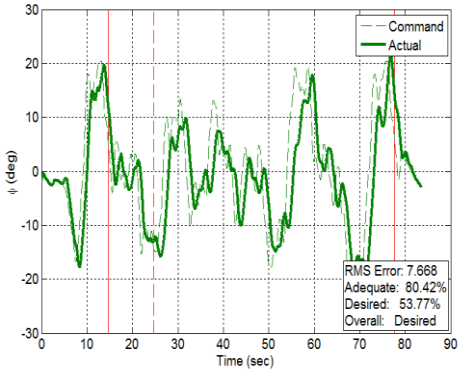

(c) Gain 2 (G2)

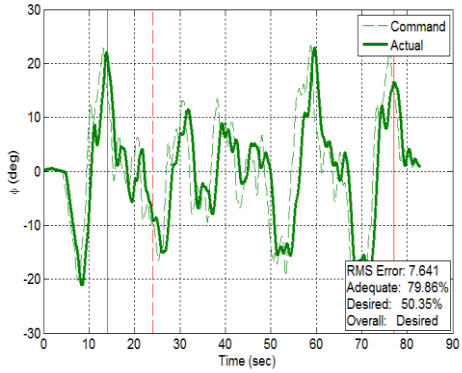

(d) Gain 2-Force 2 (G2F2)

Figure 9.16: *Roll sum-of-sines tracking performance examples for Pilot C.*

9.4.3 System Error

The system error signals for the four example Pilot C configurations in pitch (linear failure, nonlinear failure, G2, and G2F1) are shown in Figure 9.17 and Figure 9.18. For the SAFE-Cue cases, the solid horizontal lines in the time series plots indicate the threshold at which the system is engaged. Below each system error time history is its associated scalogram. The scalograms as defined in Appendix A show the wavelet-based time-varying power spectral density of the system error signal for each configuration. The scalogram as plotted is a function of frequency, time, and absolute power. The absolute power is computed as [units^2/(Hz)] but is displayed as a [units^2/(rad/s)]. A nominal or well performing configuration is one that shows little to no peaking in the resulting system error scalogram.

The system error for the linear failure case in Figure 9.17(a) is very small, barely deviating from 0 deg/s. This is expected given that baseline performance is recoverable by the adaptive controller if adequate control authority remains to do so as in the case of the reduced effectiveness failure, the linear failure. In the case of reduced effectiveness and rate limit, the nonlinear failure, the physically available control authority is inadequate for baseline performance to be fully restored, resulting in unfavorable pilot-vehicle coupling. This is seen in the system error in Figure 9.17b in which the signal oscillates between roughly ±10 deg/s. Differences in the two failure cases are reflected in the scalograms in Figure 9.17(a) and Figure 9.17(b). The peaks in the Figure 9.17(a) scalogram are almost imperceptible, whereas the peaks in the Figure 9.17(b) scalogram are very obvious and correspond to the oscillatory regions of the associated time history. The system error signals in Figure 9.18(a) and Figure 9.18(b) for the two SAFE-Cue configurations show a significant reduction as compared to the nonlinear failure configuration. The system error stays within about ±1.5 deg/s for both cases. This reduction is reflected in their scalograms, which show very small amplitude peaks that are almost imperceptible at this scale.

The system error signals for the four example Pilot C roll configurations (baseline, nonlinear failure, G2, and G2F2) are shown in Figure 9.19. Here, the system error for the baseline in Figure 9.19a is very small, almost non-existent. The measure for the nonlinear failure, on the other hand, is very large as seen in Figure 9.19b in which it oscillates between ±40 deg/s. The scalograms for these cases reflect this drastic difference in signal activity. The peaks in the Figure 9.19(a) baseline case scalogram are effectively nonexistent, whereas the peaks in the Figure 9.19(b) scalogram approach a value of 3 $(\text{deg/s})^2/(\text{rad/s})$. The system error signal for the two SAFE-Cue configurations in Figure 9.20(a) and Figure 9.20 (b) again show significant reductions in error and associated scalograms power as compared to the nonlinear failure configuration, remaining within about ±4.0 deg/s for both, 10% of the system error observed with the nonlinear failure only case. The scalograms for these two configurations are not distinguishable from the baseline given the scale set by the nonlinear failure configuration.

9.4.4 Crossover Frequency

Figure 9.21 shows example pitch and roll pilot-vehicle system frequency response comparisons for selected configurations. These plots give an indication of how the pilot was able to compensate with the SAFE-Cue system active and in the presence of the nonlinear failure compared to the linear failure or baseline system cases. Note that for the pitch SAFE-Cue example, the achieved crossover frequency [23], indicated by the open circle, nearly replicates that of the linear failure case, which as discussed previously, approximates the baseline response. Note also the -20 dB/decade slope or “k/s-like” or “integrator-like” magnitude response in both examples around the frequency region of crossover – the expected crossover model [23] result for a compensatory task. For the roll examples, this behavior is again observed; however, the crossover frequency is lower for the SAFE-Cue case. This result corresponds well with pilot opinion that desired performance was achievable with this SAFE-Cue configuration, but with added pilot compensation.

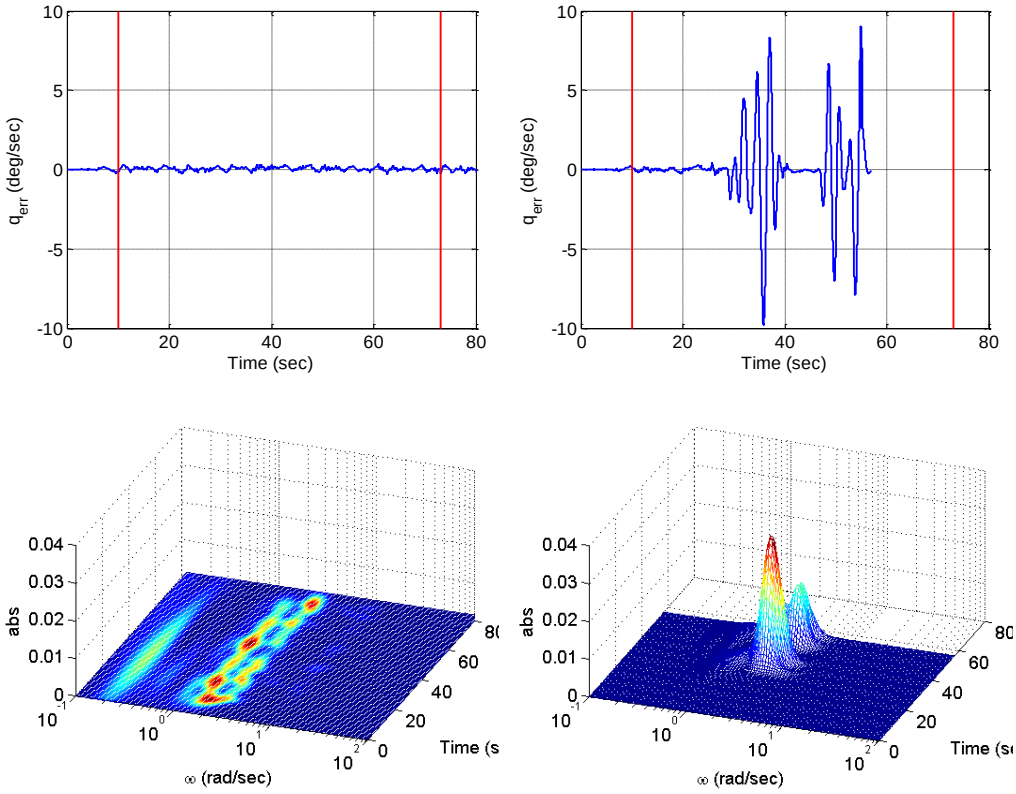

(a) Linear Failure (LF) *(b) Nonlinear Failure (NLF)*

Figure 9.17: *Pitch rate system error for Pilot C linear and nonlinear failure example cases.*

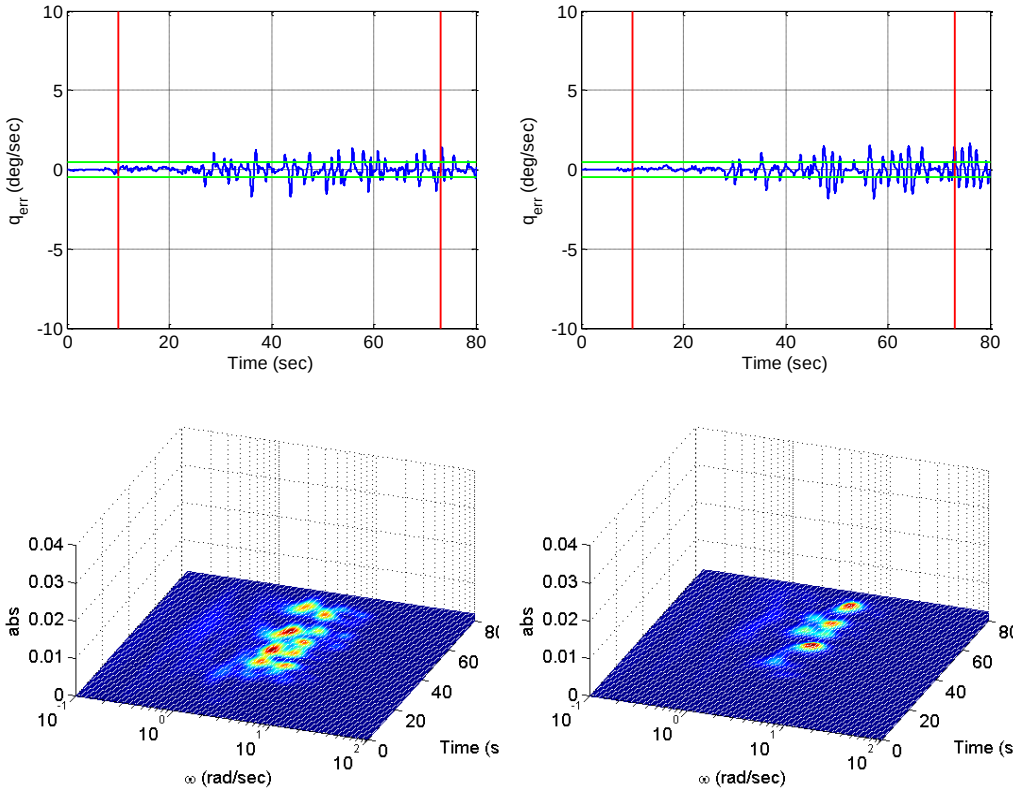

(a) Gain 2 (G2) *(b) Gain 2-Force 1 (G2F1)*

Figure 9.18: *Pitch rate system error for Pilot C SAFE-Cue example cases.*

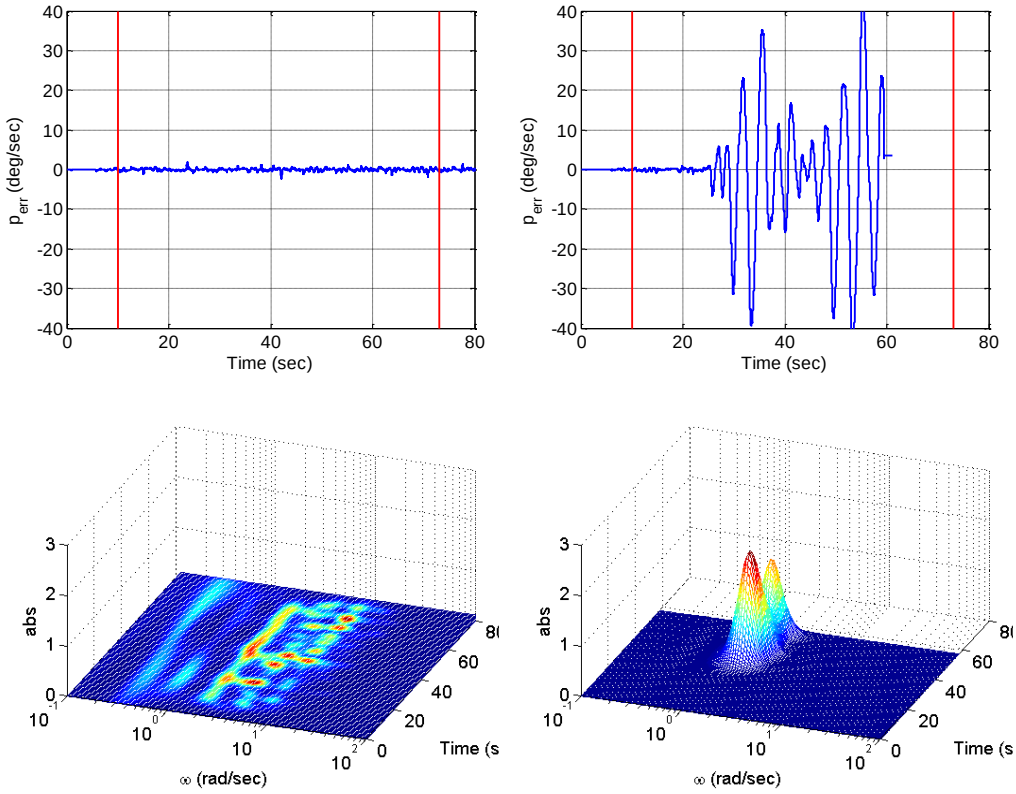

(a) Baseline (BL) *(b) Nonlinear Failure (NLF)*

Figure 9.19: *Roll rate system error for Pilot C baseline and nonlinear failure example cases.*

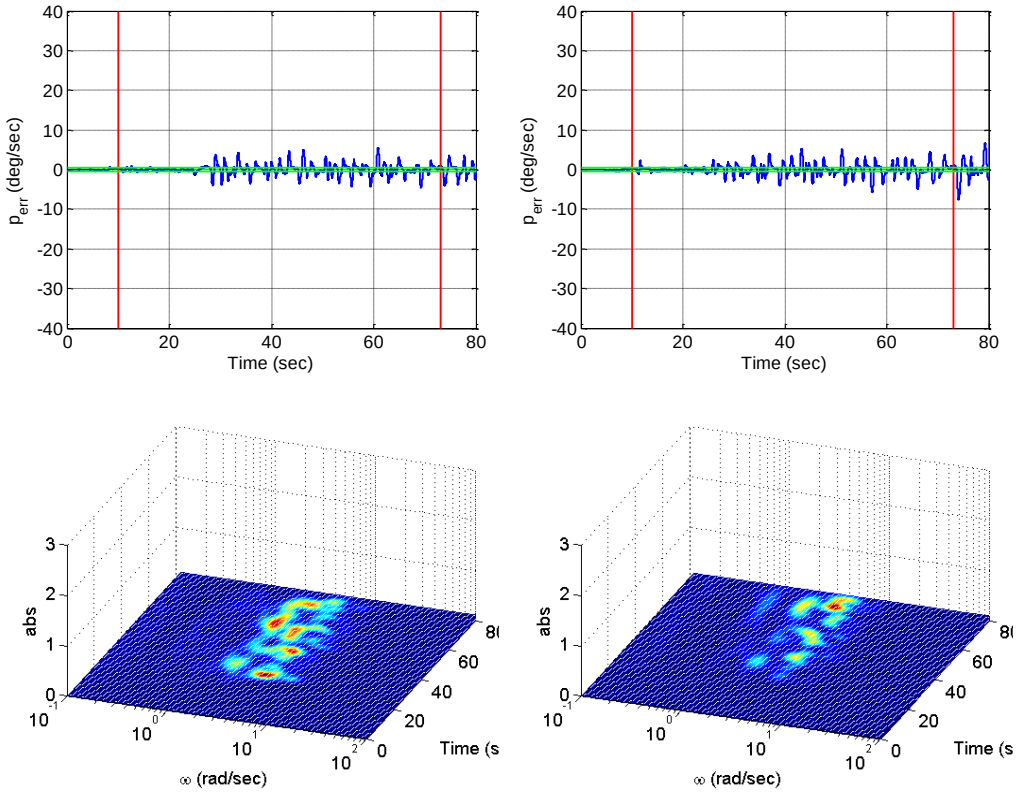

(a) Gain 2 (G2) *(b) Gain 2-Force 2 (G2F2)*

Figure 9.20: *Roll rate system error for Pilot C SAFE-Cue example cases.*

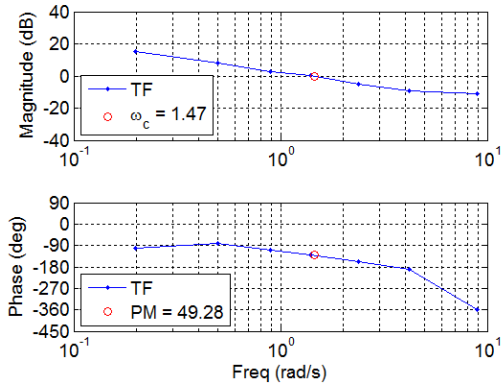

(a) Pitch Linear Failure (LF)

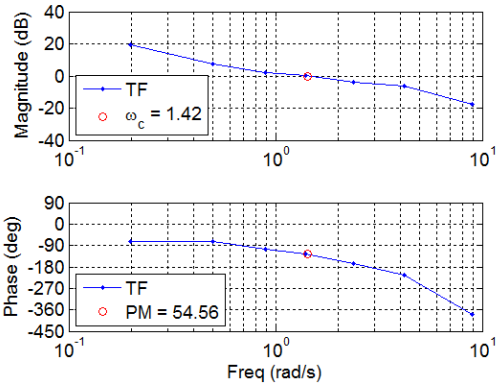

(b) Pitch Gain 2-Force 1 (G2F1)

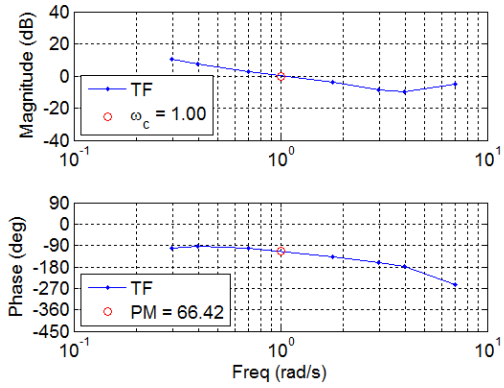

(c) Roll Baseline (BL)

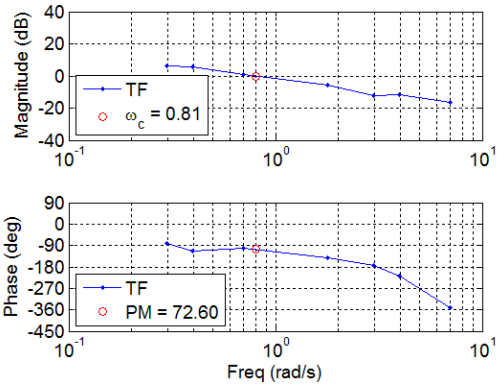

(d) Roll Gain 2-Force 2 (G2F2)

Figure 9.21: *Example pilot-vehicle system describing functions for Pilot C.*

9.5 Pilot Opinion Results

9.5.1 Pilot Ratings

Pilot ratings for the "blind" evaluation second sorties are shown in Figure 9.22(a) for pitch and Figure 9.22(b) for roll. The plots show PIO Tendency Ratings versus Cooper-Harper Handling Qualities Ratings. In this format, the best configurations migrate to the lower left, while the worst configurations migrate to the upper right. In some cases, repeat runs of selected configurations were made. Typically, these repeats were for the baseline or nonlinear failure cases and were intended to recalibrate the pilots with configurations known, to the test conductors, to have either

an expected level of handling qualities, that is, good for the baseline and poor for the nonlinear failure configurations.

For the most part in pitch (left hand side plots), the upper right is dominated by the nonlinear failure cases as expected. The lower left not only features baseline cases, but also several SAFE-Cue configurations. There were also several cases, including SAFE-Cue configurations that fell in the mid-range rating area, but for the most part these were still an improvement over the nonlinear failure cases where control was lost. The results show that for each pilot there was at least one SAFE-Cue configuration that brought about significantly improved results. Note that because of a "golden arm" technique, Pilot A never saw a configuration where the Safety Pilot took control even though clear PIO tendencies were exposed. Here "golden arm" refers to the pilot's ability to sense and avoid the impending flying qualities cliff by effectively shaping his inputs to avoid the deleterious effects of the control surface rate limiting. Thus, the highest handling qualities ratings assigned were a 5 and 6 for the two nonlinear failure only cases.

For the roll evaluations (right hand side plots), the focus should be placed on the results of Pilot C. Pilot A did not make any roll evaluations due to mechanical issues with the Learjet, and Pilot B had areas of concern with the roll task as described previously. Pilot C found that several SAFE-Cue configurations completely suppressed the oscillation tendencies of the nonlinear failure cases that without SAFE-Cue consistently resulted in loss of control. This was seen as an improvement in PIO suppression even over the baseline. In terms of handling qualities, the slower, heavier response of the SAFE-Cue configurations resulted in increased pilot compensation when compared to the baseline, but desired performance could often still be achieved.

9.5.2 Debrief Questionnaire

The pilot debrief questionnaires used in the flight test evaluations are shown in Figure 9.23 through Figure 9.26. The questionnaire results for the three pilots are shown in Figure 9.27. Note that the questionnaire results reflect the assessments of the pilots to both the familiarization flight and the blind evaluation flight. Furthermore, Pilot B felt that several cases were not tested and therefore left those responses unfilled. All three pilots favorably rated the baseline aircraft configuration with the adaptive controller. All three pilots also favorably rated the SAFE-Cue gain only cases; however, the results were stronger for the combined SAFE-Cue gain and force feedback cases. Results were more mixed when the pilots were asked to consider the addition of a cockpit display. Pilot A strongly agreed and preferred an auditory tone, while Pilot B disagreed, and Pilot C was neutral.

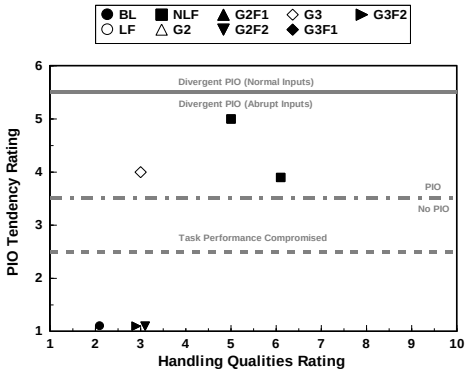

(a) Pilot A

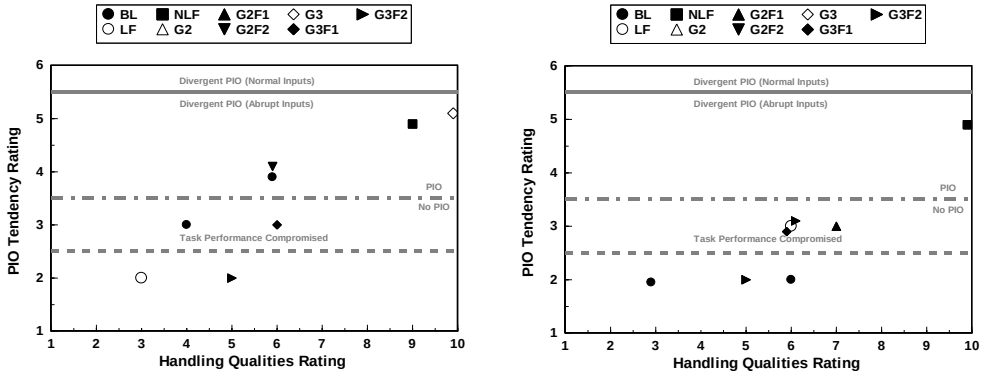

(b) Pilot B

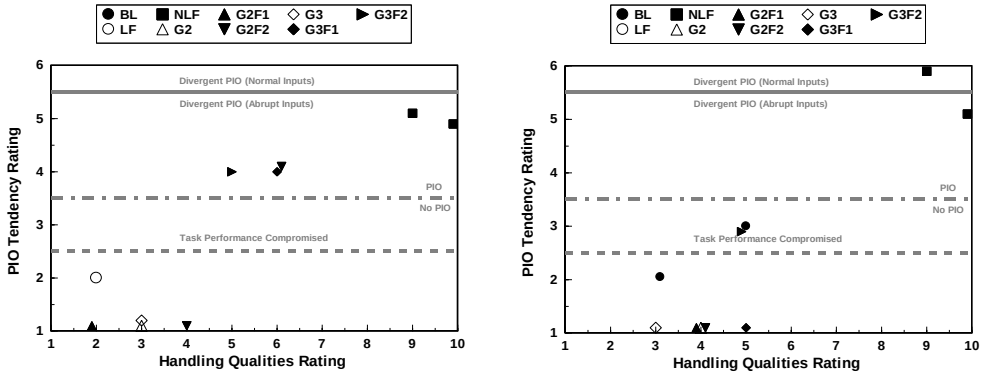

(c) Pilot C

Pitch Evaluations *Roll Evaluations*

Figure 9.22: *Pilot opinion ratings from the "blind" evaluation flights.*

	Strongly Disagree	Disagree	Neither Agree Nor Disagree	Agree	Strongly Agree
Provided representative transport aircraft response or better for the Pitch SoS task with no PIO tendencies;	○	○	○	○	○
Provided representative transport aircraft response or better for the Roll SoS task with no PIO tendencies;	○	○	○	○	○
Provided representative transport aircraft response or better for the Bank Angle Capture & Hold task with no PIO tendencies;	○	○	○	○	○
For the pitch task, the actions of the adaptive controller were non-intrusive in the absence of reduced rate and/or position limits.	○	○	○	○	○
For the roll tasks, the actions of the adaptive controller were non-intrusive in the absence of reduced rate and/or position limits.	○	○	○	○	○

Figure 9.23: *Questionnaire for baseline controller with single aisle transport aircraft model.*

	Strongly Disagree	Disagree	Neither Agree Nor Disagree	Agree	Strongly Agree
In the presence of a failure, the SAFE-Cue gain aided my ability to complete the Pitch SoS task when compared to the "failure-only" case;	○	○	○	○	○
In the presence of a failure, the SAFE-Cue gain aided my ability to complete the Roll SoS task when compared to the "failure-only" case;	○	○	○	○	○
In the presence of a failure, the SAFE-Cue gain aided my ability to complete the Bank Angle Capture & Hold task when compared to the "failure-only" case;	○	○	○	○	○
The benefits of the SAFE-Cue gain were clearly demonstrated when compared to the "failure-only" case.	○	○	○	○	○

Figure 9.24: *SAFE-Cue questionnaire for command path gain only cases.*

	Strongly Disagree	Disagree	Neither Agree Nor Disagree	Agree	Strongly Agree
In the presence of a failure, the SAFE-Cue gain and feedback force aided my ability to complete the Pitch SoS task when compared to the "failure-only" case;	○	○	○	○	○
In the presence of a failure, the SAFE-Cue gain and feedback force aided my ability to complete the Roll SoS task when compared to the "failure-only" case;	○	○	○	○	○
In the presence of a failure, the SAFE-Cue gain and feedback force aided my ability to complete the Bank Angle Capture & Hold task when compared to the "failure-only" case;	○	○	○	○	○
The benefits of the SAFE-Cue gain and feedback force were clearly demonstrated when compared to the "failure-only" case.	○	○	○	○	○

Figure 9.25: *Questionnaire for SAFE-Cue gain and force feedbcak cases.*

	Strongly Disagree	Disagree	Neither Agree Nor Disagree	Agree	Strongly Agree
A cockpit display that identified when the SAFE-Cue was active would be a helpful addition to the system.	○	○	○	○	○

Figure 9.26: *Questionnaire regarding addition of a SAFE-Cue cockpit display.*

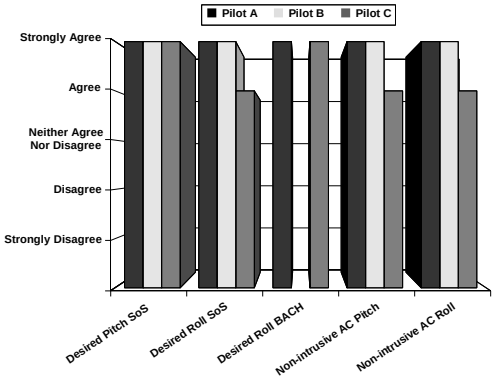

(a) Baseline Aircraft

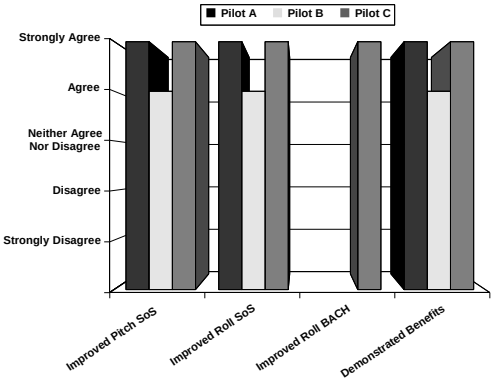

(b) SAFE-Cue Gain Only

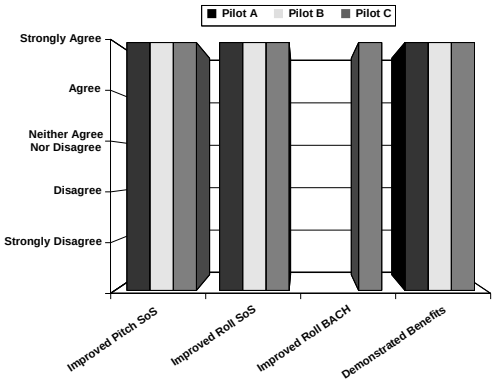

(c) SAFE-Cue Gain and Force

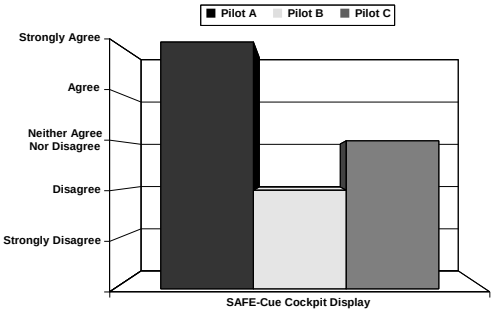

(d) Addition of a SAFE-Cue Cockpit Display

Figure 9.27: *Pilot debrief questionnaire results.*

9.6 Conclusions

The purpose of the flight test program described herein was to validate the Smart Adaptive Flight Effective Cue system or SAFE-Cue as a means to mitigate pilot-vehicle system loss of control including pilot-induced oscillations in the presence of damage/failures. The selected adaptive controller and SAFE-Cue system integrated well with the Calspan Learjet In-Flight Simulator model following system, allowing for real-time operations and on-the-fly parameter adjustments. In the presence of only the reduced control surface effectiveness, the linear failure, the adaptive controller compensated well and effectively restored near baseline configuration performance. For the reduced control surface effectiveness plus rate limiting, the nonlinear failure, Pilots B and C routinely reached a Learjet safety trip indicating loss of control, while Pilot A demonstrated a "golden arm" technique that preserved control, but nevertheless clearly exposed configuration deficiencies including increased pilot-induced oscillation tendencies.

From the task performance, system error scalograms, and crossover frequency metrics and pilot ratings and questionnaire results, there is a clear mitigating effect of the SAFE-Cue technology from which several conclusions can be drawn. In general, the pilots preferred and responded best to the linear or nearly linear SAFE-Cue mechanizations that resulted in a more predictable aircraft response. In the presence of the nonlinear failure, several gain only and gain plus force feedback SAFE-Cue configurations resulted in performance that approached that of the baseline healthy aircraft for each pilot. Finally, there were individual differences noted between pilots regarding SAFE-Cue configuration preference. A larger pilot sample size is needed to explore these preferences and eventually assign bounds or ranges to the mechanization parameters.

As the SAFE-Cue technology advances, there will likely be differences in system mechanization requirements between aircraft types as well. Thus, the ranges that define "good" force cue and gain reduction intensities could eventually be established for diverse aircraft types. Finally, while the flight test results described in this paper were achieved in the presence of a representative adaptive controller, the SAFE-Cue technology is completely general in approach and with verification it can be applicable to any fly-by-wire aircraft. Active inceptor technology is required to fully utilize the system with force feedback cueing.

9.7 References

1. Klyde, D. H., A. K. Lampton, N. D. Richards, B. Cogan, "Flight Test Evaluation of a Loss of Control Mitigation System," *J. of Guidance, Control, and Dynamics*, Vol. 40, No. 4, April 2017, pp. 981-997.

2. Belcastro, C. M., and J. V. Foster, "Aircraft Loss of Control Accident Analysis," AIAA Paper No. 2010-8004 presented at the *Guidance, Navigation, and Control Conference*, Toronto, CA, Aug. 2-5, 2010.

3. https://www.sbir.gov/content/aviation-safety-0, accessed on January 16, 2022.

4. Arnold, E., "PIO Testing of Transport Category Aircraft – Issues and Observations," *53rd Symposia of the Society of Experimental Test Pilots*, Anaheim, CA, Sept. 2009.

5. Hageman, J. J., M. Smith and S. Stachowiak, *Integration of Online Parameter Identification and Neural Network for In-flight Adaptive Control*, NASA/TM-2003-212028, October, 2003.

6. Williams-Hayes, P. S., *Selected Flight Test Results for Online Learning Neural Network-Based Flight Control System*, NASA/TM-2004-212957, 2004.

7. Burken, J. J., P. S. Williams-Hayes, J. T. Kaneshige, S. Stachowiak, "Adaptive Control Using Neural Network Augmentation for a Modified F-15 Aircraft," *14th Mediterranean Conference on Control and Automation*, Ancona, Italy, June 2006.

8. Burken, J. J., P. S. Williams-Hayes, J. T. Kaneshige, *Reconfigurable Control with Neural Network Augmentation for a Modified F-15 Aircraft*, NASA/TM-2006-213678, April, 2006.

9. Bosworth, J. T., and P. Williams-Hayes, *Flight Test Results from the NF-15B Intelligent Flight Control System (IFCS) Project with Adaptation to a Simulated Stabilator Failure*, NASA/TM-2007-214629, Dec. 2007.

10. Ward, D. G., J. F. Monaco, and M. Bodson, "Development and Flight Testing of a Parameter Identification Algorithm for Reconfigurable Control," *J. Guidance, Control, and Dynamics*, Vol. 21, No. 6, Nov. - Dec. 1998, pp. 948-956.

11. Ward, D. G. and J. F. Monaco, "System identification for retrofit reconfigurable control of an F/A-18," *J. of Aircraft*, Vol. 42, No. 1, Jan. – Feb. 2005, pp. 63-72.

12. Liu, Y., X. Tang, G. Tao, S. M. Joshi, "Adaptive Failure compensation for aircraft tracking control Using Engine Differential Based Model," *American Control Conference*, Mineapolis, MN, June, 2006.

13. Calise, A. J., S. Lee, M. Sharma, "Development of a Reconfigurable Flight Control Law for Tailless Aircraft," *J. of Guidance, Control, and Dynamics*, Vol. 24, No. 5, Sept.-Oct. 2001, pp. 896-902.

14. Gregory, I., E. Xargay, C. Cao and N. Hovakimyan, "Flight Test of L1 Adaptive Controller on the NASA AirSTAR Flight Test Vehicle," *AIAA Guidance, Navigation and Control Conference*, Toronto, Canada, 2010.

15. Ackerman, K., E. Xargay, R. Choe, N. Hovakimyan, M. C. Cotting, R. B. Jeffrey, M. P. Blackstun, T. P. Fulkerson, T. R. Lau, and S. S. Stephens, "L1 Stability Augmentation System for Calspan's Variable Stability Learjet," AIAA 2016-0631 presented at the *AIAA Science and Technology Forum and Exposition 2016: AIAA Guidance, Navigation, and Control Conference*, San Diego, CA, Jan. 4-8, 2016.

16. Graham, D. and D. T. McRuer, "A Retrospective Essay on Nonlinearities in Aircraft Flight Control," *J. of Guidance, Control, and Dynamics*, Vol. 14, No. 6, Nov.-Dec. 1991, pp. 1089-1099.

17. Klyde, D. H., C. Y. Liang, D. J. Alvarez, N. Richards, R. J. Adams, and B. Cogan, "Mitigating Unfavorable Pilot Interactions with Adaptive Controllers in the Presence of Failures/Damage," AIAA Paper 2011-6538 presented at the *Atmospheric Flight Mechanics Conference*, Portland, OR, Aug. 8-11, 2011.

18. Richards, N. D., R. J. Adams, D. H. Klyde, and B. Cogan, "Flight-Test Evaluation of Adaptive Controller for Flying Qualities Specification and Protection," *J. of Guidance, Control, and Dynamics*, Vol. 38, No. 12, Dec. 2015, pp. 2241-2256.

19. Klyde, D. H., C. Y. Liang, N. Richards, R. J. Adams, and B. Cogan, "Use of Active Inceptor Cueing to Mitigate Pilot-Vehicle System Loss of Control," AIAA Paper 2012-4765 presented at the *Guidance, Navigation, and Control Conference*, Minneapolis, MN, Aug. 13-16, 2012.

20. Klyde, D. H., and D. McRuer, "Development of Smart-Cue and Smart-Gain Concepts to Alleviate Pilot-Vehicle System Loss of Control," *J. of Guidance, Control, and Dynamics*, Vol. 32, No. 5, Sept.-Oct. 2009, pp. 1409-1417.

21. Mitchell, D.G., and Hoh, R.H., *Development of Methods and Devices to Predict and Prevent Pilot-Induced Oscillations*, AFRL-VA-WP-TR-2000-3046, Jan. 2000.

22. Mitchell, D. G., R. H. Hoh, B. L. Aponso, and D. H. Klyde, *Proposed Incorporation of Mission-Oriented Flying Qualities into MIL-STD-1797A*, WL-TR-94-3162, Oct. 1994.

23. McRuer, D. T., and E. S. Krendel, *Mathematical Models of Human Pilot Behavior*, AGARDograph No. 188, Jan. 1974.

10. Build-Up of the Active Inceptor Cueing Force

A little bit of force for big (inceptor) moves. Seemed to help. Not worrying about compensating.

NASA Armstrong Test Pilot, April 2013

Parts of this chapter have been published as:

Title	Use of Active Inceptor Cueing to Mitigate Pilot-Vehicle System Loss of Control
Conference	AIAA Paper No. 2012-4765 presented at the Guidance, Navigation, and Control Conference, Minneapolis, MN, 13-16 Aug. 2012
Authors	D. H. Klyde, C. Y. Liang, N. Richards, and B. Cogan

10.0 BUILD-UP OF AN ACTIVE INCEPTOR CUEING FORCE

Loss of control has been identified as the leading cause of jet transport accidents. High profile accidents have illustrated the need to address pilot response to upsets and unusual attitudes. Another issue no less important is that associated with pilot-vehicle system loss of control. This refers to those incidents that result from the pilot's active manual control of the aircraft and most commonly occur in the form of so called pilot-induced oscillations. Regardless of the implied "fault" of the pilot, these events result from issues with the airframe and flight control system and not the pilot [1]. Examples described in this chapter include events with modern fly-by-wire transports in commercial operation and flight test events associated with the evaluation of new adaptive control schemes under various failure conditions. While not always the root cause, flight control system nonlinearities such as control surface rate and position limits are key components in these events. To mitigate loss of control events of this type, force feedback via an active control inceptor and corresponding command path gain adjustments have been investigated using piloted simulation and flight test evaluations. This chapter describes the development of effective pilot cueing techniques that make up the Smart-Cue/Smart-Gain system from Chapters 7 and 8 that addresses control surface actuator rate limiting and the Smart Adaptive Flight Effective Cue or SAFE-Cue from Chapter 9 that addresses more general flight control system nonlinear behavior, particularly that behavior associated with adaptive controllers. This chapter is largely taken from the material in [2].

10.1 Introduction

A study conducted by The Boeing Company of world-wide commercial jet transport accidents has found the most common events to be associated with loss of control [3]. Many of the events that result in loss of aircraft and fatalities result from the inability of the pilots to recover from upsets and unusual attitudes. Another class of loss of control events is associated with the pilot's attempt to tightly control the aircraft, often in response to some triggering event in the environment, for example, turbulence or severe crosswinds, or aircraft, for example, flight control system failures or unexpected transitions. While these incidents do not typically generate the same attention associated with upset loss of control events, a recent review conducted by the FAA found that pilot-vehicle system loss of control in the form of PIO continues to be a persistent problem in transport category aircraft often resulting in significant hull damage, injuries, and more rarely fatalities [4]. A summary of recent documented events for all aircraft types as well as a complete description of the interacting components of PIO can be found in [1] and [5].

To help mitigate these types of loss of control, research described in this thesis has focused on the use of active inceptor cueing together with adaptive command path gain adjustments to alert the pilot of the impending trouble and to constrain the resulting control actions of the pilot so that loss of control can be avoided. The first concept that was developed and evaluated via piloted simulation and flight test was the Smart-Cue/Smart-Gain system [6,7], Chapters 7 and 8. This system was designed to address loss of control scenarios associated with control surface actuator rate limiting, a primary contributor to all of the documented severe PIOs that have occurred with modern fly-by-wire aircraft [8] and the focus of this thesis. Building on the Smart-Cue/Smart-Gain lessons, a concept, the Smart Adaptive Flight Effective Cue or SAFE-Cue, was developed

to mitigate pilot-vehicle system loss of control in the presence of an active adaptive control system as described in Chapter 9.

The basic Smart-Cue idea is to restore in a fly-by-wire system configuration a force feedback cue akin to an actuator "valve-bottoming" characteristic [6]. Note that Smart-Cue can be applied to non-FBW manual control systems as well; however, the implementation may be more hardware intensive. Cueing and corrective forces, the Smart-Cue, are presented to the pilot as a "proprioceptive display." Following checkout flight tests where the Smart-Cue alone had limited success, piloted simulation was used to rapidly prototype the Smart-Gain concept. Past work includes the PIO Suppression Filter used on the space shuttle that employs command path gain reduction techniques [9]. Such techniques estimate the frequency of the pilot's input and then attenuate the input as a function of this frequency. The approach does not, however, take the response of the control system into consideration, so the pilot input is attenuated whether or not it is needed. With the Smart-Gain, the pilot input is attenuated as a function of the same measured Position Error used to define the Smart-Cue. The feasibility of the Smart-Cue/Smart-Gain approach using an active control inceptor implemented in a variable stability aircraft was successfully demonstrated in a flight test program conducted with five evaluation test pilots [7] as described in Chapter 8.

The Smart-Cue/Smart-Gain approach served as the launching point for the SAFE-Cue development. The SAFE-Cue innovative cueing system provides force feedback to the pilot via an active control inceptor with corresponding command path gain adjustments based on a measured System Error between the adaptive controller response and a nominal system response. The SAFE-Cue alerts the pilot that the adaptive control system is active, provides guidance via force feedback cues, and attenuates commands, thus ensuring pilot-vehicle system stability and performance in the presence of damage or failures. While the focus in this work featured an adaptive controller, the SAFE-Cue concept is completely general and can be applied to any flight control system implementation to mitigate loss of control. The system was successfully evaluated in flight as described in Chapter 9 and in [10].

This chapter will describe the process in which the combined coulomb friction plus gradient force is created for the Smart-Cue and SAFE-Cue as well as added details regarding the need for an adaptive command path gain, the Smart-Gain and SAFE-Cue gain.

10.2 Quantifying the Handling Qualities Cliff

10.2.1 Defining the Handling Qualities Cliff

When approaching instability, linear system performance degrades in a manner that is predictable to a pilot. As nonlinearities are introduced, however, gradual degradations can be replaced by sudden changes in aircraft behavior resulting in the so called "handling qualities cliff." With few warning signs provided by the aircraft as the pilot approaches such a cliff, loss of control can easily occur. An example divergent PIO is shown in Figure 10.1. This is the Pilot 6 loss of control event from Chapter 8. Repeated here, the pilot is attempting a precision offset landing with an aileron maximum rate of ±30 deg/s. The rate limit nonlinearity results in a diverging PIO as the pilot attempts the final centerline capture. Fortunately, the likelihood of finding a handling qualities cliff in transport category aircraft outside of flight test is rare. Of course, this also means

that pilots are typically not prepared to respond when such an encounter occurs. To provide an effective alerting and, if necessary, constraining mechanism, one must first be able to identify an impending cliff. In the case of control surface rate limiting, for example, it is not good enough to simply identify when the rate limiter is active. Because of the nature of rate limiting [8], an aircraft can routinely operate at or near a rate limit without threat of loss of control. Thus, to alert the pilot of an active rate limit would diminish the effectiveness of the alert due to the number of false alarms.

For Smart-Cue/Smart-Gain and SAFE-Cue, the concept of dynamic distortions from Chapter 6 and [6] is used to define potential flying qualities cliffs. The common theme in both concepts is that the actual flight control system is in some way deviating from an ideal system. The pilot is expecting one type of response, but the actual system is behaving differently because of the distortion in the dynamic system response. The concept of dynamic distortion served as a motivation for the Smart-Cue/Smart-Gain development. The attempt to quantify such conceptual terms as "distortions" and "idealized systems" served as innovative and unifying principles underlying the development of corrective measures in the form of inceptor force feedback cues and later command path gain adjustments.

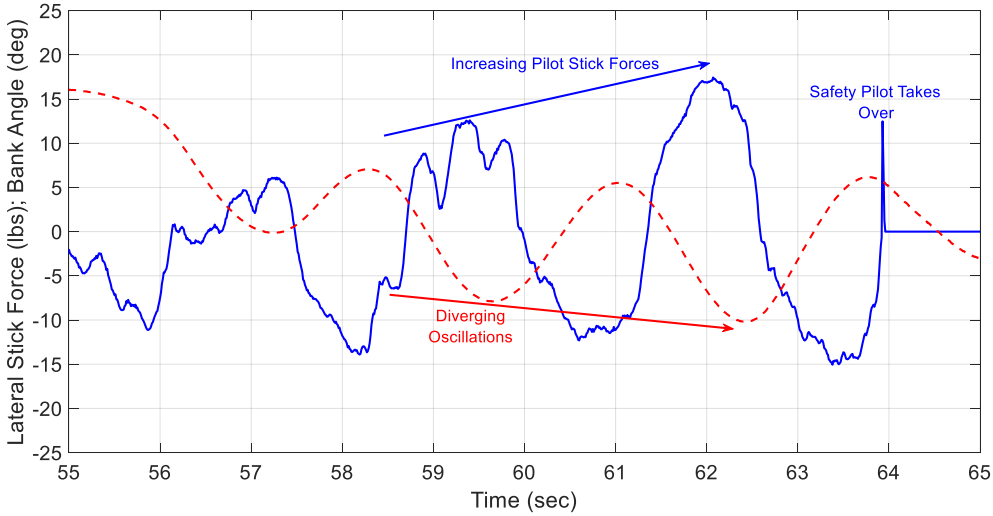

Figure 10.1: *Example flight test divergent PIO.*

10.2.2 The Smart-Cue/Smart-Gain Position Error

To determine the magnitude of the cueing force or the extent of the command path gain attenuation, a commanded surface position (δ_c) and actual surface position (δ) are used to define a Position Error (δ_{error}) via an ideal linear system (δ_{ideal}) as shown in Figure 10.2. Here, the Position Error is the difference between the ideal linear system response and the actual manual flight control system response, $\delta_{error} = \delta_{ideal} - \delta$. The Position Error thus reflects differences due

to distortions in the actual system. The magnitude of this difference increases as the pilot-vehicle system approaches a handling qualities cliff.

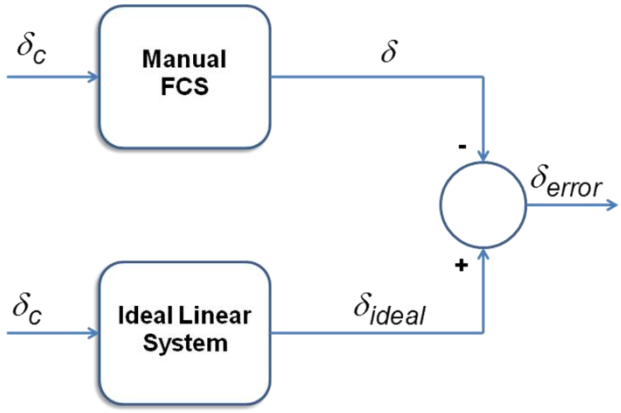

Figure 10.2: *Smart-Cue/Smart-Gain control surface Position Error measure.*

Two flight test examples of Position Error measurements are shown in Figure 10.3. Both examples are lateral axis cases as the pilot attempted a precision offset landing with an aileron maximum rate of ±30 deg/s [7]. The Position Error displayed in the Figure 10.3(a) plot was generated from a rate limited only run, shown in Figure 10.1. This run is characterized by a large error near 47 seconds that is associated with the initial correction to the runway centerline and Position Errors that are increasing in amplitude beginning at 57 seconds that are associated with the final centerline capture. Note that, because of the resulting PIO, the safety pilot took control of the aircraft as indicated after the third diverging oscillation (see Figure 10.1). In Figure 10.3(b) the Position Error measured from a Smart-Cue/Smart-Gain run is shown. In this case the maximum aileron rate was again ±30 deg/s, but the magnitude of the measured Position Error is greatly reduced when compared to the rate limit only case. Furthermore, the pilot was able to complete the task with no tendency for PIO. There is a noted numerical oscillation in the Position Error around 38 seconds, but this artifact had no impact on the task performance.

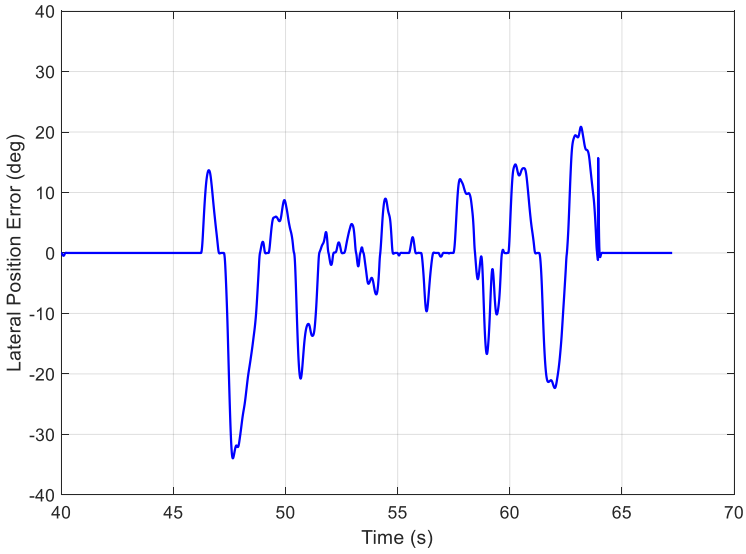

(a) Rate limit only case

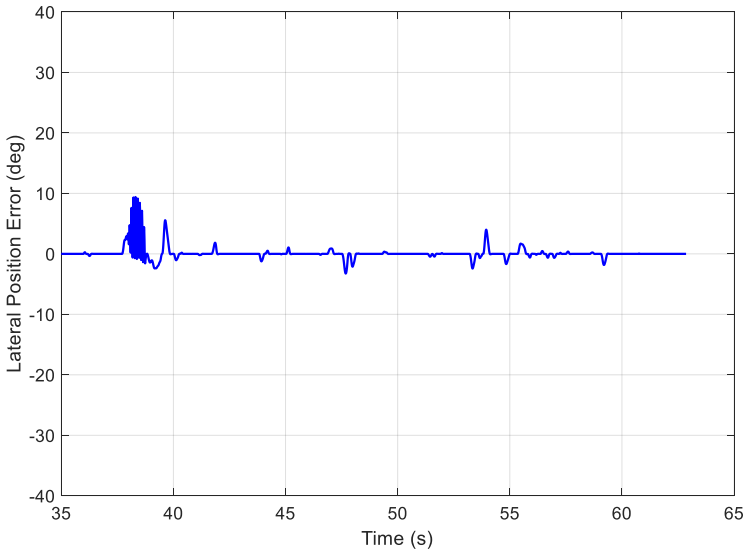

(b) Rate limit plus Smart-Cue/Smart-Gain

Figure 10.3: *Position Error measures for two precision offset landing flight test example runs.*

10.2.3 The SAFE-Cue System Error

Like the Position Error for Smart-Cue/Smart-Gain, the System Error computation is a key function of the SAFE-Cue mechanization. In general, to compute the error a comparison is made between a model-based nominal system response and the adaptive control system response. The difference between the selected signals is the System Error. Initially, the use of both the elevator surface position and the pitch rate output signal were explored analytically and in the simulator. As described above the elevator surface position was a useful measure for the Smart-Cue/Smart-Gain implementations where the concern was control surface rate limiting, an isolated flight control system element. This measure was not, however, appropriate with an active adaptive controller. The adaptive controller is attempting to compensate for an elevator surface failure, so any error computation between the adaptive and nominal systems based on this parameter will result in SAFE-Cue actions that attempt to suppress the actions of the adaptive controller. In contrast, a System Error measure based on the pitch rate output as illustrated in the Figure 10.4 block diagram allows for a direct comparison between the response of the adaptive and nominal systems. That is, the adaptive controller is attempting to restore the response of the nominal system in the presence of a failure or damage. As the responses of these two systems diverge, the error will build, thus providing the measure needed from which to activate the SAFE-Cue feedback force and command path gain reduction.

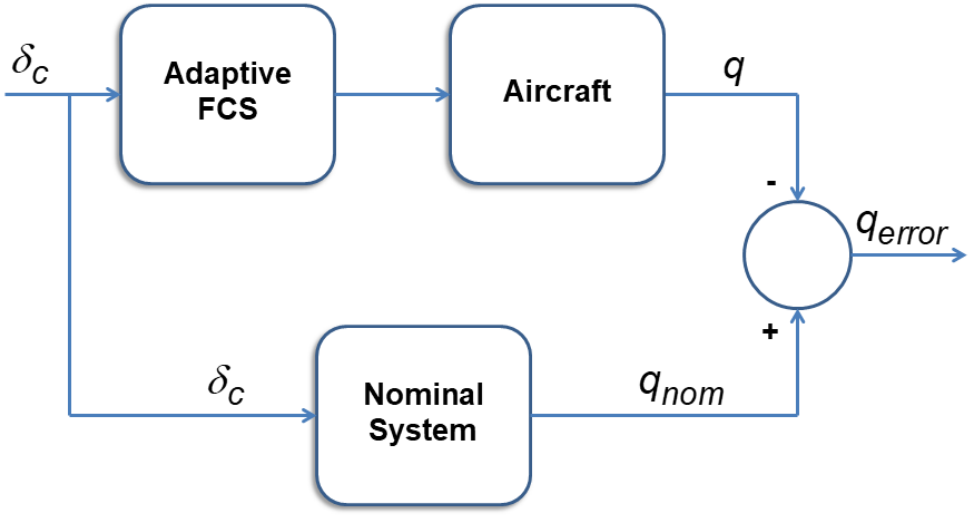

Figure 10.4: *SAFE-Cue pitch rate System Error measure.*

Two System Error examples from the flight test evaluations of the SAFE-Cue concept are shown in Figure 10.5. Both examples are from a scenario in which there is a 25% reduction in elevator effectiveness and corresponding reductions in the elevator rate and position limits. In both cases the pilot was performing the pitch axis sum-of-sines tracking task from Chapter 9. For the failure only case of Figure 10.5(a), large System Error oscillations develop soon after the failure is introduced and persist for the remainder of the run. In sharp contrast is the elevator failure with

SAFE-Cue active case of Figure 10.5(b). While the System Error does increase after the failure is introduced, the magnitude remains bounded with peak values below ±2 deg/s.

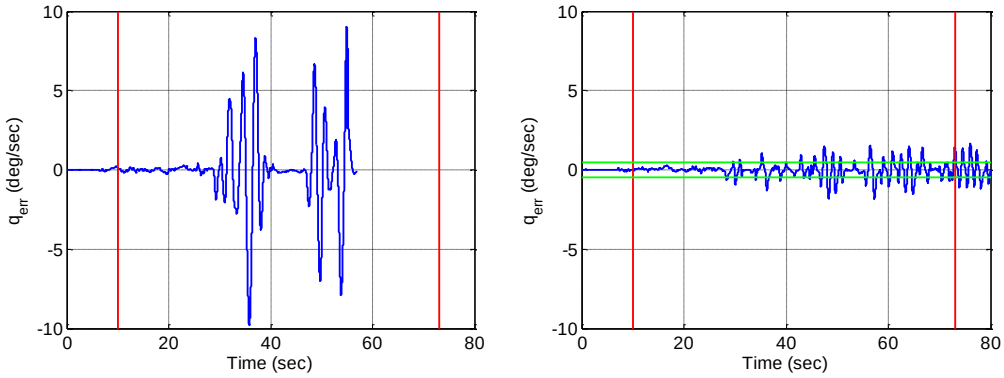

(a) Elevator failure only case *(b) Elevator failure plus SAFE-Cue*

Figure 10.5: *System Error measures for two piloted simulation example runs.*

10.3 Building a Better Cue

The inceptor force cues were first designed and evaluated via piloted simulation in a fixed-base simulator that featured a McFadden hydraulic control loader and inceptor that was representative of a F/A-18A/B center stick. Engineering evaluations were first used to develop candidate configurations that were then evaluated more formally be test pilots to down-select configurations for flight test. The checkout flights described in Chapters 8 and 9 were used to refine the candidate cues with a test pilot evaluator before proceeding to the formal evaluations. Note that the checkout flight test pilots did not serve as Smart-Cue/Smart-Gain or SAFE-Cue evaluators in the formal flight test campaigns.

Although the fundamental force feedback concept has remained essentially fixed once verified in flight test, many options are available regarding how the Smart-Cue or SAFE-Cue is mechanized and integrated within a modern flight control system. As the force feedback cue builds, it first provides an alerting function of an impending handling qualities cliff. Then as the force increases, it provides a constraining function, so that inputs that may lead the pilot-vehicle system over the cliff will be avoided. For the Smart-Cue, as mentioned above, piloted simulation was used to develop the mechanizations that were eventually evaluated in flight. Several feedback force options were considered individually and in various combinations. Options included a force that produced an effective spring gradient change, a coulomb friction force, and damping forces based on control stick velocity and the rate of change of the Position Error. For the initial SAFE-Cue mechanizations, lessons learned from the Smart-Cue simulator and flight test evaluations were used to more rapidly define effective design options.

10.3.1 The Smart-Cue Gradient Force Feedback Cue

In a typical fly-by-wire system, the inceptor dynamics can be represented most simply by a second order system characterized by a spring gradient, damping, and inertia. Thus, when introducing a force feedback cue, a fundamental force type to consider is one that changes the effective spring gradient. The options for such a cue are shown in Figure 10.6 through Figure 10.9 wherein each case is shown as if it was one feedback element of a larger block diagram. The four options include a limiting case "hard stop," Figure 10.6, a linear gradient, Figure 10.7, a dual gradient, Figure 10.8, and a parabolic gradient, Figure 10.9. The parabolic gradient may also be approximated by a series of three or more linear gradients. For all options the gradient force is zero whenever the Position Error input (δ_{PE_f}) is below a defined threshold. Here, the "f" subscript indicates that this is the Position Error associated with the force feedback. This threshold may be zero in the limiting case, that is, the feedback forces are always active, or may expand as needed for a given application to create a dead zone wherein no feedback forces are generated until the error exceeds the defined value. Once outside this dead zone, the magnitude of the feedback force increases with increasing Position Error according to the defined function.

Following engineering evaluations, two commercial test pilots participated in the initial simulator evaluations of the gradient force feedback cue. Pitch axis evaluations were made with a sum-of-sines tracking task, while roll axis evaluations were made with a bank angle capture and hold task. For the pitch axis, the evaluations focused on variations in the linear gradient option of Figure 10.7. The hard stop option was not strongly considered as there was a desire to define mechanizations that would guide the pilot to successful task completion with reasonable performance. The hard stop may prevent loss of control, but at the expense of task performance or it may require the pilot to ultimately abandon the task. Both pilots found the gradient cue to be helpful in preventing loss of control, although the preferred force levels differed somewhat between the two pilots. While the cue was reasonably effective in the pitch axis, it was clear that other options were needed to improve the results.

Although only limited roll axis evaluation runs were conducted, much was learned. First, the cueing was not particularly effective in this initial mechanization because a first order filter placed on the Smart-Cue signal resulted in a significant lag in the perceived cueing force. Also, there was a significant "wobble" noted as any significant lateral stick movement was attempted. Later investigations found that the magnitude of the wobble increases as stick damping decreases. The wobble appeared to result from the inability of the limb dynamics of the pilot in the lateral axis to counter a strong gradient only force. The oscillations or wobble had been noted prior to the exposure of the commercial pilots by engineer evaluators, but the increased lateral stick damping used at that time masked the phenomenon. When the lateral stick damping was reduced, the oscillations became more prominent. The oscillations are clearly evident in Figure 10.10(a), a lateral stick position time series plot that was taken from a bank angle capture and hold evaluation task run. The approximate frequency of the oscillation is 16.6 rad/s (2.65 Hz). The gradient cue produced similar stick "wobbles" in the checkout flights, see Figure 10.10(b), which were found to be very objectionable by the pilot. With this occurrence and the success of other force feedback options, the gradient force was no longer considered as a solitary cueing mechanism.

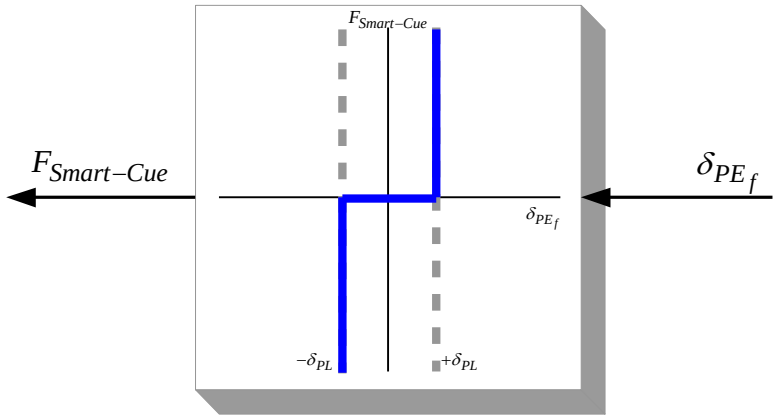

Figure 10.6: *Gradient feedback force cue options – Hard Stop.*

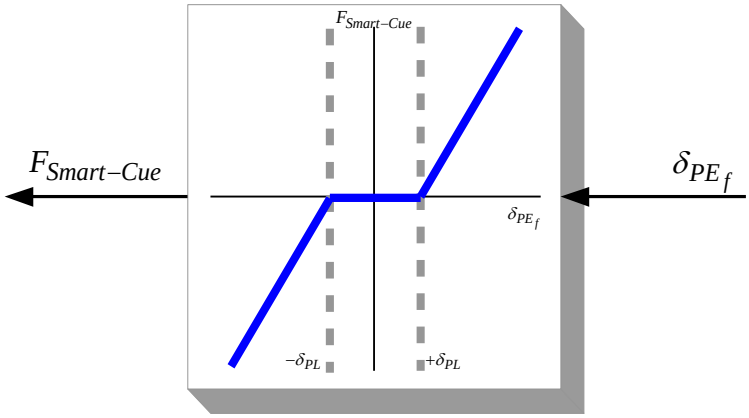

Figure 10.7: *Gradient feedback force cue options – Linear Gradient.*

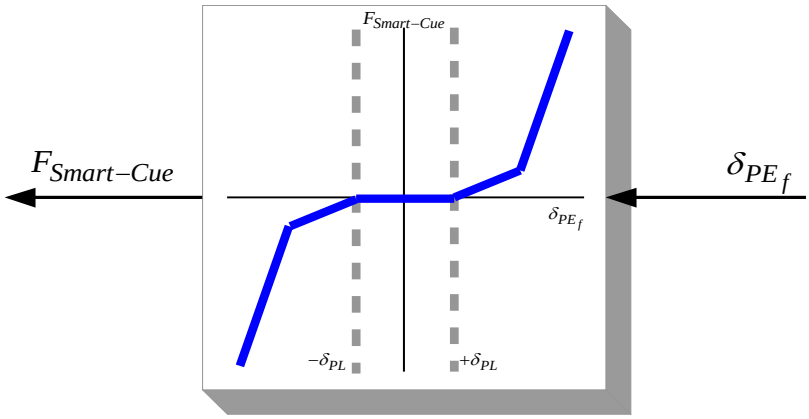

Figure 10.8: *Gradient feedback force cue options – Dual Gradient.*

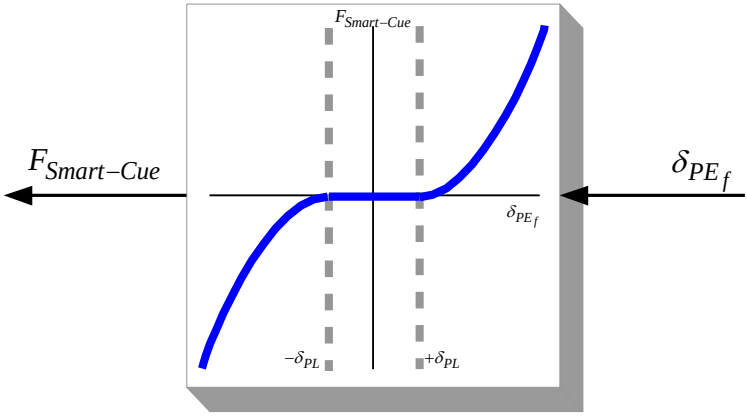

Figure 10.9: *Gradient feedback force cue options – Parabolic Gradient.*

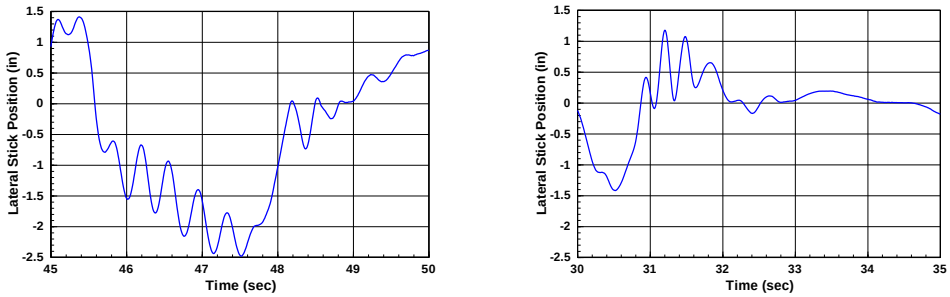

(a) Simulator example *(b) Flight verification*

Figure 10.10: *Lateral stick oscillations resulting from gradient force feedback cueing.*

10.3.2 Other Smart-Cue Options

Initial piloted simulation results indicated that the gradient force can provide an effective cue to the pilot, at least in the pitch axis. The feel of the cue, however, was not always "smooth," and in the roll axis, a roll ratchet condition was often observed. To enhance the performance of the force feedback cue, a damping component was considered. Two damping force options were defined. In the first option, the damping force was computed as a function of the Position Error and stick velocity. In this case the damping force is zero whenever the Position Error is less than or equal to the defined threshold. The stick velocity signal is then passed through a second order Butterworth filter before the damping force is computed. In the second option, the damping force was computed as a function of the rate of change of Position Error. Once again, the damping force is zero whenever the Position Error is less than or equal to the defined threshold. To provide a smooth onset, the damping force is increased from zero to its full value using a gain. Similar to the first damping force option, the Position Error rate signal is passed through a second order Butterworth filter before the damping force is computed. Evaluation of the damping force options via piloted simulation revealed no significant added benefit when used alone or in combination with the gradient force.

Following the simulator evaluations by commercial test pilots, the desire for an improved constraining force mechanism led to the definition of a coulomb friction-like Smart-Cue force. The benefit of this type of force cue is that no reactive force is generated when the stick is not in motion. Once implemented, this new cue appeared to work well in an engineering simulation checkout. The friction force is a function of the sign of the stick velocity and is activated when the computed Position Error exceeds the defined threshold. This cue worked well in many cases and it eliminated the observed roll ratchet phenomenon, however, a better solution soon came to light.

10.3.3 The Combined Force Feedback Cue

By exploring options in a piloted simulator, it was found that a combination of the gradient and friction force together produced a much-improved force cue. When combined, the two types of forces seemed to "take the edge off" of the shortcomings found with the individual forces. Similar to the friction force alone, the combined force did not result in the roll ratchet observed with the gradient force alone. The benefits of this new combined force were confirmed in formal piloted simulation evaluations with two guest test pilots from the United States Air Force Test Pilot School. Flight test evaluations of the Smart-Cue and Smart-Gain systems found that in terms of both pilot opinion and task performance the combined force provided the most beneficial inceptor cue, especially when used with the Smart-Gain [7,11].

Given the success of the combined friction and gradient force Smart-Cue, such a combination of force feedback cues became a natural starting point for the initial SAFE-Cue developments. Figure 10.11 and Figure 10.12 show SAFE-Cue System Error, friction and gradient feedback forces, and total feedback force time histories for two example runs from the SAFE-Cue flight test evaluations [10]. Each figure shows a 30-second segment of the overall runs. The combined SAFE-Cue force case with a less aggressive SAFE-Cue gain of Figure 10.11 received an HQR 5/PIOR 4, while the improved combined SAFE-Cue force plus gain case of Figure 10.12 received an HQR 2/PIOR 1. Note that no feedback forces are generated as long as the System Error remains below the System Error threshold values.

When comparing the two evaluation runs, the impact of the SAFE-Cue gain can clearly be seen in the magnitude and duration of the forces. The presence of a more effective time-varying gain adjustment greatly reduces the feedback forces required. One might surmise then that the feedback forces may not be needed at all. It is important to point out, however, that the best ratings were achieved for those failure cases when the SAFE-Cue gain and forces were both active. Another interesting feature of the two forces is that the gradient force builds more slowly but has a longer decay. The friction force on the other hand, peaks and decays rapidly. Because the friction force is a function of the stick velocity and not position, it is also more likely to rapidly change direction. As a result, the gradient and friction forces are frequently opposite in sign.

The total force results from a combination of the gradient and friction forces as shown in the bottom panels of Figure 10.11 and Figure 10.12. Here, the impact of a more aggressive adaptive SAFE-cue gain, that is, one that responds more rapidly and allows for a larger gain reduction, is to reduce the amplitude of the cueing force and the percentage of task time where a cueing force was required. The Combined SAFE-Cue force was clearly preferred by the pilots compared to either force given in isolation. Still, there is considerable design space to identify more optimum mechanizations.

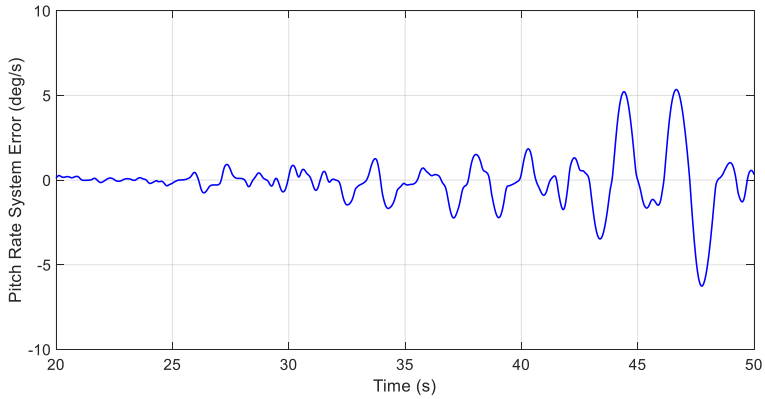

(a) System Error

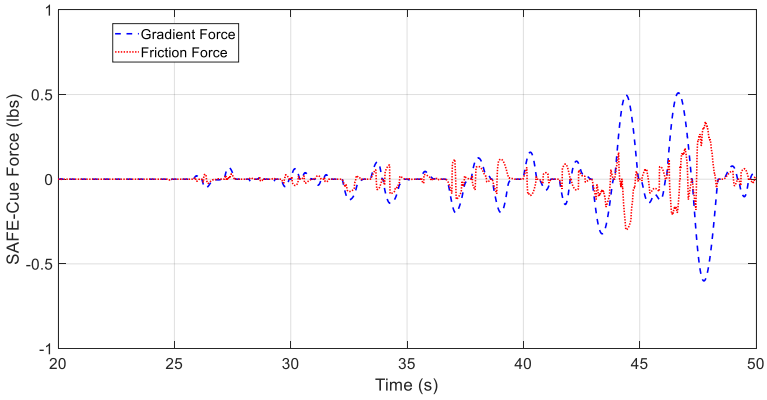

(b) SAFE-Cue component forces

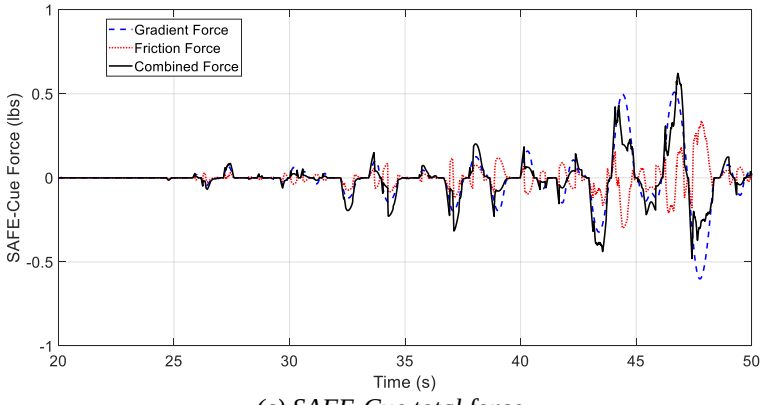

(c) SAFE-Cue total force

Figure 10.11: *Example SAFE-Cue forces for combined force case with less aggressive SAFE-Cue gain.*

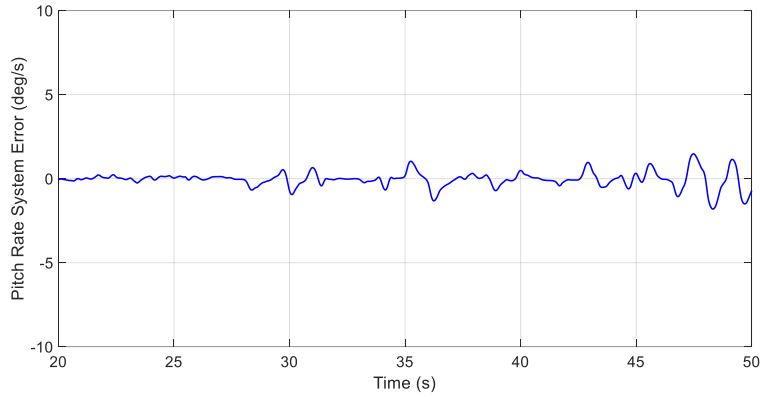

(a) System Error

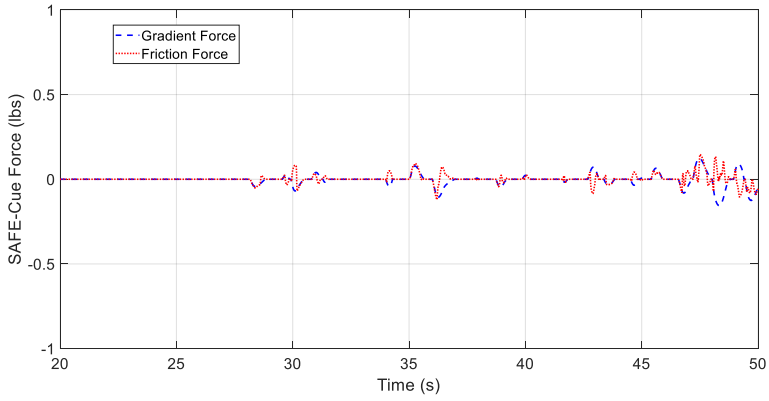

(b) SAFE-Cue component forces

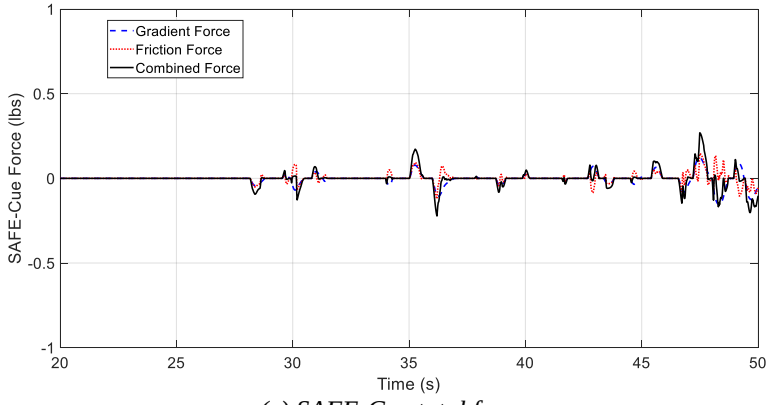

(c) SAFE-Cue total force

Figure 10.12: *Example SAFE-Cue forces for combined force case with more aggressive SAFE-Cue gain.*

10.4 The Adaptive Command Path Gain

10.4.1 The Need for a Smart-Gain

A second design concept that is also based on a measure of dynamic distortion, the *Smart-Gain*, evolved from the Smart-Cue checkout flight process. The Calspan Learjet In-Flight Simulator was used to conduct both the checkout flights and formal evaluation flights for the Smart-Cue program. During the checkout flight sorties, several Smart-Cue mechanizations were found to work well for the cruise evaluations in both the pitch and roll axes. Results from the precision offset landing task, however, were far less certain. First, the evaluation pilot appreciated that the Smart-Cue gave an apparent "trough" in which it was safe to move the stick in the presence of significant control surface rate limiting. The size of the trough was more pronounced when the force cueing increased as a function of Position Error. Despite numerous attempts, a force cueing level could not be found that allowed the pilot to comfortably make the required roll axis corrections associated with the offset landing without "fighting" the Smart-Cue forces. These results led to a post flight debrief discussion of possible command path gain adjustments as an alternative to the high feedback forces that would still take advantage of the positive alerting mechanism observed in the checkout evaluations.

Piloted simulation was used to rapidly prototype such a concept, the Smart-Gain, that is a gain that varies in intensity with the level of dynamic distortion. Techniques like the PIOS filter used on the Shuttle do not, however, take the response of the flight control system or vehicle into consideration, so the pilot input is attenuated whether or not this attenuation is needed. With the Smart-Gain, the pilot input is attenuated as a function of the Position Error, the measure of dynamic distortion. A threshold is again used to turn the Smart-Gain on and off. The threshold may be set independently to the values used for the Smart-Cue.

The Smart-Gain was found to be a critical innovation. Repeated successful landings were accomplished during the formal evaluation process with best results coming from a Smart-Cue/Smart-Gain combination [7].

10.4.2 The SAFE-Cue Gain

For the SAFE-Cue implementation, the adaptive command path gain reduction filter is also a function of the pitch rate System Error. When the System Error exceeds the threshold value, which can be different from that used for the SAFE-Cue force, the command path gain is reduced linearly as a function of increasing System Error to a prescribed minimum value. Initially, a minimum value of 0.25 for the resulting gain was used. Thus, the pilot would not observe an instantaneous gain reduction greater than 75%. Instead, the slope of the reduction can be varied to increase or decrease the rapidity of the gain reduction. The gain reduction is adaptive in that it is only active when the System Error threshold is exceeded, and then the magnitude of the reduction is a function of the instantaneous size of the error.

Two SAFE-Cue gain examples from flight test are shown in Figure 10.13. In the first case, Figure 10.13(a), no feedback forces are present, only the command path gain adjustments. Here, the pilot did find significant performance improvements compared to the failure only case with HQR

3/PIOR 1 pilot ratings. When the feedback force cues were added in the Figure 10.13(a) example, further improvements in performance were observed by the pilot, HQR 2/PIOR 1, and more limited SAFE-Cue gain activity was required, see Figure 10.13(b). The pilot found this case to be similar in performance with that of the baseline.

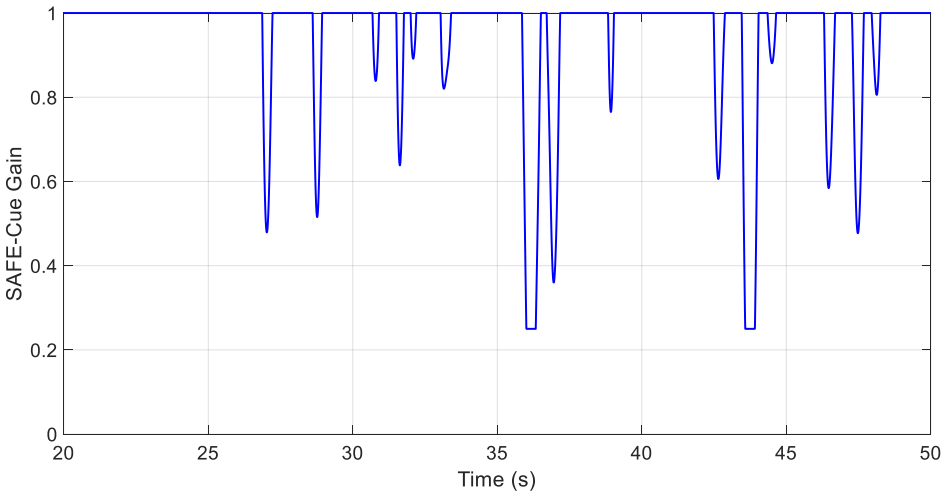

(a) SAFE-Cue gain only case

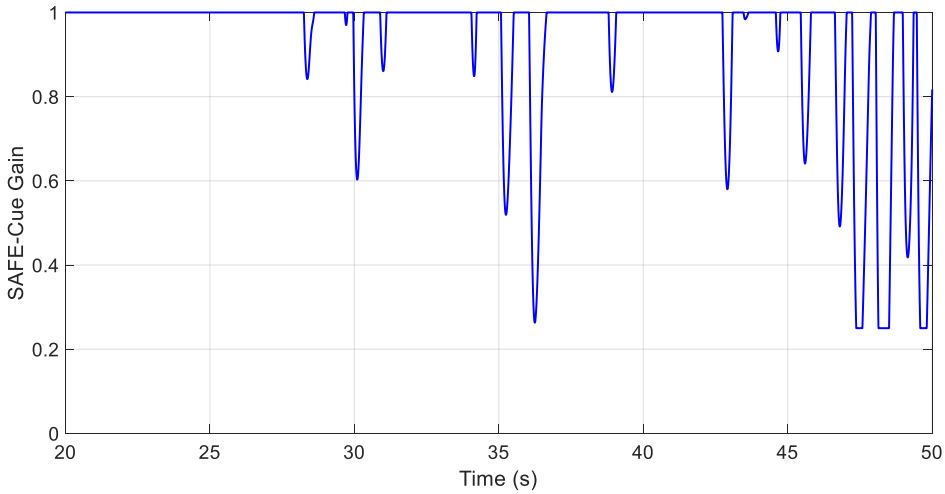

(b) SAFE-Cue combined force and gain case

Figure 10.13: *SAFE-Cue command path gain activity from two example flight test runs.*

10.5 Conclusions

Pilot force cueing via an active control inceptor can be used in combination with adaptive command path gain reductions to mitigate pilot-vehicle system loss of control. Two such concepts have been developed for this role, the Smart-Cue/Smart-Gain that was developed to alleviate the impact of control surface actuator rate limiting and the SAFE-Cue that was developed to improve pilot-vehicle performance in the presence of an adaptive flight controller and failures or damage.

For Smart-Cue/Smart-Gain the Position Error was used to provide a quantitative measure of dynamic distortion, while for SAFE-Cue the pitch rate System Error measure was found to be an effective means of distinguishing performance of the adaptive system with failure/damage and a nominal (healthy) system. Piloted simulation and flight test results have shown these measures to be an appropriate indicator of impending flying qualities cliffs that are associated with flight control system nonlinear behavior. For both concepts the feedback force that resulted in the best performance and most favorable pilot opinion resulted from a combination of an effective gradient and coulomb friction force. A combination of Smart-Cue feedback force and Smart-Gain command path gain adjustments was found to best mitigate the impact of control surface actuator rate limiting. Similarly, the SAFE-Cue combined force and gain were most effective at suppressing pilot-vehicle system oscillations for the given failure/damage scenarios, allowing the pilots to focus on the task at hand rather than simply maintaining control.

The SAFE-Cue approach has wider applicability beyond that of adaptive control. Given an active inceptor, the output System Error can be used as the catalyst for the SAFE-Cue force feedback or adaptive gain reduction whenever the flight control system, that is, conventional, fly-by-wire, adaptive, etc., significantly deviates from the nominal system behavior as a protection against loss of pilot-vehicle system control.

10.6 References

1. Anon., *Aviation Safety and Pilot Control*, prepared by the National Research Council Committee on the Effects of Aircraft-Pilot Coupling and Flight Safety, National Academy Press, Washington, D.C., 1997.

2. Klyde, D. H., C. Y. Liang, N. Richards, B. Cogan, "Use of Active Inceptor Cueing to Mitigate Pilot-Vehicle System Loss of Control," AIAA Paper No. 2012-4765 presented at the *Guidance, Navigation, and Control Conference*, Minneapolis, MN, 13-16 Aug. 2012.

3. Anon., "Statistical Summary of Commercial Jet Airplane Accidents: Worldwide Operations 1959-2010," *Boeing Commercial Airplanes*, Seattle, WA, June 2011.

4. Arnold, E., "PIO Testing of Transport Category Aircraft – Issues and Observations," *53rd Symposia of the Society of Experimental Test Pilots*, Anaheim, CA, Sept. 2009.

5. Mitchell, D. G. and D. H. Klyde, "Identifying a Pilot-Induced Oscillation Signature: New Techniques Applied to Old Problems," *Journal of Guidance, Control, and Dynamics*, vol. 31,no. 1, pp. 215-224, 2008.

6. Klyde, D. H., and D. T. McRuer, "Development of Smart-Cue and Smart-Gain Concepts to Alleviate Pilot-Vehicle System Loss of Control," *J. of Guidance, Control, and Dynamics*, Vol. 32, No. 5, Sept.-Oct. 2009, pp. 1409-1417.

7. Klyde, D. H., and C. Y. Liang, "Approach and Landing Flight Test Evaluation of Smart-Cue and Smart-Gain Concepts," J. *of Guidance, Control, and Dynamics*, Vol. 32, No. 4, July-Aug. 2009, pp. 1057-1070.

8. Klyde, D. H., and D. G. Mitchell, "Investigating the Role of Rate Limiting in Pilot-induced Oscillations," *J. Guidance, Control, and Dynamics*, Vol. 27, No. 5, Sept.-Oct. 2004, pp. 804-813.

9. Smith, J. W., and J. W. Edwards, *Design of a Nonlinear Adaptive Filter for Suppression of Shuttle Pilot-Induced Oscillation Tendencies*, NASA TM-81349, 1980.

10. Klyde, D. H., A. K. Lampton, N. D. Richards, B. Cogan, "Flight Test Evaluation of a Loss of Control Mitigation System," *J. of Guidance, Control, and Dynamics*, Vol. 40, No. 4, April 2017, pp. 981-997.

11. Klyde, D. H., and C. Y. Liang, "Flight Assessment of Pilot Behavior with Smart-Cue and Smart-Gain Concepts Active," AIAA 2009-5606 presented at *Atmospheric Flight Mechanics Conference*, Chicago, IL, Aug. 10-13, 2009.

Part III: PIO Detection

11. Exposing Unique Pilot Behaviors from Flight Test Data Leads to a New PIO Detection Method

From the start of manned flights, pilots have recognized that no handling task can be accomplished perfectly. "Good enough" has always instinctively been characterized as a certain maximum amount of error; the boundary between success and failure.

William R. Gray III, Chief Test Pilot, USAF Test Pilot School, from "A Generalized Handling Qualities Flight Test Technique Utilizing Boundary Avoidance Tracking," AIAA-2008-1648

Parts of this chapter have been published as:

Title	Exposing Unique Pilot Behaviors from Flight Test Data
Conference	AIAA Paper No. 2015-0239 presented at the Science and Technology Forum and Exposition 2015: AIAA Atmospheric Flight Mechanics Conference, Kissimmee, Florida, January 5-9, 2015
Authors	D. H. Klyde, P. C. Schulze, and P. M. Thompson

11.0 EXPOSING UNIQUE PILOT BEHAVIORS FROM FLIGHT TEST DATA LEADS TO A NEW PIO DETECTION METHOD

The flight test program described in Chapter 9 was undertaken to evaluate the Smart Adaptive Flight Effective Cue (SAFE-Cue) pilot-vehicle system loss of control mitigation concept. Three experienced test pilots participated in the flight test evaluations that were conducted using the Calspan Learjet In-Flight Simulator. While the focus of the program was to assess the SAFE-Cue system performance in the presence of failure/damage scenarios, the pilots were also exposed to the baseline aircraft configuration several times during their evaluations. The baseline configuration was designed to have Level 1 handling qualities for the sum-of-sines tracking and bank angle capture and hold tasks that were evaluated as part of the "blind" configurations presented to each pilot. Because of a mechanical issue, only two of the three pilots conducted the roll axis evaluations. From analysis of the test data it was clearly evident that the pilots employed disparate control strategies, with one using an unexpected "bang-bang" technique that resulted in a sustained pilot-induced oscillation (PIO). Based on the resulting pilot comments and ratings, the "bang-bang" pilot did not recognize that he was in a sustained PIO. In contrast, the other pilot was able to achieve desired performance with no tendency for PIO. Using a variety of analysis approaches, the two baseline configuration runs were explored in detail to assess the observed differences. Analysis results revealed that both pilots provided lead compensation, however, there were significant differences in pilot input power and effective time delay. Over the course of one baseline configuration evaluation run, the "bang-bang" pilot fixated his input power at a single frequency with a significantly higher gain and an additional 100 msec of effective delay. A new time-varying PIO metric introduced herein clearly illustrates the observed differences in pilot behavior. The material in this chapter was largely taken from [1].

11.1 Introduction

Pilot behavior models have long been used to describe how the human operator interacts with flight vehicles. It is beyond the scope of this paper to review the many important works in this area from McRuer and Jex [2], Hess [3], and, more recently, a series of works from TU Delft [4,5], among others. This paper instead refers to three fundamental modes of dynamic behavior that comprise the range of human pilot control possibilities as part of a pilot-vehicle system [6]. These modes correspond to the three-pathway structure shown in Figure 11.1. The pathways are internal organizations of the pilot's perceptions. They underlie and correspond to the following pilot control behavior patterns:

- Compensatory (Closed-loop): pilot control governs outputs conditioned by pilot-vehicle system errors;
- Pursuit (Combined Open- and Closed-loop): pilot control is dependent on pilot-vehicle system errors plus known or induced input commands and/or system outputs; and
- Precognitive (Open-loop): highly-skilled and practiced pilot programmed control outputs to command the aircraft to a new state.

In both compensatory and pursuit operations the pilot is highly interactive with the aircraft on a continuous basis, whereas in precognitive operations the pilot's actions are essentially discrete and independent of the aircraft's response during the time period of the pilot's programmed command. Precognitive behaviors constitute the vast majority of pilot activities in nominal aircraft maneuvers where the pilot's outputs are a stored repertory that are released in a timely and appropriate fashion. These open-loop sequences may be short, as with a pseudo bang-bang control, or long, as in generating a synchronous sine wave. The aircraft simply responds without further pilot intervention. Of course, if the ultimate response is not as desired, the pilot may insert another control sequence. In compensatory and pursuit processes the pilot is part of a feedback control process, with all of the advantages, for example, continuous reduction of errors and disadvantages, for example, possible instabilities associated with this kind of control.

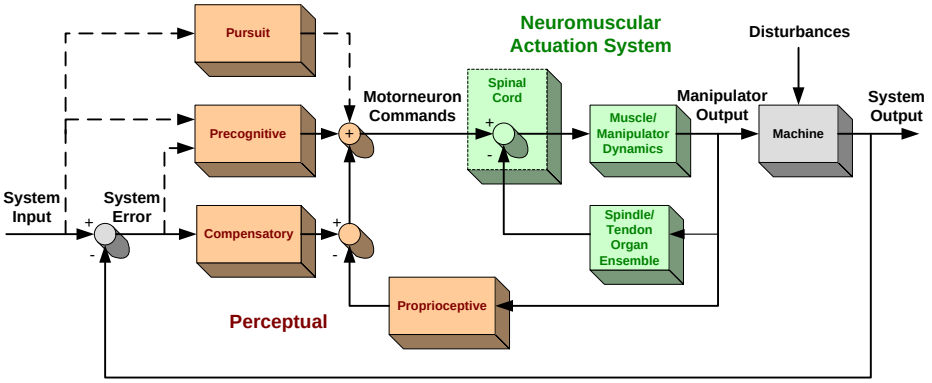

Figure 11.1: *Three modes of perceptually centered model of pilot behavior.*

A block diagram for the compensatory control scenario is shown in Figure 11.2. Here, the pilot controls the system output, *m*, in response to the displayed error, *e*. This is the scenario of interest for this paper as the pilots were asked to track a displayed error on a head-down display. When the system input, *i*, is a known forcing function such as a sum-of-sines, then each element of the pilot-vehicle system can be identified from the flight test data. For these cases, the pilot describing functions can be determined and the type of pilot compensation employed can therefore be identified.

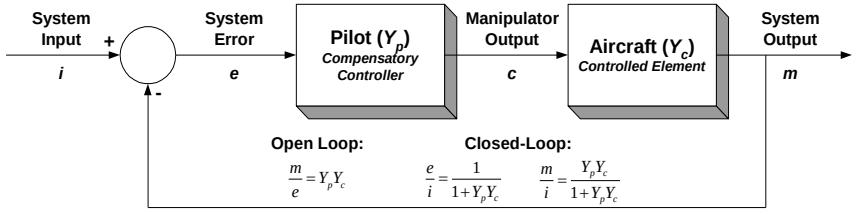

Figure 11.2: *Compensatory control scenario.*

When attempting to minimize error in a compensatory control scenario, the pilot-vehicle system behavior is well predicted by the crossover model [6]. That is, at frequencies near the crossover frequency (the zero dB magnitude crossing of the *m*/*e* transfer function) the open loop pilot-vehicle system frequency response will look like an integrator plus an effective time delay:

$$Y_p Y_c = \frac{K}{j\omega} e^{-\tau j\omega} \tag{11.1}$$

where Y_p is the pilot describing function, Y_c is the controlled element, that is, the vehicle, K is a gain, and τ is an effective time delay. The bottom line is that the pilot adds compensation, typically lead compensation at a minimum, to achieve this result. Often, in high gain closed-loop control scenarios such as sum-of-sines tracking, the resulting pilot-vehicle system will have small phase margins, on the order of 10-20 degrees, as shown in Figure 11.3. Such cases are often seen in simulators where the pilot feels more at ease to increase his or her gain beyond the levels that would be seen in a flight test environment where the "seat of the pants" cues often temper pilot aggressiveness [7]. If something causes this phase margin to go away, for example, excessive effective time delay or flight control system nonlinearities such as control surface rate limiting [8], a PIO can result.

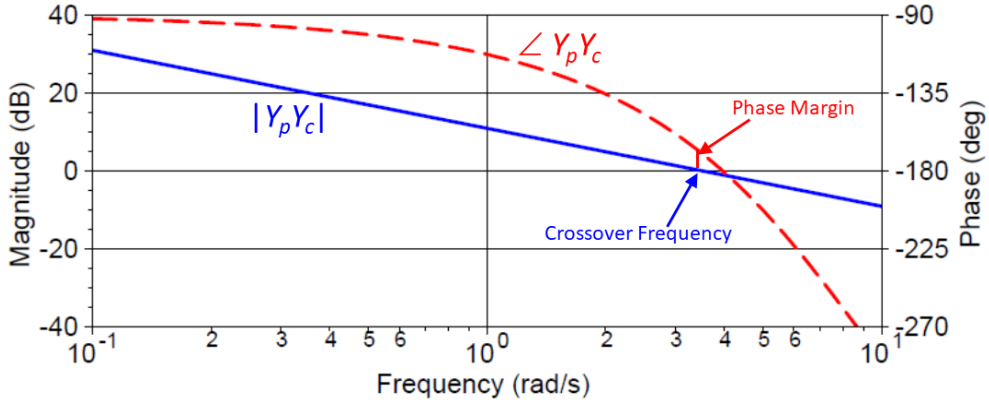

Figure 11.3: *Compensatory control pilot-vehicle system frequency response.*

During a flight test program that was evaluating the SAFE-Cue pilot-vehicle system loss of control mitigation scheme [9], one of the three evaluation pilots displayed a unique "bang-bang" control strategy while performing a roll axis tracking task. This behavior was observed for all aircraft configurations presented to the pilot. For those on board the aircraft, it was clear that this pilot had an adverse physiological response to the pitch tracking tasks evaluations, which then impacted the roll tracking tasks that followed. In this chapter, the observed behavior of this pilot is analyzed and compared to assess the impact of this unique control strategy on task performance, compensation, and resulting pilot opinion ratings. As part of the analysis, a new time-varying PIO metric is introduced that clearly illustrates the differences in the observed pilot behaviors.

11.2 Comparing Two Pilots

In this section, the baseline configuration runs of Pilot B and Pilot C from the SAFE-Cue evaluations in Chapter 9 are examined in the time and frequency domains. While Pilot B exhibited the "bang-bang" approach throughout his roll evaluations, the focus herein is on the baseline configuration that was designed to have Level 1 handling qualities with no PIO tendencies.

11.2.1 Time Series

Referring back to the compensatory system block diagram of Figure 11.2, the key time series signals are the sum-of-sines command input, *i*, shown in Figure 9.11 from Chapter 9, the pilot stick force command, *c*, and the vehicle bank angle response, *m*, shown below in Figure 11.4 and Figure 11.5 for the two pilots. The error signal, *e*, is generated by taking the difference between the commanded roll angle and the actual roll angle, $e = i - m$.

When examining the pilot stick force inputs and the resulting bank angle responses, differences between the two cases are clearly seen. Beginning with Pilot C, Figure 11.5, continuous control inputs of varying frequencies are seen with peak amplitudes between ±5 lbs. The resulting roll angle response reflects the tracked sum-of-sines input. For Pilot B, on the other hand, the time series reveal a much different pilot command, a "bang-bang" command that fixates on a single frequency and grows in intensity as the run progresses with peak magnitudes of ±10 lbs, see Figure 11.4. The resulting bank angle response reflects the sum-of-sines command but with significant oscillations that persist throughout the run. The magnitude of these oscillations varies from ±5 to ±10 degrees as the overall vehicle response follows the command.

In Figure 11.6, the time series from Figure 11.4 and Figure 11.5 are plotted as input/output pairs to better expose any 180° out-of-phase characteristics that are a key signature of PIO [10]. Again, beginning with Pilot C, there is no evidence of out-of-phase characteristics in his run. The same is not true for Pilot B. Here, Pilot B's command is 180° out-of-phase with the attitude response of the aircraft for essentially the entire run. The oscillations are not divergent, but they are of a significant amplitude. An intriguing note is that Pilot B did not recognize the PIO that his inputs were sustaining. In almost all cases, PIO reflects some vulnerability of the aircraft. In this case, the aircraft configuration was PIO resistant based on the applied criteria highlighted in Chapter 9, piloted simulation evaluations, checkout flight verification, and formal flight test evaluations [9]. It therefore appears from the time series analysis that this PIO may have resulted primarily from pilot technique.

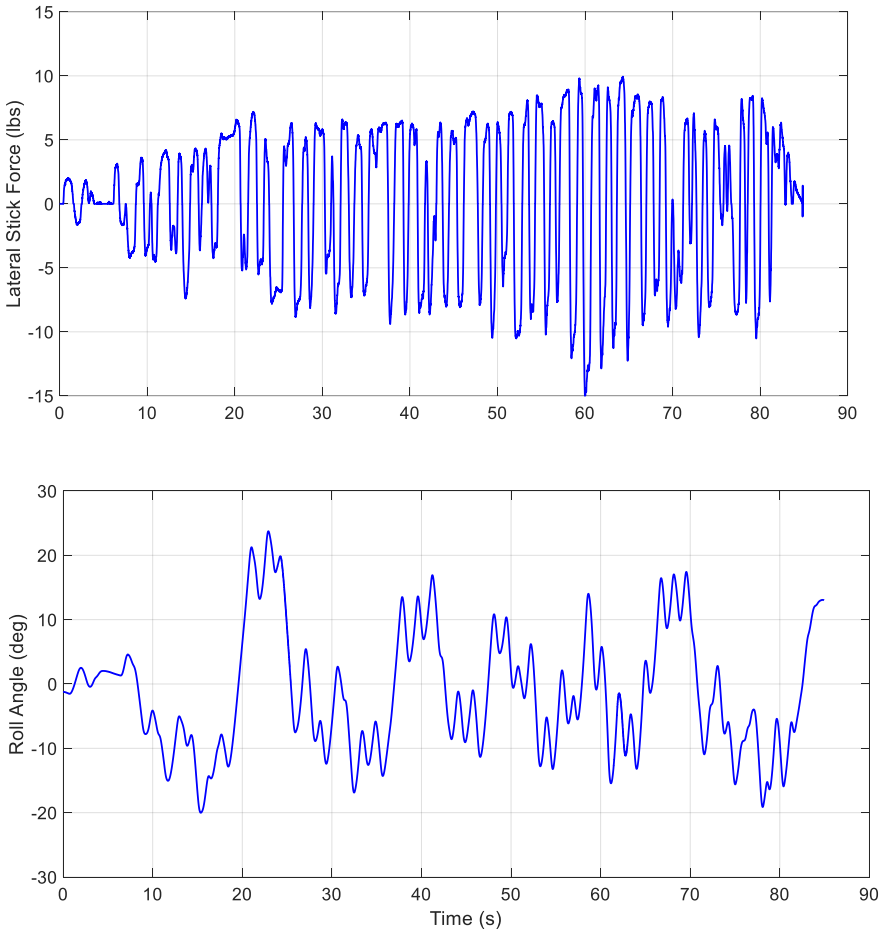

Figure 11.4: *Lateral stick force and bank angle time series for the SAFE-Cue baseline configuration Pilot B run.*

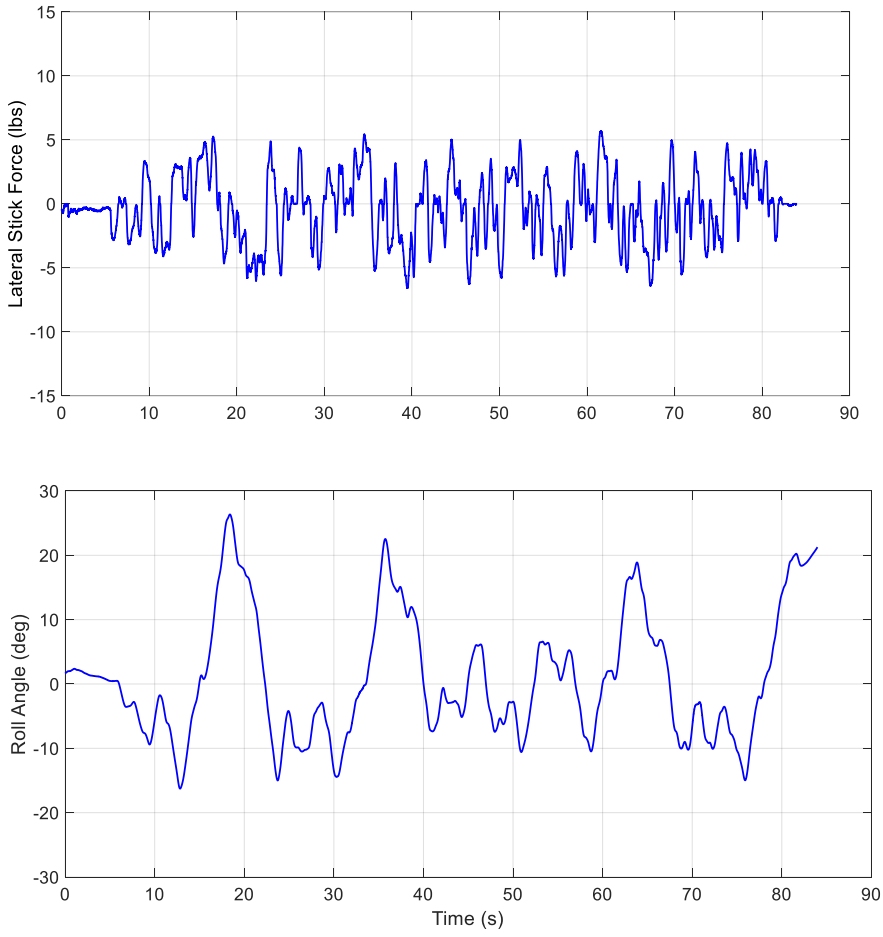

Figure 11.5: *Lateral stick force and bank angle time series for the SAFE-Cue baseline configuration Pilot C run.*

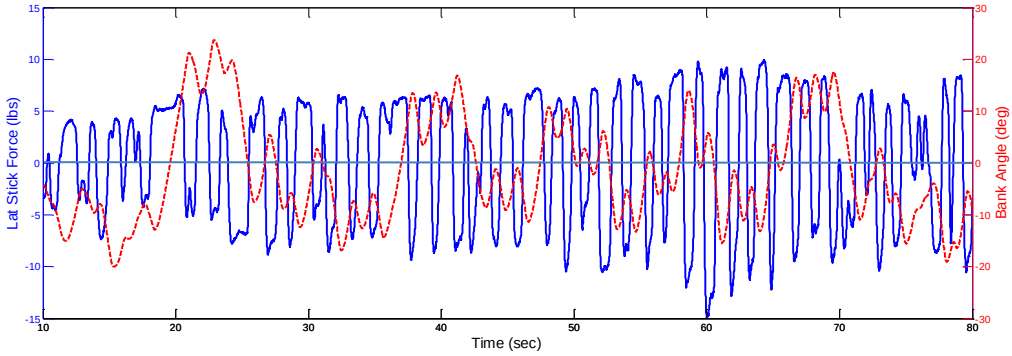

(a) Pilot B – sustained out-of-phase behavior

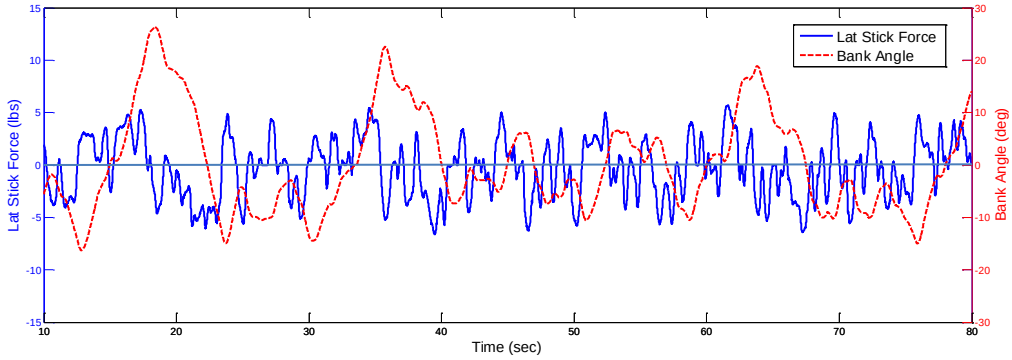

(b) Pilot C – nominal compensatory behavior

Figure 11.6: *Evidence of pilot-induced oscillations.*

11.2.2 Task Performance

Figure 11.7 provides an illustration of task performance via a direct comparison of achieved bank angle response versus commanded bank angle for each pilot. Differences between the two pilots are clearly evident in the figures. The more aggressive input reversal-reversal or bang-bang style of Pilot B results in an achieved bank angle response that consistently oscillates about the command signal. In stark contrast, the Pilot C achieved bank angle response more or less smoothly follows the commanded bank angle with no oscillation tendencies. The Pilot C approach results in a lower RMS error than Pilot B and a Level 1 Cooper-Harper Handling Qualities Rating [11] with no observed PIO tendencies. He did see some undesirable motions, but nothing that impacted task performance. Pilot B, on the other hand, rated the configuration much more harshly, a borderline Level 2/Level 3. Furthermore, his PIO Tendency Rating [12,13] of 2 indicates that he was not only unaware that he was in a sustained PIO, but also that the oscillations were a primary source of his degraded performance. This result is somewhat unusual

for test pilots, but far less so for operational pilots, both military and commercial, because these pilots are, in general, not exposed to the concept of PIO as part of their training. Why did this happen? As mentioned in the introduction, Pilot B seemed to display a negative physiological response to the repeated sum-of-sines tracking beginning with the pitch axis runs that were conducted first in each sortie. Given such a negative reaction, it is not unreasonable to assume that the physical discomfort could impact actual and perceived performance, and the resulting opinion ratings. As summarized in [9], Pilot B assigned 7 of 16 pitch and roll configurations, nearly half, a HQR 6, a trend not seen in the other pilots.

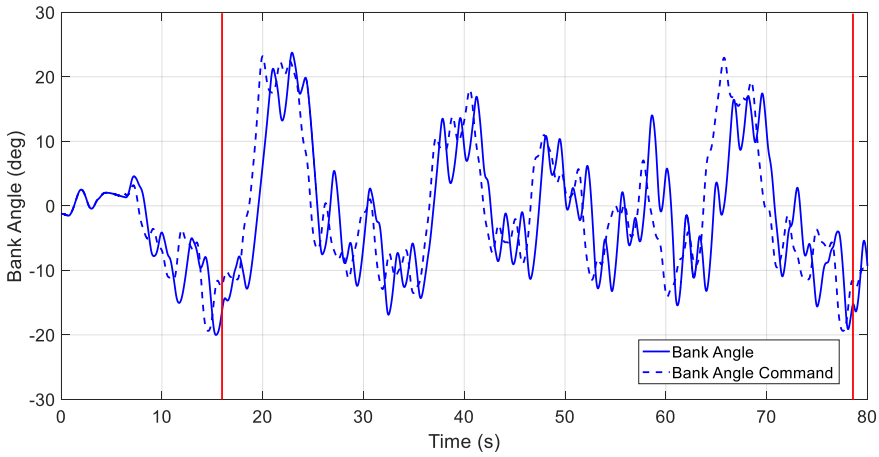

(a) Pilot B, RMS Error = 7.665, HQR 6/PIOR 2

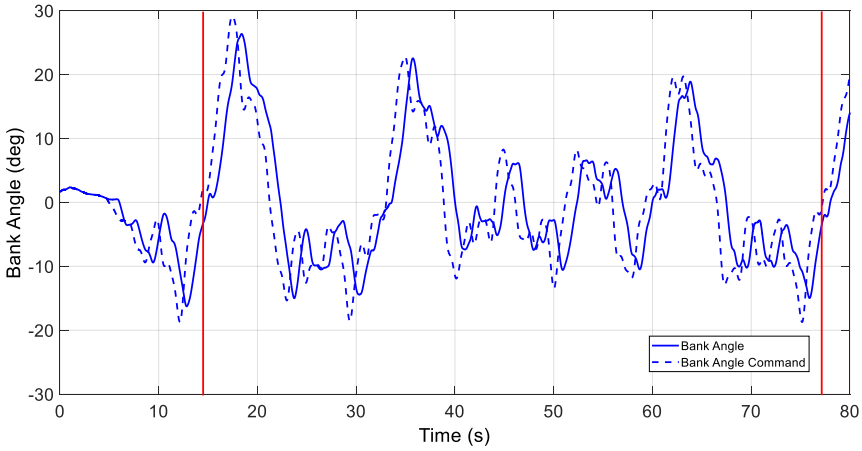

(b) Pilot C, RMS Error = 6.75, HQR 3/PIOR 2

Figure 11.7: *Bank angle versus bank angle command.*

11.2.3 Input Power Spectral Densities and Scalograms

Frequency domain analyses were conducted to further explore differences between Pilot B and C. First, fast Fourier transform (FFT) methods focusing only on the discrete sum-of-sines frequencies were used to obtain the stick force power spectral density plots for each pilot. The results are shown in Figure 11.8 where the sum-of-sines frequency points are shown as the filled circles and the raw FFT is shown as a thin line. Note that, as expected, there is essentially no power at frequencies other than the seven sum-of-sines frequencies. In the computation used herein, the FFT provided averaged input power over the task scoring time.

For Pilot B, the peak power at the 3.9 rad/s frequency is more than double the power at any of the other frequencies indicating that he had fixated his inputs at this frequency. In contrast, Pilot C has an essentially flat input power across the seven frequencies. His peak power at the 1.8 rad/s falls near the roll mode inverse time constant as is typical for a roll axis task. The peak power of Pilot B, on the other hand, is well above not only the Dutch roll mode (2.4 rad/s), but also the roll mode (0.82 rad/s). Given these differences, it is interesting to note that the power at the three lowest frequencies is essentially the same for both pilots. This is also true for the highest frequency. Thus, the primary differences between the two pilots with respect to their input power occurs at only three frequencies, but these differences are significant. For Pilot C, his power drops off above the 1.8 rad/s frequency, while Pilot B's power increases above this frequency to a peak power that is approximately 2.5 times higher than Pilot C's peak power.

For more than a decade, wavelet-based system identification tools have been used to explore the time-varying nature of pilot-vehicle systems [10,14,15]. As defined in Appendix A, scalograms provide a time-varying look at the power of a given signal. In Figure 11.9, lateral stick force scalograms are shown for both pilots. Each figure shows power versus frequency and time. Essentially, each power versus time "slice" represents a power spectral density plot at that time. Starting with Pilot C's scalogram, it is seen that the pilot behavior was consistent over the length of the run with the dominant power peak at 1.8 rad/s frequency. The behavior of Pilot B, on the other hand, varies over the length of the run. Over the first 20 seconds or so, the pilot is more or less focused at 1.8 rad/s frequency with nearly equivalent power at the next two high frequencies. Over the next 10 seconds, he gradually transitions to the 3.9 rad/s frequency and once there, his power increases significantly over the next 20 seconds peaking at a power that is approximately 10 times higher than Pilot C's peak power before dropping off again to end the run. It will be shown in the subsequent analysis that it is this behavior that drives the PIO in Pilot B's run.

11.2.4 Pilot-Vehicle System Responses

As described in the introduction, the known sum-of-sines input allows for describing functions to be identified for the complete pilot-vehicle system using FFT-based methods. Results are shown in Figure 11.10 for the pilot, Y_p, the open-loop system, Y_pY_c, and the closed-loop system. In comparing pilot describing functions, Figure 11.10(a), it is seen that both pilots are adding lead compensation. For Pilot B, however, the lead compensation begins at a lower frequency and is more aggressive in terms of gain than that of Pilot C. For Pilot B, the resulting phase lead is observed between 2 and 4 rad/s. The cost of Pilot B's more aggressive compensation is significantly more phase lag at higher frequencies.

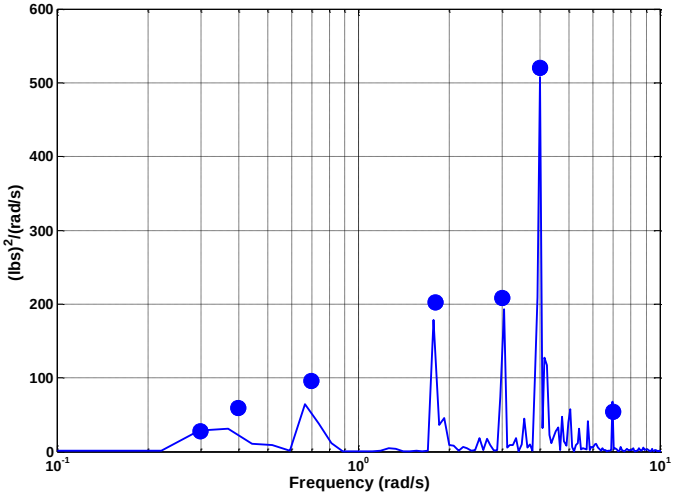

(a) Pilot B

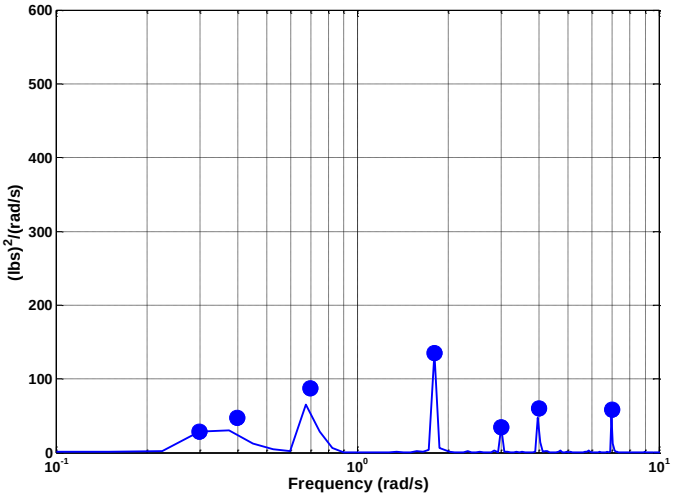

(b) Pilot C

Figure 11.8: *Lateral stick force power spectral density plots.*

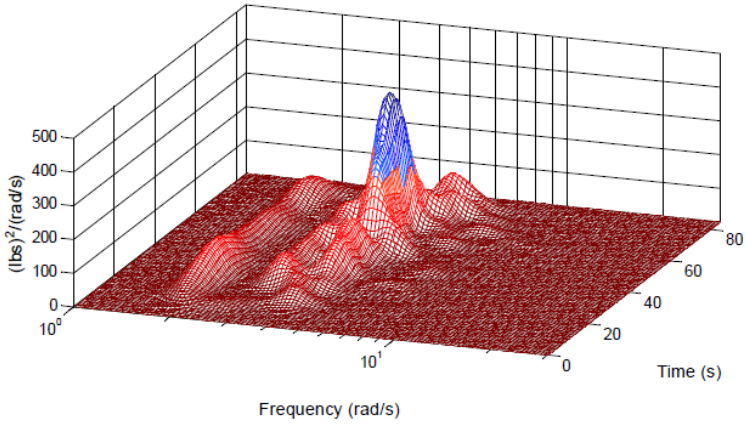

(a) Pilot B

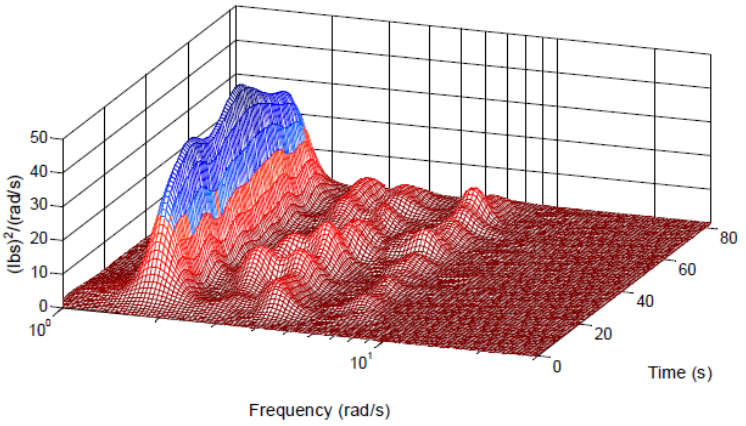

(b) Pilot C

Figure 11.9: *Lateral stick force scalograms.*

The open-loop describing functions are shown in Figure 11.10(b). Note that Pilot C has made good the crossover model [2,6] with a "k/s-like" magnitude response from the lowest frequency through the crossover frequency just below 2 rad/s. Pilot B, on the other hand, has a magnitude response slope that shallows compared to Pilot C due to the more aggressive lead compensation. Furthermore, the combined pilot-vehicle response of Pilot B has a more significant phase roll-off. Combined with his higher crossover frequency, this will result in a more oscillatory closed-loop response and in this case a PIO. This is further illustrated by the significant closed-loop system peak magnification for Pilot B in Figure 11.10(c). No such peak is present for Pilot C. These describing functions thus illustrate that the more aggressive lead compensation and crossover frequency and the corresponding increased phase lag at higher frequencies resulted in the sustained PIO for Pilot B, while Pilot C saw no PIO tendencies.

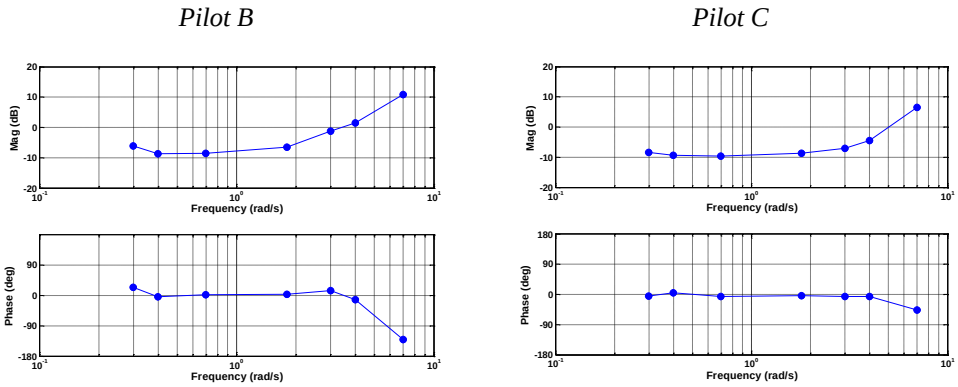

(a) Pilot describing functions (Y_p)

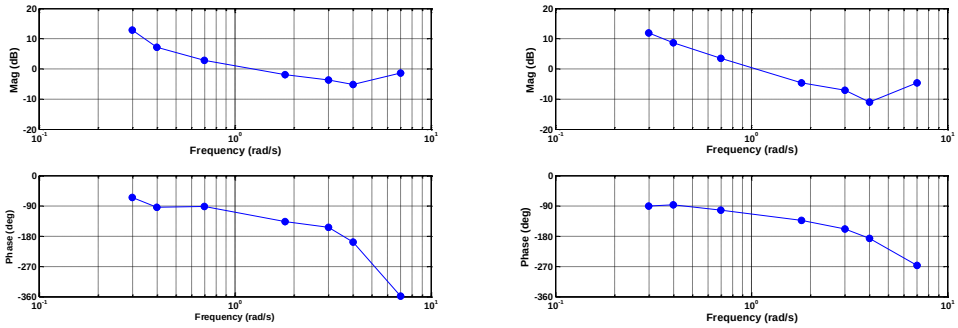

(b) Pilot-vehicle open-loop describing functions (Y_pY_c)

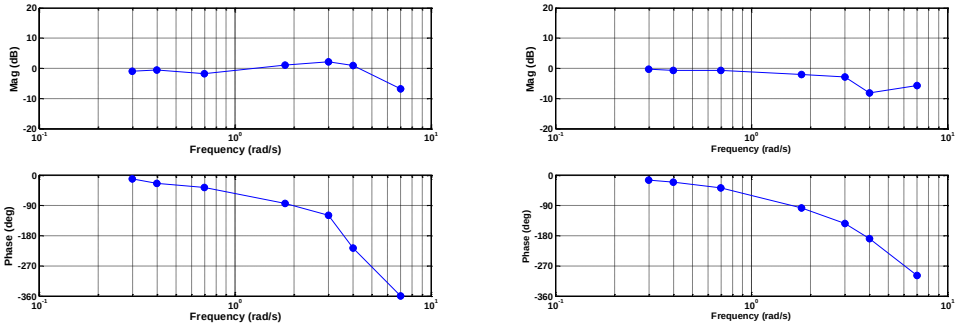

(c) Pilot-vehicle closed-loop describing functions [$Y_pY_c/(1+ Y_pY_c)$]

Figure 11.10: *Pilot-vehicle system describing functions.*

Though not shown in Figure 11.10, the pilot-vehicle system describing function analysis can also identify the controlled element, $Y_c = m/c$ (from Figure 11.2), where m is the roll rate and c is the lateral stick force. The resulting phase responses of the controlled element for the two baseline configuration runs are shown in Figure 11.11. If the controlled element response were fully linear, the two phase responses would overlay. This is not, however, the case as the Pilot B cases displays more phase lag then is seen for the Pilot C run. The added phase lag results from intermittent aileron control surface rate limiting in the Pilot B case. The baseline configuration had a 100 deg/s maximum aileron rate, which was more than adequate for the evaluation tasks used herein – unless the pilot inputs feature large amplitude commands at higher frequencies as was the case with Pilot B. As discussed previously, Pilot B had sustained and significant input power at 3.9 rad/s that resulted in the approximately 15 degrees of added phase lag shown in the figure at this frequency.

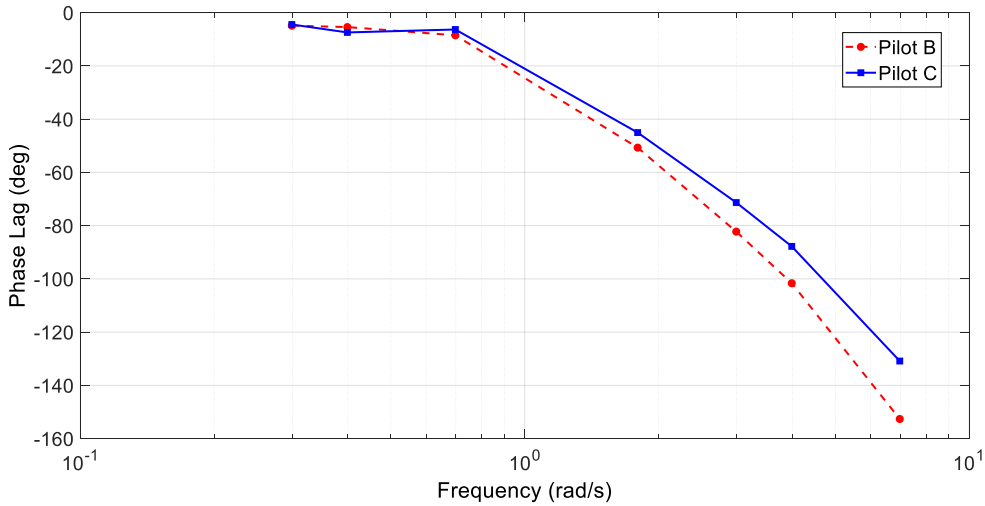

Figure 11.11: *Controlled Element Phase Lag Comparison.*

Using a gain, first order leads, and effective time delay terms, transfer function fits were made to the Y_p describing functions shown in Figure 11.10(a). The resulting frequency responses are shown in Figure 11.12 where the solid lines show the resulting magnitude response and dashed lines show the resulting phase response fits to the magnitude (circles) and phase (squares) data from Figure 11.10(a). For Pilot B, an emphasis was made to match the magnitude and phase at 3.9 rad/s where so much of his input power was concentrated. The resulting fits reveal higher gain, more aggressive lead compensation, and 100 msec more effective delay for Pilot B when compared to Pilot C. The more aggressive technique combined with the added delay resulted in the sustained PIO for Pilot B, where Pilot C found his compensation to be consistent with a Level 1 airplane. The reader is reminded here that despite the sustained oscillations, Pilot B did not recognize that he was in a PIO. He did, however, recognize the "extensive compensation" he was employing as reflected in his handling qualities rating of 6 (borderline Level 2/3). It is somewhat

unusual to see a double lead term in the pilot model, however, similar best "fits" to experimental data have been noted and explored in the literature [16].

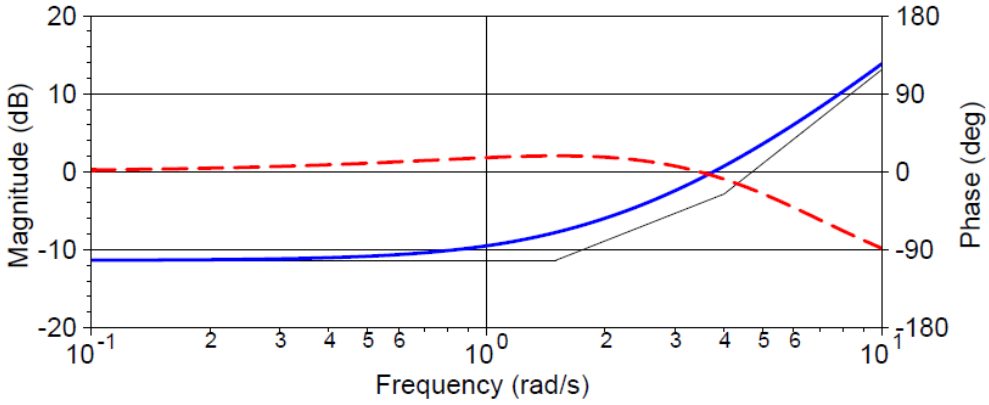

$$Y_p = 0.045(s+1.5)(s+4)e^{-0.55s}$$

(a) Pilot B

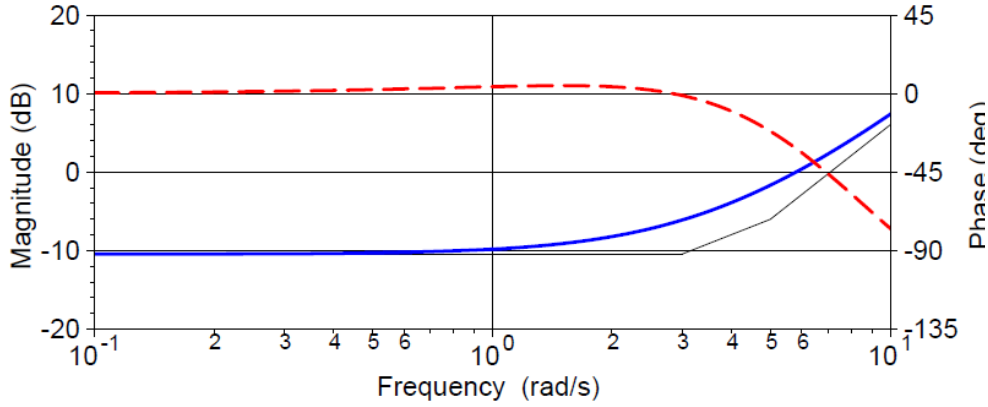

$$Y_p = 0.02(s+3)(s+5)e^{-0.45s}$$

(b) Pilot C

Figure 11.12: *Transfer function fits to pilot, Y_p, describing functions.*

11.3 A Scalogram-based PIO Detection Metric

Previous work [10] has shown that scalograms, as defined in Appendix A, could be used to graphically expose potential PIO susceptibility. Furthermore, the Power Frequency [15] metric was defined to provide a means to better correlate observed pilot input activity with handling

qualities ratings. Still it seemed possible to find a direct measure of PIO susceptibility using scalogram-derived data that has not yet been identified. The real-time oscillation verifier (ROVER) developed by Mitchell, et al. [17] uses estimated frequency, phase, and input/output magnitudes as key PIO flags. More recently, Jones, et al. have proposed a new PIO metric [18] known as the Phase Aggression Criterion that computes a "phase distortion" in the time domain between input and output signals. These methods feature parameters or analogs that can be identified from appropriately selected scalograms.

Building upon this past work, a new scalagram-based PIO metric was conceived that features a time-varying measure of peak input power at a given time versus weighted phase lag. The input signal is $c(t)$ and the controlled element is $Y_c(\omega)$, respectively, stick force and roll rate to stick force in this example. The scalogram $P(\omega,t)$ is the input power versus both frequency and time. The peak input power versus time is,

$$P_{max}(t) = P(\omega_{max}(t),t) \tag{11.2}$$

where $\omega_{max}(t)$ is the frequency at which the maximum power occurs, and the phase lag versus time is,

$$\phi_{max}(t) = \text{phase}(Y_c(\omega_{max}(t))) \tag{11.3}$$

A weighted version of both frequency and phase takes into account the spread across frequency of the power and presents a better visual comparison using peak input power versus weighted phase lag. The weighting functions are:

$$\begin{aligned}
\hat{\omega}_{max}(t) &= \frac{1}{\Psi(t)}\int_0^\infty P^2(\omega,t)\omega d\omega \\
\hat{\phi}_{max}(t) &= \frac{1}{\Psi(t)}\int_0^\infty P^2(\omega,t)\phi(\omega) d\omega \\
\Psi(t) &= \int_0^\infty P^2(\omega,t) d\omega
\end{aligned} \tag{11.4}$$

Results for the two example cases used in this chapter are shown in Figure 11.13. To generate the proposed metric plot on the right, the intermediate computations shown on the left were generated. First, the peak input power is computed directly from the scalograms of the lateral stick force time series. Next, a weighted frequency is computed based on pilot input power. For Pilot C, the weighted frequency remains at approximately 2 rad/s for the entire run. For Pilot B, on the other hand, the weighted frequency increases from 2 rad/s to just under 4 rad/s over the first half of the run and then remains at this level for the remainder of the run. This weighted frequency is then used to compute a weighted phase lag from the aircraft controlled element roll rate phase responses shown in Figure 11.11. It is possible to compute phase directly from scalograms [19], but noise sensitivity is an issue as frequency increases. Thus, the FFT-based phase results offer an averaged or smoothed phase computation.

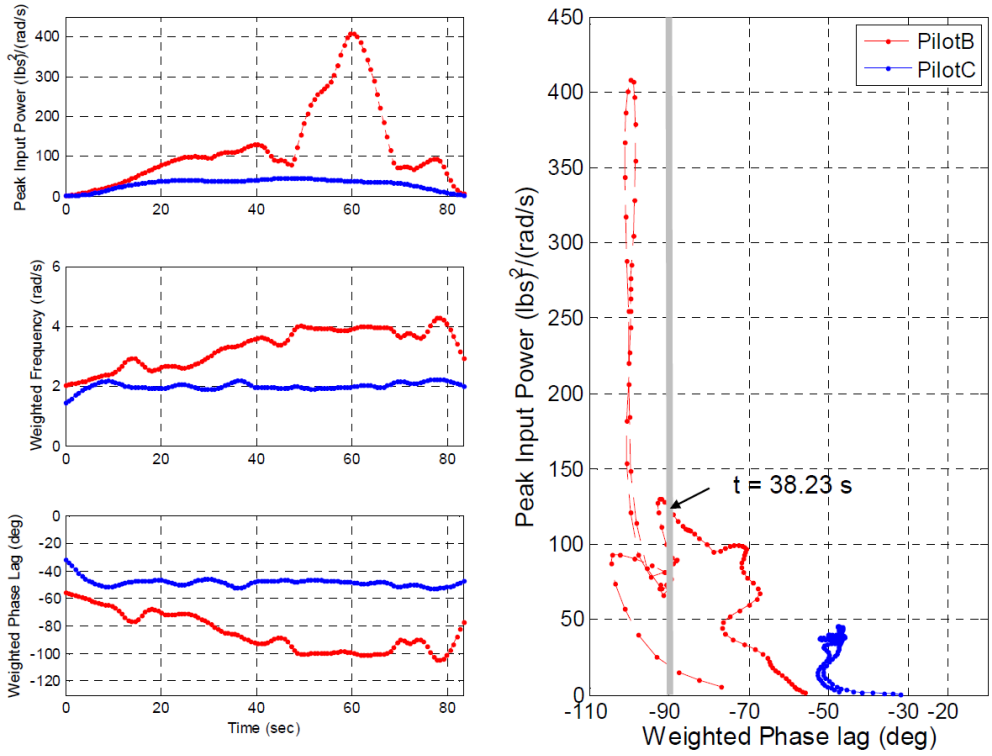

Figure 11.13: *The Inceptor Peak Power – Phase PIO metric.*

The weighted phase lag is derived from a rate, not an attitude frequency response, so PIO susceptibility is defined in the neighborhood of -90 degrees of phase lag. If the pilot was operating only as a pure gain, the phase lag associated with the PIO would be exactly -90 degrees. Because of additional pilot compensation, this ideal case is rarely the observed case. Reviewing the Pilot C fitted transfer function from Figure 11.12, there is little added phase lag or lead from the pilot at the 2 rad/s. For Pilot B, on the other hand, approximately 20 degrees of added phase lag results when the pilot is operating at the nearly 4 rad/s frequency. Combined with the phase lag from the controlled element, a PIO results. This result is clearly differentiated in the peak power versus weighted phase lag plot. The Pilot C case does not build up in amplitude and there is significant margin from the critical phase lag range near -90 degrees. For the Pilot B case, on the other hand, the input power grows significantly over the course of the run and from approximately the 38 second point of the run, the locus of points enters the critical phase lag region and remains in this region for the remainder of the run.

11.4 Conclusions

As part of a flight test evaluation of the Smart Adaptive Flight Effective Cue or SAFE-Cue system, disparate pilot behaviors were observed when evaluating the baseline aircraft

configuration in the roll axis. From the analysis of the flight test data, the following conclusions are made.

The time response data revealed a “bang-bang” pilot control behavior for Pilot B that was in stark contrast to that observed in the Pilot C input response. Furthermore, the time response data revealed the presence of a pilot-induced oscillation in the Pilot B run that is sustained throughout the run. Analysis of the power spectral density plots computed from the lateral stick force time series of the two pilots revealed an input power for Pilot C that drops off above 1.8 rad/s frequency, while Pilot B’s power increases above this frequency to a peak power that is approximately 2.5 times higher than Pilot C’s peak power. In these cases, the power was averaged over the scoring time for the tracking task. Using time-varying scalograms, Pilot C’s peak input power was found to remain at a frequency of approximately 2 rad/s for the entire run. The frequency of Pilot B’s input power, on the other hand, varied over the length of the run. Beginning at approximately 20 seconds, Pilot B gradually transitions from a peak power at around 2 rad/s to a peak power around 4 rad/s and once there, the power increases significantly over the next 20 seconds peaking at a value that is approximately 10 times higher than Pilot C’s peak power.

Pilot-vehicle system describing functions illustrated that the more aggressive lead compensation and crossover frequency and the corresponding increased phase lag at higher frequencies resulted in the sustained pilot-induced oscillation for Pilot B, while Pilot C saw no such tendencies. Using a gain, first order leads, and effective time delay terms, transfer function fits were made to the pilot describing functions. The resulting fits revealed higher gain, more aggressive lead compensation, and 100 msec more effective delay for Pilot B when compared to Pilot C. Despite the sustained oscillations, Pilot B did not recognize that he was in a PIO. He did, however, recognize the “extensive compensation” he was employing as reflected in his handling qualities rating of 6.

Building upon past work, a new scalagram-based PIO metric was conceived that features a time-varying measure of peak input power at a given time versus weighted phase lag. Results showed that the Pilot C case did not build up in amplitude and there was significant margin from the critical phase lag range near -90 degrees. For the Pilot B case, the input power grew significantly over the course of the run and from approximately the 38 second point of the run, the locus of points entered the critical phase lag region and remained in this region for the remainder of the run. Though a much more thorough review of available data is required to elevate this analysis method to that of a candidate PIO criterion, the results presented in this chapter show promise.

Finally, the diverse analysis methods employed in this chapter revealed many facets of pilot behavior that can produce diverse results when conducting the same evaluation task with the same aircraft configuration. Thus, it cannot be emphasized enough the importance of a thorough analysis of the quantitative data in contrast to an over reliance on the qualitative pilot comments and ratings. Both are important, and both are needed for more complete comprehension of the pilot-vehicle system. In the next chapter, the utility of the proposed PIO metric is explored using the Smart-Cue/Smart-Gain flight test database that was introduced in Chapter 8.

11.5 References

1. Klyde, D. H., P. C. Schulze, and P. M. Thompson, "Exposing Unique Pilot Behaviors from Flight Test Data," AIAA Paper No. 2015-0239 presented at the *Science and Technology Forum and Exposition 2015: AIAA Atmospheric Flight Mechanics Conference*, Kissimmee, Florida, January 5-9, 2015.

2. McRuer, D. T., and H. R. Jex, "A Review of Quasi-Linear Pilot Models," *IEEE Trans. Human Factors in Electronics*, Vol. HFE-8, No. 3, Sept. 1967, pp. 231 to 249.

3. Hess, R. A., "A Pilot Modeling Technique for Handling-Qualities Research," AIAA Paper No. 1980-1624 presented at the *Atmospheric Flight Mechanics Conference*, Danvers, MA, 11-13 Aug. 1980.

4. Breur, S. W., D. M. Pool, M. M. van Paassen, and M. Mulder, "Effects of Displayed Error Scaling in Compensatory Roll-Axis Tracking Tasks," AIAA 2010-8091 presented at the *Modeling and Simulation Technologies Conference*, Toronto, ON, 2-5 Aug. 2010.

5. Zollner, H. G. H., D. M. Pool, H. J. Damvfeld, M. M. van Paasen, and M. Mulder, "The Effects of Controlled Element Break Frequency on Pilot Dynamics During Compensatory Target-Tracking," AIAA 2010-8092 presented at the *Modeling and Simulation Technologies Conference*, Toronto, ON, 2-5 Aug. 2010.

6. McRuer, D. T., and E. S. Krendel, *Mathematical Models of Human Pilot Behavior*, AGARDograph No. 188, Nov. 1973.

7. Klyde, D. H., A. K. Lampton, P. C. Schulze, D. J. Alvarez, R. Johnson, and L. Rowe, "The Real Flight Approach to Assess Simulator Force Cueing Fidelity," AIAA Paper No. 2013-5161 presented at the *Atmospheric Flight Mechanics Conference*, Boston, MA, 19-22 Aug. 2013.

8. Klyde, D. H., and D. G. Mitchell, "Investigating the Role of Rate Limiting in Pilot-induced Oscillations," *J. Guidance, Control, and Dynamics*, Vol. 27, No. 5, Sept.-Oct. 2004, pp. 804-813.

9. Klyde, D. H., A. K. Lampton, N. D. Richards, B. Cogan, "Flight Test Evaluation of a Loss of Control Mitigation System," *J. of Guidance, Control, and Dynamics*, Vol. 40, No. 4, April 2017, pp. 981-997.

10. Mitchell, D. G. and D. H. Klyde, "Identifying a Pilot-Induced Oscillation Signature: New Techniques Applied to Old Problems," *J. of Guidance, Control, and Dynamics*, vol. 31, no. 1, Jan.-Feb. 2008, pp. 215-224.

11. Cooper, G.E., and Harper, Jr., R.P., *The Use of Pilot Rating in the Evaluation of Aircraft Handling Qualities*, NASA TN D-5153, Apr. 1969.

12. DiFranco, D. A., *Flight Investigation of Longitudinal Short Period Frequency and PIO Tendencies*, AFFDL-TR-66-163, June 1967.

13. Weingarten, N. C., and C. R. Chalk, *In-Flight Investigation of Large Airplane Flying Qualities for Approach and Landing*, AFWAL-TR-81-3118, Sept. 1981.

14. Thompson, P. M., D. H. Klyde, and M. Brenner, "Wavelet-Based Time-Varying Human Operator Models," AIAA Paper 2001-4009 presented at *Atmospheric Flight Mechanics Conference*, Montreal, Canada, 6-9 August 2001.

15. Lampton, A., and D. H. Klyde, "Power Frequency: A Metric for Analyzing Pilot-in-the-Loop Flying Tasks," *J. of Guidance, Control, and Dynamics*, Vol. 35, No. 5, Sept.-Oct. 2012, pp. 1526-1537.

16. Pool, D. M., P. M. T. Zaal, H. J. Damveld, M. M. van Paassen, and M. Mulder, "Pilot Equalization in Manual Control of Aircraft Dynamics," proceedings of the *2009 IEEE International Conference on Systems, Man, and Cybernetics*, San Antonio, TX, Oct. 2009.

17. Mitchell, D.G., Arencibia, A.J., and Muñoz, S., "Real-Time Detection of Pilot-Induced Oscillations," AIAA-2004-4700, presented at *Atmospheric Flight Mechanics Conference*, Providence, RI, Aug. 2004.

18. Jones, M., and M. Jump, "Subjective and Objective Evaluation of PIO Tendencies," paper presented at *70th Annual Forum of the American Helicopter Society International*, Montreal, Quebec, 20-22 May 2014.

19. Thompson, P. M., D. H. Klyde, E. N. Bachelder, and T. J. Rosenthal, *On-line Loss of Control Detection using Wavelets*, NASA CR-2005-212873, July 2005.

12. Assessment of a Scalogram-Based PIO Metric with Flight Test Data

If there is one overwhelming recommendation that can be made, it is that all parties involved in the development of a new aircraft must always be prepared for the occurrence of PIO. It should not come as a complete surprise.

David Mitchell, Mitchell Aerospace Research, from Development of Methods and Devices to Predict and Prevent Pilot-Induced Oscillations, WL-TR-2000-3046

Parts of this chapter have been published as:

Title	Assessment of a Scalogram-Based PIO Metric with Flight Test Data
Conference	AIAA-2017-1641 presented at the Science and Technology Forum and Exposition 2017: AIAA Atmospheric Flight Mechanics Conference, Grapevine, TX, Jan. 9–13, 2017
Authors	D. H. Klyde, P. C. Schulze, R. Mello, and D. G. Mitchell
Title	Assessment of a Scalogram-Based Pilot-Induced Oscillation Metric with Flight Test and Simulation Data
Journal	Journal of Guidance, Control, and Dynamics, vol. 43, no. 11, Nov. 2020, pp. 2058-2072
Authors	D. H. Klyde, P. C. Schulze, R. Mello, D. G. Mitchell, N. Cameron, C. Cunliffe, and M. White

12.0 ASSESSMENT OF A SCALOGRAM-BASED PIO METRIC WITH FLIGHT TEST DATA

From advanced military aircraft to modern commercial transports and from business jets to rotorcraft, fly-by-wire flight control systems are now common place. This offers designers the ability to tailor response types via various flight control modes to specific missions or flight conditions. The mode transitions, envelope limiting, and control surface rate and position saturation that can accompany fly-by-wire designs may lead to pilot-vehicle system loss of control in the form of pilot-induced oscillations (PIO). With most fly-by-wire designs, the PIO tendencies have surfaced in flight test allowing for modifications that can reduce these tendencies. Building on the candidate metric introduced in Chapter 11, this chapter explores the use of a wavelet scalogram-based metric that considers the time-varying peak pilot input power as a function of the controlled element phase at the frequency of the peak power, all of which are elements of the previously defined PIO signature. A flight test database generated in the evaluation of the Smart-Cue/Smart-Gain PIO mitigation concept is used to assess the utility of the proposed approach. The results of the assessment indicate that the new metric was successful at identifying correctly both PIO and non-PIO cases. The contents of this chapter were largely based on [1,2].

12.1 Introduction

As discussed in [3], PIO have a distinct signature as described in the following four conditions that must be present:

Condition 1: There must be an oscillation. Oscillatory behavior is often observed in normal piloted operation and cannot be taken, alone, as a precursor to PIO. Attempts have been made to characterize non-oscillatory events that might fit some of the other conditions listed below.

Condition 2: The aircraft response must be out of phase with the pilot input. There will be a measurable state that shows an approximately 180 degree phase difference with the pilot's inputs, the most common states being pitch or roll attitude. This condition was observed by Chalk [4] and occurs in the vast majority of documented PIOs [5].

Condition 3: The frequency of the oscillation must be in a range where PIO occurs. Although catastrophic PIO have been observed at frequencies near the phugoid mode [6], the most common frequencies by far are between about 1 and 8 rad/s. As an example, Figure 12.1 from [7] shows a cross plot of average PIO frequency versus maximum peak-to-peak amplitude of angular rate, Figure 12.1(a), and amplitude of cockpit control force input, Figure 12.1(b), for a representative sampling of PIOs. Small-amplitude roll oscillations, usually identified as "roll ratchet," and often not considered to be PIO at all, occur at frequencies above 10 rad/s, and at least one yaw oscillation or "yaw chatter" was observed at 25 rad/s. The most severe events (solid symbols), however, are between about 1 and 8 rad/s. Figure 12.1 classifies PIOs that were identified in their references as clearly being relatively severe or relatively mild; the severe event at almost 8 rad/s and peak-to-peak pitch rate amplitude of 40 deg/s was the well-known T-38A PIO [8].

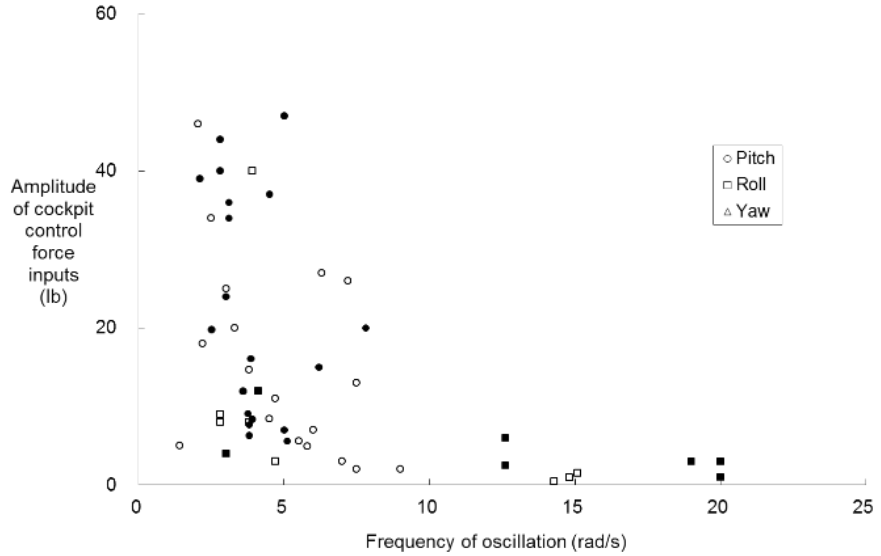

(a) Amplitude of cockpit control force input

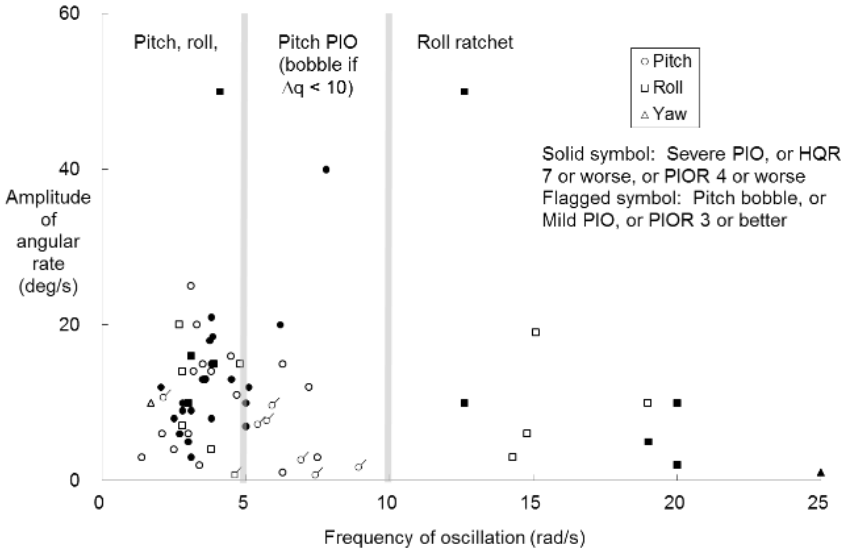

(b) Amplitude of angular rate

Figure 12.1. *Frequency and amplitude distribution of documented PIOs [7].*

Condition 4: The amplitude of control inputs, aircraft responses, or both, must be large enough to care. Pilots typically apply numerous small-amplitude inputs at the frequency range corresponding to PIO. As long as the control inputs and aircraft responses are sufficiently small, the pilot will not consider it a sign of PIO even if the frequency and phase angle are in the PIO region. PIO with surface rate limiting, classified as Category II PIO [9], may have very large control inputs with aircraft response minimized by the rate limiting. If the rate limiting is sufficiently intrusive, the pilot may even consider it to be a severe event, and if the rate limiting causes a loss of augmentation, a divergent PIO may, and probably will, result.

It is possible to make general characterizations for oscillatory phenomena based on Figure 12.1.

- *Roll ratchet/yaw chatter* are characterized by oscillations at frequencies above about 2 Hz (12 rad/s). Maximum angular rates are normally about 10 deg/s or less, though ratchets with roll rates as high as 50 deg/s have occurred. Control forces are always relatively low, however, generally below about 5 lbs. They can be considered violent if accompanied by large side accelerations. Occurrence in roll is usually related to excessive control sensitivity; in yaw related to Dutch roll damping.
- *Pitch bobble* can occur at any frequency between about 1 and 9 rad/s, but most commonly at frequencies above 5 rad/s. Bobble is characterized by maximum pitch rates of 10 deg/s or less and maximum control forces of 5 lbs or less.
- *High-frequency pitch PIOs* have frequencies above 5 rad/s, and severe PIOs can exhibit pitch rates from less than 10 deg/s to at least 40 deg/s. Control forces are usually above 10 lbs, but severe PIOs can also have forces well below 10 lbs.

Pitch, roll, and yaw PIOs that are most often destructive occur below about 5 rad/s. Angular rates are usually below 25 deg/s, though at least one case, the YF-16 “flight zero” incident [10], reached roll rates of 50 deg/s. There is no obvious separation between severe and non-severe PIOs in this frequency range. Many of the low-pitch-rate severe events in Figure 12.1a resulted from extreme actuator rate limiting; very high control forces, solid circles between 35 and 45 lbs in Figure 12.1(b), generated only small pitch rates and the pilots assigned these cases Handling Qualities Ratings [11] (HQRs) of 8, 9, or 10.

This chapter explores the use of these PIO signature characteristics to define a new PIO metric, the Inceptor Peak Power-Phase metric that can be used to identify PIO in a real-time flight test environment.

12.2 The Inceptor Peak Power – Phase Metric

12.2.1 Defining the Proposed Metric[3]

Previous work [3] has shown that scalograms, as defined in Appendix A, could be used to graphically expose potential PIO susceptibility. Furthermore, the Power Frequency [15] metric was defined to provide a means to better correlate observed pilot input activity with handling qualities ratings. Still it seemed possible to find a direct measure of PIO susceptibility using scalogram-derived data that has not yet been identified.

The real-time oscillation verifier (ROVER) developed by Mitchell, et al. [12] uses estimated frequency, phase, and input/output magnitudes as key PIO flags. More recently, Jones, et al. have proposed a new PIO metric [13] known as the Phase Aggression Criterion (PAC) that computes a "phase distortion" in the time domain between input and output signals. These methods feature parameters or analogs that can be identified from appropriately selected scalograms.

Building upon this past work, a new scalagram-based PIO metric was conceived that features a time-varying measure of peak input power at a given time versus weighted phase lag. The input signal is $c(t)$ and the controlled element is $Y_c(\omega)$, respectively, stick force and roll rate to stick force in this example. The scalogram $P(\omega,t)$ is the input power versus both frequency and time. The peak input power versus time is,

$$P_{max}(t) = P(\omega_{max}(t),t) \tag{12.1}$$

where $\omega_{max}(t)$ is the frequency at which the maximum power occurs, and the phase lag versus time is,

$$\phi_{max}(t) = \text{phase}(Y_c(\omega_{max}(t))) \tag{12.2}$$

A weighted version of both frequency and phase takes into account the spread across frequency of the power and presents a better visual comparison using peak input power versus weighted phase lag. In short, the weighted version yields a more robust trajectory by reducing the discretized response of the non-weighted version. The weighting functions are:

[3] For completeness, Section 12.2.1 below has been repeated from Chapter 11.

$$\hat{\omega}_{max}(t) = \frac{1}{\Psi(t)} \int_0^\infty P^2(\omega,t)\omega d\omega$$
$$\hat{\phi}_{max}(t) = \frac{1}{\Psi(t)} \int_0^\infty P^2(\omega,t)\phi(\omega) d\omega$$
$$\Psi(t) = \int_0^\infty P^2(\omega,t) d\omega$$
(12.3)

Weighted results for the two example cases used in Chapter 11 are shown in Figure 12.2. To generate the proposed metric plot on the right, the intermediate computations shown on the left were generated. First, the peak input power is computed directly from the scalograms of the lateral stick force time series. Next, a weighted frequency is computed based on pilot input power. For Pilot C, the weighted frequency remains at approximately 2 rad/s for the entire run. For Pilot B, on the other hand, the weighted frequency increases from 2 rad/s to just under 4 rad/s over the first half of the run and then remains at this level for the remainder of the run. This weighted frequency is then used to compute a weighted phase lag from the aircraft controlled element roll rate phase responses shown in Figure 11.11 from Chapter 11. It is possible to compute phase directly from scalograms, but noise sensitivity is an issue as frequency increases [14]. Thus, the fast Fourier Transform-based phase results offer an averaged or smoothed phase computation.

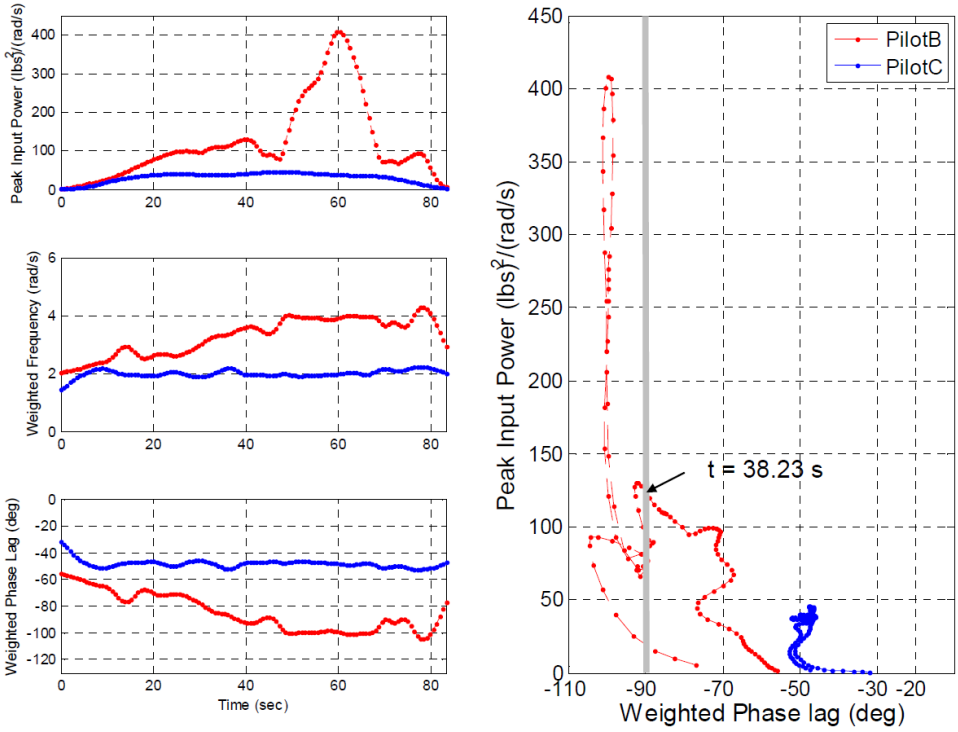

Figure 12.2: *The Inceptor Peak Power – Phase PIO metric.*

The weighted phase lag is derived from a rate, not an attitude frequency response, so PIO susceptibility is defined in the neighborhood of -90 degrees of phase lag. If the pilot was operating only as a pure gain, the phase lag associated with the PIO would be exactly -90 degrees. Because of additional pilot compensation, this ideal case is rarely the observed case. Reviewing the Pilot C fitted transfer function from Figure 11.12, there is little added phase lag or lead from the pilot at the 2 rad/s. For Pilot B, on the other hand, approximately 20 degrees of added phase lag results when the pilot is operating at the nearly 4 rad/s frequency. Combined with the phase lag from the controlled element, a PIO results. This result is clearly differentiated in the peak power versus weighted phase lag plot that feature trajectories that are a function of time. The Pilot C case does not build up in amplitude and there is significant margin from the critical phase lag range near -90 degrees. For the Pilot B case, on the other hand, the input power grows significantly over the course of the run and from approximately the 38 second point of the run, the locus of points enters the critical phase lag region and remains in this region for the remainder of the run. Because real time implementations of the wavelet-based methods have been established in previous work [14], such an implementation of the Inceptor Peak Power-Phase (IPPP) metric described herein is feasible.

12.2.2 Normalizing the Input Power

As described by the PIO signature, an out-of-phase characteristic between the pilot inceptor command and an aircraft output state is not enough to be considered a PIO. Specifically, the amplitude of the pilot input must be "large enough to care." Thus, to be an effective PIO metric, there is a need to separate those cases where there may be an out-of-phase oscillatory response, but the amplitude of the pilot input is too small to be considered PIO. The separation can be made by normalizing the inceptor peak power in some fashion such that a PIO/no PIO region can be defined. A number of normalizing terms were considered, but ultimately the historical data from Figure 12.1(a) were used. These data indicate that most of the pitch and roll severe events occurred with stick forces in the 35 to 40 lbs peak-to-peak range. Thus, an inceptor amplitude of ±17.5 lbs (35 lbs peak-to-peak) was found to cover roughly 80% of the events included in the figure. In Figure 12.3, the peak inceptor power versus phase lag plot from Figure 12.2 is repeated with the 17.5 lbs normalizing factor applied. Note that the normalizing factor is squared when applied to the peak power points at each time step. Further, the separation in character between the PIO and non PIO case remains distinct. Given this limited success, the application of the metric was next applied to a more complete flight test database in that a full range of handling qualities and PIO tendency ratings were present from several test pilot participants.

12.3 Flight Test Data Description

12.3.1 Flight Test Database

The flight test database used herein was generated during the Smart-Cue/Smart-Gain [15,16] flight test campaign that was part of a program conducted for NASA Armstrong Flight Research Center. Formal flight test evaluations were conducted from the Calspan Corporation facility at Niagara Falls Airport over the two week period from November 7-17, 2006 and the two day period from January 30-31, 2007. As described in Part II of this thesis, the Smart-Cue/Smart-Gain system was designed to mitigate the deleterious effects of control surface rate limiting that

can lead to severe Category II PIOs. The flight test database features pitch and roll cruise configurations and roll approach configurations.

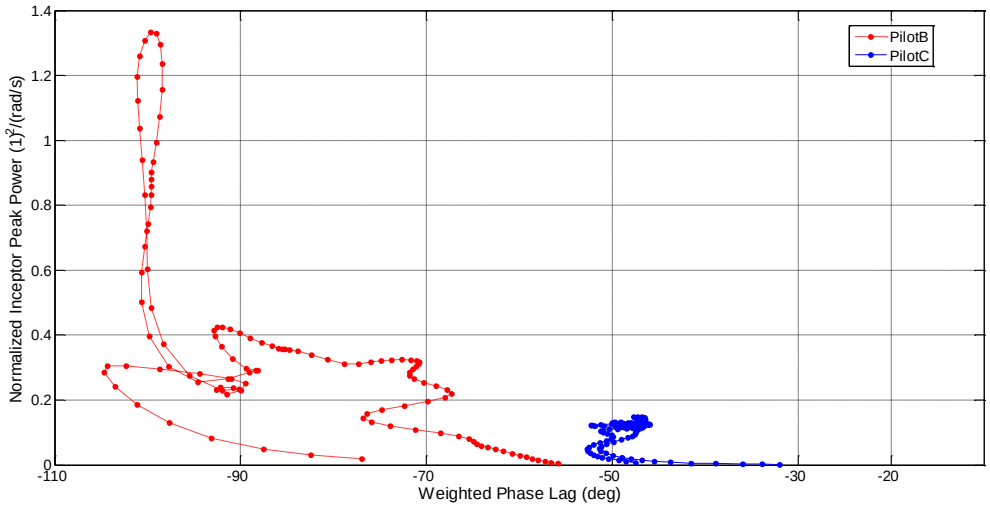

Figure 12.3: *Normalized Inceptor Peak Power-Phase (IPPP) metric.*

12.3.2 Aircraft Configurations

12.3.2.1 Pitch Cruise

The baseline pitch configuration was based on previous flight test configurations that were used in past PIO evaluation programs. The closed-loop dynamic response, shown in Figure 12.4, was designed to be similar to the 2D configuration from the famous Neal-Smith [17] program. The bare airframe configuration, however, was statically unstable. Pitch rate and angle of attack feedbacks were then used to achieve a 2D-like response as was done in the piloted simulation evaluations from [7]. As predicted by the Airplane Bandwidth plot of Figure 12.4, the baseline configuration was free of any PIO tendencies when control surface rate limiting was not present, but the configuration did have an abrupt initial response that some pilots found objectionable.

12.3.2.2 Roll Configurations

The frequency responses for the baseline roll cruise and approach configurations are shown in Figure 12.5 and Figure 12.6, respectively. The configurations were designed to allow for desired performance to be easily achieved by the pilots in the selected evaluation tasks as long as no control surface rate limits were encountered. As with the pitch cruise configuration, there were no PIO tendencies observed with the baseline roll configurations. This result was also predicted by the Airplane Bandwidth criteria as indicated in Figure 12.5 and Figure 12.6.

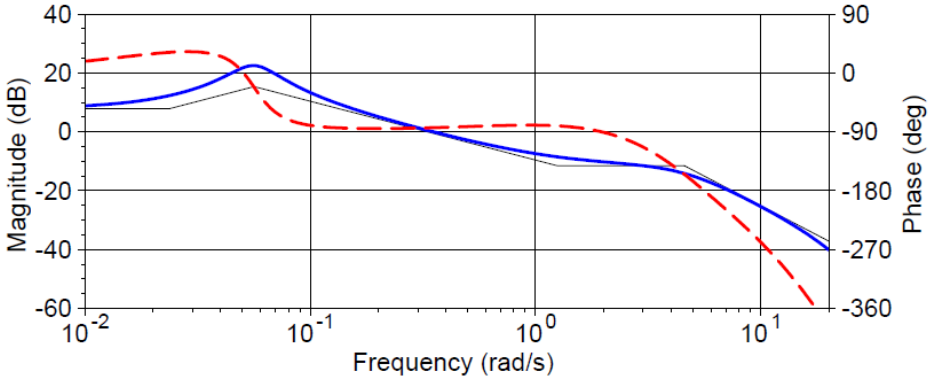

$$\frac{\theta}{F_{Lon}} = \frac{1.25e7(0.02379)(1.246)}{[0.2389, 0.05637][0.702, 4.571][0.7, 20][0.7, 75]} e^{-0.10s}$$

(a) Baseline pitch attitude to longitudinal stick force Bode frequency response

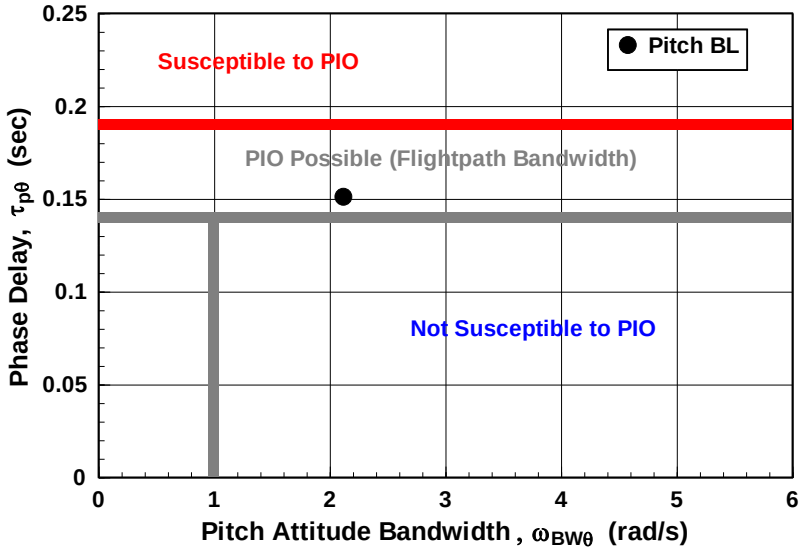

(b) Airplane Bandwidth PIO susceptibility prediction

Figure 12.4: *Pitch axis cruise configuration frequency response and Airplane Bandwidth assessment.*

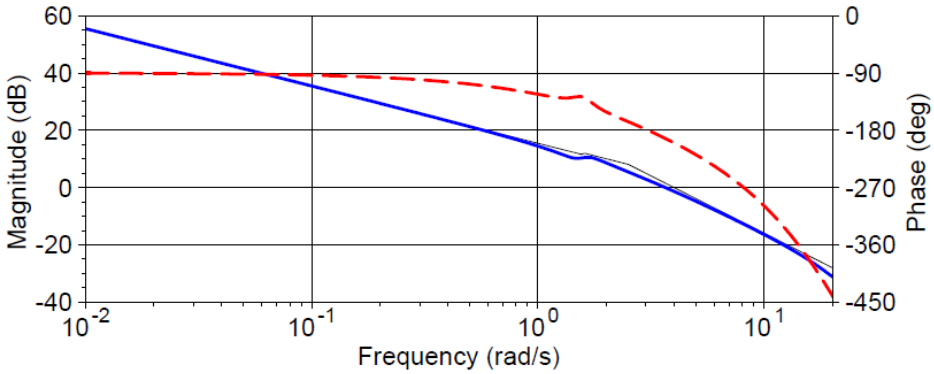

$$\frac{\phi}{F_{Lat}} = \frac{1.239e7[0.133,1.554]}{(0)[0.132,1.61](2.51)[0.7,20][0.7,44]} e^{-0.125s}$$

(a) Baseline roll attitude to lateral stick force Bode frequency response

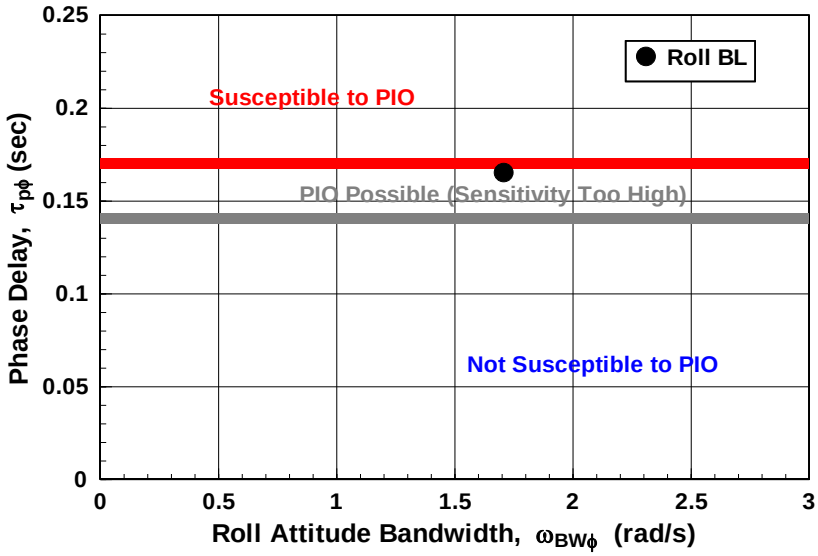

(b) Airplane Bandwidth PIO susceptibility prediction

Figure 12.5: *Roll axis cruise configuration frequency response and Airplane Bandwidth assessment.*

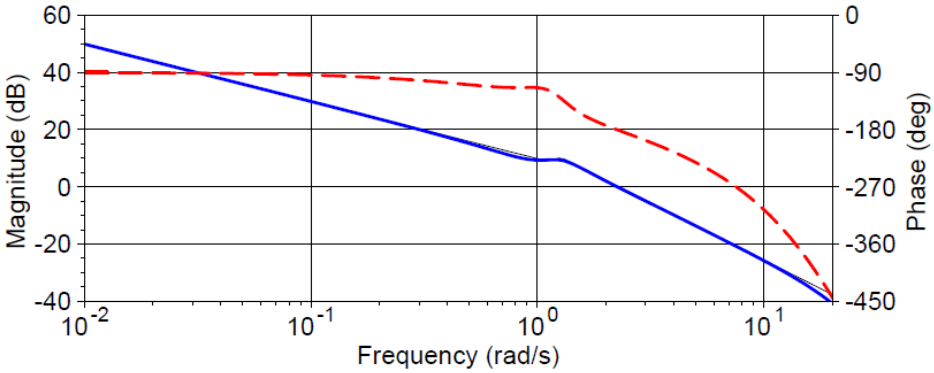

$$\frac{\phi}{F_{Lat}} = \frac{4.082e6[0.335,1.103]}{(0)[0.249,1.25](1.324)[0.7,20][0.7,44]} e^{-0.125s}$$

(a) Baseline roll attitude to lateral stick force Bode frequency response

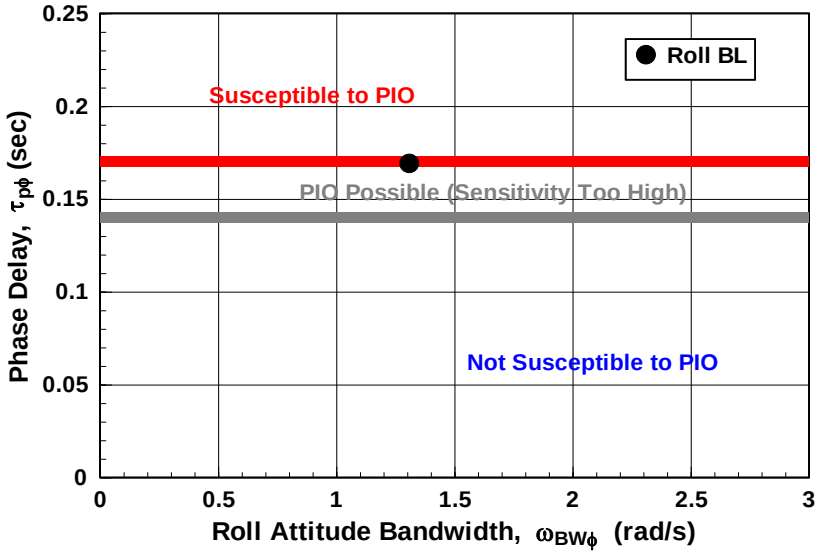

(b) Airplane Bandwidth PIO susceptibility prediction

Figure 12.6: *Roll axis approach configuration frequency response and Airplane Bandwidth assessment.*

12.3.3 Evaluation Tasks

The crew for the checkout and evaluation flights consisted of a Calspan safety pilot (SP), an evaluation pilot (EP), a Calspan flight test engineer, and the STI flight test conductor.

12.3.3.1 Cruise Tasks: Pitch Tracking and Bank Angle Capture and Hold

The Calspan Learjet head down display that was used for the cruise configuration evaluation tasks is shown in Figure 12.7. The radius of the green tracking reticle is 2 degrees, which represents adequate performance for the pitch task. The pilots estimated a 1 degree radius reticle for desired performance. The vertical tails of the command bar extend two degrees in each direction. These were used to assess performance in the lateral axis, that is, the angle from the center dot to the tip of a vertical tail is 7 degrees. The pilot estimated the 5 degree desired performance requirement by maintaining the actual roll attitude (green bar in Figure 12.7) just below the tip of the hat and the 10 degree adequate performance requirement by maintaining the actual roll attitude just above the tip of the hat.

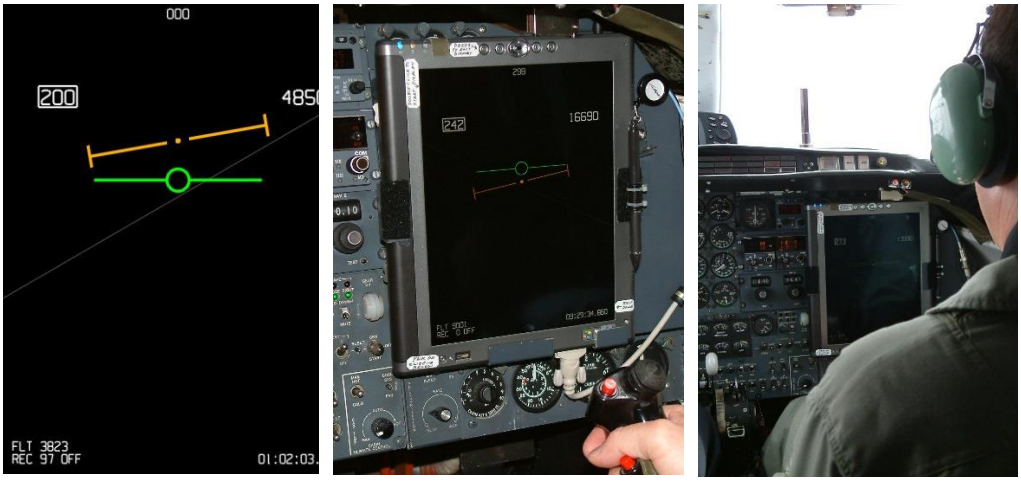

Figure 12.7: *Learjet Head-Down Tracking Task Display.*

Pitch Axis Sum-of-Sines Tracking

Objectives

- Evaluate handling qualities in a tight, closed-loop tracking task.
- Evaluate feel system and control sensitivity characteristics.
- Identify bobble or PIO tendencies.

Description

Aggressively track the displayed command bar signal (θ_c in Figure 12.8) and attempt to keep errors within the specified tolerances. An example sum-of-sines signal is shown in Figure 12.9. The sine wave frequencies were identified in Chapter 9.

Desired Performance

- ±1 degree (half of the radius of the displayed target reticle) 50% of the time.

Adequate Performance

- ±2 degrees (radius of the displayed target reticle) 50% of the time.

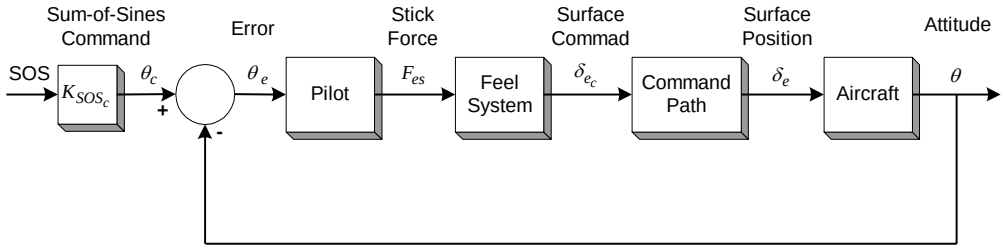

Figure 12.8: *Sum-of-sines tracking task integration.*

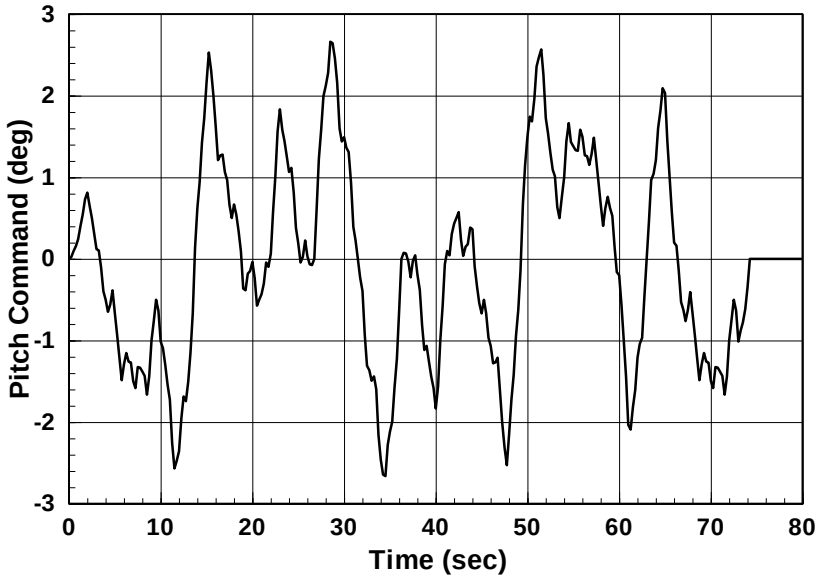

Figure 12.9: *Example pitch axis sum-of-sines command signal.*

Bank Angle Capture and Hold

Objectives

- Evaluate ability to roll and capture a bank angle.
- Identify maneuverability limitations and PIO tendencies.

Description

From steady, wings level flight roll and capture the commanded bank angle identified on the head-down display and maintain this bank angle within the specified tolerance until the command bar displays the next capture angle. Captures were repeated until the pilot was ready to evaluate the configuration.

Desired Performance

- ±5° bank angle.
- No more than one bank angle overshoot for each capture. Magnitude of overshoot remains within the desired region.

Adequate Performance

- ±10° bank angle.
- No more than one bank angle overshoot for each capture. Magnitude of overshoot remains within the adequate region.

12.3.3.2 Approach Task: Precision Offset Landing

All of the approach and landing evaluations were made at Niagara Falls airport. The evaluation task was the precision offset landing task described below.

Task Objectives

- Evaluate ability to precisely control horizontal and vertical flightpath and airspeed.
- Evaluate ability to precisely control sink rate and attitude in the flare.
- Evaluate tendency for nose bobble or PIO.
- Evaluate control sensitivity and harmony in landing.

Task Description

The offset landing task consists of a visual approach during which the evaluation pilot aligns the aircraft approximately 300 feet off the runway centerline (see Figure 12.10). At 150 to 200 feet above the ground, the EP corrects back to the centerline and attempts to touchdown within the desired parameters. The decision to correct is made by the SP. Offsets to the left or right can be used interchangeably; however, the direction of offset may often be dictated by the desire to turn away from civilian aircraft waiting in the hold short area. Typically, offsets were made to the right in this flight test program to take advantage of the drainage ditch visual cue located

approximately 250-300 ft to the right of runway 28R. Each landing was treated as a “must land” situation in order to ensure an elevated pilot gain.

During a typical landing pattern evaluation, the safety pilot configured the aircraft for landing, selecting the proper flight control experiment, and engaging the variable stability system while on downwind. The evaluation pilot took control on base turn and lines up on final for the offset landing. The offset correction was initiated on the call from the safety pilot. A precise flared landing was attempted using the instrument landing markers as the desired touchdown point. These markers are located 1,000 feet from the threshold. Upon touchdown, the safety pilot took control of the airplane and performed the takeoff and turn to downwind, while the evaluation pilot provided comments and ratings for that configuration.

Desired Performance

- Approach airspeed maintained within ± 5 kts.
- Touchdown within 5 feet of centerline (main wheels on centerline).
- Touchdown within ± 250 feet of aimpoint.
- Sink rate – smooth touchdown.
- No PIO.

Adequate Performance

- Approach airspeed maintained within -5 kts/+10 kts.
- Touchdown within 25 feet of centerline.
- Touchdown within ± 500 feet of aimpoint.
- No PIO

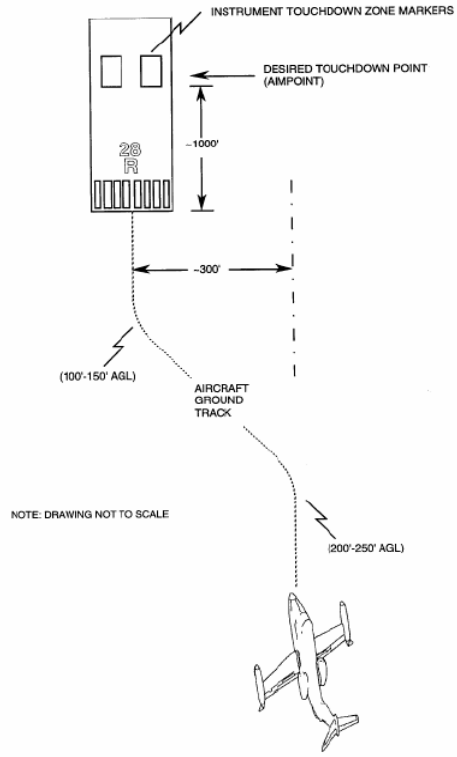

Figure 12.10: *Precision offset landing task requirements and approach [18] to Niagara Falls Airport.*

12.3.4 Pilot Ratings

Ratings from three test pilot participants are included in the data set used herein, Pilots 5, 6, and 7. Four other pilots, Pilots 1 – 4, but they did not complete all three evaluation tasks in their sorties. All three were experienced in assigning pilot ratings, however, the assessment of PIO tendencies was a relatively new experience for Pilot 5. Ratings for the pitch tracking, bank angle capture and hold, and precision offset landing tasks are provided in Table 12.1, Table 12.2, and Table 12.3, respectively. The baseline configurations are shown in blue and as indicated by PIOR tendency ratings of 1 and 2 were found to be PIO free for all three tasks. The configurations with the reduced control surface rate limits are shown in red with PIO noted for all three tasks. Finally, the reduced rate limit with Smart Gain15 active configurations are shown in black or gray. The G2 (gray) configurations are not as aggressive at mitigating the rate limiting and, as expected, have degraded ratings in comparison to the G1 (black) configurations. These G1 configurations were all PIO free, but undesirable motions were present, while the G2 configurations had PIO or PIO tendencies. These configurations were selected because they provide the full range of PIO tendency ratings from which the scalogram-based metric can be assessed.

Table 12.1: *Pitch sum-of-sines tracking task pilot ratings.*

Pilot	Configuration	Rate Limit (deg/s)	HQR	PIOR
3	Baseline (BL)	100	2	1
5	Baseline (BL)	100	3	1
6	Baseline (BL)	100	3	1
3	Rate Limit Only	10	8	5
3	Rate Limit Only	10	10	5.5
5	Rate Limit Only	10	7	4
6	Rate Limit Only	10	8	4
5	Rate Limit + Gain	10	4.5	3
6	Rate Limit + Gain	10	4	2

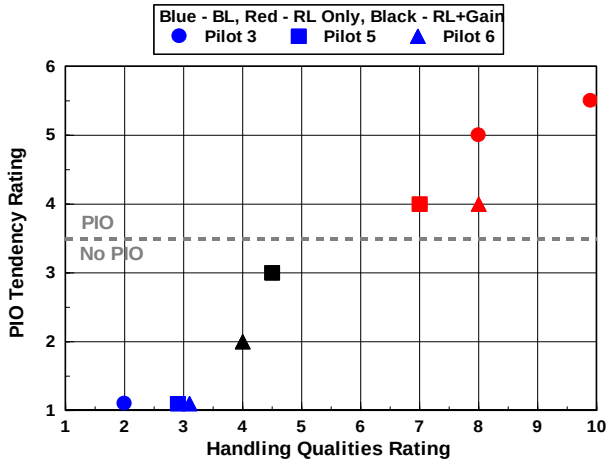

Table 12.2: *Bank angle capture and hold task pilot ratings.*

Pilot	Configuration	Rate Limit (deg/s)	HQR	PIOR
3	Baseline (BL)	150	3	2
5	Baseline (BL)	150	4	2
6	Baseline (BL)	150	4	2
3	Rate Limit Only	30	7	4
5	Rate Limit Only	30	7	4
6	Rate Limit Only	30	8	4
3	Rate Limit + Gain	30	5	3
5	Rate Limit + Gain	30	5.5	3
6	Rate Limit + Gain	30	5	2

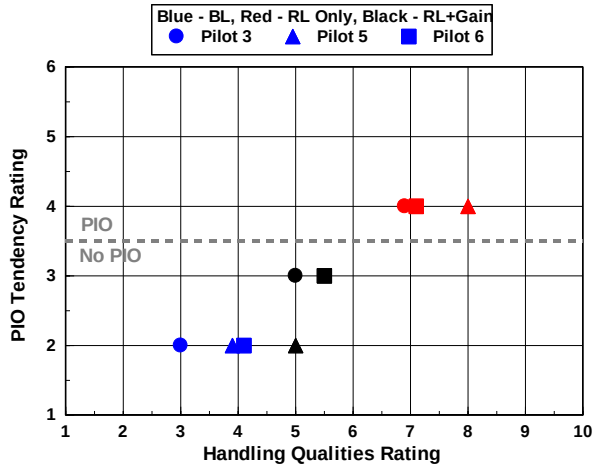

Table 12.3: Precision offset landing task pilot ratings.

Pilot	Configuration	Rate Limit (deg/s)	HQR	PIOR
5	Baseline (BL)	150	5	1
6	Baseline (BL)	150	3	1
5	Rate Limit Only	25	8.5	4
6	Rate Limit Only	30	10	5
5	Rate Limit + Gain (G1)	25	4	2
6	Rate Limit + Gain (G2)	30	5	3
5	Rate Limit + Gain (G2)	25	6.5	3.5
6	Rate Limit + Gain (G2)	30	8	4

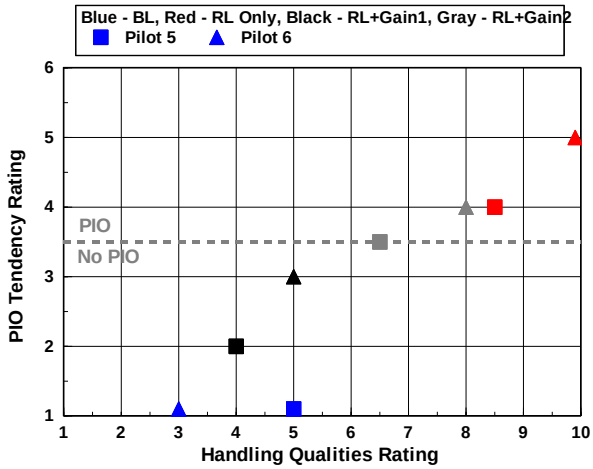

12.4 Assessment of the Proposed PIO Metric

12.4.1 Application

There is a total of 26 cases in the flight test database used herein. After reviewing the complete set of results, preliminary PIO/no-PIO boundaries were established along the -90 deg phase lag vertical and the 0.25 normalized inceptor input peak power horizontal. This results in a PIO region for inceptor input peak power versus phase lag points that have more than -90 degrees of phase lag at the weighted frequency and a normalized peak power that is greater than 0.25. These boundaries provide for cases wherein out-of-phase character may be present, but at pilot input amplitudes that are not a concern for PIO.

The pitch axis sum-of-sines tracking results are shown in Figure 12.11. Individual plots are included for the baseline, rate limited only, and rated limited plus Smart-Gain cases. For this task, the PIO/no-PIO cases were correctly identified based on the PIO tendency ratings assigned by the evaluation test pilots in all but one rate limited only case. This Pilot 5 case reaches a normalized peak power of 0.15 at a phase lag of approximately -110 degrees. No PIO cases were noted for the baseline or rate limited plus Smart-Gain cases, none of which approach the PIO boundary.

Results for the bank angle capture and hold cases are shown in Figure 12.12. For this task, the PIO/no-PIO cases were correctly identified as indicated by the assigned pilot ratings in all but one case. First, all of the baseline cases were clearly no-PIO cases. Next, the three rate limited only cases were all identified as PIO cases. Note that the Pilot 5 case just “kisses” the 0.25 normalized gain boundary. Regardless of an actual crossing, any case that comes this close to the PIO boundary should be reviewed more closely, especially since the PIO tendency of the configuration was clearly revealed by the rating of Pilot 5 and the results of the other two pilots. The missed case was the Pilot 3 rate limited plus Smart-Gain case. As will be shown in the next section, the pilot PIO tendency rating of 3 was appropriate for the configuration, but the metric detection of PIO was also justified.

The precision offset landing task results are shown in Figure 12.13 (baseline and rate limited only cases) and Figure 12.14 (rate limit plus Smart-Gain cases). For this task, the IPPP metric was again successful in correctly identifying all but one of the cases as measured by the assigned pilot ratings. First, while there was out-of-phase character noted, there was absolutely no PIO tendencies observed with the baseline cases. This is clearly illuminated by the metric application wherein the out-of-phase points are all significantly below the 0.25 normalized peak power boundary. Both rate limited only cases were rated as PIO prone and this too is captured by the metric. Two Smart-Gain aggressiveness levels were evaluated in the flight test program. The PIO tendencies of the Gain 2 cases were correctly identified. For the Gain 1 cases, however, the Pilot 6 case clearly entered the PIO region, but was only assigned a PIO Tendency rating of 3. An examination of the time histories for this case in the next section indicates that this rating may have been too generous on the part of Pilot 6.

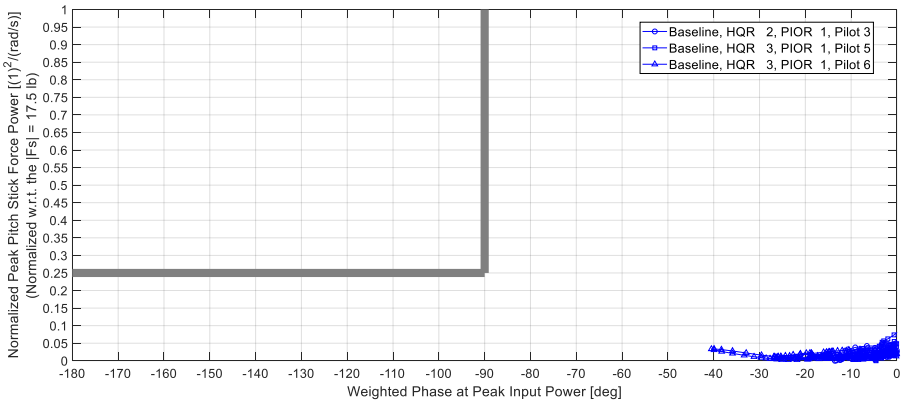

(a) Baseline cases

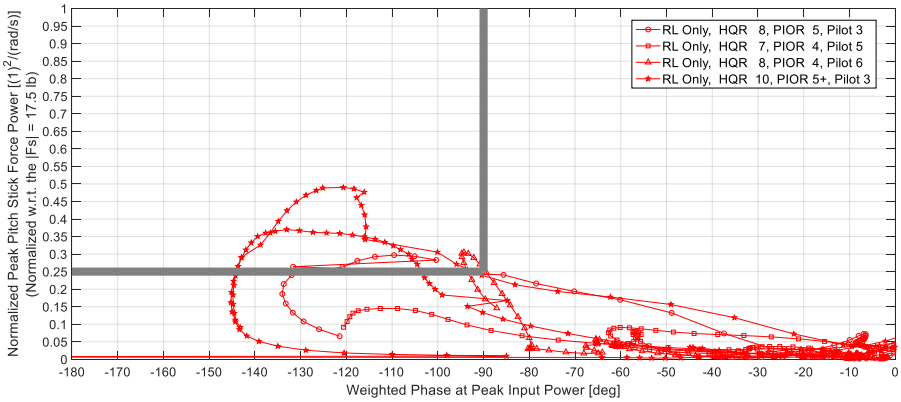

(b) Rate limit only cases

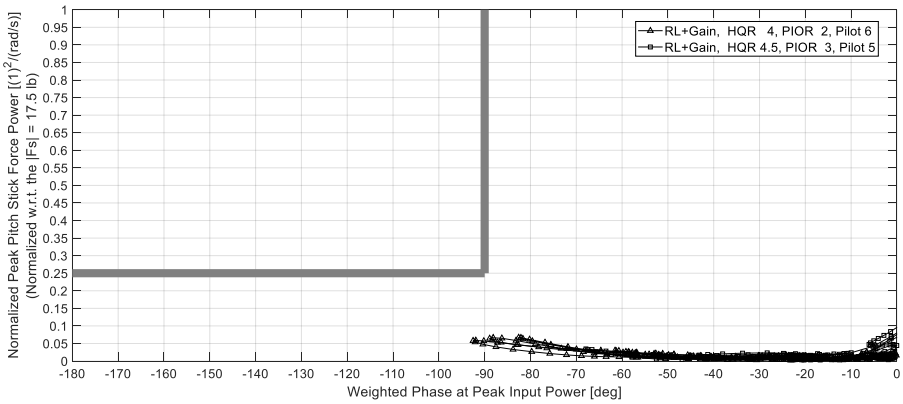

(c) Rate limit + gain cases

Figure 12.11: *IPPP metric applied to the example pitch sum-of-sines tracking cases.*

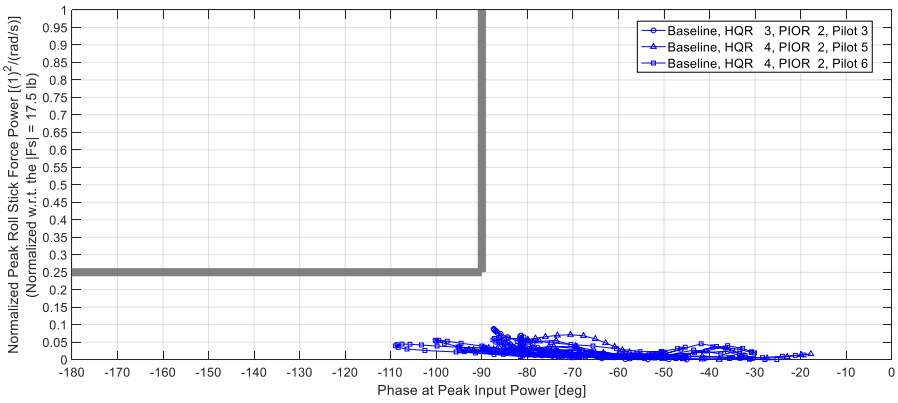

(a) Baseline Cases

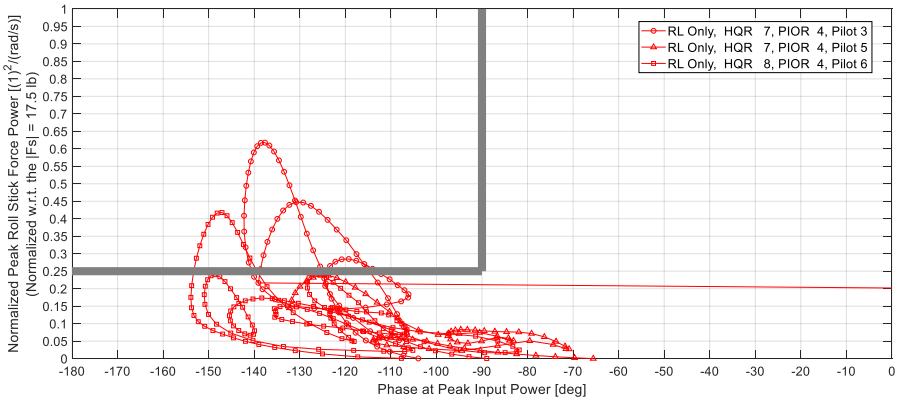

(b) Rate Limit Only Cases

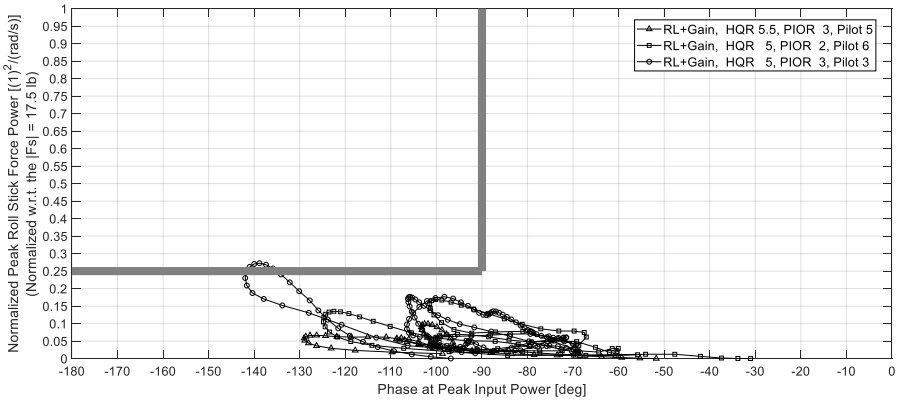

(c) Rate Limit + Gain Cases

Figure 12.12: *IPPP metric applied to the example bank angle capture and hold cases.*

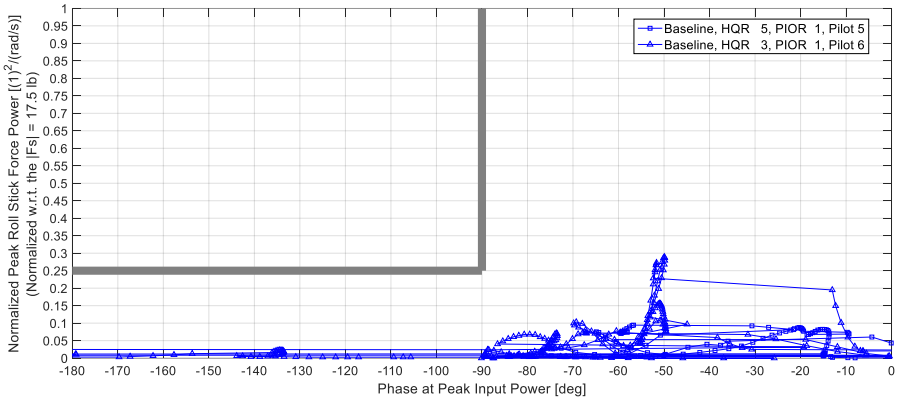

(a) Baseline Cases

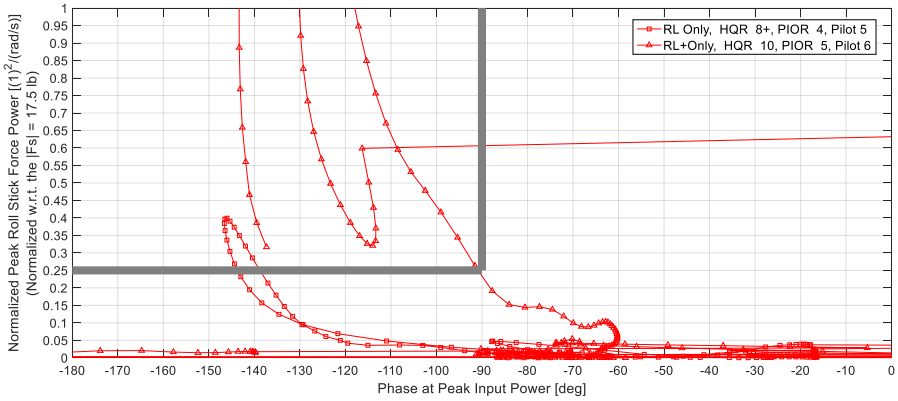

(b) Rate Limit Only Cases

Figure 12.13: *IPPP metric applied to the example precision offset landing baseline and rate limit only cases.*

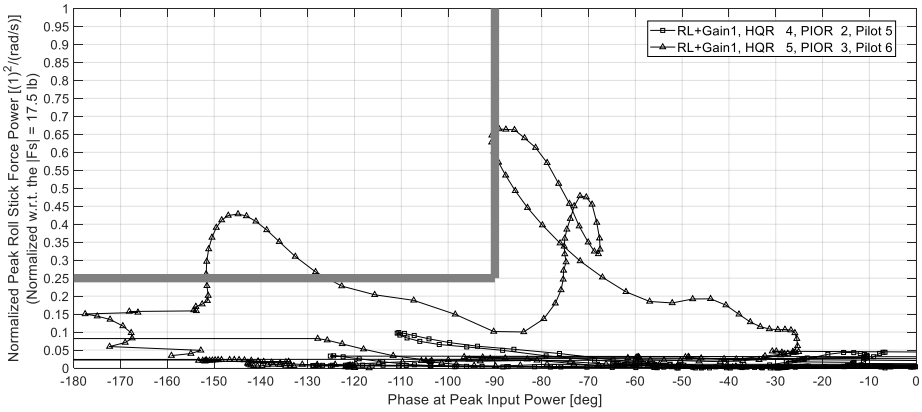

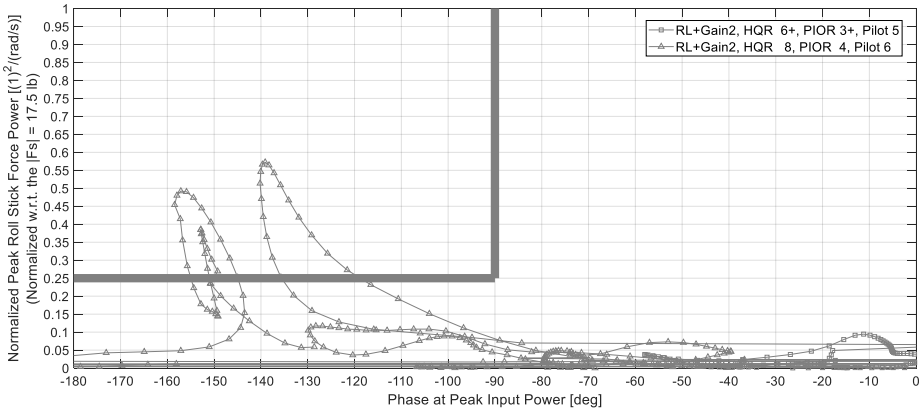

(c) Rate Limit + Gain Cases

Figure 12.14: *IPPP metric applied to the example precision offset landing rate limit plus Smart-Gain cases.*

12.5 Discussion of Results

Of the 26 flight test cases, 23 out of the 26 cases were correctly identified as PIO or No-PIO using the boundaries established herein for the IPPP metric. The three "missed" cases and the "close-call" case are given a closer look here.

Figure 12.15(a) shows time histories for the Pilot 5 pitch sum-of-sines tracking run for the rate limited only case that received a PIO tendency rating of 4, but did not meet the IPPP amplitude requirement even though the out-of-phase requirement was met. In reviewing the pitch attitude and longitudinal stick responses, there is a distinct 1.5 cycles of out-of-phase pilot-vehicle system behavior early in the run, that is, 3 to 7 seconds, but the inceptor amplitudes here are quite small. Later in the run beginning around 38 seconds, the out-of-phase behavior returns for another 1.5

cycles and here the inceptor amplitudes are growing, but a Learjet variable stability system safety trip cuts the run short at approximately 41 seconds. It is therefore reasonable to assume that the trajectory of the IPPP for this case may have continued into the PIO region instead of peaking at a normalized inceptor peak power of 0.15. For the Figure 12.15(b) case, there is a large bank angle overshoot observed at each initial attitude capture, but with the third capture, a PIO develops and results in task termination during the second cycle. This results in a borderline PIO detection case where the IPPP trajectory just reaches the 0.25 normalized peak power boundary. Based on the further examination of these two cases, the metric is working as intended, so no changes to the boundaries are warranted.

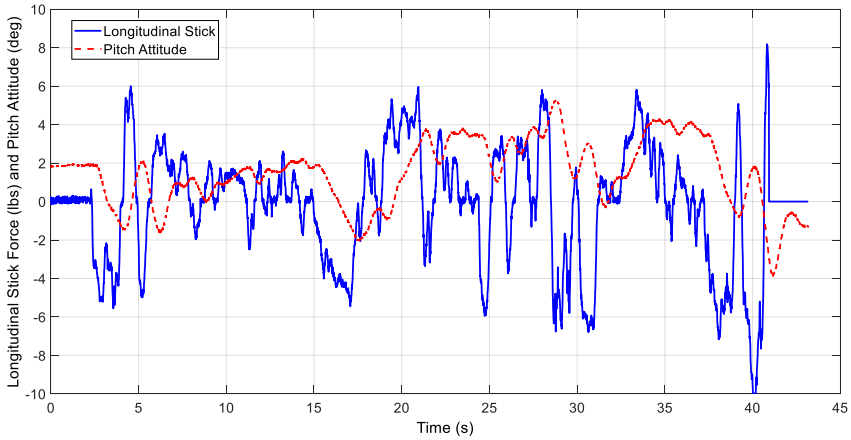

(a) Missed case, Pilot 5 pitch sum-of-sines, rate limit only case

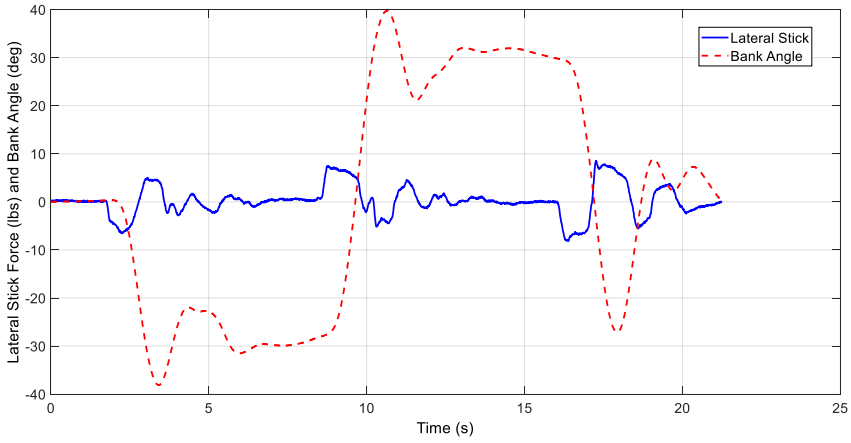

(b) Borderline case, Pilot 5 bank angle capture and hold, rate limit only

Figure 12.15: *Missed case where PIO was not predicted and a borderline case.*

Figure 12.16 presents the lateral stick force and bank angle time histories for the two cases in which the IPPP metric indicated PIO, but the pilots provided PIO tendency ratings of 3 that indicates no PIO. Beginning with the Pilot 3 bank angle capture and hold run shown in Figure 12.16(a), several oscillations of a PIO are clearly evident in the first capture. While the remaining captures typically show an overshoot of the desired attitude, there are no further sustained oscillations. Thus, one can see that the pilot may have noted the oscillations on the first capture, but these tendencies did not appear in any of the subsequent seven captures as he adjusted to the new configuration. Thus, the assigned rating of 3 is reasonable, but a detected PIO by the IPPP metric is also correct. Given this result, the control law designer would be strongly encouraged to "fix" the observed handling qualities deficiencies of this rate limit plus gain configuration.

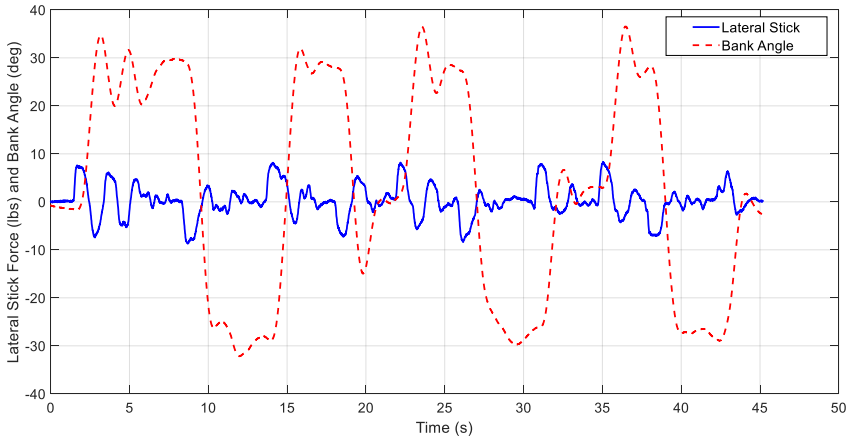

(a) Pilot 3 bank angle capture and hold, rate limit + gain

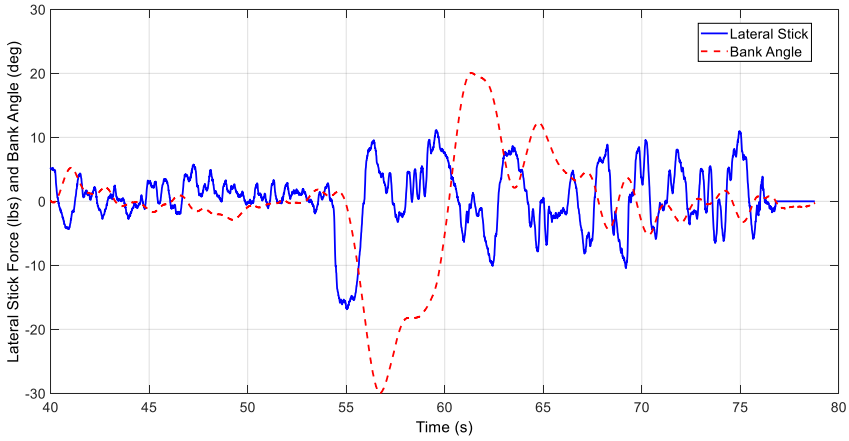

(b) Pilot 6 precision offset landing, rate limit + G1

Figure 12.16: *Missed cases where PIO was predicted.*

Time histories for a second case wherein PIO was indicated by the IPPP metric, but not via the assigned PIO tendency rating is shown in Figure 12.16(b). This is the Pilot 6 rate limit plus Gain 1 Smart-Gain case, the IPPP metric trajectory twice enters the PIO region. The first crossing into the PIO region is associated with the large input amplitude that comes with the pilot's initial correction to the runway centerline at approximately 54 seconds. The second crossing is associated with the three plus PIO cycles noted as the pilot attempts to capture and hold the runway centerline beginning at approximately 61 seconds. In this case, the sustained oscillations were missed by the pilot and his resulting PIO tendency rating of 3 was too lenient. Based on the further examination of these two "missed" cases, the IPPP metric is again working as intended, and so changes to the boundaries are again not warranted.

12.6 Conclusions

As new aircraft continue to be introduced with configurations that are designed to push performance and efficiency envelopes using advanced fly-by-wire control system concepts, the potential for pilot-induced oscillations (PIO) will continue to be a concern. In this chapter, the utility of the inceptor peak power-phase (IPPP) PIO metric was explored using a flight test database that featured 26 cases, three evaluation tasks, three evaluation test pilots, and a full range of assigned PIO tendency ratings. Before applying the metric, characteristics of the PIO signature were applied to define a normalizing term for the inceptor peak power. Initial PIO/no-PIO boundaries were established, and the effectiveness of these boundaries was assessed using the 26 flight test cases. The results of the assessment initially found that 23 of the 26 cases were correctly identified as a PIO or no-PIO case based on the assigned PIO tendency ratings. Further analysis of the three "missed" cases revealed that the metric was working as intended and no modifications to the current boundaries was needed. The IPPP metric can be used analytically as a PIO predictive tool or as a real-time monitoring tool. While the results shown herein are promising, further investigation of the IPPP approach is recommended with currently available or newly collected flight test data using a variety of aircraft configurations, that is, PIO susceptible and PIO resistant, and evaluation tasks.

12.7 References

1. Klyde, D. H., P. C. Schulze, R. Mello, and D. G. Mitchell, "Assessment of a Scalogram-Based PIO Metric with Flight Test Data," AIAA-2017-1641 presented at the *Science and Technology Forum and Exposition 2017: AIAA Atmospheric Flight Mechanics Conference*, Grapevine, TX, Jan. 9–13, 2017.

2. Klyde, D. H., P. C. Schulze, R. Mello, D. G. Mitchell, N. Cameron, C. Cunliffe, and M. White, "Assessment of a Scalogram-Based Pilot-Induced Oscillation Metric with Flight Test and Simulation Data," *J. of Guidance, Control, and Dynamics*, Vol. 43, No. 11, Nov. 2020, pp. 2058-2072.

3. Mitchell, D. G., and D. H. Klyde, "Identifying a Pilot-Induced Oscillation Signature: New Techniques Applied to Old Problems," *J. Guidance, Control, and Dynamics*, Vol. 31, No. 1, Jan. – Feb. 2008, pp 215 – 224.

4. Chalk, C.R., "Calspan Presentation of PIO and the Effects of Rate Limiting," *Flight Vehicle Integration Panel Workshop on Pilot Induced Oscillations*, AGARD-AR-335, Feb. 1995, pp. 12-1 – 12-12.

5. Klyde, D.H., McRuer, D.T., and Myers, T.T., *Unified Pilot-Induced Oscillation Theory, Volume I: PIO Analysis with Linear and Nonlinear Effective Vehicle Characteristics, Including Rate Limiting*, WL-TR-96-3028, Dec. 1995.

6. Newell, F., *Investigation of Phugoid Effects on GCA Landings*, WADC TR 57-650, Dec. 1957.

7. Mitchell, D. G., and R. H. Hoh, *Development of Methods and Devices to Predict and Prevent Pilot-Induced Oscillations*, AFRL-VA-WP-TR-2000-3046, Dec. 2000.

8. Ashkenas, I. L., Jex, H. R., and McRuer, D. T., *Pilot-Induced Oscillations: Their Cause and Analysis*, Norair Report NOR-64-143, July 1964.

9. Anon., *Aviation Safety and Pilot Control: Understanding and Preventing Unfavorable Pilot-Vehicle Interactions*, National Academy Press, Washington D.C., 1997.

10. Smith, J.W., *Analysis of a Lateral Pilot-Induced Oscillation Experienced on the First Flight of the YF-16 Aircraft*, NASA TM-72867, Sept. 1979.

11. Cooper, G.E., and Harper, Jr., R.P., *The Use of Pilot Rating in the Evaluation of Aircraft Handling Qualities*, NASA TN D-5153, Apr. 1969.

12. Mitchell, D.G., Arencibia, A.J., and Muñoz, S., "Real-Time Detection of Pilot-Induced Oscillations," AIAA-2004-4700, presented at *Atmospheric Flight Mechanics Conference*, Providence, RI, Aug. 2004.

13. Jones, M., and M. Jump, "Subjective and Objective Evaluation of PIO Tendencies," paper presented at *70th Annual Forum of the American Helicopter Society International*, Montreal, Quebec, 20-22 May 2014.

14. Thompson, P. M., D. H. Klyde, E. N. Bachelder, and T. J. Rosenthal, *On-line Loss of Control Detection using Wavelets*, NASA CR-2005-212873, July 2005.

15. Klyde, D. H., and D. T. McRuer, "Development of Smart-Cue and Smart-Gain Concepts to Alleviate Pilot-Vehicle System Loss of Control," *J. of Guidance, Control, and Dynamics*, Vol. 32, No. 5, Sept.-Oct. 2009, pp. 1409-1417.

16. Klyde, D. H., and C. Y. Liang, "Approach and Landing Flight Test Evaluation of Smart-Cue and Smart-Gain Concepts," J. *of Guidance, Control, and Dynamics*, Vol. 32, No. 4, July-Aug. 2009, pp. 1057-1070.

17. Neal, T. Peter, and Rogers E. Smith, *An In-Flight Investigation to Develop Control System Design Criteria for Fighter Airplanes*, AFFDL-TR-70-74, Volume I, Dec. 1970.

18. Deppe, P. R., C. R. Chalk, and M. F. Shafer, *Flight Evaluation of an Aircraft with Side and Center Stick Controllers and Rate-Limited Ailerons*, NASA CR-198055, Nov. 1996.

13. Conclusions and Recommendations

Experience has shown that almost all high performance aircraft are likely to have PIO episodes sometime in their development or early operational experience, leading to yet another "ad hoc" solution at a great price. To put this evil genie back in the bottle will require an effective broadly-based program of analytical, experimental, and flight research that has proved to be difficult to mount and sustain.

Duane McRuer, 22nd Minta Martin Lecture, "Human Dynamics and Pilot-Induced Oscillations," Massachusetts Institute of Technology, December 2, 1992.

13.0 CONCLUSIONS AND RECOMMENDATIONS

While not at the scale required, the work described herein has attempted to address the challenge made by Duane McRuer in his 22nd Minta Martin Lecture [1] wherein he called for a broadly-based program of analytical, experimental, and flight research to mitigate the ongoing threat to safety of flight posed by pilot-induced oscillations (PIO). Given that modern PIO phenomena are dominated by the presence of control surface actuator rate limiting, the goals of this thesis were as follows:

To address Category II PIO, the goals of this thesis are to
Provide enhanced comprehension and analysis methods, in-flight mitigation methods, and valid detection methods.

The theories, analyses, mitigation, and detection methods featured in this thesis were designed to be general and are therefore not tied to a particular aircraft type, flight control system architecture, or cockpit inceptor configuration.

13.1 Part I: Comprehension and Analysis Methods

13.1.1 Chapter 2: The Nature of Control Surface Actuator Rate Limiting

The focus of the Comprehension and Analysis Methods sections of this thesis, beginning with Chapter 2, is on the role of rate limiting in PIO. The earliest well-documented PIO event that featured rate limiting was the first flight of the X-15 aircraft in 1959. This event is one of the most analyzed of all PIO events. Among the earliest is the analysis documented in [2] that features the development of describing function approximations for a rate limited actuator and an inverse describing function technique used to predict limit cycle oscillations and their frequencies. Attention to the effects of rate limiting and other system nonlinearities surfaced again in conjunction with the severe PIOs that occurred with the YF-12 aircraft during aerial refueling. A description of the nonlinear analysis of these events was done at NASA by Smith and Berry [3]. More recent highly documented PIO events that involved rate limiting include the YF-22 [4] and JAS-39 [5] events. These events that resulted in significant damage to the YF-22 and the loss of two JAS-39 aircraft inspired a new thrust in handling qualities research that emphasized comprehension, prevention, and alleviation of the nonlinear effects associated with rate limiting.

For PIO to occur, there must be a trigger [6,7]. Following the well-publicized crashes of the YF-22 and the JAS-39 aircraft in the early 1990's, it was speculated that rate limiting was a trigger for most PIOs on fly-by-wire aircraft. After the research efforts of the 1990's, it was concluded that rate limiting can be a trigger for PIO. Sometimes PIO can also be the cause of the rate limiting. Further, it is possible to encounter severe rate limiting without a PIO. Comprehension of these possible outcomes is important if Category II PIOs are to be mitigated in design or via on-board counter measures such as the PIO suppression filter used on the Space Shuttle [8].

In this chapter, a simplified model of a control surface actuator was introduced to study the nature of rate limiting. Using this simple model, the linear characteristics of the actuator response are completely defined in terms of its time constant, T, or bandwidth frequency, ω_a, wherein $T = 1/\omega_a$. As such, the linear response is frequency dependent. Three distinct actuator response regions were identified – linear, near saturation, and highly saturated. The near saturation region features intermittent rate limiting, but the overall response remains quasi-linear. The highly saturated region, however, is characterized not only by the input command frequency, but also by the maximum rate and amplitude of the input. That is, the nonlinear response is both amplitude and frequency dependent. Comparing the simplified model with a high order actuator model from a high-performance aircraft verified the utility of the simplified approach for the study of pilot-vehicle system interactions including PIO.

Main finding of Chapter 2
A simplified nonlinear model of a control surface actuator with rate limiting approximates the dynamic behavior of higher order actuator models in the frequency range that is relevant for PIO analysis and can therefore be used to enhance comprehension of Category II PIO.

13.1.2 Chapter 3: The Exact Describing Function and Approximations

For modern pilot-vehicle systems, simulation with a focus on time domain methods remains the tool of choice for analysis of nonlinear systems. Although powerful, computer simulation results are specific to the given set of model parameters. In this way, the nonlinear simulation serves as a system performance verification tool. In Chapter 3, describing function techniques were introduced as an analytical alternative to computer simulation. There are important reasons to exercise describing function techniques, the most important of which with respect to the analysis of Category II PIO is that describing function results can be generalized. Describing functions also provide extensions of linear graphical procedures. In this research, describing functions that apply to the simplified model introduced in Chapter 2 were developed.

Describing function methods were derived that characterize the nature of rate limiting with a focus on the linear, near saturation, and highly saturated regions of performance. Using the simplified nonlinear model, it was shown that a closed-loop rate limited actuator is characterized by not only an added phase lag, but also a significant reduction in actuator bandwidth. Further, the sudden onset of these characteristics can be brought about by only small changes in input command amplitudes, especially when the pilot is operating in a high-gain closed-loop task. By using the exact describing function analysis methods described in the chapter, the characteristics associated with actuator rate limiting that can lead to PIO were quantified, in terms of known command input and actuator design parameters. Further, more easily computed describing function approximations were defined in terms of these command input and design parameters. Using example cases for all three regions, the describing function results were shown to be conservative, that is, the added phase lag due to the rate limiting was over-estimated when compared to the exact describing function case.

Main finding of Chapter 3
Describing function methods can be used to accurately estimate the magnitude attenuation, added phase lag, and bandwidth reduction resulting from control surface actuator rate limiting.

13.1.3 Chapter 4: PIO Limit Cycle Prediction using the X-15 as a Case Study

A key motivation for developing the describing functions (approximate and exact) defined in Chapter 3 is to predict closed-loop pilot-vehicle system limit cycles [2] referred to here as Category II PIO. A synchronous pilot longitudinal closed-loop system with a rate limited actuator nonlinear element in series with linear elements is shown in Figure 4.1. For this synchronous behavior, it has been demonstrated that when sinusoidal inputs appear in pilot-vehicle systems, a pilot can essentially duplicate the sinusoid with no phase lag up to frequencies of about 3 Hz (about 20 rad/sec) [9]. For these synchronous cases, the pilot can be represented by a pure gain (K_p) as shown in the Figure 13.1 block diagram.

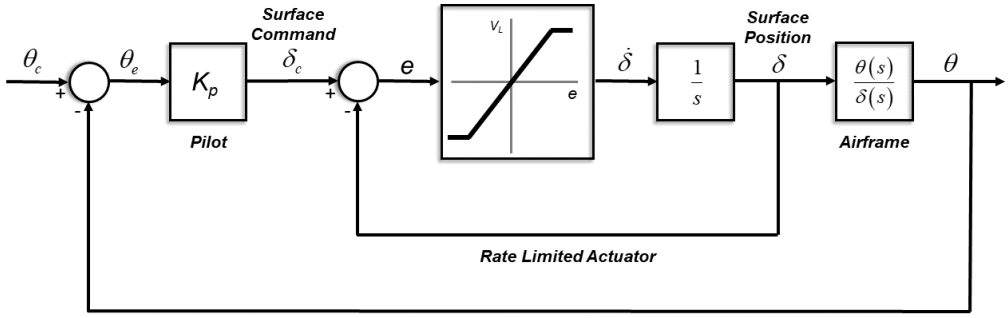

Figure 13.1: *Synchronous pilot closed-loop system with nonlinear actuator.*

The criterion for a neutrally damped oscillation is simply that the open-loop amplitude ratio is 1.0 (0 dB) and the phase is -180°. For an oscillation to persist in the Figure 13.1 example, the synchronous pilot-vehicle system with a series nonlinear element must satisfy the following equation:

$$G(j\omega)N(j\omega, A) = -1 \tag{13.1a}$$

or

$$G(j\omega) = \frac{-1}{N(j\omega, A)} \tag{13.1b}$$

In the equation, $G(j\omega)$ represents the frequency dependent linear elements (K_p and θ/δ in Figure 13.1) and $N(j\omega,A)$ represents the frequency and amplitude dependent nonlinear element (the describing function δ/δ_c in Figure 13.1).1

Chapter 4 illustrates via a famous flight test example that rate limiting of control surface actuators can have dire effects on handling qualities and PIO. The magnitude of the effects depends on three basic factors: (1) how long the actuator is rate-limited; (2) how much more the pilot-vehicle system demands of the airplane; and (3) the consequences on aircraft dynamics of encountering the limit. Fundamentally, rate limiting introduces added phase lag into the response of the aircraft. This alone can be sufficient to lead to PIO, depending upon the characteristics of the aircraft. Flight 1-1-5 of the X-15 provides a perfect example of this effect, wherein an aircraft configuration that had good predicted handling qualities by linear system measures, still had a severe Category II PIO due to the control surface actuator rate limiting. In the X-15 example used here, the PIO frequency was significantly reduced from the linear neutral stability frequency, thus displaying the profound impact of actuator rate limiting. This result takes on added significance in light of the inability of the linear criteria and metrics to identify the PIO susceptibility of this configuration.

Main finding of Chapter 4
For Category II PIO cases where the rate limiting occurs in series with an otherwise linear system, inverse describing function techniques can be used to predict the limit cycle or PIO frequency.

13.2 Part II: Category II PIO Mitigation Methods

13.2.1 Chapter 5: Historical Precedents for Inceptor Cueing

In the Chapter 5 review of historical examples, it was shown the aircraft designers have long used inceptor artificial feel mechanisms to restore or provide cues to the pilot when flying aircraft with indirect flight control systems. Further, it was shown that the fundamental understanding of PIO is sufficient to devise mitigation methods. Whether using a suppression filter or a control surface actuator rate limiting compensation scheme, the industry has introduced mechanisms through which the deleterious effects of rate limiting can be mitigated at least partially, but often at the expense of handling qualities and pilot-vehicle system task performance. The challenge addressed in the subsequent chapters of Part II was to devise new methods that can not only mitigate PIO susceptibility due to rate limiting but also maintain desirable handling qualities and task performance.

Main finding of Chapter 5
There is strong historical precedent that the use of inceptor cueing to the pilot can be an effective means to mitigate the deleterious effects of control surface actuator rate limiting.

13.2.2 Chapter 6: Defining Dynamic Distortion

At present, the aircraft flying qualities community has sufficient understanding of pilot-vehicle systems in general to make the case that effective vehicle dynamic characteristics for a given design can be considered to be either ideal or good enough. Departures from these nominally ideal properties can then be labeled as "distortions" that may underlie pilot-vehicle system problems. A common example is control surface rate limiting that is the focus of this thesis, where deviation from ideal or desirable values has been shown to lead to PIOs in some circumstances. Another example is mis-rigging of control system elements, such as mechanical maladjustments leading to control system backlash or excessive hysteresis.

The common theme is that the actual manual flight control system is in some way deviating from an ideal system. The pilot is expecting one type of response, typically a linear response that has predictable characteristics, but the actual system is behaving differently because of the distortion. Within this general context, Ralph A'Harrah while at NASA Headquarters proposed the "Loss of Control Inhibition System" (LOCIS) wherein distortions are detected, and appropriate cues are then introduced to the pilot by way of compensation to mitigate the distortions (U.S. Patents #7,285,932 and #7,285,933). It was recognized at the time that this was still a general concept that had yet to be made concrete or specific. It served as a motivation for the work reported in Part II of this thesis to attempt to quantify such conceptual terms as "distortions" and "idealized systems" as unifying principles underlying the development of corrective measures in the form of controller cues. To advance this generalized theme, concrete examples were needed. Thus, the critical distortion involving control surface rate limiting as the key factor in Category II PIO [10] and subsequent loss of control was selected for the work described in Chapter 6.

The analysis of an F-14 flight test database in this chapter provided the following findings and observations. Although the concept of dynamic distortion was initially somewhat ill-defined, it was nonetheless shown to be an effective means of identifying key flight control system nonlinearities such as rate limiting. When dynamic distortion was defined in terms of a simplified ideal linear system represented by the steady state system characteristics, rate limiting distortions were identified particularly well; however, the concept as defined in these terms was not a "catch all" for all of the items that can lead to unfavorable pilot-vehicle interactions such as PIO, for example, poor aircraft dynamics, inappropriate control stick sensitivity, etc. Furthermore, command path filters that are commonplace in modern systems, also result in a dynamic distortion when compared to the steady state gearing. The results of this analysis thus demonstrated that an "idealized system" response that can provide a more robust measure of dynamic distortion was still needed.

Main finding of Chapter 6
Departures from an ideal flight control system response reveal the impact of dynamic distortion associated with control surface actuator rate limiting.

13.2.3 Chapter 7: A Simplified "Ideal Linear System"

In Chapter 7, an idealized manual control system concept is defined to quantify the concept of dynamic distortion and introduce the Smart-Cue and Smart-Gain concepts to mitigate Category II pilot-induced oscillations (PIO). The basic idea in applying the ideal system concept is to restore a force feedback cue in a fly-by-wire system configuration. This is the heart of the Smart-Cue concept. As shown in Figure 13.2, the commanded surface position and actual surface position are used to define a Position Error via an ideal linear system that can be as simple as a unity gain. Comparisons of the Position Error with idealized manual control system characteristics, that is, Position Lag, will therefore reflect differences, due to distortions in the actual system. Cueing and corrective haptic forces, the Smart-Cue, are then presented to the pilot as a "proprioceptive display." Nominally the mechanization of this feature will be based on an inceptor with active back-drive capability. In principle, the back-drive mechanism is an adjustable spring gradient artificial feel system force producer that constitutes a proprioceptive display.

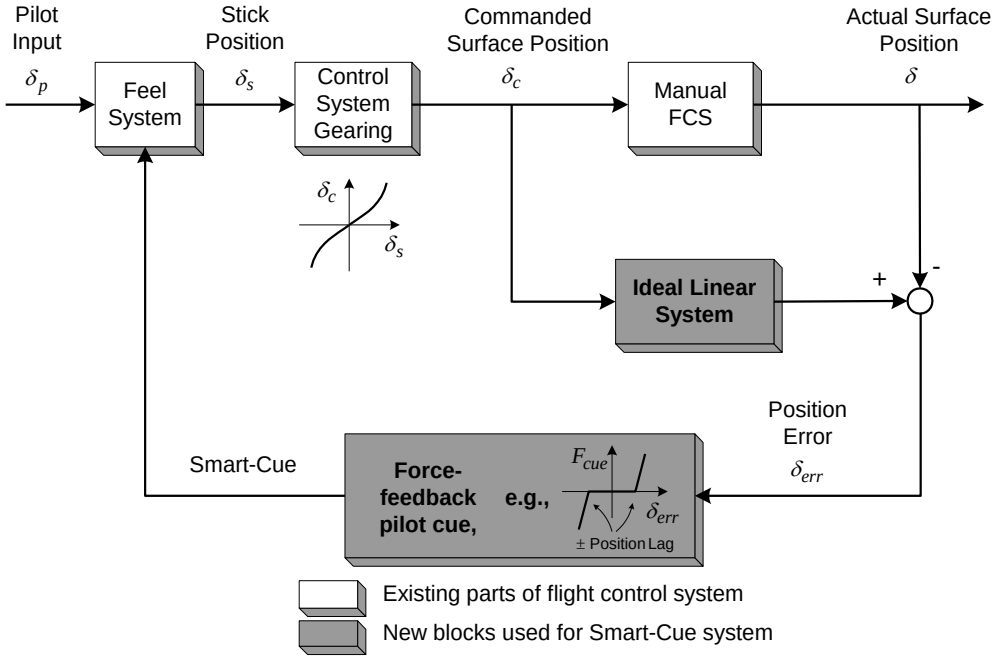

Figure 13.2: *Implementation of the Smart-Cue system.*

A second design concept that is also based on a measure of dynamic distortion, the *Smart-Gain*, evolved from the checkout flight process [11] wherein the Smart-Cue alone was not a sufficient mitigation method, but discussions with the evaluation pilots introduced the idea of an adaptive command path gain based on Position Error. Piloted simulation was used to rapidly prototype such a concept, the *Smart-Gain*. Past work including the PIO suppression filter [8] used on the space shuttle employs command path gain reduction techniques. Such techniques estimate the

frequency of the pilot's input, and then attenuate the input as a function of this frequency. This technique does not, however, take the response of the control system into consideration, so the pilot input is attenuated whether or not it is needed. With the Smart-Gain, the pilot input is attenuated as a function of the Position Error, the measure of dynamic distortion, as shown in Figure 13.3. A Position Lag metric is used to turn the Smart-Gain "on" and "off." The Position Lag may be set independently to the values used for the Smart-Cue.

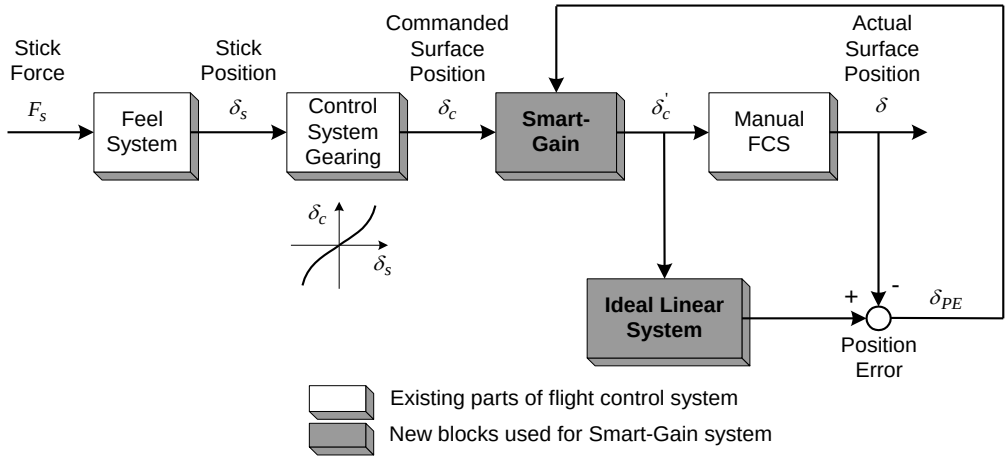

Figure 13.3: *Implementation of the Smart-Gain system.*

Chapter 7 described the development of an innovative means to alert, constrain and thereby alleviate loss of control associated with unfavorable pilot-vehicle systems interactions including pilot-induced oscillations that are often present in high gain, closed-loop operations. "Ideal" pilot to surface relationships were used to measure the impact of control system effects, such as control surface rate limiting, that distort the actual control system response. The Position Error measure of this "dynamic distortion" was used to develop; 1) a command path gain adjustment mechanism, a Smart-Gain, and 2) active alerting and constraining proprioceptive and tactile feedback cues to the cockpit controller, a Smart-Cue, when predetermined dynamic distortion boundaries, the Position Lag metric, are exceeded. The Smart-Gain and Smart-Cue concepts were developed and refined via piloted simulation before ultimately being evaluated and refined via flight test as described in Chapter 8.

Main finding of Chapter 7
A measure of control surface actuator dynamic distortion based on an ideal linear system response can be used to define an adaptive command path gain and an active alerting and constraining inceptor force cue to alleviate unfavorable pilot-vehicle coupling and mitigate PIO.

13.2.4 Chapter 8: Approach and Landing Flight Evaluation of Smart-Cue and Smart-Gain Concepts

The Calspan Learjet In-Flight Simulator was used to evaluate the Smart-Cue/Smart-Gain PIO mitigation system using both cruise flight and approach and landing evaluation tasks. The working area for the checkout and evaluation flights was along the southern shore of Lake Ontario with all approach and landing evaluations made at Niagara Falls airport. The crew for the checkout and evaluation flights consisted of a Calspan safety pilot, an evaluation pilot, a Calspan flight test engineer, and the Systems Technology, Inc. (STI) flight test conductor. The evaluation pilots were exposed to the Smart-Cue and Smart-Gain mechanizations using the Learjet in a ground simulation mode prior to formal flight test evaluations. This gave the pilots some sense of how the cues and gain reduction would engage in flight.

The baseline configuration was designed to be PIO free, while the rate limited configurations were designed to be susceptible to PIO. While configured via the Learjet Variable Stability System (VSS), the baseline configuration was similar to the Learjet sans the VSS with its yaw damper engaged. Smart-Gain only and combined Smart-Cue and Smart-Gain cases were then introduced with the rate limited configurations to assess the effectiveness of the system in mitigating PIO. The configurations were "blind" to the evaluation test pilots, that is, the pilot did not know what configuration was being assessed run-to run. Upon touchdown, the safety pilot would take control and return the aircraft via a "touch and go" to the desired landing approach starting point wherein the evaluation pilot would again be given control of the aircraft. While the safety pilot was in control, the evaluation pilot would provide ratings and comments for the selected configuration. Given available flight test time, repeat runs of selected configurations were made at the discretion of the STI flight test conductor.

For the roll axis approach and landing evaluations, the clear performance enhancer for all three evaluation test pilots was the Smart-Gain. Addition of the Smart-Cue, however, was an important performance benefit for two of the three pilots. For these pilots, the evaluation flights took place on a day with significant cross winds and turbulent air that resulted in added workload for the precision offset landing task. The same Smart-Gain and combined force Smart-Cue produced the best results for both pilots. This combination consistently gave desired performance with no PIO tendencies over repeated evaluations, which was significant considering that the wind conditions varied from run to run. The third pilot flew on a calm air day, which allowed him to use smoother pilot inputs associated with his lower gain technique. In this environment, the Smart-Gain alone did much of the work and only small Smart-Cue forces that may have been imperceptible to the pilot were ever present.

Main finding of Chapter 8
When used together, the Smart-Gain and Smart-Cue were found to enhance flight safety in the approach and landing task by significantly reducing pilot-vehicle system loss of control incidents including PIO that routinely occurred with the rate limited alone configuration.

13.2.5 Chapter 9: Flight Test Evaluation of the Smart Adaptive Flight Effective Cue (SAFE-Cue)

SAFE-Cue is a software system that is designed to be integrated with an existing flight control system. To use the system as intended, an active inceptor and tailored mechanizations of the software are required. The general composition of the SAFE-Cue mechanization structure is the same for both the pitch axis and the roll axis. Here, "mechanization" simply refers to the functions defining each component of the SAFE-Cue system. The SAFE-Cue system provides force feedback to the pilot via an active control inceptor with corresponding command path gain adjustments based on a measured system error between the adaptive controller response and a nominal system response [12]. The SAFE-Cue alerts the pilot that the adaptive control system is active, provides guidance via force feedback cues, and attenuates commands, thereby ensuring pilot-vehicle system stability and performance in the presence of damage or failures. While the focus herein is on an adaptive controller, the SAFE-Cue concept is completely general and can be applied to any fly-by-wire flight control system implementation to mitigate loss of control.

The adaptive controller is described in [13]. In short, the system, as illustrated via the block diagrams of Figure 13.4, defines the magnitude of the adaptive command path gain and the intensity of the force feedback cue as a function of a pitch rate (as shown) or roll rate system error. Both systems can operate simultaneously. Thresholds on the system error are set so that there is no SAFE-Cue activity below these values. Above the threshold, the adaptive gain and force cue activate. The thresholds for the gain and force cue engage independently. The resulting force cue is a combination of a gradient-based force that approximates an effective feel system spring gradient change and a viscous friction-like force that is a function of the velocity of the inceptor motion as described further in Chapter 10 and [14]. There is only one nominal system model, so when the gain and force are both engaged, the input to the nominal system for the inceptor force feedback loop is $\delta_c^{'}$.

All SAFE-Cue flight test sorties were conducted with the Calspan Learjet In-Flight Simulator and originated from the Calspan facility at the Niagara Falls International Airport in Niagara Falls, NY. Evaluations maneuvers were conducted at an altitude of 15,000 ft and an airspeed of 250 KIAS. The duration of each sortie was just under 2 hours with approximately 1.5 hours of evaluation time. While ratings and comments were taken in both flights, the first flight was considered a familiarization flight as described in an earlier section. The first flight for each pilot was a familiarization flight in which the pilot was methodically led through the baseline configuration, the failure scenario, and the SAFE-Cue mechanizations for each axis. The flight test engineer explained what the pilot could expect before each run including how the SAFE-Cue system would affect the pilot. The pilot was asked to give a handling qualities rating (HQR) and a pilot-induced oscillation rating (PIOR) after each run and could request a repeat of the case if needed. The second flight featured "blind" evaluations, that is, the pilot had no knowledge of the various configurations as they were introduced. The baseline configuration, failure only case, and SAFE-Cue mechanizations were randomly ordered for each axis. The pilot was asked to fly and rate each without knowledge of the aircraft configuration or the SAFE-Cue mechanization. As before the pilot could request to redo a case if needed. Three test pilots, (Pilots A, B, and C), served as evaluators for the flight test campaign.

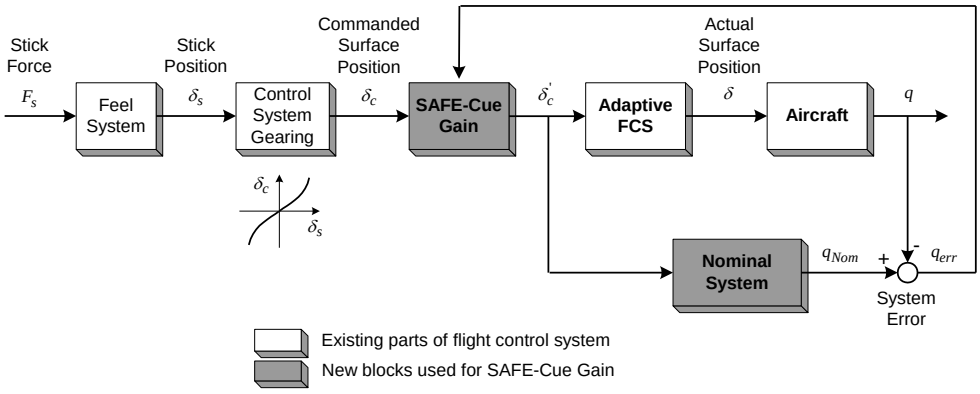

(a) Adaptive command path gain

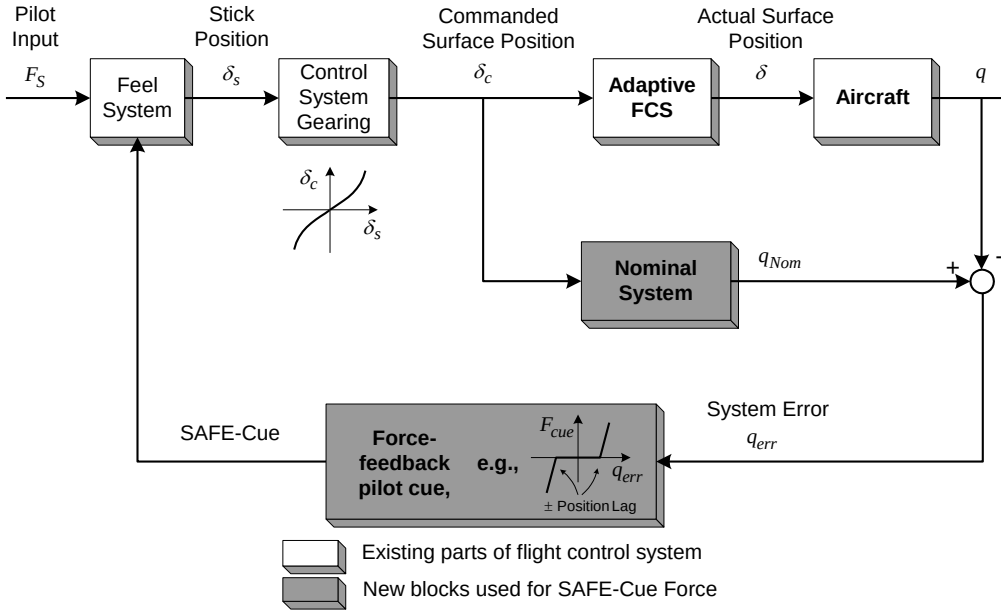

(b) Active force feedback cue

Figure 13.4: *SAFE-Cue system block diagrams.*

The purpose of the flight test program was to validate SAFE-Cue as a means to mitigate pilot-vehicle system loss of control including pilot-induced oscillations in the presence of

damage/failures. The selected adaptive controller and SAFE-Cue system integrated well with the Calspan Learjet model following system allowing for real-time operations and on-the-fly parameter adjustments. Pitch and roll sum-of-sines tracking tasks were used to evaluate the SAFE-Cue system, one at axis at a time. In the presence of only the reduced control surface effectiveness, the linear failure, the adaptive controller compensated well and effectively restored near baseline configuration performance. For the reduced control surface effectiveness plus rate limiting, the nonlinear failure, Pilots B and C routinely reached a Learjet safety trip indicating loss of control, while Pilot A demonstrated a "golden arm" technique that preserved control, but nevertheless clearly exposed configuration deficiencies including increased pilot-induced oscillation tendencies.

From the task performance, system error scalograms, and crossover frequency metrics and pilot ratings and questionnaire results, there is a clear mitigating effect of the SAFE-Cue technology from which several conclusions can be drawn. In general, the pilots preferred and responded best to the linear or nearly linear SAFE-Cue mechanizations that resulted in a more predictable aircraft response. In the presence of the nonlinear failure, several gain only and gain plus force feedback SAFE-Cue configurations resulted in performance that approached that of the baseline healthy aircraft for each pilot. Finally, there were individual differences noted between pilots regarding SAFE-Cue configuration preference. A larger pilot sample size is needed to explore these preferences and eventually assign bounds or ranges to the mechanization parameters.

As the SAFE-Cue technology advances, there will likely be differences in system mechanization requirements between aircraft types as well. Thus, the ranges that define "good" force cue and gain reduction intensities could eventually be established for diverse aircraft types. Finally, while the flight test results described in this paper were achieved in the presence of a representative adaptive controller, the SAFE-Cue technology is completely general in approach and with verification it can be applicable to any fly-by-wire aircraft. Active inceptor technology is required to fully utilize the system with force feedback cueing.

Main finding of Chapter 9
Several SAFE-Cue mechanizations were found to restore predictable adaptive control system responses in the presence of failures with task performance measures and pilot ratings/comments that approached those assigned for the baseline healthy system.

13.2.6 Chapter 10: Build-Up of an Active Inceptor Cueing Force

When approaching instability, linear system performance degrades in a manner that is predictable to a pilot. As nonlinearities are introduced, however, gradual degradations can be replaced by sudden changes in aircraft behavior resulting in the so called "handling qualities cliff." With few warning signs provided by the aircraft as the pilot approaches such a cliff, loss of control can easily occur. An example divergent PIO is shown in Figure 13.5. This is an example loss of control event first described in Chapter 8. Here, the pilot is attempting a precision offset landing with an aileron maximum rate of ±30 deg/s. The rate limit nonlinearity results in a diverging PIO as the pilot attempts the final centerline capture. Fortunately, the likelihood of finding a handling

qualities cliff in transport category aircraft outside of flight test is rare. Of course, this also means that pilots are typically not prepared to respond when such an encounter occurs. To provide an effective alerting and, if necessary, constraining mechanism, one must first be able to identify an impending cliff. In the case of control surface rate limiting, for example, it is not good enough to simply identify when the rate limiter is active. Because of the nature of rate limiting [10], an aircraft can routinely operate at or near a rate limit without threat of loss of control. Thus, to alert the pilot of an active rate limit would diminish the effectiveness of the alert due to the number of false alarms.

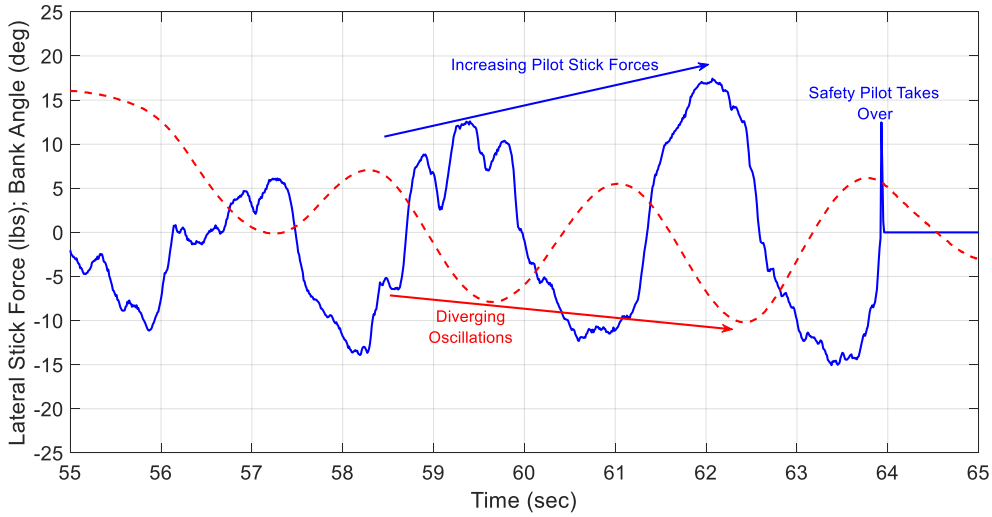

Figure 13.5: *Example flight test divergent PIO.*

Although the fundamental force feedback concept has remained essentially fixed, many options are available regarding how the Smart-Cue or SAFE-Cue is mechanized and integrated within a modern flight control system. As the force feedback cue builds, it first provides an alerting function of an impending handling qualities cliff. Then as the force increases, it provides a constraining function, so that inputs that may lead the pilot-vehicle system over the cliff will be avoided. For the Smart-Cue, piloted simulation was used to evolve the mechanizations that were eventually evaluated in flight. Several feedback force options were considered individually and in various combinations. Options included a force that produced an effective spring gradient change, a coulomb friction force, and damping forces based on control stick velocity and the rate of change of the Position Error. For the initial SAFE-Cue mechanizations, lessons learned from the Smart-Cue simulator and flight test evaluations were used to more rapidly define effective design options.

Pilot force cueing via an active control inceptor can be used in combination with adaptive command path gain reductions to mitigate pilot-vehicle system loss of control. Two such concepts have been developed for this role, the Smart-Cue/Smart-Gain that was developed to alleviate the

impact of control surface actuator rate limiting and the SAFE-Cue that was developed to improve pilot-vehicle performance in the presence of an adaptive flight controller and failures or damage.

Main finding of Chapter 10
When using active force feedback cueing to mitigate PIO, novel combinations of coulomb friction and gradient forces were found to provide the most desirable cues in both pitch and roll axis evaluations conducted in flight test.

13.3 Part III: PIO Detection

13.3.1 Chapter 11: Exposing Unique Pilot Behaviors from Flight Test Data Leads to a New PIO Detection Method

During the flight test program that was evaluating the SAFE-Cue pilot-vehicle system loss of control mitigation scheme as described in Chapter 9, one of the three evaluation pilots, Pilot B, displayed a unique "bang-bang" control strategy while performing a roll axis tracking task. This behavior was observed for all aircraft configurations presented to the pilot. For those on board the aircraft, it was clear that this pilot had an adverse physiological response to the pitch tracking tasks evaluations, which then impacted the roll tracking tasks that followed. In Chapter 11, the observed behavior of this pilot was analyzed and compared with Pilot C to assess the impact of this unique control strategy on task performance, compensation, and resulting pilot opinion ratings. As part of the analysis, a new time-varying PIO metric was introduced that clearly illustrates the differences in the observed pilot behaviors.

Building upon past work, a new scalogram-based PIO metric, the Inceptor Peak Power-Phase (IPPP), was conceived that features a time-varying measure of peak input power at a given time versus weighted phase lag. Results showed that the Pilot C case did not build up in amplitude and there was significant margin from the critical phase lag range near -90 degrees. For the Pilot B case, the input power grew significantly over the course of the run and once the locus of points entered the critical phase lag region, they remained in this region for the remainder of the run. Though a much more thorough review of available data is required to elevate this analysis method to that of a candidate PIO criterion, the results presented in this chapter show promise.

Main finding of Chapter 11
Based on the analysis of limited flight test data, the Inceptor Peak Power-Phase (IPPP) PIO detection metric was defined and successfully used to characterize flight test data from the SAFE-Cue evaluation sorties.

13.3.2 Chapter 12: Assessment of a Scalogram-Based PIO Metric with Flight Test Data

As new aircraft continue to be introduced with configurations that are designed to push performance and efficiency envelopes using advanced fly-by-wire control system concepts, the potential for pilot-induced oscillations (PIO) will continue to be a concern. In Chapter 12, the utility of the inceptor peak power-phase (IPPP) PIO metric was explored using the Smart-Cue/Smart-Gain flight test database that featured 26 cases, three evaluation tasks, three evaluation test pilots, and a full range of assigned PIO tendency ratings. Before applying the metric, characteristics of the PIO signature were applied to define a normalizing term for the inceptor peak power. Initial PIO/no-PIO boundaries were established, and the effectiveness of these boundaries was assessed using the 26 flight test cases. The results of the assessment initially found that 23 of the 26 cases were correctly identified as a PIO or no-PIO case based on the assigned PIO tendency ratings. Further analysis of the three "missed" cases revealed that the metric was working as intended and no modifications to the current boundaries was needed. While the results shown herein are promising, further investigation of the IPPP approach is recommended with currently available or newly collected flight test data using a variety of aircraft configurations, that is, PIO susceptible and PIO resistant, and evaluation tasks.

Main finding of Chapter 12
The Inceptor Peak Power-Phase (IPPP) metric can be used analytically as a PIO predictive tool or as a real-time control room monitoring tool.

13.4 General Conclusion

Pilot-induced oscillations – PIO in short – have been a handling qualities challenge for aircraft designers since the first powered flights of the Wright Brothers on December 17, 1903. Over the decades since those first flights, awareness of PIO has increased, but like an intelligent foe, PIO has adapted to the increasing complexities of the pilot-vehicle system and can now, in the age of fly-by-wire, hide within the complexities of modern flight control laws until the necessary triggering event occurs. As highlighted throughout this thesis, a common element of all the severe PIOs encountered in modern fly-by-wire aircraft is the presence of control surface actuator rate limiting. With respect to this observation, the following general conclusions are made regarding the impact of rate limiting, updated from those originally stated in [10]:

Rate limiting of control effector actuators can have dire effects on handling qualities and PIO. The magnitude of the effects depends on three basic factors:

1. How long the actuator is rate limited. This reflects the near saturation versus highly saturated cases. It is the highly saturated cases that pose the greatest threat of PIO.
2. How much more the pilot/flight control system demands of the airplane. If the mission task requires more than the system can give, the demands of the task can lead to PIO.

3. The consequences on aircraft dynamics of encountering the limit. Here, the concern is that the rate limiting can expose the pilot to the open loop unaugmented airframe dynamics that may be unstable. In cases such as the JAS 39 Gripen, this led to a catastrophic divergent PIO.

Rate limiting can cause PIO. Fundamentally, rate limiting introduces phase lag into the aircraft's response. This alone can be sufficient to lead to pilot-induced oscillations, depending upon the characteristics of the aircraft. Flight 1-1-5 of the X-15 provides a perfect example of this effect. If the aircraft is augmented, reaching a rate limit also means a sudden change in response dynamics as the aircraft transitions from the closed-loop to the open-loop response. If the open-loop response is unstable, divergent PIO is likely, especially when the additional phase lag is introduced.

Rate limiting does not necessarily cause PIO. If the response characteristics of the basic aircraft are of sufficiently high bandwidth the additional phase loss due to rate limiting will not lead to PIO. That is, the excess phase margin within the system can absorb the additional phase lag generated by the rate limiting. Designs with such margins are rare.

PIO can lead to rate limiting. If an aircraft is susceptible to PIO even when there is no rate limiting, the occurrence of sustained PIO can ultimately push control surface effectors onto their rate limits.

Rate limiting is a nonlinear phenomenon and hence is highly dependent upon pilot technique. It is possible for two pilots to have vastly different opinions of the same aircraft simply depending upon their control strategies. Despite the best attempts at devising consistent, repeatable evaluation tasks, some pilots will naturally adopt strategies that will minimize the chance of ever encountering the rate limiting. This is why it is critically important that aircraft, and highly-augmented aircraft especially, be evaluated by as many pilots as possible.

13.5 Recommendations

Building upon the research found in this thesis, the next generation of control designers are encouraged to address the challenging PIO cases that not only involve nonlinear system behavior, but also transitions between flight control system modes, that is, Category III PIO. This may prove to be significant for the emerging class of electric vertical takeoff and landing (eVTOL) rotorcraft that will almost certainly feature highly augmented vehicle dynamics and flight control modes that engage as a function of airspeed. In these cases, three or more mode transitions may occur as the vehicle accelerates from hover to cruise. For this class of vehicles as well as any other future piloted aviation system, application of appropriate PIO analysis methods, detection schemes, and mitigation approaches must be included as part of the design process from the assessment of computer simulation models, piloted simulation evaluations, and finally flight test.

13.6 References

1. McRuer, D. T., "Human Dynamics and Pilot-lnduced Oscillations," *Twenty-Second Minta Martin Lecture* given by the author as the Jerome Clarke Hunsaker Professor of Aeronautical Engineering, Massachusetts Institute of Technology, Cambridge, MA, Dec. 2, 1992.

2. Ashkenas, I. L., H. R. Jex, and D. T. McRuer, *Pilot-Induced Oscillations: Their Cause and Analysis*, Norair Report NOR-64-143, Northrop Corporation, July 24, 1964.

3. Smith, J. W., and D. T. Berry, *Analysis of Longitudinal Pilot-Induced Oscillation Tendencies of YF-12 Aircraft*, NASA TN D-7900, Febuary 1975.

4. Dornheim, M. A., "Report Pinpoints Factors Leading to YF-22 Crash," *Aviation Week and Space Technology*, 9 November 1992, pp. 53-54.

5. Rundqwist, L., and R. Hillgren, "Phase Compensation of Rate Limiters in JAS 39 Gripen," AIAA-96-3368 presented at the *Atmospheric Flight Mechanics Conference*, San Diego, CA, 29-31 July 1996.

6. McRuer, D. T., *Pilot-Induced Oscillations and Human Dynamic Behavior*, NASA CR-4683, Dec. 1994.

7. Anon., *Aviation Safety and Pilot Control*, prepared by the National Research Council Committee on the Effects of Aircraft-Pilot Coupling and Flight Safety, National Academy Press, Washington, D.C., 1997.

8. Smith, J. W., and J. W. Edwards, *Design of a Nonlinear Adaptive Filter for Suppression of Shuttle Pilot-Induced Oscillation Tendencies*, NASA TM-81349, 1980.

9. McRuer, D. T., *Pilot-Induced Oscillations and Human Dynamic Behavior*, NASA CR-4683, Dec. 1994.

10. Klyde, D. H., and D. G. Mitchell, "Investigating the Role of Rate Limiting in Pilot-induced Oscillations," *J. Guidance, Control, and Dynamics*, Vol. 27, No. 5, Sept.-Oct. 2004, pp. 804-813.

11. Klyde, D. H., and C. Y. Liang, "Approach and Landing Flight Test Evaluation of Smart-Cue and Smart-Gain Concepts," *J. of Guidance, Control, and Dynamics*, Vol. 32, No. 4, July-Aug. 2009, pp. 1057-1070.

12. Klyde, D. H., A. K. Lampton, N. D. Richards, B. Cogan, "Flight Test Evaluation of a Loss of Control Mitigation System," *J. of Guidance, Control, and Dynamics*, Vol. 40, No. 4, April 2017, pp. 981-997.

13. Richards, N. D., R. J. Adams, D. H. Klyde, and B. Cogan, “Flight-Test Evaluation of Adaptive Controller for Flying Qualities Specification and Protection,” *J. of Guidance, Control, and Dynamics*, Vol. 38, No. 12, Dec. 2015, pp. 2241-2256.

14. Klyde, D. H., C. Y. Liang, N. Richards, R. J. Adams, and B. Cogan, “Use of Active Inceptor Cueing to Mitigate Pilot-Vehicle System Loss of Control,” AIAA Paper 2012-4765 presented at the *Guidance, Navigation, and Control Conference*, Minneapolis, MN, Aug. 13-16, 2012.

APPENDIX

1.0 USE OF WAVELETS FOR TIME-VARYING PILOT-VEHICLE SYSTEM ANALYSIS

Wavelet transforms are a relatively new way of characterizing time-varying systems. Rather than just a power versus frequency relationship averaged over an entire time history, the use of wavelet transforms can produce plots of power or auto-spectrum versus both time and frequency [1]. The power frequency was developed to utilize this time-varying auto-spectrum to illustrate the differences in the frequency and intensity of signals as a function of time. This intensity has been shown to differentiate run-to-run and pilot-to-pilot characteristics in pilot-vehicle system behavior [2]. The mathematical treatment of wavelets [3] starts by defining the wavelet as a function of time $\psi(t)$ with zero average:

$$\int_{-\infty}^{\infty} \psi(t)dt = 0 \tag{A.1}$$

The wavelet is *dilated* with the scale parameter *s* and *time-translated* by the parameter *u*. The wavelet function, Equation A.2, and its Fourier transform, Equation A.3, are:

$$\psi_{u,s}(t) = \frac{1}{\sqrt{s}}\psi\left(\frac{t-u}{s}\right) \tag{A.2}$$

$$\hat{\psi}_{u,s}(f) = e^{-i2\pi fu}\sqrt{s}\,\hat{\psi}(sf) \tag{A.3}$$

To analyze phase information, a complex analytic wavelet function is used, where "analytic" means that $\hat{\psi}(f) = 0 \text{ for } f < 0$, and the 'hat' over ψ indicates that this term is estimated. The wavelet transform is defined using the wavelet function $\psi(t)$ applied to the time signal of interest:

$$W_y(u,s) = \int_{-\infty}^{\infty} y(t)\psi_{u,s}^*(t)dt = \int_{-\infty}^{\infty} \hat{y}(f)\hat{\psi}_{u,s}^*(f)df \tag{A.4}$$

In the above equation, the * indicates a complex conjugate. The wavelet transform localizes signal energy in time and frequency because:

- $\psi_{u,s}(t)$ is centered at time *u* with a spread proportional to *s*; and
- $\hat{\psi}_{u,s}(f)$ is centered at frequency 1/s with a spread proportional to 1/*s*.

Unlike the windowed Fourier transform (see Figure A1.1a), the wavelet transform time window is smaller as the frequency increases (see Figure A1.1b).

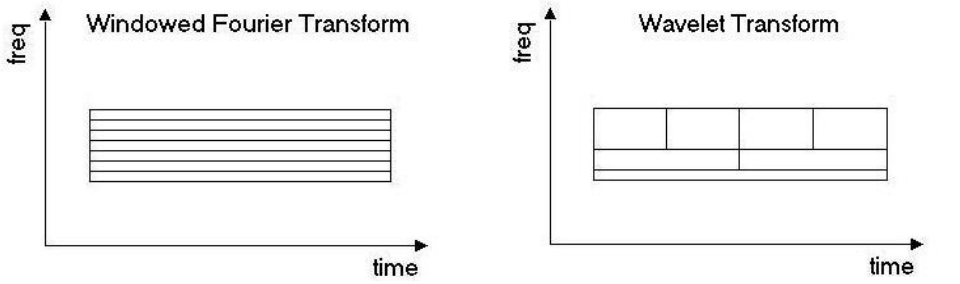

(a) Time window is constant with frequency (b) Time window decreases with frequency

Figure A1.1: *Comparison of frame sizes for windowed Fourier transforms and wavelet transforms.*

The square-magnitude of the Wavelet transform has the same units as an auto-spectrum, [units^2/Hz], but is a biased estimate. A multiplicative factor is introduced to remove the bias and the result is called the "scalogram."

2.0 SCALOGRAMS

The implementation of the scalogram presented herein is a filter bank [4] defined using wavelet functions. Each line of the filter bank in Figure A2.1 outputs the scalogram at one frequency, which corresponds to one horizontal line in Figure A1.1(b).

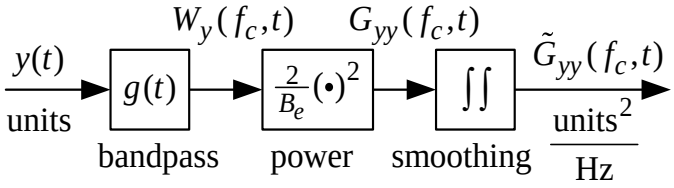

Figure A2.1: Filter bank.

The impulse response of the bandpass filter defined using the scaled wavelet function is:

$$g(t) = f_c^{1/2}\psi(f_c t)e^{+j2\pi f_c t} \tag{A.5}$$

The time signal $\psi(t)$ is now the envelope of the wavelet function. The Morlet wavelet, for example, has a bell-shaped envelope. The bandpass center frequency is f_c and the so-called equivalent bandwidth, B_e, [4] is defined by:

$$B_e = \int_{-\infty}^{\infty} |\, g(t)\,|^2 \; dt = \int_{-\infty}^{\infty} \psi^2(\tau) d\tau \tag{A.6}$$

The scalogram at a single frequency is then:

$$G_{yy}(f_c, t) = \frac{2}{B_e} |\, W_y(f_c, t)\,|^2 \tag{A.7}$$

To check units, define $y(t)$ as before with units (of the time varying signal) and define $\psi(t)$ as unitless, then $g(t)$ is $\sqrt{\text{Hz}}$, W_y is units/$\sqrt{\text{Hz}}$, B_e is unitless, and G_{yy} has units^2/Hz, which are the usual units for an auto-spectrum. The "2" in the definition of G_{yy} (A.7) makes it a one-sided auto-spectrum. If rad/s are the preferred units, then substitute $\omega_c = 2\pi f_c$ and the auto-spectrum then has units^2/(rad/s). For the analysis conducted in this thesis, the scalogram filter bank is effectively a series of FFT computations, each at a fixed window, wherein the frequency units of the computations were rad/s.

The implementation uses a finite length bandpass filter with the length of $g(t)$ equal to n_c/f_c seconds, where n_c is the number of cycles. Each point in the two-dimensional plot of $G_{yy}(f_c,t)$ is interpreted as the weighted power of the input signal $y(t)$ at the frequency f_c over a time window of length n_c/f_c. The "weight" is the wavelet function. There is no restriction on the selection of frequencies in the filter bank. The preferred choice is a log-spaced set of frequencies over a selected range.

3.0 SCALOGRAM EXAMPLE

The different frame sizes for the wavelet transform allow for transient analysis, while the windowed Fourier transform is an average response for that frame. To illustrate these differences the windowed Fourier transform and wavelet transform of a simple time series input consisting of two sinusoids of equal amplitude and duration is shown in Figure A3.1(a). Note that the auto-spectrum or power of the windowed Fourier transform, Figure A3.1(b), shows the two distinct peaks associated with the input sinusoids. The peak power and area are equivalent at each sinusoid frequency. In the top left of Figure A3.1(c) the "mother" wavelet is the Morlet [1]. The Morlet is probably the most popular of the continuous wavelet transforms and is defined by setting the window function *g(t)* to a Gaussian envelope. The Fourier transform of the Morlet with a center frequency of 1 Hz is shown in the top right of Figure A3.1(c). When compared to the windowed Fourier transform, the wavelet scalogram not only shows the peaks in power, but also shows when in time the sinusoids occurred. It is this characteristic that makes wavelets a powerful tool for detecting changes in more transient or time varying pilot-vehicle systems including PIO scenarios.

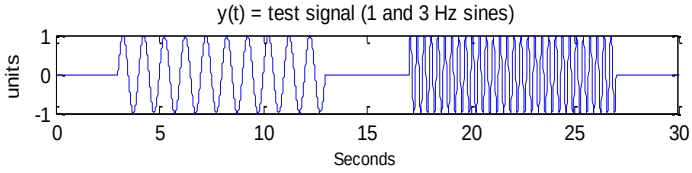

(a) 1 and 3 Hz Sine Wave Time Series

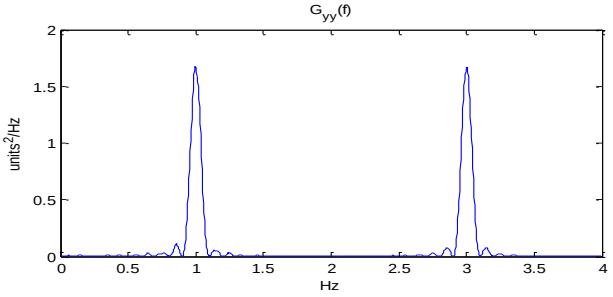

(b) Windowed Fourier Transform Auto-Spectrum

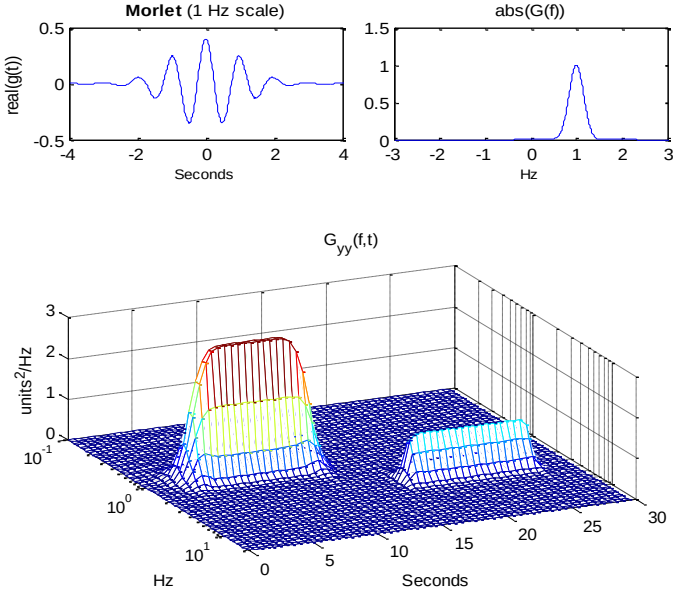

(c) Wavelet Transform Auto-Spectrum or Scalogram

Figure A3.1: *Transforms of an example time series.*

When the scalogram results presented in Figure A3.1(c) are displayed as a two dimensional plot of power versus linear frequency as shown in Figure A3.2 wherein the time axis now goes into the page and is therefore not shown, it is easier to see that the power at the two frequencies, power being the area under the curve, is the same. At the higher frequency the peak decreases and the width increases by the same amount.

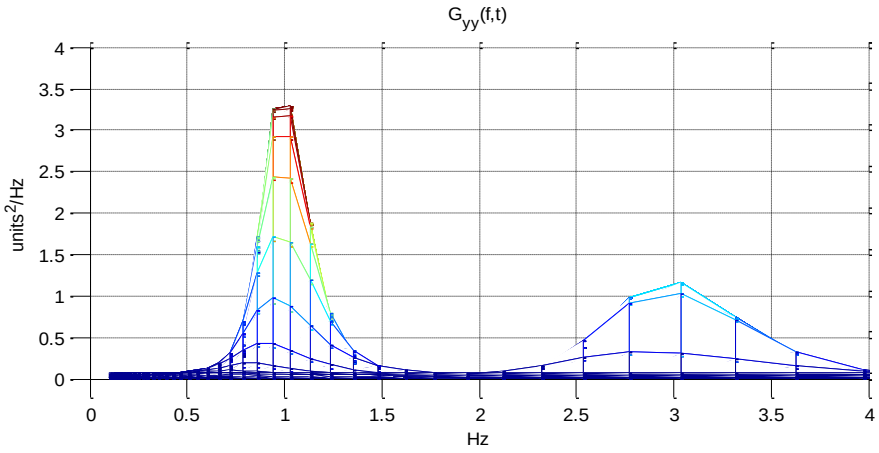

Figure A3.2: *Scalogram (linear frequency scale).*

4.0 SMOOTHING

A stochastic analysis of the filter bank is summarized in [1] and [4]. One of the properties of the G_{yy} signal in Figure A2.1, which includes the multiplicative factor $2/B_e$, is that for a stochastic input the expected value of G_{yy} equals the actual value of G_{yy}, in other words the filter bank gives an unbiased estimate [1].

If the conditions used for estimation are not ideal, and outside of an experimental setup this will almost certainly be the case, then the expected value has a large standard deviation and some sort of smoothing technique is needed. The approach herein uses averaging over both time and frequency:

$$\tilde{G}_{yy}(f_c,t) = \frac{1}{\Delta f\,\Delta t}\int_{f_c-\Delta f/2}^{f_c+\Delta f/2}\int_{t-\Delta t/2}^{t+\Delta t/2} G_{ff}(f,t)\,dt\,df \qquad \text{(A.8)}$$

The tilde is used to denote a smoothed estimate. This double integral is the last block in Figure A2.1. The expected value of the smoothed estimate is also unbiased, but what is different is the standard deviation decreases with the amount of averaging, basically being inversely proportional to the area $\Delta f \Delta t$. Of course, there is always a tradeoff between smoothing and detection of system

changes. That is, the more the signal is smoothed, the longer it will take to identify a change in the system. Also, if Δf is wide enough to average features in the time-varying system response then the estimate becomes biased.

5.0 REFERENCES

1. Thompson, P. M., D. H. Klyde, E. N. Bachelder, and T. J. Rosenthal, *On-line Loss of Control Detection using Wavelets*, NASA CR-2005-212873, July 2005.

2. Lampton, A. and Klyde, D. H., "Power Frequency – A Metric for Analyzing Pilot-in-the-Loop Flying Tasks," *Journal of Guidance, Control, and Dynamics*, Vol. 35, No. 5, September-October 2012, pp. 1526-1537.

3. Mallet, S., A Wavelet Tour of Signal Processing, Academic Press, San Diego, CA, 1998.

4. Bendat, J. S., and A. G. Piersol, Random Data Analysis and Measurement Procedures, 3rd Edition, Wiley-Interscience, New York, 2000.

ACKNOWLEDGEMENTS

My journey as a professional engineer began with Professor Paul Lord of Cal Poly Pomona. As an unofficial count, I had him as a professor at least a dozen times including my senior design class and senior project. He was not only a valued professor, but also an important mentor. In this mentor role, he encouraged me to pursue a job opportunity at Systems Technology, Inc. (STI), my professional home for the last 35 years. When I interviewed for the job, I had little knowledge of the company's long history of accomplishments and the industry leaders that made up the staff. I learned soon enough!

The first person I must acknowledge at STI is Henry Jex, STI's original Chief Scientist. Henry interviewed me for the entry level position, a 1 hour interview that lasted all day, and was my direct supervisor for my first few years at the company. Henry taught me how to be a professional engineer – analysis, data presentation, technical writing, customer interactions, and more. Any recognitions regarding STI must next include Duane McRuer and Irv Ashkenas, STI's co-founders. It was with Irv that I secured my first professional publication – a NASA contractor report involving analysis of flying wing aircraft. Mac, nobody who knew him called him Duane, became my most important professional mentor. I was fortunate to have most of my interactions with Mac after he retired and was no longer concerned with the day to day burdens of running a company. Thus, our time together at work where he was a consultant and I was a young project engineer focussed on technical learning and collaboration – handling qualities and PIO, pilot modeling, control system design and analysis, nonlinear systems, and more. Outside of work, Mac and his wife Betty took me and my wife Leila under their wings where we shared many cherished times together.

I must next acknowledge my professional collaborator for more than 30 years and, more importantly, my friend, David Mitchell. I started working with Dave while he was still at STI and never stopped. We share a passion for aircraft handling qualities and the elimination of PIO as a threat to modern aircraft. We have travelled the US and abroad with our PIO short course that we created together nearly 20 years ago and have collaborated on many projects, papers, and other professional activities. Without Dave, I would not have achieved the milestones necessary to warrant a thesis that I hope is *satisfactory without improvement* in the words of the Cooper-Harper scale.

There are many others at STI to acknowledge. First, there is Tom Myers, who in my first PIO-related project gave me the freedom to explore my crazy ideas that ultimately resulted in the exact describing function of a rate limited actuator that is an important element of this thesis. Next, I must acknowledge Dr. Chi-Ying Liang. Chi worked with me tirelessly in our piloted simulator with its McFacdden hydraulic control loader to develop what ultimately became the working Smart-Cue and Smart-Gain concepts. Dr. Amanda Lampton picked up where Chi left off and helped to adapt Smart-Cue and Smart-Gain for SAFE-Cue. While at STI, Daniel Alvarez was an important contributor to the SAFE-Cue aircraft model development. For PIO data analysis, no one has supported me more than Chase Schulze, a partner on many projects at STI to this day.

When it comes to wavelet-based identification tools, Dr. Peter Thompson was the king. Peter hepled realize the scalogram tools that Amanda and I turned into the Power Frequency metric and Chase and I tuned into the IPPP metric.

I would also like to acknowledge the business office staff at STI including Suzie Fosmore and Alyson Page who have always provided me the support I need with care and humor. Last, but certainly not least, I must recognize STI's CEO, Sanjeev Weerasuriya. Sanjeev has supported and encouraged my efforts on this thesis and has helped me to become a better leader inside STI and within the industry I serve.

Outside of STI, I would like to first acknowledge Brian Lee of Boeing Commercial Airplanes for his support of the Smart-Cue/Smart-Gain and SAFE-Cue programs wherein he provided engineering support and test pilot participants for the piloted simulation activities at STI prior to flight and the flight test campaigns at Calspan. From NASA Armstrong Flight Research Center, I recognize the efforts of Timothy Cox for Smart-Cue/Smart-Gain and Bruce Cogan for SAFE-Cue. These programs could not have been successfully completed without their guidance and support as the NASA contracting officer technical representatives. Finally, I must give a big thanks to the team at Calspan without whom there would not have been successful flight test campaigns. This especially includes the technical leadership of Paul Schifferle and the test pilot professionalism and expertise of Paul Deppe and Lou Knotts.

This thesis would not have been possible without the support of the team at TU Delft. In particular, I must give special thanks to my promotors, Dr. Max Mulder and Dr. Rene van Paassen, who guided me through this process with thoughtful guidance, encouragement, and technical leadership.

My final acknowledgements are for the most important people in my life – my family. My sons Joshua and DJ who have been and continue to be the inspiration for my desire to be a life long learner. I also acknwledge my mother, Barbara, who pushed me – hard – to reach for the stars and my brother, Michael, who shares my work ethic and many inerests. Most significantly, I acknowledge the love, support, encouragement, friendship, and patience of my wife Leila. Our partnership of nearly 30 years is the reason this thesis exists.

David H. Klyde, Cerritos, California, USA, March 2022

CURRICULUM VITAE

David Howard Klyde was born on April 21, 1965, in Buffalo, NY, USA. He attended California State Polytechnic University, Pomona where he received a B.S. in Aerospace Engineering in 1987 and a M.S. in Engineering in 1990. David joined Systems Technology, Inc. (STI) in 1987 as a Staff Engineer, Analytical. In his time at STI he rose to Staff Engineer, Research, Senior Research Engineer, Principal Research Engineer, Technical Director, and currently Vice President and Technical Director, Engineering Services. In his current role, he is responsible for government funded R&D and commercial consulting activities. This includes business development and technical direction of the engineering services team. In addition, he continues to serve as Principal Investigator on several engineering services programs.

Over his 35-year professional career, David's air vehicle experience includes dynamic analysis and system identification, flight control system design and analysis, human operator models, and handling qualities research for transport, fighter, drone, flying wing, rotorcraft and V/STOL, and hypersonic aircraft. His piloted simulation experience includes development of high speed mission task elements for the handling qualities evaluations of future vertical lift designs, development of spatial disorientation training scenarios for hexapod-based simulators, loss of control mitigation assessments using the NASA Ames Vertical Motion Simulator (VMS), rotorcraft added dynamics studies at the VMS, control inceptor force feedback cueing, on-line loss of control detection using wavelet-based techniques, handling qualities demonstration maneuvers development, moderate amplitude maneuvering criteria development, aircraft ground handling evaluations, and a hypersonic flying qualities study. His flight test experience includes loss of control alleviation and handling qualities evaluations using the Calspan Learjet in-flight simulator, ground handling evaluation of the Navy T-45 jet trainer, a probe-and-drogue demonstration maneuver evaluation program conducted by the USAF Test Pilot School using the variable stability NT-33A, a post-stall maneuvering program with the NASA F/A-18 High Alpha Research Vehicle, and a high speed flying qualities research program with a NASA SR-71.

David's rotorcraft specific experience includes: development of certification means of compliance methods for Part 23 VTOL aircraft; piloted simulation evaluation of high speed mission task elements for military rotorcraft; application of wavelet-based techniques to investigate time-varying rotorcraft dynamics especially in the presence of lightly damped slung loads; support of fly-by-wire flight control design, handling qualities assessments, and biodynamic feedthrough assessments of a new military cargo helicopter; support of the development of an active cyclic autorotation aid for naval helicopters, participation in the V-22 PIO review team, and determination of the minimum cues required to simulate rotorcraft shipboard landings.

Mr. Klyde is the co-author of the short course entitled "Pilot-Induced Oscillations: from the Wright Flyer to Fly-by-Wire." Since its inception in 2004, the course continues to be regularly taught on site for both commercial and government entities in the U.S. and abroad.

David is a Fellow and 38-Year Member, American Institute of Aeronautics and Astronautics (AIAA). His organization activities include:

Associate Editor of Journal Guidance, Control, and Dynamics (2010-present)

Co-AE for the "Loss of Control" special issue, Vol. 40, No. 4, April 2017

Member, AIAA Modeling and Simulation Technical Committee (2009-present)

Member, AIAA Corporate Member Committee (2009-present)

Corporate Member Advisory Committee, Aviation and Aeronautics (2013-2015)

Member, AIAA Atmospheric Flight Mechanics Technical Committee (1997-2008)

Committee Chair (2003-2005)

Participant in AIAA Distinguished Lecturer program (2001-2003)

Participant in AIAA E-mentor program (2007-2009)

David is a Member of the Vertical Flight Society (formerly AHS International). His organizational activities include:

Member, Handling Qualities Technical Committee (2014-present)

VFS Forum 71 Handling Qualities Deputy Session Chair (2015)

VFS Forum 72 Handling Qualities Session Chair (2016)

Handling Qualities Technical Committee Chair (2017)

David is a Member, SAE/IEEE Aerospace Control & Guidance Systems Committee (2004-present). His organizational activities include:

Planning Advisory Board (2005- present)

Chair (2010-2012)

At California State Polytechnic University, Pomona, David participates as:

Member of the Aerospace Engineering Industry Action Council (2003-present) and is Council Chair (2018-present)

Member of the School of Engineering Dean's Leadership Board (2018-present)

David's awards and honors include the following:

Outstanding Senior 1987, Aerospace Engineering Dept., California State Polytechnic University, Pomona

AIAA Certificate of Merit for Outstanding Paper at the 2006 Atmospheric Flight Mechanics Conference

"Identifying a Pilot-Induced Oscillation Signature: New Techniques Applied to Old Problems"

AIAA Certificate of Merit for 2nd Place Paper at the 2008 USAF T&E Days Conference

"Use of In-Flight Simulation to Create a Flying Qualities Database"

NASA Group Achievement Award as a participant in the NASA Very Large Air Tanker Team, May 2010

Outstanding Alumnus 2010, Aerospace Engineering Dept., California State Polytechnic University, Pomona

NASA Group Achievement Award as a participant in the Autonomous Loss-of-Control Cueing Team, August 2014

AIAA Sustained Service Award "For nearly two decades of service to AIAA including technical committee leadership, distinguished lecturer, journal associate editor, and corporate member advisory committee." presented at the AIAA Science and Technology Forum and Exposition, January 2015.

Best Paper Presentation at the 46th Society of Flight Test Engineers International Symposium, September 2015

"Flight Testing of Fused Reality Visual Simulation System"

AIAA Certificate of Merit for Outstanding Paper at the 2016 Modeling and Simulation Technologies Conference

"Development of Spatial Disorientation Scenarios for Commercial Pilot Training"

Best Paper in the Handling Qualities Session at the AHS International 73rd Annual Forum, May 2017

"Interpreting Time-Frequency Analyses of Pilot Control Activity in ADS-33E Mission Task Elements"

AIAA Certificate of Merit for Outstanding Paper at the 2017 Modeling and Simulation Technologies Conference

"Evaluation of a Steep Turn Spatial Disorientation Demonstration Scenario for Commercial Pilot Training"

Best Paper in the Handling Qualities Session at the AHS International 74th Annual Forum, May 2018

"Piloted Simulation Evaluation of Tracking MTEs for the Assessment of High-Speed Handling Qualities"

LIST OF PUBLICATIONS

Journal Publications

Klyde, D. H., P. C. Schulze, R. Mello, D. G. Mitchell, N. Cameron, C. Cunliffe, and M. White, "Assessment of a Scalogram-Based Pilot-Induced Oscillation Metric with Flight Test and Simulation Data," *J. of Guidance, Control, and Dynamics*, Vol. 43, No. 11, Nov. 2020, pp. 2058-2072.

Klyde, D. H., S. P. Pitoniak, P. C. Schulze, P. Ruckel, J. Rigsby, C. E. Fegely, H. Xin, W. C. Fell, R. Brewer, F. Conway, R. Mulato, J. Horn, C. R. Ott, and C. L. Blanken, "Piloted Simulation Evaluation of Tracking MTEs for the Assessment of High-Speed Handling Qualities," *J. of the Vertical Flight Society*, Volume 65, Number 3, July 2020, pp. 1-23(23).

Mitchell, D. G., and D. H. Klyde, "Defining Pilot Gain," *J. of Guidance, Control, and Dynamics*, Vol. 43, No. 1, Jan. 2020, pp. 85-95.

Klyde, D. H., A. K. Lampton, N. D. Richards, B. Cogan, "Flight Test Evaluation of a Loss of Control Mitigation System," *J. of Guidance, Control, and Dynamics*, Vol. 40, No. 4, April 2017, pp. 981-997.

Belcastro, C. M., J. V. Foster, G. H. Shah, I. M. Gregory, D. E. Cox, D. A. Crider, L. Groff, R. L. Newman, and D. H. Klyde "Aircraft Loss of Control Problem Analysis and Research Toward a Holistic Solution," *J. of Guidance, Control, and Dynamics*, Vol. 40, No. 4, April 2017, pp. 733-775.

Richards, N. D., N. Gandhi, A. J. Bateman, D. H. Klyde, and A. K. Lampton, "Vehicle Upset Detection and Recovery for Onboard Guidance and Control," *J. of Guidance, Control, and Dynamics*, Vol. 40, No. 4, April 2017, pp. 920-933.

Richards, N. D., R. J. Adams, D. H. Klyde, and B. Cogan, "Flight-Test Evaluation of Adaptive Controller for Flying Qualities Specification and Protection," *J. of Guidance, Control, and Dynamics*, Vol. 38, No. 12, Dec. 2015, pp. 2241-2256.

Lampton, A., and D. H. Klyde, "Power Frequency: A Metric for Analyzing Pilot-in-the-Loop Flying Tasks," *J. of Guidance, Control, and Dynamics*, Vol. 35, No. 5, Sept.-Oct. 2012, pp. 1526-1537.

Danowsky, B. P., J. P. Chrstos, Ph.D., D. H. Klyde, C. Farhat, Ph.D., and M. J. Brenner, "Evaluation of Aeroelastic Uncertainty Analysis Methods," *Journal of Aircraft*, vol. 47, no. 4, pp. 1266-1273, 2010.

Klyde, D. H., and D. McRuer, "Development of Smart-Cue and Smart-Gain Concepts to Alleviate Pilot-Vehicle System Loss of Control," *J. of Guidance, Control, and Dynamics*, Vol. 32, No. 5, Sept.-Oct. 2009, pp. 1409-1417.

Klyde, D. H., and C. Y. Liang, "Approach and Landing Flight Test Evaluation of Smart-Cue and Smart-Gain Concepts," J. *of Guidance, Control, and Dynamics*, Vol. 32, No. 4, July-Aug. 2009, pp. 1057-1070.

Mitchell, D. G. and D. H. Klyde, "Identifying a Pilot-Induced Oscillation Signature: New Techniques Applied to Old Problems," *Journal of Guidance, Control, and Dynamics*, vol. 31,no. 1, pp. 215-224, 2008.

Klyde, D. H., and D. G. Mitchell, "Investigating the Role of Rate Limiting in Pilot-induced Oscillations," *J. Guidance, Control, and Dynamics*, Vol. 27, No. 5, Sept.-Oct. 2004, pp. 804-813.

Mitchell, D. G., D. B. Doman, D. L. Key, D. H. Klyde, D. B. Leggett, D. J. Moorhouse, D. H. Mason, D. L. Raney, and D. K. Schmidt, "Evolution, Revolution, and Challenges of Handling Qualities," *J. Guidance, Control, and Dynamics*, Vol. 27, No. 1, Jan.-Feb. 2004, pp. 12-28.

Klyde, D. H., J. G. Reinsberg, E. Sanders, and A. Kokolios, "Flight Test Evaluation of Stability Augmentation Steering System for Aircraft Ground Handling," *J. Guidance, Control, and Dynamics*, Vol. 27, No.1, 2004, pp. 41-51.

Klyde, D. H., R. E. Magdaleno, and J. G. Reinsberg, "The Effect of Tire Pressure on Aircraft Ground Handling," *J. Guidance, Control, and Dynamics*, Vol. 25, No.4, 2003, pp. 558-564.

Klyde, D. H., T. T. Myers, R. E. Magdaleno, and J. G. Reinsberg, "Identification of the Dominant Ground Handling Characteristics of a Navy Jet Trainer," *J. Guidance, Control, and Dynamics*, Vol. 25, No. 3, 2002, pp. 546-552.

Klyde, D. H., D. G. Mitchell, and K. J. Latimer, "Development of the Probe-and-Drogue Handling Qualities Demonstration Maneuver," *J. Guidance, Control, and Dynamics*, Vol. 22, No. 4, July-Aug. 1999, pp. 528-535.

Klyde, D. H., D. T. McRuer, and T. T. Myers, "Pilot-Induced Oscillation Analysis and Prediction with Actuator Rate Limiting," *J. Guidance, Control, and Dynamics*, Vol. 20, No. 1, Jan. – Feb. 1997.

Conference Publications (Related to PIO)

Klyde, D. H., A. K. Lampton, D. G. Mitchell, C. Berka, and M. Rhinehart, "A New Approach to Aircraft Handling Qualities Prediction," AIAA-2021-0178 presented at the *AIAA SciTech Forum,* a Virtual Event, 11-15 and 19-21 Jan. 2021.

Klyde, D. H., P. C. Schulze, D. G. Mitchell, J. K. Tritschler, J. C. O'Connor, J. Holder, and W. Geyer, "Identifying Pilot-Induced Oscillation Tendencies in Advanced Fly-by-Wire Rotorcraft," presented at the *Vertical Flight Society 76th Annual Forum & Technology Display*, a Virtual Event, October 5–8, 2020.

Klyde, D. H., S. P. Pitoniak, P. C. Schulze, P. Ruckel, J. Rigsby, C. E. Fegely, H. Xin, W. C. Fell, R. Brewer, F. Conway, R. Mulato, J. Horn, C. R. Ott, and C. L. Blanken, "Piloted Simulation Evaluation of Tracking MTEs for the Assessment of High-Speed Handling Qualities," presented at the *AHS International 74th Annual Forum,* Phoenix, AZ, May 14–17, 2018.

Cameron, N., C. Cunliffe, M. D. White, D. H. Klyde, and R. de Mello, "Further Assessment of a Scalogram Based PIO Metric using University of Liverpool Tilt Rotor Simulation Data," AIAA-2018-1017 presented at the *Science and Technology Forum and Exposition 2018: AIAA AFM Conference*, Kissimmee, FL, Jan. 8–12, 2018.

Klyde, D. H., P. C. Schulze, R. Mello, and D. G. Mitchell, "Assessment of a Scalogram-Based PIO Metric with Flight Test Data," AIAA-2017-1641 presented at the *Science and Technology Forum and Exposition 2017: AIAA Atmospheric Flight Mechanics Conference*, Grapevine, TX, Jan. 9–13, 2017.

Mitchell, D. G., and D. H. Klyde, "Finding Commonality in the Uncommon: Encountering PIO in Flight Test," *46th Society of Flight Test Engineers International Symposium*, Lancaster, CA, 14-17 Sept. 2015.

Klyde, D. H., P. C. Schulze, and P. M. Thompson, "Exposing Unique Pilot Behaviors from Flight Test Data," AIAA Paper No. 2015-0239 presented at the *Science and Technology Forum and Exposition 2015: AIAA Atmospheric Flight Mechanics Conference,* Kissimmee, Florida, January 5-9, 2015.

Lampton, A. K., D. H. Klyde, D. C. Lee, P. C. Schulze, and B. Cogan, "Preliminary Evaluation of the SAFE-Cue Warning Display for Loss of Control Mitigation" AIAA Paper No. 2015-1544 presented at the *Science and Technology Forum and Exposition 2015: AIAA Guidance, Navigation, and Control Conference*, Kissimmee, Florida, January 5-9, 2015.

Klyde, D. H., A. K. Lampton, D. J. Alvarez, N. Richards, and B. Cogan, "Flight Test Evaluation of the SAFE-Cue System for Loss of Control Mitigation," AIAA Paper No. 2014-0447 presented at the *Science and Technology Forum and Exposition 2014: AIAA Guidance, Navigation, and Control Conference*, National Harbor, Maryland, January 13-17, 2014.

Lampton, A. K., D. H. Klyde, D. C. Lee, and B. Cogan, "Development of the SAFE-Cue System Component Mechanization for Loss of Control Mitigation" AIAA Paper No. 2014-0964 presented at the *Science and Technology Forum and Exposition 2014: AIAA Guidance, Navigation, and Control Conference*, National Harbor, Maryland, January 13-17, 2014.

Klyde, D. H., C. Y. Liang, N. Richards, B. Cogan, "Use of Active Inceptor Cueing to Mitigate Pilot-Vehicle System Loss of Control," AIAA Paper No. 2012-4765 presented at the *Guidance, Navigation, and Control Conference,* Minneapolis, MN, 13-16 Aug. 2012.

Klyde, D. H., C. Y. Liang, D. J. Alvarez, N. Richard, R. J. Adams, and B. Cogan, "Mitigating Unfavorable Pilot Interactions with Adaptive Controllers in the Presence of Failures/Damage," AIAA Paper to be presented at *Atmospheric Flight Mechanics Conference,* Portland, OR, 8-11 August, 2011.

Lampton, A. K., and D. H. Klyde, "Power Frequency – A New Metric for Analyzing Pilot-in-the-Loop Flying Tasks," AIAA Paper to be presented at *Atmospheric Flight Mechanics Conference,* Portland, OR, 8-11 August, 2011.

Klyde, D. H., P. M. Thompson, P. C. Schulze, and C. Y. Liang, "Use of Wavelet Scalograms to Characterize Rotorcraft Pilot-Vehicle System Interactions," *66th Forum of the American Helicopter Society,* Phoenix, AZ, 11-13 May, 2010.

Klyde, D. H., C. Y. Liang, and P. C. Schulze, "Applying Flight Test Lessons Learned 'On-the-Fly,'" AIAA 2009-5729 presented at *Atmospheric Flight Mechanics Conference,* Chicago, IL, August 10-13, 2008.

Klyde, D. H., and C. Y. Liang, "Flight Assessment of Pilot Behavior with Smart-Cue and Smart-Gain Concepts Active," AIAA 2009-5606 presented at *Atmospheric Flight Mechanics Conference,* Chicago, IL, August 10-13, 2008.

Klyde, D. H., and D. McRuer, "Development of Smart-Cue and Smart-Gain Concepts to Alleviate Pilot-Vehicle System Loss of Control," AIAA 2008-6209 presented at *Atmospheric Flight Mechanics Conference,* Honolulu, Hawaii, August 18-21, 2008.

Klyde, D. H., and C. Ying-Liang, "Approach and Landing Flight Test Evaluation of Smart-Cue and Smart-Gain Concepts," AIAA 2008-6210 presented at *Atmospheric Flight Mechanics Conference,* Honolulu, Hawaii, 18-21 August, 2008.

Mitchell, D. G., and D. H. Klyde, "Identifying a Pilot-Induced Oscillation Signature: New Techniques Applied to Old Problems," AIAA2006-6495 presented at *AIAA Atmospheric Flight Mechanics Conference,* Keystone, CO, 21-24 August 2006.

Klyde, D. H., and D. G. Mitchell, "A PIO Case Study – Lessons Learned Through Analysis," AIAA 2005-5813 presented at the *Atmospheric Flight Mechanics Conference,* San Francisco, CA, 15-18 Aug. 2005.

Mitchell, D. G., and D. H. Klyde, "Testing for Pilot-Induced Oscillations," AIAA 2005-5811 presented at the *Atmospheric Flight Mechanics Conference,* San Francisco, CA, 15-18 Aug. 2005.

Mitchell, D. G., and D. H. Klyde, "Recommended Practices for Exposing Pilot-Induced Oscillations or Tendencies in the Development Process," AIAA 2004-6810 presented at the *USAF Developmental Test and Evaluation Summit,* Woodland Hills, CA, 16-18 Nov. 2004.

Klyde, D. H., P. M. Thompson, E. N. Bachelder, and T. J. Rosenthal, "Evaluation of Wavelet-Based Techniques for Detecting Loss of Control," AIAA Paper No. 2004-4072 presented at *Atmospheric Flight Mechanics Conference,* Providence, RI, 16-18 August, 2004.

Thompson, P. M., D. H. Klyde, E. N. Bachelder, and T. J. Rosenthal, "Development of Wavelet-Based Techniques for Detecting Loss of Control," AIAA Paper No. 2004-5064 to be presented at *Atmospheric Flight Mechanics Conference*, Providence, RI, 16-18 August, 2004.

Klyde, D. H., and D. G. Mitchell, "Extraction of Pilot-Vehicle Characteristics in the Presence of Rate Limiting," AIAA 99-1069 presented at *37th Aerospace Sciences Meeting and Exhibit*, Reno, NV, January 11 – 14, 1999.

Mitchell, D. G., V. Sahasrabudhe, and D. H. Klyde, "Determining Bandwidth in the Presence of Nonlinearities," AIAA 99-0639 presented at *37th Aerospace Sciences Meeting and Exhibit*, Reno, NV, January 11 – 14, 1999.

Mitchell D. G., and D. H. Klyde, "A Critical Examination of PIO Prediction Criteria," AIAA-98-4335 presented at *Atmospheric Flight Mechanics Conference*, Boston, MA, August 10 – 12, 1998.

Klyde, D. H., D. T. McRuer, and T. T. Myers, "PIO Analysis with Actuator Rate Limiting," AIAA-96-3342 presented at *Atmospheric Flight Mechanics Conference*, San Diego, CA, July 29 – 31, 1996.

McRuer, D. T., D. H. Klyde, and T. T. Myers, "Development of a Comprehensive PIO Theory," AIAA-96-3433 presented at *Atmospheric Flight Mechanics Conference*, San Diego, CA, July 29 – 31, 1996.